Carlos Fernando Ávila Rodrigues

Evolução estrutural, reologia e magmatismo associado à tectônica transcorrente no Domínio Ceará Central, Província Borborema

São Paulo
2021

UNIVERSIDADE DE SÃO PAULO
INSTITUTO DE GEOCIÊNCIAS

Evolução estrutural, reologia e magmatismo associado à tectônica transcorrente no Domínio Ceará Central, Província Borborema

Carlos Fernando Ávila Rodrigues

Tese apresentada ao Programa de Pós-Graduação em Mineralogia e Petrologia para obtenção do título de Doutor em Ciências

Orientador: Carlos José Archanjo

SÃO PAULO
2021

UNIVERSIDADE DE SÃO PAULO
INSTITUTO DE GEOCIÊNCIAS

Evolução estrutural, reologia e magmatismo associado à tectônica transcorrente no Domínio Ceará Central, Província Borborema

CARLOS FERNANDO ÁVILA RODRIGUES

Orientador: Prof. Dr. Carlos José Archanjo

Tese de Doutorado

N° 641

COMISSÃO JULGADORA

Dr. Carlos José Archanjo(USP)

Dra. Renata da Silva Schmitt (UFRJ)

Dr. Luiz Gustavo Ferreira Viegas (UNB)

Dr. Sérgio Pacheco Neves (UFPE)

Dra. Carla Cristine Porcher (UFRGS)

SÃO PAULO
2021

Em homenagem a meu pai, Sávio Ávila Rodrigues

Agradecimentos

Esta obra é fruto de um esforço coletivo e não teria sido exitosa sem as devidas contribuições e incentivos de diversos professores e colegas. Portanto, expresso meus sinceros agradecimentos abaixo.

À minha mãe, Eliete, pelo respeito e apoio sempre dados incondicionalmente. À Laura, por alegrar a vida de nossa família.

Aos colegas do Instituto de Geociências da USP, Antomat, Daniel, Alisson, Kauê e Rodrigo, pelas longas discussões cotidianas que fizeram despertar novas idéias, consolidar algumas e desacreditar outras.

Ao estimado povo cearense, que em mais de uma ocasião teve decisiva participação na exploração geológica, seja por gentilmente auxiliar com carros atolados, ou por guiar a então desconhecidos milonitos e pseudotaquilitos.

Aos professores do Instituto de Geociências e do Instituto de Astronomia, Geofísica e Ciências Atmosféricas da USP, Maria Hellena de Hollanda, Marcos Egydio-Silva, Frederico Faleiros, Ricardo Trindade e Maria Irene Raposo. Aos funcionários do Instituto de Geociências, Renato, Samuel, Ideval, Katherine, Alexandre e Giovani. Em particular, devo agradecer aos ensinamentos do professor Mário Campos, em trabalhos de campo, sala de aula e laboratório.

À comunidade internacional de desenvolvedores de softwares livres, especialmente aos desenvolvedores de QGIS[1], GIMP[2], Inkscape[3], Freeplane[4] e Zotero[5].

À Universidade de São Paulo, ao Instituto de Geociências e ao Instituto de Astronomia, Geofísica e Ciências Atmosféricas, pelo apoio logístico, educacional e material. À Fundação de Amparo à Pesquisa do Estado de São Paulo (FAPESP) pelo apoio financeiro à execução desta tese, através dos projetos 2016/22226-9, 2019/10167-6 e 2017/21440-0.

---

1 QGIS Development Team (YEAR). QGIS Geographic Information System. Open Source Geospatial Foundation Project. http://qgis.osgeo.org

2 The GIMP Development Team. (2019). GIMP. Retrieved from https://www.gimp.org

3 https://inkscape.org/

4 https://www.freeplane.org/wiki/index.php/Home

5 https://www.zotero.org/

Aos professores John Platt e Haakon Fossen, pela oportunidade para colaboração e pelos fundamentais ensinamentos em teoria de deformação, reologia e tectônica.

Em especial, ao professor e orientador Carlos Archanjo, por ter concedido a oportunidade de realizar este ambicioso projeto de doutorado por ele concebido, por compartilhar um vasto conhecimento prático e teórico, e por ter conduzido este projeto com assertividade, maestria e, sobretudo, paciência.

Por último, a meu pai, Sávio, por ensejar a curiosidade dos naturalistas, e pelos exemplos de esclarecimento e autenticidade.

“Earth has not any thing to show more fair
Dull would he be of soul who could pass by
A sight so touching in its majesty”
William Wordsworth

Resumo

Estágios finais da orogênese Brasiliana (800–550 Ma) na Província Borborema do nordeste do Brasil são marcados por zonas de cisalhamento transcorrentes associadas a plutonismo granítico. No Domínio Ceará Central, as zonas de cisalhamento Senador Pompeu (NE) e Tauá (NNW) possuem cinemática conjugada (destral e sinistral, respectivamente) e circunscrevem terrenos caracterizados por metamorfismo de alto grau e migmatização. Consistem de gnaisses miloníticos, milonitos a ultramilonitos, cataclasitos e pseudotaquilitos. Em suas ombreiras e núcleos occorrem os batólitos graníticos Quixadá, Quixeramobim, Tauá, Pedra Lisa e Nova Russas. As relações genéticas entre magmatismo e evolução estrutural da transcorrência permitem determinar o real papel tectônico das zonas de cisalhamento durante a convergência e exumação no orógeno. Para este fim, as zonas de cisalhamento e plútons graníticos foram investigados por estudos de campo, análise estrutural e microestrutural (com difração de elétrons retroespalhados - EBSD), análise de tramas magnéticas (por Anisotropia de Susceptibilidade Magnética - ASM), geocronologia (U-Pb SHRIMP) e termocronologia (Ar-Ar). Os granitos associados às zonas de cisalhamento possuem estruturas de deformação em estado magmático e em estado sólido de alta temperatura que corroboram sua colocação em sincronicidade com a deformação transcorrente. Suas idades de cristalização são concordantes em c. 584 Ma. O caráter conjugado para o par Senador Pompeu-Tauá promove extrusão para nordeste do bloco interno do Domínio Ceará Central. Os enxames de diques Ematuba, Independência e Marrecas, que também foram formados em 584 Ma, têm uma orientação consistente com a direção de encurtamento esperada para o par cisalhante. Na junção entre as zonas de cisalhamento Senador Pompeu e Tauá forma-se um zíper de fechamento destral expresso pela zona de cisalhamento de Cococi (majoritariamente coberta pela bacia homônima). O batólito sin-tectônico de Tauá exibe uma prolongada história de cristalização entre 584 e 571 Ma. Seus stocks internos mais tardios Várzea do Boi (571 Ma) e Lagoa de Pedra (576 Ma) exibem intercalação concêntrica de fácies bimodais (granitos e dioritos), estruturas de mistura de magmas e hibridização, e textura maciça, indicando pouca influência da deformação regional. Foliações e lineações magnéticas medidas por ASM em geral são concordantes com a estrutura circular dos corpos. Localmente, tramas magnéticas truncam contatos magmáticos em orientação consistente com a deformação regional. Dioritos e granitos têm

valores intermediários de susceptibilidade magnética ($K \sim 0.5$ mSI) e fases paramagnéticas e ferromagnéticas magmáticas formam sua trama. Baixos valores de anisotropia ($P \sim 5\%$) indicam a fraca influência da deformação, que se deve a uma interferência de forças de corpo e forças tectônicas enfraquecidas de estágios finais de orogênese. Nas proximidades da junção entre as zonas de cisalhamento Senador Pompeu e Tauá, granitos sin-tectônicos e milonitos possuem idades Ar-Ar de anfibólio e biotita de 577–562 Ma e 561–554 Ma, respectivamente. Integração dos termocronômetros disponíveis (aproximadamente de 700 °C em 580 Ma a 300 °C em 560 Ma) permitem determinar elevadas taxas de resfriamento para as zonas de cisalhamento transcorrentes de 20–40 °C/Myr. Tal resfriamento se deu cerca de 20 Myr depois do resfriamento do bloco interno do Domínio Ceará Central. A trajetória horária *P-T-t* das unidades principais revelam que o resfriamento do bloco interno foi causado por uma exumação a taxas entre 1.9 e 5.8 mm/yr. Entre c. 610 e 530 Ma, o terreno foi exumado lentamente a taxas entre 0.3 e 0.9 mm/yr. O resfriamento diferencial rápido das zonas de cisalhamento se deve a um regime termal próprio causado pelo magmatismo. As interações cinemáticas no par conjugado Senador Pompeu-Tauá provocam episódios de espessamento e afinamento, registrados amplamente em marcadores de deformação finita e vorticidade (varáveis em torno de $W = 0.71$) nos granitos sin-tectônicos. Zíperes de fechamento destral se formam ao longo da zona de cisalhamento Senador Pompeu por junção com zonas sinistrais (e.g. Hebrón e Cococi) onde se encontram justapostos critérios destrais e sinistrais. Uma inclinação pós-orogênica de cerca de 3° expôs um perfil da crosta ao longo da zona de cisalhamento Senador Pompeu, com a transição rúptil-dúctil em sua parte média registrada por um feixe de alta tensão de fluxo de até 200 MPa. Uma simulação reológica-mecânica da variação da espessura de zonas de cisalhamento com base em um perfil de resistência apropriado e comparação com o aumento sistemático da largura, de < 2 km no segmento sul para 20–30 km no segmento norte, indica que a taxa de cisalhamento foi de c. 10 mm/yr. Deflexão de unidades litológicas indicam um rejeito mínimo de 50–75 km, indicando que a longevidade da transcorrência possivelmente se caracteriza em c. 584–570 Ma.

Palavras-chave: Granito, geocronologia, termocronologia, microestruturas de deformação, evolução estrutural, tramas magnéticas, cinemática

Abstract

Final stages of the Brasiliano orogeny (800–550 Ma) in the Borborema Province of northeast Brazil are marked by large transcurrent shear zones associated to granite plutonism. In the Ceará Central Domain, the Senador Pompeu (NE) and Tauá (NNW) shear zones have a conjugate kinematics (right and left-lateral, respectively) and outline terranes characterized by high-grade metamorphism and migmatization. They consist of mylonitic gneisses, mylonites and ultramylonites, cataclasites and pseudotachylites. Granite batholiths (Quixadá, Quixeramobim, Tauá, Pedra Lisa and Nova Russas) occur at its shoulders and core. Genetic relations between magmatism and the structural evolution of strike-slip deformation allow determination of the real role of shear zones for accomodating convergence and exhumation of the orogen. To that end, the shear zones and granite plutons were investigated through detailed field studies, structural and microstructural analysis (with Electron Backscatter Diffraction - EBSD), magnetic fabric analysis (with Anisotropy of Magnetic Susceptibility - AMS), geochronology (U-Pb SHRIMP) and thermochronology (Ar-Ar). Shear zone-bounded granites display magmatic and solid state deformation structures that support its emplacement synchronous with strike-slip deformation. Their crystallization ages are concordant at c. 584 Ma. Therefore, the conjugate character of the Senador Pompeu-Tauá pair leads to northeastwards extrusion of the internal block of the Ceará Central Domain. The Ematuba, Independência and Marrecas dyke swarms, which also formed at 584 Ma, have an orientation consistent with the implied shortening direction. At the junction of the Senador Pompeu and Tauá shear zones a dextral closing zipper is formed, materialized in the Cococi shear zone (buried by the homonymous basin). The syn-tectonic Tauá batholith has a protracted crystallization history between 584 and 571 Ma. Its internal and latest stocks Várzea do Boi (571 Ma) and Lagoa de Pedra (576 Ma) exhibit a concentric layering of bimodal facies (granites and diorites), magma mingling structures, hybridization, and massive texture, indicating minor influence of regional deformation. Magnetic foliations and lineations determined with AMS are generally concordant with the circular structure of the stocks. Locally, magnetic fabrics cross-cut magmatic contacts in orientations consistent with the regional deformation field. Diorites and granites have intermediate magnetic susceptibility ($K \sim 0.5$ mSI) and both paramagnetic and ferromagnetic phases form its magnetic signal. Low fabric anisotropy ($P \sim 5\%$) indicate

the weak influence of deformation, which is a combination of body forces and waning tectonic forces in late stages of orogenesis. In the proximity to the shear zone junction, syn-tectonic granites and mylonites have amphibole and biotite Ar-Ar ages of 577–562 Ma and 561–554 Ma, respectively. Integration of available thermochronometers (approximately from 700 °C at 580 Ma to 300 °C at 560 Ma) allow determination of fast cooling rates for transcurrent shear zones of 20–40 °C/Myr. This cooling event occurred c. 20 Myr after cooling of the internal block of the Ceará Central Domain. Clockwise *P-T-t* paths of the main geologic units show that the cooling of the internal block followed fast exhumation at rates between 1.9 and 5.8 mm/yr. Between c. 610 and 530 Ma, the terrane was exhumed as a coherent unit at rates between 0.3 and 0.9 mm/yr. The rapid differential cooling of the shear zones is caused by an internal thermal regime related to magmatism. Kinematic interactions in the conjugate Senador Pompeu-Tauá pair led to episodes of thickening and thinning, recorded in gauges of strain and vorticity (variable around $W = 0.71$) in the syn-tectonic granites. Dextral closing zippers form along the Senador Pompeu shear zone at junctions with left-lateral shear zones (e.g. Hebrón and Cococi) where right and left-lateral kinematic criteria are found juxtaposed. A post-orogenic tilt of 3° exposed a crustal profile along the Senador Pompeu shear zone, with the brittle-ductile transition at its middle segment recorded by a beam of high flow stress up to 200 MPa. A rheological-mechanical simulation of the shear zone width increase with depth based on a suitable strength profile and comparison with the systematic increase of width from < 2 km in the southern segment to 20–30 km in the northern segment, indicate a slip rate of c. 10 mm/yr. Deflection of lithological markers yield a minimum offset of 50–75 km, bracketing the longevity of transcurrent deformation to 584–570 Ma.

Keywords: Granite, geochronology, thermochronology, deformation microstructures, structural evolution, magnetic fabrics, kinematics

Sumário

Sumário . . . . . **xv**

Lista de ilustrações . . . . . **xx**

Lista de tabelas . . . . . **xxxv**

1 INTRODUÇÃO **3**

1.1 Apresentação **3**

1.2 Estrutura da tese **6**

1.3 Reologia da crosta continental e zonas de cisalhamento . **7**

1.4 Magmatismo sin-tectônico em zonas de limites de placas **10**

2 MÉTODOS **17**

2.1 Geocronologia U-Pb em zircão **17**

2.2 Termocronologia por Ar-Ar **18**

2.3 Tramas magnéticas **21**

2.3.1 Fundamentos de magnetismo de rochas e mineralogia magnética 21

2.3.2 Anisotropia de susceptibilidade magnética 29

2.3.3 Anisotropia de magnetização remanente 30

2.4 Difração de Elétrons Retroespalhados - *EBSD* **31**

3 GEOLOGIA REGIONAL **37**

3.1 Resumo da estratigrafia e evolução tectônica **37**

3.2 Magmatismo sin-transcorrência **43**

4 ZIPPERED SHEAR ZONE MODEL FOR INTERACTING SHEAR ZONES IN THE BORBOREMA PROVINCE, BRAZIL, AS CONSTRAINED BY UPB DATING **47**

4.1 Abstract **47**

4.2 Introduction . . . 48
4.3 Geological setting . . . 49
4.4 The Senador Pompeu and Tauá shear zones . . . 50
4.5 Analytical methods . . . 53
4.6 Results . . . 54
4.6.1 SHRIMP ages . . . 54
4.6.1.1 Quixadá and Quixeramobim . . . 54
4.6.1.2 Nova Russas and Pedra Lisa plutons . . . 55
4.6.1.3 Ematuba, Independência and Marrecas dyke swarms . . . 56
4.6.2 Magmatic deformation structures and mylonites . . . 57
4.6.3 Vorticity and kinematic analysis . . . 62
4.7 Discussion: a kinematic model for the TSZ-SPSZ interaction 64
4.7.1 Timing of shear zone activity . . . 64
4.7.2 Shear zone interaction . . . 68
4.7.3 Tectonic implications . . . 71
4.8 Conclusions . . . 72
4.9 Acknowledgements . . . 73

5 SHEAR ZONE COOLING AND FABRICS OF SYNKINEMATIC PLUTONS EVIDENCE TIMING AND RATES OF OROGENIC EXHUMATION IN THE NORTHWEST BORBOREMA PROVINCE (NE BRAZIL) . . . 75
5.1 Abstract . . . 75
5.2 Introduction . . . 76
5.3 Geological setting . . . 77
5.3.1 The Ceará Central domain . . . 77
5.3.2 The interacting Senador Pompeu and Tauá shear zones . . . 79
5.4 Results . . . 80
5.4.1 Field relations and petrography . . . 80
5.4.2 Magnetic fabrics . . . 85
5.4.2.1 Magnetic mineralogy . . . 85
5.4.2.2 Anisotropy of magnetic susceptibility (AMS) and Anhysteretic Remanence (AAR) . . . 89

5.4.3 U-Pb SHRIMP geochronology . . . 91
5.4.4 $^{40}Ar/^{39}Ar$ thermochronology . . . 95
5.4.5 Argon closure temperatures and cooling rates . . . 97
5.5 Discussions . . . 100
5.5.1 Timing of pluton emplacement . . . 100
5.5.2 Magnetic fabrics, magma emplacement and relation to shear zone . . . 101
5.5.3 Cooling and exhumation of the Ceará Central domain . . . 104
5.6 Conclusions . . . 111
5.7 Acknowledgements . . . 112

6 RHEOLOGY, SHEAR ZONE WIDTH, MICROSTRUCTURAL EVOLUTION AND TECTONICS OF A ZIPPERED STRIKE-SLIP SHEAR ZONE: THE SENADOR POMPEU SHEAR ZONE, NORTHERN BORBOREMA PROVINCE, BRAZIL . . . 113
6.1 Abstract . . . 113
6.2 Introduction . . . 114
6.3 Geological setting . . . 116
6.4 Methods . . . 120
6.4.1 Electron Backscatter Diffraction (EBSD) . . . 120
6.4.2 Standard procedure of noise reduction and segmentation of EBSD data . . . 120
6.4.3 Cross et al. (2015) procedure . . . 121
6.4.4 Electron Microprobe Analysis (EMPA) . . . 121
6.5 Results . . . 122
6.5.1 Field relations, structural architecture and microstructures . . . 122
6.5.2 Crystallographic fabrics . . . 130
6.5.3 Recrystallized grain size paleopiezometry . . . 133
6.5.4 Geobarometry of syn-tectonic intrusions . . . 136
6.6 Discussions . . . 138
6.6.1 Microstructures, active slip systems and deformation temperatures . . . 138
6.6.2 Flow stress . . . 143

6.6.3 Pluton emplacement depth and crustal tilting 144
6.6.4 Simulating shear zone width as a function of depth 147
6.6.5 Zippered segments and reversed kinematics 152
6.6.6 Tectonic implications 153
6.7 Conclusions 156

7 CONSIDERAÇÕES FINAIS E CONCLUSÕES 159
7.1 Interação de zonas de cisalhamento, magmatismo sincrônico e extrusão de bloco 159
7.2 Tramas magnéticas em plútons circulares tardi-cinemáticos 160
7.3 Resfriamento e exumação do Domínio Ceará Central . . . 162
7.4 Reologia, cinemática e evolução estrutural de zonas de cisalhamento 163

APÊNDICES 167

APÊNDICE A – SUPPORTING INFORMATION: ZIPPERED SHEAR ZONE MODEL FOR INTERACTING SHEAR ZONES IN THE BORBOREMA PROVINCE, BRAZIL, AS CONSTRAINED BY UPB DATING 169
A.1 Introduction 169

APÊNDICE B – SUPPLEMENTARY MATERIAL: SHEAR ZONE COOLING AND FABRICS OF SYNKINEMATIC PLUTONS EVIDENCE TIMING AND RATES OF OROGENIC EXHUMATION IN THE NORTHWEST BORBOREMA PROVINCE (NE BRAZIL) 181
B.1 Rock magnetism and Magnetic Anisotropy data 181
B.2 U-Pb isotopic data 184
B.3 Ar isotopic data 190
B.4 Calculation of closure temperatures and cooling rates . . . 193

B.5 Python sample script 199

APÊNDICE C – SUPPLEMENTARY MATERIAL: RHEOLOGY, SHEAR ZONE WIDTH, MICROSTRUCTURAL EVOLUTION AND TECTONICS OF A ZIPPERED STRIKE-SLIP SHEAR ZONE: THE SENADOR POMPEU SHEAR ZONE, NORTHERN BORBOREMA PROVINCE, BRAZIL 207

C.1 Mineral chemistry of feldspar and amphibole 207

Referências 217

Lista de ilustrações

Figura 1 – Limites de placas (linhas pretas) e zonas de limites de placas (polígonos pretos) ativos com nomes das placas indicados. Adaptado de Şengör et al. (2019). 4

Figura 2 – a) Perfil de resistência conceitual para a litosfera continental. b) Bloco diagrama mostrando a diferenciação da crosta continental com base em composição (estimada por velocidades de ondas P, V_P) e estratificação reológica. TRD - transição rúptil-dúctil. Adaptado de (Karlstrom and Williams, 1998). Parâmetros de fluxo para quartzo, feldspato e olivina são obtidos de Platt (2015a), Rybacki and Dresen (2000) e Freed et al. (2012), respectivamente. 8

Figura 3 – a) Resistência limítrofe dada por rochas intactas e resistência real de rochas enfraquecidas de zonas de cisalhamento. A resistência de rochas intactas (esquerda) é a mesma apresentada na Figura 2. A resistência de rochas enfraquecidas (direita, linha tracejada marca a resistência de rochas intactas) compreende tanto enfraquecimento rúptil (e.g. aumento da pressão de poro ou redução do coeficiente de atrito) como dúctil (e.g. recristalização e transformações metamórficas). b) Simulação de perfil de espessura cumulativa de zona de cisalhamento (w) na litosfera continental com base na resistência limítrofe. Adaptado de Platt and Behr (2011c) e Holdsworth (2004). 9

Figura 4 – Relação entre viscosidade e reologia de magmas, e cristalinidade (razão de volume de sólidos para volume de líquido). SLT - transição sólido-líquido, MCT - transição de conectividade de *melt*. Adaptado de de Rosenberg and Handy (2005) e Blenkinsop (2005). 13

Figura 5 – (a) Orientação preferencial de forma de porfiroclastos de feldspato potássico em granitóide do batólito Quixeramobim. A foliação magmática é paralela à base da foto. (b) Granito porfirítico do batólito Quixeramobim. Megacristais de feldspato potássico definem uma trama de forma que caracteriza o fluxo magmático (paralelo à base da foto). Plagioclásio (cor avermelhada) e feldspato potássico da matriz são subédricos e preservam sua forma magmática. Quartzo apresenta elongações com baixa razão axial (c. 2:1) devido à deformação no estado sólido. 15

Figura 6 – a) Espectro de idades de Ar-Ar mostrando perda de Ar e consequentemente idades mais jovens nas primeiras etapas de aquecimento (etapas em preto). b) Espectro de idades de Ar-Ar mostrando forma de sela indicando possível excesso de Ar (etapas em preto). 20

Figura 7 – Tipos de magnetização possíveis em minerais formadores de rochas. M_r - magnetização remanente, M_s - magnetização de saturação, H_c - coercividade, H_{cr} - coercividade de remanência. Adaptado de Bouchez (1997). 22

Figura 8 – a) Curva termomagnética teórica calculada segundo a função de Langevin mostrando a magnetização paramagnética em função da temperatura. Adaptado de Tauxe (2005). b) Curva termomagnética experimental para rocha rica em biotita. 23

Figura 9 – Curva teórica de aquisição de magnetização calculada segundo a função de Langevin mostrando a saturação da magnetização paramagnética (M/M_s) com o aumento do campo indutor (H). A curva pontilhada mostra a aproximação para a susceptibilidade paramagnética (Equação 2.4) quando $KT >> m_b\mu_0 H$. Adaptado de Tauxe (2005). 24

Figura 10 – Direções principais de susceptibilidade magnética em a) anfibólio, b) mica e c) quartzo. Os eixos a, b e c são eixos da cela unitária. Adaptado de Borradaile and Jackson (2010) e Lagroix and Borradaile (2000). 25

Figura 11 – Tipos de ferromagnetismo com indicação da magnetização espontânea resultante (M_S). As duas camadas de setas de spin representam sub-retículos de momentos magnéticos. 25

Figura 12 – Magnetização teórica de minerais ferromagnéticos em função de a' conforme a teoria de campo molecular de Weiss. As interseções das funções dadas pelas equações 2.5 e 2.6 é indicada com quadrados. Adaptado de Dunlop and Özdemir (1997) 26

Figura 13 – Espectro de coercividade para agregados sintéticos de magnetita com tamanhos de grão médio de 5 e 0.1 µm. Adaptado de Jackson et al. (1988). 28

Figura 14 – Esquema das etapas de preparação de amostras para EBSD. Adaptado de Barbosa (2009). 32

Figura 15 – Ilustração esquemática do sistema de EBSD (*Electron Backscatter Diffraction*) no microscópio eletrônico de varredura (modificado de Reed 2006). 33

Figura 16 – Padrão de difração de elétrons retroespalhados não processado de um cristal de hematita. 34

Figura 17 – Etapas de operação de uma análise de EBSD (*Electron Backscatter Diffraction*) até indexação. 35

Figura 18 – a) Gondwana Oeste. AC - Cráton Amazônico, SFC - Cráton São Francisco, KHC - Cráton do Kalahari, CC - Cráton do Congo, SHC - Cráton do Saara, WAC - Cráton Oeste África. b) Mapa geológico-tectônico do Domínio Ceará Central. O Maciço de Tróia inclui o Complexo Cruzeta e os complexos gnáissicos-migmatíticos Riacianos. 38

Figura 19 – Diagrama de evolução de neodímio para os batólitos Quixadá-Quixeramobim e Tauá, construído a partir de dados adaptados de Cavalcanti et al. (2012) e Nogueira (2004) após correção para idades U-Pb SHRIMP obtidas por Ávila et al. (2019). DM - manto empobrecido, CHUR - *Chondritic Uniform Reservoir*. TSQ - Tamboril-Santa Quitéria. . . . 42

Figura 20 – Compilação de geoquímica de elementos maiores e dados de composição modal para os plutons sin-tectônicos estudados (referências indicadas). a) Diagram TAS (*total alkalis-silica*). Limites dados por Le Maitre (2002). b) Diagrama Harker de K_2O *versus* SiO_2. Limites dados por Peccerillo and Taylor (1976). c) Diagrama de saturação em alumina. d) Diagrama AFM (álcalis, Fe, Mg). Limites dados por Irvine and Baragar (1971). d) Diagrama QAP (quartzo, álcali-feldspato, plagioclásio). 44

Figura 21 – a) Geological map of the central West Gondwana Orogen. b) Geological map of the Ceará Central domain (CCD). The studied plutons are indicated by their respective names. See Figura 22 for sample locations. Note that all maps have the north rotated 45° clockwise. . 51

Figura 22 – Structural lineaments interpreted from multispectral CBERS4 images and magnetic anomaly map (inset). Sample locations are shown with mean $^{206}Pb/^{238}U$ ages and their respective codes (QXD - Quixadá, QX141 - Quixeramobim, NR - Nova Russas, PL - Pedra Lisa, EMA - Ematuba, DIND - Independência, MAR2 - Marrecas). Lineation plunges are less than 30°. 54

Figura 23 – Weighted average $^{238}U/^{238}U$ ages for the granitoid plutons and felsic dyke swarms. Sample codes are as defined in Figure 2. Vertical lengths are analytical errors at 2σ centred at the age. Grey bars are weighted average ages with 2σ uncertainty. For cathodoluminescence images, concordia plots and data of individual analyses see Supporting Information. Dark red weighted average is calculated for Marrecas sample without the four youngest ages. 56

Figura 24 – a) Gamma ray spectrometry map (ternary composition) of Senador Pompeu shear zone (SPSZ). Lithological control points give offset estimates of 66, (A1-A2) 96 (B1-B2) and 68 km (C1-C2). b) Megacrystic facies SPO of the Quixeramobim batholith (magmatic foliation is horizontal). c) Megacrystic Quixeramobim granitoid with solid-state deformation (elongate quartz) overprinting magmatic deformation (strong SPO of equant feldspars), SPSZ. d) SPSZ mylonite zone with banded ultramylonites, protomylonites and lightly deformed porphyritic granites. e) Pseudotachylite in southern segment of SPSZ. All figures have dextral shear sense. 60

Figura 25 – a) Magmatic fabric of porphyritic facies of Pedra Lisa pluton. Foliation trace is horizontal. b) Microstructure of Pedra-Lisa pluton deformed at sub-magmatic to magmatic conditions. c) Intermediate-temperature quartz-feldspar mylonite at the fault-bounded walls of Nova Russas pluton. d) Low-temperature S-C mylonite of southern TSZ. Note micrometer-sized muscovite laths e) High-temperature mylonite of middle segment of TSZ preserved from cataclastic deformation. f) Cataclastic groundmass formed after brittle deformation overprinting high-temperature mylonites (preserved pods indicated). All figures have sinistral shear sense. 61

Figura 26 – Kinematic vorticity and strain ellipsoid estimates of megacrystic facies of the Quixeramobim pluton deformed by the Senador Pompeu shear zone (SPSZ). Left charts show shape ratio of feldspar porphyroclasts (R) versus angle between feldspar long axis and the foliation plane (ϕ). $\bar{R}$ is the estimate of mean critical ratio (R_c). Right charts are strain estimates according to Fry (1979), where R_f is ellipsoid aspect ratio and θ is the clockwise angle between ellipsoid long axis and foliaton pole (chart north). In all cases the foliation plane is horizontal. 65

Figura 27 – Kinematic vorticity and strain ellipsoid estimates of megacrystic facies of the Pedra Lisa and Nova Russas plutons deformed by the Tauá shear zone (TSZ). Left charts show shape ratio of feldspar porphyroclasts (R) versus angle between feldspar long axis and the foliation plane (ϕ). $\bar{R}$ is the estimate of mean critical ratio (R_c). Right charts are strain estimates according to Fry (1979), where R_f is ellipsoid aspect ratio and θ is the clockwise angle between ellipsoid long axis and foliaton pole (chart north). In all cases the foliation plane is horizontal. 66

Figura 28 – Relationship between percentage of pure shear relative to simple shear and kinematic vorticity (W_k). Red and blue error bars at two standard deviations centered at the means for estimates of Senador Pompeu shear zone (SPSZ) and Tauá shear zone (TSZ). 67

Figura 29 – Model describing the geometrical framework and kinematic interactions between the Senador Pompeu (SPSZ) , Tauá (TSZ), Sabonete-Inharé (SISZ) and Cococi (CSZ) shear zones in the Ceará Central Domain (CCD). See text for discussion. 70

Figura 30 – a) Central West Gondwana. Red frame gives location of b). Note that the map is rotated c. 45° clockwise relative to the true north of b). b) Geological map of the Northwest Borborema Province. Red inset shows location of Figura 31. 79

Figura 31 – Geological map of Várzea do Boi (VB) and Lagoa de Pedra (LP) stocks within the Tauá magmatic suite. Polar histograms are given for the different subsets of structural lineaments. Strike of Tauá (TSZ) and Sabonete-Inharé (SISZ) are given for reference. See location in Figura 30b. 81

Figura 32 – Field relations in the Várzea do Boi and Lagoa de Pedra stocks and micrographs. a) Micrograph of fine-grained diorite facies showing pronounced trachytic texture of feldspar laths (fs) and oriented hornblende while quartz (qz) is equant and undeformed. b) Micrograph of hybrid facies showing hornblende clot (hbl) and ocellar quartz (oc) with hornblende reaction rim. c) Micrograph of anorthosite showing adcumulus texture with tiger-symplectite in pyroxene. d) Comingling of diorite (di) and granite (gr) facies with a vertical zone of hybridization (hy) in between. e) Intramagmatic flow of diorite (di) in granite (white seams). f) Fracture stockwork within diorite (di) filled with granite melt (gr). g) Microdiapirism of granitic melt (gr) frozen in its dioritic substrate (di). h) Small-scale convolutions in contact between mingled granite (gr) and diorite (di). Compass for scale. i) Hybrid (hy) enclave within coarse-grained granite (gr). Coin for scale. j) Coarse-grained diorite (cdi) blocks enclosed in comingled fine-grained granite (gr) and diorite (di). 84

Figura 33 – Locations of Anisotropy of Magnetic Susceptibility (AMS) sites for Várzea do Boi (VB) and Lagoa de Pedra (LP) stocks and distribution of bulk susceptibility. Inset shows susceptibility histogram. 86

Figura 34 – Representative rock magnetic properties and fabrics for the Várzea do Boi and Lagoa de Pedra plutons. 88

Figura 35 – Map of magnetic foliation (normal to K_3) and lineation (K_1) for the Várzea do Boi (VB) and Lagoa de Pedra (LP) stocks. Stereographic projections are equal area and lower hemisphere. Data for sites are plotted as scatter, whereas full set of measured specimens is plotted as density contouring (in multiples of uniform distribution, MUD). . 91

Figura 36 – a) Kernel probability distribution of $^{206}Pb/^{238}U$ for two replicate U-Pb SHRIMP analyses (samples VB1A and CA124) of the diorite facies from Várzea do Boi stock, and their combined distribution. b) U-Pb concordia diagram for the two combined replicate analyses of the Várzea do Boi stock. Legend as in a). c) U-Pb concordia diagram for the Lagoa de Pedra stock. d) U-Pb concordia diagram for the Iapi stock. All ellipses and ages at 2σ uncertainty. Concordia ages in red. 94

Figura 37 – Ar-Ar ages for amphibole and biotite mineral separates for the studied plutons. a) Ematuba dyke, amphibole, b) Tauá shear zone mylonite, biotite, c) Iapi stock, amphibole, d) Iapi stock, biotite, e) Várzea do Boi stock, amphibole, f) Várzea do Boi stock, biotite. Height of bars and uncertainty are given at 2σ level. Steps forming a plateau are highlighted in red. 96

Figura 38 – U-Pb and Ar-Ar ages plotted against closure temperature of their respective isotopic systems. Lines connect ages obtained from the same sample (for Ar-Armineral ages) or from samples collected from the same outcrop or geological unit (zircon U-Pb and amphibole Ar-Ar). The equivalent depth of a normal continental geotherm is given in the right axis for reference. 106

Figura 39 – P-T-t path for the Ceará Central domain and bounding transcurrent shear zones. Filled boxes indicate the general P-T range constrained by thermochronological, geochronological and thermobarometric data. Ages shown are approximate according to 1) Ganade de Araujo et al. (2014b), 2) Castro (2004), 3) this study, 4) Ávila et al. (2019) and 5) Garcia et al. (2018). For further details refer back to text. 109

Figura 40 – Total magnetic anomaly map of the Borborema Province, reduced to pole. White lines show occurrences of low-temperature mylonite zones. Shear zones from northwest to southeast: SO - Sobral-Pedro II, TA - Tauá, SP - Senador Pompeu, OR - Orós, JA - Jaguaribe, PO - Portalegre, PA - Patos, BO - Boqueirão dos Cochos, SC - Serra do Caboclo, AI - Afogados da Ingazeira, CX - Coxixola, CN - Cruzeiro do Nordeste, FN - Fazenda Nova, PE - Pernambuco. Inset shows location of the map frame in West Gondwana, in which dark grey areas are cratons and light grey areas are orogens. AC - Amazonian Craton, WAC - West Africa Craton, SFC - São Francisco Craton, SHC - Saharan Craton, CC - Congo Craton, KHC - Kalahari Craton. 116

Figura 41 – Geological map of the Senador Pompeu shear zone. Geological cross sections (AA' to GG') are given in Figura 42. TSZ - Tauá shear zone, OSZ - Orós shear zone, HSZ - Hebrón shear zone. Stereographic projections show foliation poles (blue), stretching lineations (red), mean lineation (black) and the mean foliation (black line) is indicated by their strike and dip (e.g. N44E,76SE). 118

Figura 42 – Geological cross sections of the northern segment of the Senador Pompeu shear zone. Represented dips of units and strucures are true (from field measurements) but vertical dimensions are not to scale. a) AA'. b) BB'. Symbology of geological units is similar to that of Figura 41. 123

Figura 43 – a) Mylonitic biotite-gneiss showing S, C and C' foliations, and (right-lateral) boudinaged quartz-feldspar layer. b) Mylonitic biotite-gneiss with hyper-extended pegmatite dykes, S, C and C' foliations. c) Protomylonitic Serra do Deserto augen-gneiss with right-lateral σ-type porphyroclasts. d) Várzea da Onça mylonitic biotite-gneiss showing pronounced foliation (mm-scale compositional layering) and stretching lineation. Elsewhere in the same unit right-lateral σ-type porphyroclasts are found in hyper-extended pegmatite dykes. e) Interlayered amphibolitic mylonites and metagreywacke biotite-gneiss with leucosome from the Algodões-Choró metamorphic suite at the Coqueirinho fold system. f) Mylonitic biotite-gneiss with S, C and C' foliations showing right-lateral shear. 125

Figura 44 – Micrographs of mylonitic gneisses of the northern segment of the Senador Pompeu shear zone, displayed from north (a) towards the south (c). a) Aphyric biotite (bt)-muscovite (mt) mylonitic gneiss of metagreywacke that occurs north of the AA' cross section of Figura 42. Microstructure is dominated by mixed quartz and feldspar with average grain size of c. 0.5 mm. Quartz may form ribbons locally, and rounded quartz "droplets" of < 0.1 mm (qz) that occur mixed in quartz-feldspar layers are the product of dismembered myrmekites. b) Biotite mylonitic gneiss (sample from mylonite shown in Figura 43d). Quartz and feldspar occur in mixed layers as in a), but cuspate feldspar-quartz boundaries (fs) and feldspar pinch-and-swell structures are visible around quartz ribbons. Quartz grain boundaries are irregular to lobate, indicating grain boundary migration recrystallization. Note coarse grained quartz (c. 1 mm) in quartz ribbons. c) Biotite (bt)-hornblende (hbl) mylonitic gneiss formed from deformed amphibolite of the Algodões Choró suite (sample from mylonite shown in Figura 43e). Remaining feldspar porphyroclasts have incipient undulose extinction, subgrain microstructure (sg) and mechanical twinning (mt). Hornblende in lower right corner 126

Figura 45 – a) Deformed porphyritic granitoid of the Quixeramobim batholith. b) Mylonitic garnet amphibolite of the Algodões-Choró metamorphic suite with right-lateral SC structure and σ-type feldspar porphyroclasts. c) Strongly deformed muscovite-leucogranite of the Senador Pompeu batholith. d) Ultramylonite of the core of the middle segment of the Senador Pompeu shear zone with right-lateral σ and δ-type porphyroclasts. e) Sidewall-ripout with incipient recrystallization. f) Stromatic migmatite of the Mombaça unit. 128

Figura 46 – Micrographs of mylonites from the middle segment of the Senador Pompeu shear zone, displayed from north (a) towards the south (f). a) Muscovite-biotite-garnet (grt) schist from metagreywacke of the Algodões-Choró unit (sample from Figura 45b). S-C foliation and asymmetric feldspar porphyroclasts show right-lateral shear. Quartz shows subgrain microstructure (sg) and sutured/irregular grain boundaries (ir). b) Muscovite bearing mylonite from the sheared Senador Pompeu batholith (sample from Figura 45c). Dynamic recrystallization affects quartz, feldspar and muscovite. c) Porphyroclastic muscovite-biotite mylonite with compositional banding. Feldspar porphyroclasts have abundant flame perthites (fp) and subgrain microstructures, and occur as fish in quartz ribbons (fs). Quartz displays sutured and lobate grain boundaries, and undulose extinction. d) Quartz vein in mica-schist showing straight grain boundaries, subgrain microstructures and right-lateral grain elongation fabric. Quartz grain size c. 15 µm. e) Quartz layer in muscovite-biotite mylonite (sample from Figura 45d). Relict quartz of 50–100 µm is elongated parallel to foliation (qz) and grain boundary bulges are c. 15 µm (blg). Feldspar shows bulges (fs). f) Striped ultramylonitic granitoid with feldspar porphyroclasts in fully mixed quartz-feldspar-mica groundmass with grain size of c. 10 µm. 129

Figura 47 – Gneiss of the Hebrón shear zone with left-lateral SC foliation and σ-type porphyroclasts. b) Mylonites and ultramylonites of the Senador Pompeu shear zone with right-lateral σ-type feldspar porphyroclasts. c) Megacrystic granitoid of the Quixeramobim batholith with shape preferred orientation of feldspar megacrysts indicating magmatic deformation. d) Ultramylonite and pseudotachylitic breccia of the core of the Senador Pompeu shear zone. e) Ultramylonite and pseudotachylite of the core of the Senador Pompeu shear zone. f) Brecciated chloritized granitoid southest of the Senador Pompeu shear zone; no structures indicate ductile deformation. g) Mingled diorite and granodiorite of the Várzea do Lote granitoid showing magmatic deformation. h) Ultramylonite with σ-type porphyroclasts. See locations in Figura 42. 131

Figura 48 – Micrographs of mylonites from the southern segment of the Senador Pompeu shear zone, displayed from north (a) towards the south (f). a) Ultramylonite of intermediate-mafic composition. Feldspar and hornblende occur as rounded porphyroclasts in mixed groundmass. b) Quartz-feldspar mylonite. Feldspar porphyroclasts are intensely fractured and boudinaged, and rich in flame perthites (fs). Quartz (qz) laminae are recrystallized fully to a grain size of c. 30 µm, grain boundaries are straight and polygonal, and relict porphyroclasts have subgrain microstructures. c) Deformed quartz-feldspar gneiss. Quartz is strongly elongated to large axial ratios and has incipient recrystallization by local development of grain boundary bulges of c. 10 µm (qz). Feldspar is comminuted by microfracturing and subsequent boudinage. 132

Figura 49 – Quartz ⟨c⟩ axis pole figure for sample CA001 from a mylonitic gneiss of the high-temperature segment of the Senador Pompeu shear zone (SPSZ). ⟨c⟩ axis measurements were carried out with a universal stage. Scale in multiples of uniform distribution (MUD). 133

Figura 50 – Pole figures (a–j) and inverse pole figures (k–o) for quartz from mylonites from the middle and southern segments of the Senador Pompeu shear zone (SPSZ), obtained from EBSD analyses. Figures a) to e) are for ⟨c⟩ axes and f) to j) for ⟨a⟩ axes. Inverse pole figure plots the X sample direction. Samples are arranged from southwest (left) to northeast (right) along the shear zone. Scale in multiples of uniform distribution (MUD). 134

Figura 51 – EBSD maps showing CI (confidence index, top row) and reconstructed grain maps colored by orientation (bottom row). 136

Figura 52 – Ternary feldspar diagram with 700 °C solvus calculated by activity matching between plagioclase and alkali-feldspar (Benisek et al., 2010). Grey circles are feldspar compositions calculated from Electron Microprobe Analyses of the diorite facies of the Tauá batholith. Tie lines connect exsolution compositions (black squares). 138

Figura 53 – Typical crystallographic preferred orientation types found in naturally deformed quartz aggregates and their corresponding dominant slip system (Schmid and Casey, 1986; Toy et al., 2008). 139

Figura 54 – Range diagram constructed from deformation microstructures of mylonites from the Senador Pompeu shear zone (SPSZ) as approximate microstructural temperature gauges. Red triangles indicate the location of normal projections of the Quixadá and Tauá batholiths on the SPSZ. Red lines are continental geothermal gradients for a "normal" crust (c. 25 °C km^{-1}) and orogenic crust (c. 35 °C km^{-1}; Vanderhaeghe 2012) placed to match the depth profile indicated by the emplacement depths of the Quixadá and Tauá batholiths. 142

Figura 55 – a) Water fugacity (red) is interpolated through a dataset of f_{H_2O} created at different values of pressure and temperature using the Withers' fugacity calculator (based on the equation of state of Pitzer and Sterner 1995; https://www.esci.umn.edu/people/researchers/withe012/fugacity.htm. A normal geotherm is calculated by solving a steady state geotherm for the crust ($T = T_s + [(zq_m)/k] + [(q_s - q_m)h_r/k][1 - \exp(-z/h_r)]$), similar to that shown in Figura 54 at a gradient of c. 25 °C km^{-1}. b) Black lines show frictional criteria using Byerlee's law (internal friction of 0.85; Byerlee et al. 1978) for wrench (solid black line) and thrust (dashed black line) faults (Sibson, 1974). The viscous flow curves are calculated with quartz flow parameters determined by Hirth et al. (2001) and strain rates of 10^{-16} s^{-1} (with the shallowest brittle-ductile transition), 10^{-15} s^{-1}, 10^{-14} s^{-1}, 10^{-13} s^{-1} (with the deepest brittle-ductile transition). 149
Figura 56 – Fabric isogon map around the Senador Pompeu shear zone, extracted from structural grain in satellite imagery. See map location in Figura 41. 150
Figura 57 – Cumulative shear zone widths for variable strain rates (a - 10^{-13} to d - 10^{-16} s^{-1}) and slip rates (1 - blue, 5 - orange, 10 - green to 50 mm/yr - red). Solid black line is the maximum width of the Senador Pompeu shear zone (SPSZ) measured in GIS using fabric isogon maps. Dashed black line is the minimum width of the most distinct shear corridor of the SPSZ measured with satellite imagery and field relations. Notice that while we extrapolate shear zone widths up to the surface, the frictional viscous transition is located at around 12 km depth (Figura 55b), above which the true shear zone will not be much wider than just the discrete zone of brittle damage. 152
Figura 58 – U-Pb concordia diagram and cathodoluminescence image for Quixadá (QXD sample) zircons. Analysed spots are tagged with $^{206}Pb/^{238}U$ ages at 1σ errors. 173
Figura 59 – U-Pb concordia diagram and cathodoluminescence image for Quixeramobim (QX141 sample) zircons. Analysed spots are tagged with $^{206}Pb/^{238}U$ ages at 1σ errors. 174

Figura 60 – U-Pb concordia diagram and cathodoluminescence image for Nova Russas (NR sample) zircons. Analysed spots are tagged with $^{206}Pb/^{238}U$ ages at 1σ errors. 175
Figura 61 – U-Pb concordia diagram and cathodoluminescence image for Pedra Lisa (PL sample) zircons. Analysed spots are tagged with $^{206}Pb/^{238}U$ ages at 1σ errors. 176
Figura 62 – U-Pb concordia diagram and cathodoluminescence image for Ematuba (EMA sample) zircons. Analysed spots are tagged with $^{206}Pb/^{238}U$ ages at 1σ errors. 177
Figura 63 – U-Pb concordia diagram and cathodoluminescence image for Independência (DIND sample) zircons. Analysed spots are tagged with $^{206}Pb/^{238}U$ ages at 1σ errors. 178
Figura 64 – U-Pb concordia diagram and cathodoluminescence image for Marrecas (MAR sample) zircons. Analysed spots are tagged with $^{206}Pb/^{238}U$ ages at 1σ errors. 179
Figura 65 – U-Pb concordia diagram and cathodoluminescence images of zircons from Várzea do Boi stock (CA124). Analysed spots are tagged with $^{206}Pb/^{238}U$ ages at 1σ errors. 186
Figura 66 – U-Pb concordia diagram and cathodoluminescence images of zircons from Várzea do Boi stock (VB1A). Analysed spots are tagged with $^{206}Pb/^{238}U$ ages at 1σ errors. 187
Figura 67 – U-Pb concordia diagram and cathodoluminescence images of zircons from Iapi stock (IA). Analysed spots are tagged with $^{206}Pb/^{238}U$ ages at 1σ errors. 188
Figura 68 – U-Pb concordia diagram and cathodoluminescence images of zircons from Lagoa de Pedra stock (LP). Analysed spots are tagged with $^{206}Pb/^{238}U$ ages at 1σ errors. 189
Figura 69 – Histograms of simulated dT/dt. 195
Figura 70 – Histograms of simulated dT/dt. 196
Figura 71 – Histograms of simulated T_C. 197
Figura 72 – Histograms of simulated T_C. 198

Lista de tabelas

Tabela 1 – Kinematic vorticity (W_k), percentage of pure shear (PS%), aspect ratio of strain ellipsoid (R_f), angle of ellipsoid long axis to foliation (θ) and thinning estimates (a) for megacrystic magmas occurring in the Senador Pompeu (SPSZ) and Tauá (TSZ) shear zones. 63

Tabela 2 – Calculated cooling rates (2σ uncertainty) and closure temperatures (with differences to first and third quartiles). * Inferred temperature ranges for metamorphism. ** No mineral pair available. 99

Tabela 3 – Recrystallized grain sizes obtained from EBSD and the corresponding estimates of flow stress according to the piezometer law of Stipp and Tullis (2003), i.e. $D = 10^{3.56\pm0.27}\sigma^{-1.26\pm0.13}$. Averages of grain sizes obtained by root mean squares (RMS). D_{full} is RMS of full population of grains reconstructed from the standard method. D_{recr} and D_{relict} are RMS of recrystallized and relict fraction of grains according to the method of Cross et al. (2017), for which the piezometer law used was $D = 10^{3.91\pm0.41}\sigma^{-1.41\pm0.21}$. . . . 135

Tabela 4 – U-Pb analysis data for Quixadá batholith. * discarded. Errors are 1σ. 169

Tabela 5 – U-Pb analysis data for Quixeramobim batholith. * discarded. Errors are 1σ. 170

Tabela 6 – U-Pb analysis data for Nova Russas batholith. * discarded. Errors are 1σ. 170

Tabela 7 – U-Pb analysis data for Pedra Lisa plutons. * discarded. Errors are 1σ. 171

Tabela 8 – U-Pb analysis data for Ematuba dykes. * discarded. Errors are 1σ. . 171

Tabela 9 – U-Pb analysis data for Independência dykes. * discarded. Errors are 1σ. 172

Tabela 10 – U-Pb analysis data for Marrecas dykes. * discarded. Errors are 1σ. . 172

Tabela 11 – Magnetic susceptibility and anisotropy measurements for the Lagoa de Pedra stock. N = number of sites, K_M = magnetic susceptibility, P = degree of anisotropy, T = shape paramenter, Dec. = Declination, Inc. = Inclination, αK = maximum angle of 2σ uncertainty ellipse. . 182

Tabela 12 – Magnetic susceptibility and anisotropy measurements for the Várzea do Boi stock. N = number of sites, K_M = magnetic susceptibility, P = degree of anisotropy, T = shape parementer, Dec. = Declination, Inc. = Inclination, αK = maximum angle of 2σ uncertainty ellipse. . 183
Tabela 13 – U-Pb analysis data. Errors are 1σ. Ages are calculated after correction for common Pb. * Discarded. 185
Tabela 14 – Ar isotope data from step heating analyses. Errors are 2σ. 191
Tabela 15 – Ar isotope data from step heating analyses. Errors are 2σ. 192
Tabela 16 – Probability distributions used for the parameters input to calculations of T_C and dT/dt. 194
Tabela 17 – Mineral chemistry of amphibole. 208
Tabela 18 – Mineral chemistry of amphibole (continued). 209
Tabela 19 – Mineral chemistry of amphibole (continued). 210
Tabela 20 – Mineral chemistry of plagioclase. 211
Tabela 21 – Mineral chemistry of plagioclase (continued). 212
Tabela 22 – Mineral chemistry of plagioclase (continued). 213
Tabela 23 – Mineral chemistry of plagioclase (continued). 214
Tabela 24 – Mineral chemistry of plagioclase (continued). 215

1 Introdução

1.1 Apresentação

A teoria da tectônica de placas é baseada na localização da deformação e magmatismo em limites de placas em relação aos quais se movem blocos litosféricos rígidos (Cox and Hart, 2009). Tal localização é notória em limites de placas oceânicas. Os continentes, por sua vez, apresentam ampla distribuição geográfica de deformação manifesta em terremotos, falhas ativas, vulcanismo, e cadeias montanhosas. A impossibilidade de delinear limites de placas igualmente discretos nos continentes levou à definição de "zonas de limites de placas" (Figura 1; Stein and Sella 2013), caracterizadas por intensa deformação entre e dentro de blocos pouco rígidos (i.e. baixa espessura elástica; Jordan and Watts 2005). Sua principal expressão estrutural se dá em zonas de cisalhamento. Com a distinção entre zonas de limites, de baixa rigidez, e os blocos circunscritos, de alta rigidez, houve um crescente interesse na determinação mais precisa da evolução geológica, propriedades reológicas e contribuição cinemática real de zonas de cisalhamento em cinturões orogênicos.

Diversas ocorrências mundiais são conhecidas de sistemas regionais de zonas de cisalhamento transcorrentes com centenas de km, expostos em profundidades equivalentes à crosta média ou inferior de orógenos colisionais e associados a plutonismo e metamorfismo de alta temperatura (Hutton and Reavy, 1992; Karlstrom and Williams, 2008). Estes conjuntos de cisalhamento são vistos como fundamentais para acomodação de encurtamento e convergência durante a orogênese. A relação temporal e espacial entre o alojamento dos magmas, a deformação nas zonas de cisalhamento e a deformação no embasamento oferece uma pista importante a respeito da evolução tectônica de cadeias de montanhas (Archanjo et al., 2002, 2013), e da capacidade de transporte de magmas pela crosta (Cavalcante et al., 2016). Por comporem até 50% do volume da crosta continental, magmas graníticos presumidamente têm um papel fundamental nos processos de orogênese, particularmente por seu potencial de advecção de calor (Karlstrom and Williams, 2008). Magmas aprisionados no núcleo de orógenos, mesmo em baixas porcentagens, são capazes de provocar episódios de soerguimento e exumação

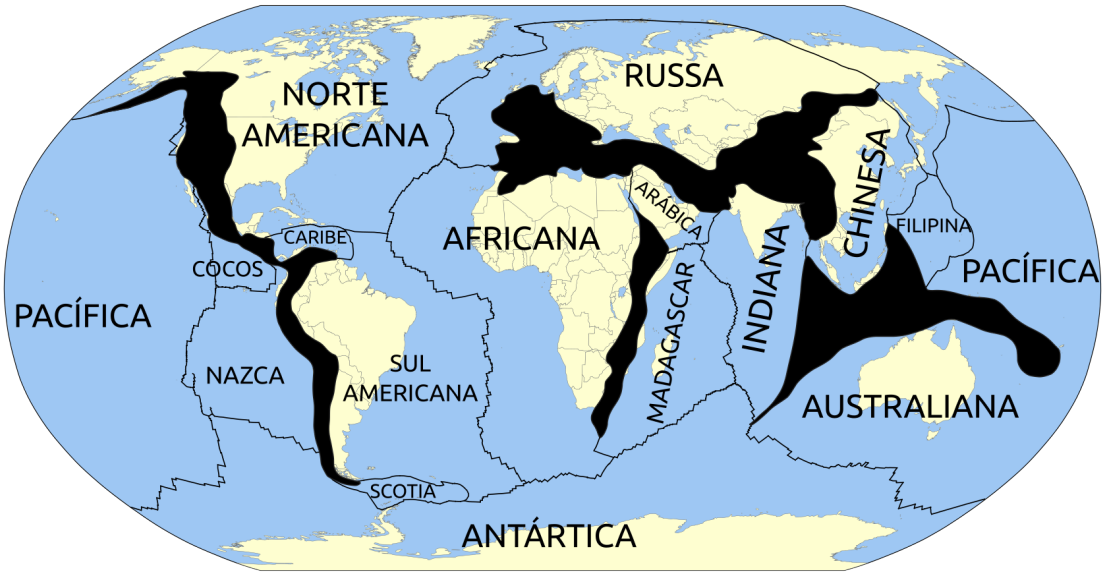

Figura 1 – Limites de placas (linhas pretas) e zonas de limites de placas (polígonos pretos) ativos com nomes das placas indicados. Adaptado de Şengör et al. (2019).

de unidades profundas (Hollister and Crawford, 1986) como amplamente aceito para o modelo de fluxo canalizado do núcleo cristalino (*Greater Himalayan Sequence*) no Himalaia (Beaumont et al., 2006).

Como na maior parte de zonas de transcorrência são verificadas componentes predominantemente horizontais de cisalhamento (strike-slip), tais descontinuidades têm o papel fundamental de acomodar o deslocamento lateral de blocos supostamente rígidos entre si. Desta percepção foi concebido que em orógenos não confinados, a extrusão lateral da crosta promovida pela convergência de blocos rígidos é marcada pelo desenvolvimento de extensas zonas de cisalhamento com alta taxa de deslizamento (Tapponnier et al., 1982). Por exemplo, é amplamente aceito que o bloco da Indochina sofreu extrusão lateral durante o Mioceno pela colisão Himalaiana (Royden et al., 2008). Embora tal conceito tenha ganhado notoriedade, no platô Tibetano (localidade-tipo), dados de geodésia e interferometria de radar mostram que a crosta se deforma de maneira aproximadamente contínua, e as zonas de cisalhamento não apresentam em geral taxas de *slip* suficientemente elevadas (Zhang et al., 2004). Portanto, o estudo de sistemas de transcorrência deve ser criterioso e multi-disciplinar antes que se possa estabelecer uma interpretação para seu papel tectônico. No caso particular, um sistema de transcorrên-

cia pode se formar para acomodar a dissipação da deformação em pequena escala (e.g. em terminação de zonas de cisalhamento; Storti et al., 2003), em grandes províncias (e.g. cinturões Hercinianos da Europa Ocidental; Hutton and Reavy, 1992), ou devido a partição de deformação em convergências oblíquas (Molnar and Dayem, 2010).

Um dos mais expressivos sistemas de transcorrência se encontra na Província Borborema do Nordeste do Brasil, conhecida amplamente por extensas zonas de cisalhamento, intenso magmatismo tardi-orogênico e metamorfismo de alto grau formados na orogênese Brasiliana (Almeida et al., 1981; Vauchez et al., 1995). As diversas relações estruturais entre plutonismo e deformação foram amplamente estudadas em torno das zonas de cisalhamento Patos e Pernambuco, auxiliando no entendimento da evolução crustal e deformação dos domínios (Archanjo et al., 2008, 2009, 2002, 1995, 1994; Neves et al., 1996, 2000b).

Longa atividade em arco magmático, metamorfismo de ultra-alta pressão, e grandes unidades que registram metamorfismo em fácies granulito de alta pressão (Ganade de Araujo et al., 2014a,b) marcam a importância tectônica do Domínio Ceará Central no noroeste da Província Borborema. Este domínio é caracterizado por intenso plutonismo tardi-orogênico de proporções batolíticas (Almeida, 1987; Neves, 1991; Nogueira, 2004) associado a transcorrência nas zonas de cisalhamento Senador Pompeu e Tauá (Vauchez et al., 1995). Nestas faixas miloníticas a deformação de temperatura baixa a intermediária contrasta com a ampla migmatização registrada nas unidades internas do domínio, e sua evolução térmica e estrutural ainda é pouco conhecida, bem como o papel da interação entre as duas grandes falhas com cinemática supostamente conjugada.

Através do estudo detalhado do magmatismo dos plutons alojados às margens das zonas de cisalhamento Senador Pompeu e Tauá e de sua evolução estrutural, nesta tese é abordada a história tectônica tardia do Domínio Ceará Central durante a orogênese Brasiliana, com o objetivo de se detalhar o as relações genéticas entre a transcorrência e o plutonismo granítico, os processos de deformação e exumação orogênicos, e de reconstituir um perfil de resistência para a crosta nesta região. Em síntese, o conjunto de dados geocronológicos-estruturais permitem caracterização da natureza da interação entre zonas de cisalhamento sincrônicas, das tramas magmáticas dos plútons e sua relação com a deformação, da história térmica das zonas de cisalhamento, do papel da transcorrência no Domínio Ceará Central, e dos atributos reológicos das zonas de cisalhamento.

1.2 Estrutura da tese

No presente capítulo introdutório (Capítulo 1), é feita uma discussão sintética acerca de deformação e magmatismo em sistemas de zonas de cisalhamento de transcorrência com ênfase nos aspectos fundamentadores do tema abordado.

O Capítulo 2 consiste de uma descrição breve da teoria e aplicação dos métodos de estudo. Para coleta de dados e análises desta tese foram aplicados geocronologia U-Pb, termocronologia Ar-Ar, Anisotropia de Susceptibilidade Magnética (ASM) e Difração de Elétrons Retroespalhados (EBSD).

O Capítulo 3 descreve a evolução geológica e estratigrafia do Domínio Ceará Central a partir de revisão bibliográfica.

O conteúdo da tese é apresentado em forma de artigos científicos. O Capítulo 4 contém o artigo "*Zippered Shear Zone Model for Interacting Shear Zones in the Borborema Province, Brazil, as Constrained by UPb Dating*", publicado na revista Tectonics[1]. Nele são analisados dados inéditos de geocronologia U-Pb de granitos cujas estruturas revelam sincronicidade com a deformação de transcorrência.

O Capítulo 5 contém o artigo "*Shear zone cooling and fabrics of synkinematic plutons evidence timing and rates of orogenic exhumation in the northwest Borborema Province (NE Brazil)*" publicado na revista Precambrian Research[2]. Através de integração de dados de geocronologia U-Pb e termocronologia Ar-Ar com dados de ASM obtidos em plútons tardi-tectônicos este trabalho determina as as relações entre resfriamento, exumação e deformação nas zonas de cisalhamento.

Por fim, o Capítulo 6 apresenta em forma de artigo um estudo da reologia da zona de cisalhamento Senador Pompeu, sua cinemática e ocorrência de zíperes e longevidade com o objetivo de determinar a causa de seu distinto zonamento de condições de deformação.

O Capítulo 7 apresenta conclusões e considerações finais com uma visão global da transcorrência no Domínio Ceará Central a partir do conjunto de estudos feitos.

[1] Ávila et al. (2019); DOI: 10.1029/2019TC005547
[2] Ávila et al. (2020); DOI: 10.1016/j.precamres.2020.105940

1.3 Reologia da crosta continental e zonas de cisalhamento

A capacidade secular de resistência a tensões tectônicas na litosfera se deve à sua estrutura reológica. Baixos gradientes geotérmicos conferem uma alta viscosidade à camada limite mecânica no manto superior que, associada à alta resistência à fricção/-fratura na crosta superior, garante estabilidade de escudos cratônicos e regiões semelhantes. Além de corroborada por medidas de espessura elástica de até 100 km (Jordan and Watts, 2005), esta estratificação reológica clássica (conhecida como "sanduíche de geléia" Bürgmann and Dresen, 2008) é construída a partir de critérios de fricção/fratura e leis de fluxo das fases maiores em suas respectivas profundidades (Figura 2a). Na transição (10–15 km) entre a zona sismogênica da crosta superior e a crosta média, a resistência à fricção é superior à tensão de escoamento do quartzo, e mecanismos termoativados de deformação viscosa ocorrem com deformação rúptil; os dois processos ocorrem sob alta tensão, constituindo na transição fricção-fluxo de viscosidade a principal seção sustentadora da crosta (Holdsworth, 2004; Karlstrom and Williams, 1998). Abaixo desse nível, a baixa resistência depende da composição mineral, sendo dominada por plagioclásio na crosta inferior, e olivina-piroxênio no manto com alta viscosidade (Figura 2b).

Regiões estáveis com uma espessa camada limite mecânica no manto representam um limite superior para a resistência da litosfera. Lateralmente, mudanças em regimes térmicos, arranjo estrutural e heterogeneidade composicional da crosta média (Karlstrom and Williams, 2008) provocam importantes variações nos perfis de resistência. É amplamente reconhecido que diversos processos atuam ao longo do tempo para enfraquecer falhas e zonas de cisalhamento (Imber et al., 2001; Scholz, 1988) devido a, dentre outros fatores, reações metamórficas e transformações microestruturais. A resistência mecânica da litosfera é controlada pelas rochas mais fracas que a compõe (Townend and Zoback, 2000). Zonas de falhas e cisalhamento são concebidas como geneticamente dependentes de mecanismos de enfraquecimento e vistas como descontinuidades de baixa resistência (Wallis et al., 2013). Assim, elas controlam a resistência cumulativa secular da litosfera (Bürgmann and Dresen, 2008), que é reduzida de valores experimentais de limite de tensão de escoamento (centenas de MPa) a tensões observadas em falhas

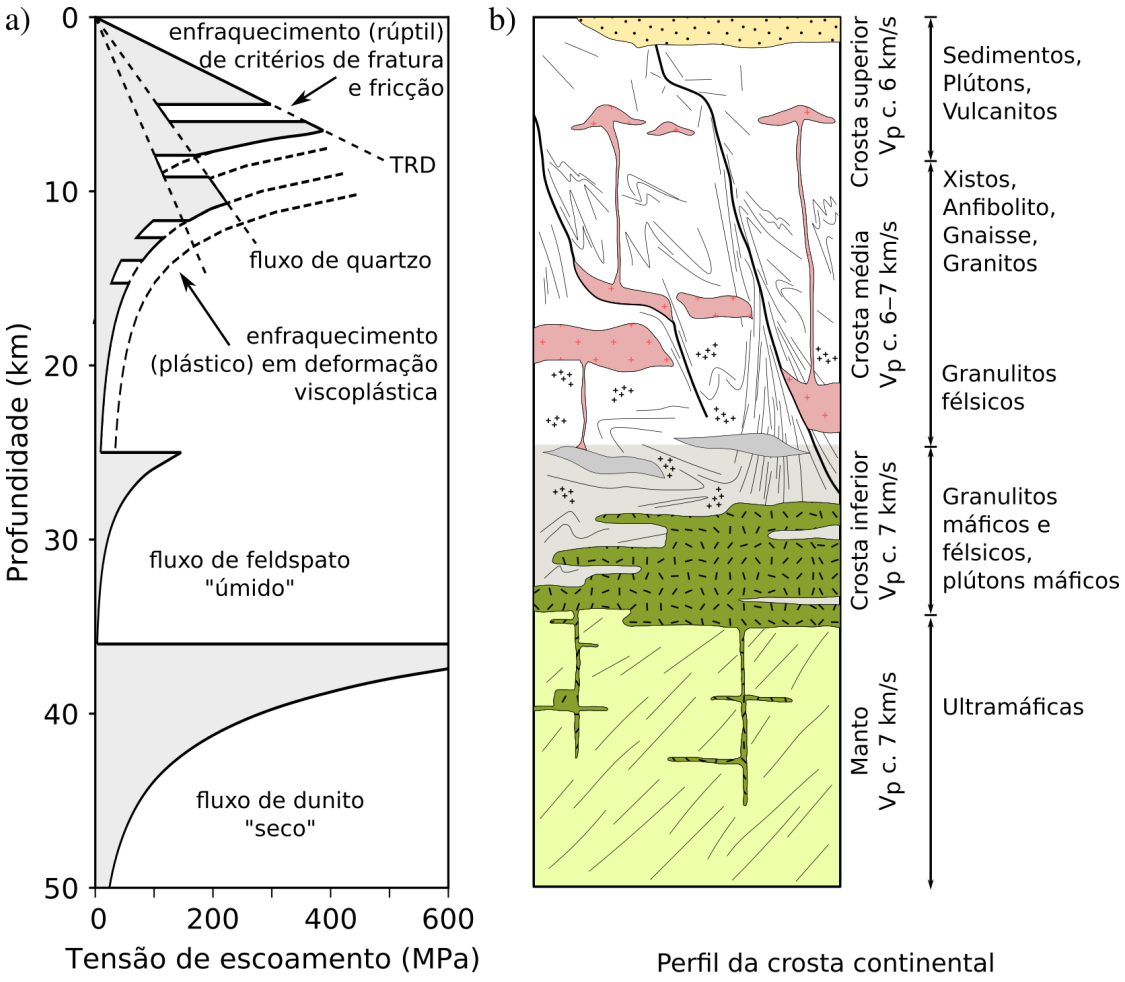

Figura 2 – a) Perfil de resistência conceitual para a litosfera continental. b) Bloco diagrama mostrando a diferenciação da crosta continental com base em composição (estimada por velocidades de ondas P, V_P) e estratificação reológica. TRD - transição rúptil-dúctil. Adaptado de (Karlstrom and Williams, 1998). Parâmetros de fluxo para quartzo, feldspato e olivina são obtidos de Platt (2015a), Rybacki and Dresen (2000) e Freed et al. (2012), respectivamente.

modernas e zonas de cisalhamento exumadas (< 100 MPa;; Wallis et al. 2013; Zoback et al. 1987). O registro da resistência e condições de deformação são encontrados nas microestruturas de rochas de zonas de cisalhamento e comparação com os produtos de deformação experimental em materiais geológicos (Mendes and Lagoeiro, 2012; Parsons et al., 2016; Pryer, 1993).

Com o aumento da profundidade, um típico perfil de estruturas e microestruturas se

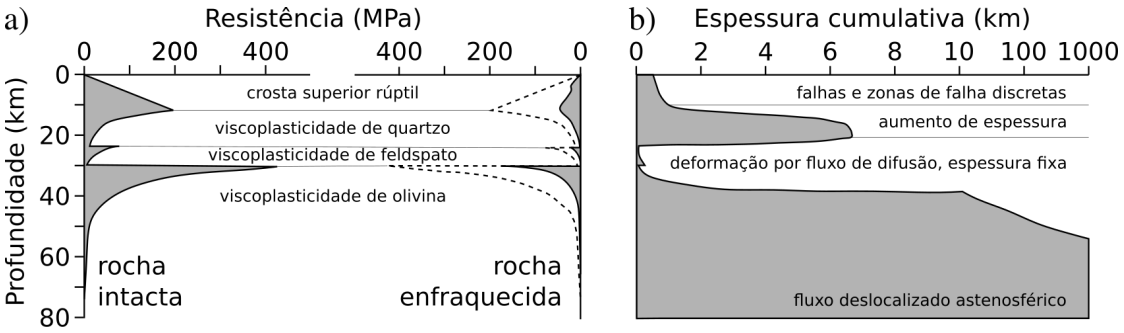

Figura 3 – a) Resistência limítrofe dada por rochas intactas e resistência real de rochas enfraquecidas de zonas de cisalhamento. A resistência de rochas intactas (esquerda) é a mesma apresentada na Figura 2. A resistência de rochas enfraquecidas (direita, linha tracejada marca a resistência de rochas intactas) compreende tanto enfraquecimento rúptil (e.g. aumento da pressão de poro ou redução do coeficiente de atrito) como dúctil (e.g. recristalização e transformações metamórficas). b) Simulação de perfil de espessura cumulativa de zona de cisalhamento (w) na litosfera continental com base na resistência limítrofe. Adaptado de Platt and Behr (2011c) e Holdsworth (2004).

desenvolve em zonas de cisalhamento (Figura 2a). Em temperaturas da crosta média a inferior, quartzo e feldspato exibem microestruturas de plasticidade intracristalina, fluxo por difusão e os grãos formados por recristalização dinâmica são grossos indicando tensões de fluxo de c. 10 MPa. Gnaisses miloníticos bandados se formam constituindo corredores de fluxo com cisalhamento consistente por dezenas de kilômetros de espessura (e.g. zona de cisalhamento Patos leste da Província Borborema; Viegas et al., 2014). Exumação progressiva durante deformação é conhecida em ambientes extensionais (Cooper et al., 2017), transcorrentes (West and Hubbard, 1997) e contracionais (Toy et al., 2008). Com redução da temperatura, novas estruturas e microestruturas se sobrepõe às antigas em espessuras menores. Em profundidades de crosta média até a transição fricção-fluxo de viscosidade, formam-se bandas de cisalhamento estreitas com intensa recristalização dinâmica de quartzo em pequenos grãos indicando alta tensão (até 100 MPa) que se deforma por plasticidade intracristalina. Milonitos e ultramilonitos de baixa temperatura formam nesta profundidade típicas zonas de cisalhamento com espessura cumulativa que podem chegar até alguns kilômetros (Cooper et al., 2017).

Considerando-se uma zona de cisalhamento com velocidade de deslizamento V, a

taxa de deformação de cisalhamento $\dot{\varepsilon}$ é dada por

$$\dot{\varepsilon} = V/w,$$

em que w é a espessura de cisalhamento. Se V é fixa, um aumento de $\dot{\varepsilon}$ causa localização da deformação. Ainda se conhece pouco sobre as relações entre a localização da deformação (i.e. espessura ativa de zonas de cisalhamento), transições reológicas e cinemática. Perfis de resistência teóricos (Figura 3a) são construídos pela premissa de uma taxa de deformação constante, e portanto w constante. Rocha intacta da crosta transmite tensão diferencial à zona de cisalhamento e deforma-se a um valor negligível de $\dot{\varepsilon}$ comparável em qualquer profundidade. Platt and Behr (2011c) propuseram a hipótese de que o perfil de resistência de rocha intacta determina um valor limítrofe de tensão diferencial para zonas de cisalhamento onde mecanismos de enfraquecimento aceleram a taxa de deformação. Recristalização dinâmica gera agregados finos e ativam uma dependência com tamanho de grão d que auxilia nos mecanismos de plasticidade intracristalina (i.e. $\dot{\varepsilon} \propto d$). Com as transformações estruturais e composicionais que seguem a localização, um perfil de enfraquecimento permanente se perpetua em zonas de falhas e cisalhamento (e.g. modelo banana split de resistência; Bürgmann and Dresen 2008). Conforme modelo desenvolvido por Platt and Behr (2011a), aplicando as leis de fluxo ao perfil de tensão diferencial limítrofe de rochas intactas é possível calcular de forma simplificada a espessura cumulativa w, que deslocaliza com a profundidade devido ao aumento da viscosidade em agregados com reologia dependente de d (Figura 3b).

1.4 Magmatismo sin-tectônico em zonas de limites de placas

Magmas podem causar significativo enfraquecimento da crosta e localização da deformação, seja por ocorrerem em pequenas porcentagens facilitando mecanismos de deformação, ou por advecção de calor em grandes volumes (Hollister and Crawford, 1986); por sua vez, os processos de deformação em zonas de cisalhamento podem facilitar extração, ascensão e alojamento de magmas, e deixar neles o registro da deformação regional (Paterson et al., 1998). Em zonas de limites de placas há uma forte associação espacial e/ou de sincronicidade entre granitos e zonas de cisalhamento. Por esta razão,

plutonismo e deformação são comumente interpretados como geneticamente correlatos. Estudos geoquímicos mostram que os plutons associados a zonas de cisalhamento transcorrentes em cinturões orogênicos variam de máficos a félsicos e são caracterizados por alto teor de K e elementos incompatíveis, formados por mistura de magmas provenientes de fusão parcial do manto e da crosta (Hollanda et al., 2003; Neves et al., 2000a; Vaughan and Scarrow, 2003). Em alguns casos se pôde mostrar que estas zonas de cisalhamento tem raízes na base da crosta (Klemperer et al., 2013), em consonância com a aparente ligação estrutural e temporal entre magmatismo e deformação. Assim, estas províncias caracterizadas por intenso plutonismo e zonas de cisalhamento sincrônicos em zonas de limites de placas podem ser pensadas como uma associação tectonomagmática distinta (Vaughan and Scarrow, 2003) na qual pode haver um controle estrutural na extração de *melt* (Brown and Solar, 1998), migração de magmas, alojamento (Hutton and Reavy, 1992) e erupção (Wadge and Cross, 1988), ou a presença de grande volume magmático na crosta pode facilitar localização da deformação e nucleação de zonas de cisalhamento (Neves and Vauchez, 1995).

Em muitos casos de plútons associados a zonas de cisalhamento a suposta relação de causa não é provada (Stipp et al., 2004). As formas dos assoalhos de intrusões graníticas reveladas por levantamentos geofísicos frequentemente não possuem suas zonas alimentadoras enraizadas nas zonas de cisalhamento que margeiam, mas em sítios localmente extensionais (Vigneresse, 1995). Schmidt and Paterson (2000) e Paterson and Schmidt (1999) mostraram que o magmatismo em redes de transcorrência (e.g. a Província Borborema) é um processo deslocalizado, e que a ocasional associação espacial com zonas de cisalhamento se deve a densidade de ambas as feições. Neste caso, a origem desse abundante magmatismo não tem relação com as estruturas da crosta e é independentemente associada a processos tectônicos de maior escala como *slab breakoff* (ao final da subducção; von Blanckenburg and Davies, 1995) ou delaminação manto litosférico (Houseman et al., 1981). Muitas intrusões têm uma longa história de cristalização registrada por idades U-Pb em zircões (Samperton et al., 2015; Schoene et al., 2012) que representam seu crescimento incremental. Entretanto, como descrito por Glazner et al. (2004), taxas de ascensão de magmas são tais que plútons grandes se formam em menos de 0.1 Myr, indicando que as taxas de deformação que seriam necessárias para geração de espaços (100–1000 mm/yr) são consideravelmente elevadas em comparação com taxas de deformação tectônica ($<$ 100 mm/yr). Portanto, geração

de *melt* e sua extração por interação com deformação tectônica (Weinberg et al., 2006) tende a ser o fator controlador de taxas de magmatismo (Petford et al., 2000).

Não obstante, as estruturas de deformação de corpos plutônicos e suas relações com encaixantes revelam que as descontinuidades da crosta marcadas em grandes estruturas de transcorrência têm papel fundamental na geração de espaços para alojamento dos magmas, e incontáveis estudos de petrologia estrutural elucidaram os potenciais mecanismos (Bouchez, 1997; Paterson et al., 1989; Petford et al., 2000). Detalhes cronológicos dos processos de deformação em estruturas que acomodam encurtamento em orógenos podem ser determinados através de relações transversais com os corpos ígneos associados, sendo possível interpretar longevidade, *timing*, e taxas dos processos de cisalhamento (Ingram and Hutton, 1994; Searle et al., 2011).

Por ocorrerem em cinturões dominantemente transpressivos (D'Lemos et al., 1992; Hutton and Reavy, 1992; Ingram and Hutton, 1994), os corpos plutônicos sin-tectônicos associados a zonas de limites de placas dependem da ocorrência de sítios extensionais para serem alojados. Estes são marcados por intrusões assimétricas e podem ser formados como *pull-aparts* e estruturas transtensivas diversas (Guineberteau et al., 1987; Hofmann et al., 2009), em terminações de zonas de cisalhamento (Hutton, 1988b), ou devido a contrastes de competência no embasamento (Weinberg et al., 2004). Durante a evolução de uma zona de cisalhamento, seus segmentos individuais sofrem deformação que varia entre transpressiva e transtensiva. Sítios extensionais são criados e destruídos (Hutton, 1988a; Weinberg et al., 2006), permitindo que o alojamento de magmas se dê de forma episódica, sem necessidade de ocorrência permanente de estruturas de transtensão. Isso se deve a variações em direções principais de encurtamento, heterogeneidades estruturais e composicionais, taxas de deformação, interação de zonas de cisalhamento e reorientação de blocos na crosta (Weinberg et al., 2006).

Armadilhas transtensivas preservadas frequentemente na crosta média e superior são características de intrusões passivas, nas quais a taxa de geração de espaço por deformação tectônica excede a taxa de adição de magmas (Hutton, 1988a; Stevenson, 2009). Este modo de colocação é favorecido pelo crescente número de estudos que descrevem intrusões que foram construídas por injeções discretas e sucessivas de magmas ao longo de até alguns milhões de anos (Coleman et al., 2004; de Saint Blanquat et al., 2011; Ingram and Hutton, 1994). Em geral, intrusões têm aspecto espacial tabular, independente da escala, formado por acreção de *sheets* que crescem horizontalmente e em

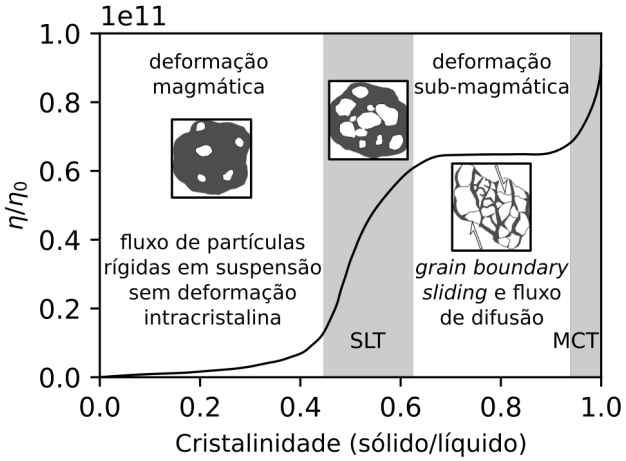

Figura 4 – Relação entre viscosidade e reologia de magmas, e cristalinidade (razão de volume de sólidos para volume de líquido). SLT - transição sólido-líquido, MCT - transição de conectividade de *melt*. Adaptado de de Rosenberg and Handy (2005) e Blenkinsop (2005).

seguida por espessamento, indicando que tanto plútons rasos como profundos compartilham um mecanismo básico de formação (McCaffrey and Petford, 1997; Petford et al., 2000).

Muitos corpos plutônicos se formam por intrusão ativa, na qual geram espaço por deslocamento das encaixantes (McCaffrey and Petford, 1997). Estas são tipicamente concebidas como intrusões profundas e diapíricas formadas pelo alojamento de grandes volumes de magmas com pouca porcentagem de sólidos. Muitos plútons exibem estruturas magmáticas (microdiápiros, texturas de resfriamento, *pillows*) que marcam a interação e mistura entre magmas amplamente fundidos, i.e. com baixa fração de cristais (Wiebe, 2016). Isto indica que em alguns casos uma câmara magmática pode ser formar por diapirismo (Miller and Paterson, 1999; Weinberg and Podladchikov, 1994), embora este conceito tenha caído em descrédito devido às elevadas taxas de deformação necessárias para migração de diápiros. Sob transpressão, a construção de plútons pode ainda se dar por acumulação de *sheets* alojados gradativamente como diques (Ingram and Hutton, 1994).

A confirmação de sincronicidade se faz pela identificação de uma auréola de metamorfismo de contato nas rochas encaixantes deformadas pela intrusão e pelo emba-

samento, na qual ocorrem porfiroblastos (e.g. granada) rotacionados em concordância com o padrão de deformação regional (Paterson et al., 1989). Entretanto, uma intrusão pode não ser capaz de trazer calor suficiente por advecção, ou o gradiente térmico com as encaixantes pode não ser propício para desenvolver um distinto metamorfismo de contato. Magmas alojados sob altas temperaturas (i.e. crosta média e inferior) por intrusão ativa formam nas encaixantes um padrão concêntrico de estruturas (semelhante ao típico baloneamento; Ramsay, 1989). Nas extremidades alongadas do corpo, as estruturas concêntricas das encaixantes se paralelizam à estrutura do embasamento formando junções tríplices de foliação (Brun and Pons, 1981), indicando interferência entre a deformação de encurtamento das encaixantes e a deformação tectônica do embasamento (Pons et al., 1992; Stevenson, 2009).

Critérios de sincronicidade adicionais podem ser encontrados em estruturas internas e microestruturas de intrusões que sofreram deformação tectônica com presença de *melt*. Durante um vasto intervalo de cristalinidade (porcentagem de volume de fundido) os sólidos ocorrem livremente e o magma tem efetivamente uma reologia de suspensão plástica (Petford, 2009). Com a progressiva cristalização, a viscosidade da suspensão aumenta gradativamente, e, em seguida, abruptamente, na transição reológica em que o arcabouço sólido se estabelece pela conectividade dos cristais (Arzi, 1978; Blenkinsop, 2005). Embora seja estritamente não-Newtoniano, o magma só desenvolve um limite de tensão de escoamento (*yield strength*) sob esta alta cristalinidade (Kerr and Lister, 1991). Hoover et al. (2001) determinaram que a fração crítica de *melt* teórica varia entre 15 e 40% (Figura 4), a depender primordialmente da forma dos cristais e tipo de empacotamento. Embora arcabouços localizados de cristais podem ser encontrados em baixas cristalinidades na natureza devido ao mecanismo de formação de concreções (*synneusis;* Philpotts et al., 1998; Vance, 1969), a determinação de Rosenberg and Handy (2005) para a "transição sólido-líquido" (SLT) em c. 40% de volume de *melt* é amplamente aceita.

Com uma cristalindade abaixo da SLT, a suspensão caracteriza o estado magmático de fluxo. Neste intervalo, enclaves máficos estirados (schlieren) registram deformação (Fowler and Paterson, 1997) e porfiroclastos anisométricos na suspensão são progressivamente rotacionados a uma orientação preferencial de forma segundo a foliação de fluxo do estado magmático (Figura 5a; Arbaret et al. 2000). Se a orientação preferencial de forma é sintaxial com a estrutura do embasamento gerada por deformação tectônica,

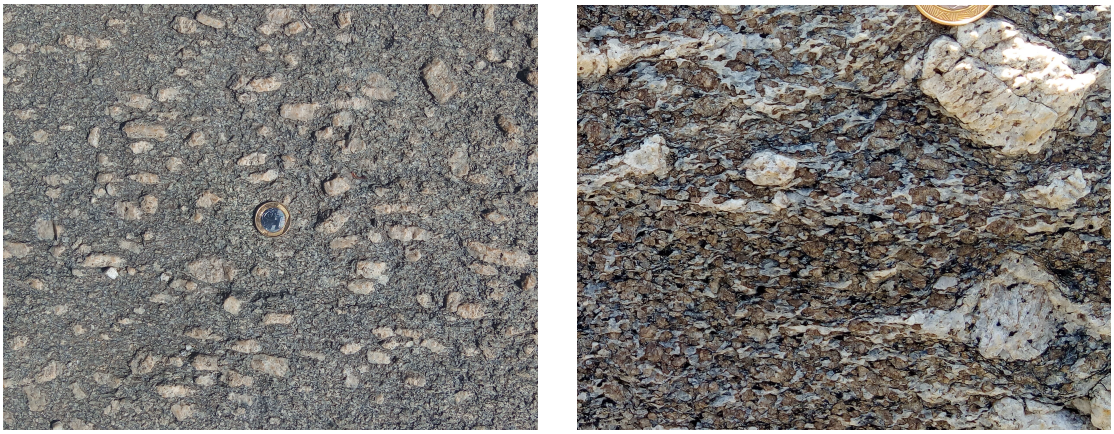

(a) (b)

Figura 5 – (a) Orientação preferencial de forma de porfiroclastos de feldspato potássico em granitóide do batólito Quixeramobim. A foliação magmática é paralela à base da foto. (b) Granito porfirítico do batólito Quixeramobim. Megacristais de feldspato potássico definem uma trama de forma que caracteriza o fluxo magmático (paralelo à base da foto). Plagioclásio (cor avermelhada) e feldspato potássico da matriz são subédricos e preservam sua forma magmática. Quartzo apresenta elongações com baixa razão axial (c. 2:1) devido à deformação no estado sólido.

pode-se supor que a mesma foi responsável pela deformação magmática do plúton. Os critérios descritos são facilmente obliterados devido à brevidade dos processos magmáticos em comparação à deformação tectônica (de Saint Blanquat et al., 2011) e nos casos em que a deformação subsequente no estado sólido for alta.

Estritamente, alojamento sin-cinemático determinado pelo critério de orientação preferencial de forma de porfiroclastos e schlieren precisam ser confirmados pela identificação de uma transição gradativa entre deformação no estado magmático e deformação no estado sólido em alta temperatura (Miller and Paterson, 1994). Se a quantidade de deformação no estado sólido for baixa, quartzo será deformado preferencialmente devido à sua baixa viscosidade formando elongações de baixa razão axial (agregados lenticulares de quartzo com deformação interna, Figura 5b; Hutton 1988a), e precipitação de *melt* tardio ocorrerá em sombras de pressão e microfraturas (Bouchez et al., 1992).

Granitos com texturas maciças e equigranulares comumente possuem tramas de deformação magmáticas crípticas e aparentemente isotrópicas. Estudos petrográficos de

detalhe mostram que, embora fraca, a orientação preferencial de forma de várias fases magmáticas representa o padrão regional de deformação tectônica (Bouchez, 1997) e podem ser reveladas com Anisotropia de Susceptibilidade Magnética (ASM). Esta ferramenta fundamentadora de petrologia estrutural, revela padrões estruturais relacionados à ascensão e colocação de magmas, e sua subsequente deformação (Cruden et al., 1999).

Com o aumento da cristalinidade, o arcabouço sólido se fecha progressivamente enquanto o espaço intercristalino é preenchido pelos líquidos finais da fusão. Este líquido intersticial permite que mecanismos de deformação como fluxo de difusão e deslizamento de borda de grãos sejam ativados com deformação intracristalina negligível. Quando a porcentagem de *melt* cai abaixo de 7%, a interconexão de líquido intersticial deixa de ocorrer por todo o volume do magma, e um aumento de viscosidade de algumas ordens de magnitude é observado, descrito por Rosenberg and Handy (2005) como transição de interconectividade de *melt* (MCT, Figura 4). Em torno desta, fraturas sin-magmáticas de cristais mais grossos como feldspato e anfibólio são preenchidas com *melt* do qual se formam fases tardias como quartzo e feldspato que podem ser usadas como critério de deformação sin-magmática (Bouchez et al., 1992).

2 Métodos

2.1 Geocronologia U-Pb em zircão

Para obter as idades das unidades ígneas estudadas e da deformação relacionada foi feita datação de zircões magmáticos pelo método U-Pb em SHRIMP (*Sensitive High-Resolution Ion Microprobe*). No sistema U-Th-Pb, as cadeias de decaimento de ^{238}U para ^{206}Pb, ^{235}U para ^{207}Pb, e ^{232}Th para ^{208}Pb, têm meia-vida λ de 4.5 Gyr, 0.7 Gyr e 14 Gyr, respectivamente. Idades absolutas (t) são obtidas com base na composição isotópica dos elementos do sistema, i.e. da concentração de isótopos-filho (D) e radioativos (N), e podem ser calculadas de forma simplificada segundo a equação da idade, dada por

$$D = D_0 + N(e^{\lambda t} - 1), \tag{2.1}$$

em que D_0 é a quantidade não-radiogênica de isótopos-filho.

O alto peso atômico do U impede fracionamento diferencial entre seus isótopos de modo que as razões ^{238}U/^{206}Pb e ^{235}U/^{207}Pb podem ser usadas como teste cruzado de acurácia das idades absolutas medidas. O diagrama de ^{238}U/^{206}Pb versus ^{235}U/^{207}Pb tem em sua curva concórdia todas as idades concordantes. Este foi introduzido por Wetherill (1956) e é a forma padrão de avaliar discordância entre as duas razões. Por exemplo, alteração secundária por perda de Pb fica evidenciada na linha discordia. Quando a concordância é verificada, é costumeiro apresentar as idades de forma resumida sob uma média ponderada (Miles and Woodcock, 2018; Schoene, 2014) com a razão isotópica mais apropriada para o intervalo de idade (e.g. razão ^{238}U/^{206}Pb para o Neoproterozóico devido à sua meia-vida mais elevada em comparação a ^{235}U/^{207}Pb).

Comum em rochas ígneas, o zircão constitui um sistema geocronológico rico (Allègre, 2008) devido a substituição de U e Th e ausência Pb durante sua cristalização. Resistência ao intemperismo e um caráter refratário a processos secundários (e.g. hidrotermalismo e metamorfismo de baixo grau) permitem que esse mineral seja um robusto registro da idade de solidificação do magma, dado que sua temperatura de fechamento é em torno de 800 °C. Metamorfismo de alto grau e fusão parcial entretanto são capazes de provocar recristalização total ou parcial de zircões e portanto registrar tal evento. O

uso deste mineral para determinação de idades de unidades geológicas tem sido a ferramenta básica do estudo de evolução crustal e história tectônica da Província Borborema (Brito Neves, 1975; Ganade de Araujo, 2014).

O SHRIMP é uma técnica *in situ* de espectrometria de massa de íons secundários que é capaz de uma resolução temporal final de c. 1% (c. 5 My no Neoproterozóico). O feixe de íons primário tem um diâmetro de 20 µm e pode ser focalizado no ponto de escolha do cristal. Para as análises, os zircões são separados conforme procedimento padrão de britagem, moagem, peneiração, separação hidrodinâmica, separação magnética e separação por gravidade (Sato et al., 2014). A fração separada é embutida em resina e polida para seccionar os cristais de zircão em meia largura. Por microscopia ótica e catodoluminescência em microscópio eletrônico de varredura, as texturas internas dos cristais são observadas com o objetivo de selecionar os mais preservados, límpidos e indicadores do processo de formação que se pretende datar. Cristais em rochas ígneas e metamórficas têm frequentemente um núcleo com zonamento oscilatório típico de cristalização em magmas, truncado por uma margem que pode ter textura de zonamento formada em estágios tardios de solidificação, ou ser maciça e com zonação irregular, formada por recristalização metamórfica (Corfu, 2003).

2.2 Termocronologia por Ar-Ar

A termocronologia por datação Ar-Ar em concentrados de silicatos compostos de K é uma das principais técnicas utilizadas para o entendimento da exumação de unidades orogênicas a partir de temperaturas elevadas. Minerais concentrados têm ^{39}K convertido em ^{39}Ar por irradiação de nêutrons e são posteriormente análisado por espectrometria com liberação de Ar em volumes discretos por etapas sucessivas de aquecimento. Os experimentos analíticos desse estudo foram conduzidos com um laser de Nd-YVO_4 acoplado a um espectrômetro de massa ARGUS VI (Thermo Scientific) no Laboratório de Geocronologia de Gases Nobres do Centro de Pesquisas Geocronológicas da USP. Para processamento dos dados foram usados ArArCalc v2.6e e Isoplot 3.7.

^{40}K sofre decaimento para ^{40}Ar com meia-vida de 11.9 Gyr e constitui um sistema rico dado que Ar não ocorre nos silicatos. Em datação convencional por K-Ar, ^{40}K pode ser determinado por espectrometria de massa ou espectroscopia de dispersão de energia (EDS), dado a fixa composição isotópica desse elemento. A composição isotópica de Ar

é medida separadamente por métodos independentes. Para garantir que a mesma massa seja analisada para obtenção das concentrações e razões isotópicas de K e Ar, é feita a transformação de ^{39}K em ^{39}Ar através de irradiação de minerais portadores de K por nêutrons de alta velocidade, causando captura de nêutron e perda de próton. Durante o tempo Δt de irradiação, a produção de ^{39}Ar é dada por

$$^{39}\mathrm{Ar} = {}^{39}\mathrm{K}\Delta t \int_{min\,e}^{max\,e} \phi_e \sigma_e de,$$

em que ϕ_e é a densidade de fluxo dos elétrons com energia e e σ_e é a seção transversal de captura de ^{39}K por nêutrons de energia e. Dada a constante ^{40}K/^{39}K, é possível substituir a produção de ^{39}Ar na equação de datação (Equação 2.1) para se obter a idade t a partir de

$$t = \frac{1}{\lambda} \ln[J(^{40}\mathrm{Ar}/^{39}\mathrm{Ar}) + 1],$$

em que λ é a constante de decaimento e o fator J é obtido por análise de padrões com idades conhecidas (Allègre, 2008).

Para as amostras desse estudo e o padrão de sanidina de *Fish Canyon* (Phillips and Matchan, 2013), as irradiações foram feitas no reator nuclear da TRIGA da *Oregon State University*. Os concentrados minerais foram analisados no Laboratório de Geocronologia de Gases Nobres do Centro de Pesquisas Geocronológicas da Universidade de São Paulo. Aquecimento incremental foi feito com laser de Nd-YVO_4 e o gás extraído foi analisado com o espectrômetro de massa ARGUS VI. Os concentrados de minerais foram obtidos por procedimento padrão de britagem, moagem, peneiração, separação magnética e catação com lupa. Um estudo textural preliminar é feito para selecionar amostras com cristais de biotita, muscovita e anfibólio livres de alteração e homogêneos.

Ar extraído por aquecimento incremental em etapas é retirado de sítios da estrutura dos cristais com capacidades de difusão progressivamente menores. Em baixas temperaturas é liberado gás nas bordas dos minerais, que podem ter sido afetadas por processos secundários e isolam um núcleo (presumidamente) preservado. Para detalhar estes registros nas idades de Ar-Ar, a sequência de razões isotópicas em cada etapa de liberação é representada com um diagrama do espectro de idades (Figura 6). Perda de Ar pode ocorrer quando o mineral é mantido sob temperaturas da sua zona de retenção parcial (abaixo de sua temperatura de fechamento para difusão) ou em temperaturas

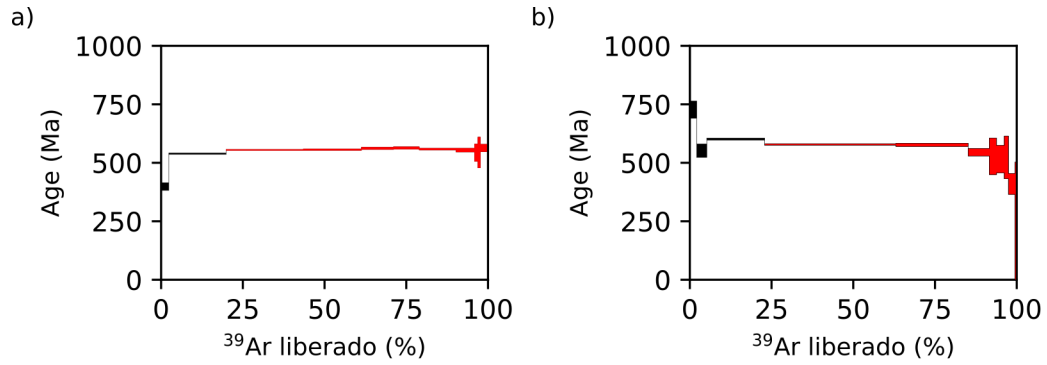

Figura 6 – a) Espectro de idades de Ar-Ar mostrando perda de Ar e consequentemente idades mais jovens nas primeiras etapas de aquecimento (etapas em preto). b) Espectro de idades de Ar-Ar mostrando forma de sela indicando possível excesso de Ar (etapas em preto).

intermediárias durante longo tempo (Dunlap, 2000) e afeta principalmente as bordas dos cristais, gerando um padrão de idades mais jovens no diagrama do espectro de Ar (Figura 6a). Excesso de Ar tem uma origem ainda debatida, atribuída genericamente a altas pressões parciais de Ar em fluidos intersticiais (Dickin, 2018). Seu registro se dá nas bordas dos minerais analisados, gerando uma idade aparente mais antiga e um aspecto de sela/vale ao espectro de Ar (Figura 6b). Quando existem etapas de liberação de Ar subsequentes com idades que se sobrepõem dentro da incerteza e compreendem mais de 50% do volume de Ar da análise, pode se calcular uma idade platô (Figuras 6a e 6b), por uma média ponderada pelo inverso das incertezas de cada etapa.

Para o uso de idades de Ar de silicatos como biotita, muscovita e anfibólio como marcadores de exumação é preciso determinar a temperatura de fechamento T_C na qual a difusão dos isótopos radiogênicos se torna negligível e o sistema geocronológico é considerado fechado. Uma solução analítica para T_C de um sistema mineral com relação a difusão de Ar foi obtida por Dodson (1973) a partir da equação de Arrhenius $D = D_0 \exp -R/RT$, em que D é o coeficiente de difusão na temperatura T, E é a energia de ativação, R é a constante dos gases, e D_0 é a difusividade. Supondo um resfriamento linear (dT/dt) a taxas suficientemente baixas, T_C é dada por

$$E/RT_C = \ln\left(\frac{-ART_C^2 D_0}{a^2 E dT/dt}\right).$$

A é o fator de forma do mineral (55 para esfera, 27 para prisma e 9 para formas ta-

bulares) e a é o raio de difusão que pode ser o tamanho médio dos grãos ou o raio de difusão efetiva. A solução para dT/dt é obtida de forma recursiva com suposição de T_C inicial (e.g. 550 °C para anfibólio). Em geral, as temperaturas de fechamento de biotita, muscovita e anfibólio são em torno de 300–350 °C, 400–450 °C e 500–550 °C, respectivamente. Assim, elas compreendem um intervalo de temperatura de exumação sin-orogênica associada a soerguimento de rochas da crosta inferior-média para a crosta superior.

2.3 Tramas magnéticas

2.3.1 Fundamentos de magnetismo de rochas e mineralogia magnética

Na primeira metade do século XX, a conhecida Anisotropia de Susceptibilidade Magnética (ASM) das rochas foi atribuída à sua textura e estrutura interna (Borradaile and Jackson, 2010). Apesar da complexa relação entre anisotropias magnéticas (de susceptibilidade e remanência), sinal magnético dos minerais constituintes da rocha e sua trama, a ASM se tornou uma ferramenta amplamente aplicada em geologia estrutural. Em casos de rochas aparentemente isotrópicas ou unidades rochosas muito heterogêneas, ASM é uma técnica capaz de revelar as estruturas (Bouchez, 1997; Viegas et al., 2013). A revisão teórica apresentada a seguir sobre magnetismo, mineralogia magnética e anisotropia magnética é baseada em Butler (1992), Dunlop and Özdemir (1997), Tauxe (2005) e Lowrie (2007).

No estudo magnético de petrotramas são feitas determinações da magnetização de amostras de rocha e de suas variações segundo a direção no material geológico. Magnetização induzida $\vec{M}$ é provocada pela aplicação de um campo externo $\vec{H}$ segundo a proporcionalidade da susceptibilidade magnética k ($\vec{M} = k\vec{H}$, dada em A/m). A magnetização remanente $\vec{M}_r$ é espontânea e existe mesmo na ausência de um campo externo. Diversos fenômenos que se dão no interior de um material podem gerar um campo magnético em seu volume, correspondente à magnetização. Cargas em movimento inseridas em um campo magnético sofrem uma força de Lorentz na direção normal ao plano de deslocamento e das linhas do campo $\vec{B}$. Em elétrons de dado material, a superposição de sua trajetória e da força de Lorentz causam uma precessão dos orbitais em torno de

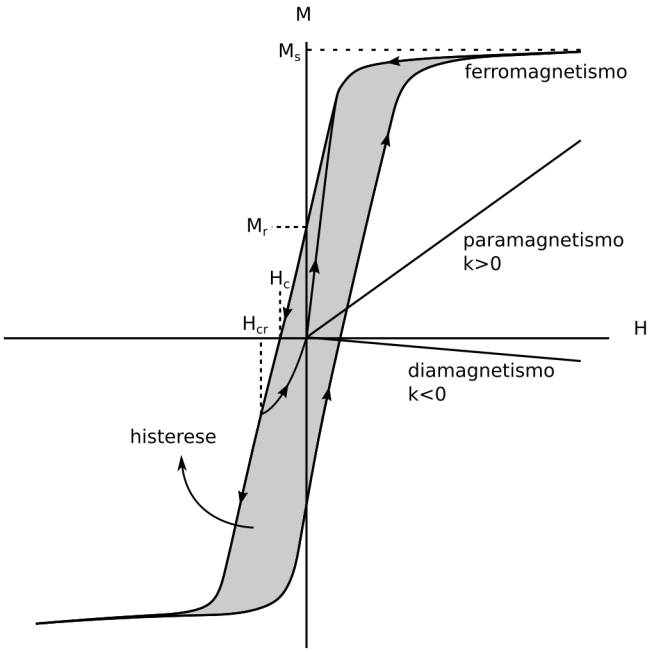

Figura 7 – Tipos de magnetização possíveis em minerais formadores de rochas. M_r - magnetização remanente, M_s - magnetização de saturação, H_c - coercividade, H_{cr} - coercividade de remanência. Adaptado de Bouchez (1997).

$\vec{B}$. Esta chamada precessão de Larmor dá origem a um campo no sentido oposto, caracterizando a magnetização diamagnética (Figura 7). Diamagnetismo é uma propriedade de todos os materiais que depende da estrutura cristalina e composição química, e a susceptibilidade diamagnética de minerais formadores de rocha é da ordem de -10^{-3} mSI. A susceptibilidade diamagnética tem o papel principal de diluir a contribuição das susceptibilidades para- e ferromagnética.

Em metais de transição como Fe, Cr, Mn, Ni e Ti elétrons desemparelhados geram momentos magnéticos permanentes em seus átomos que podem produzir magnetizações mais intensas nos minerais, dependendo de seu estado de oxidação. Quando inseridos em um campo magnético externo $\vec{H}$ os momentos magnéticos tendem a se alinhar, sendo perturbados apenas por vibrações térmicas que impedem o alinhamento pemanente de longo alcance. Com base na energia de alinhamento de momentos magnéticos e sua dependência com a temperatura, o modelo de Langevin expressa a relação geral para

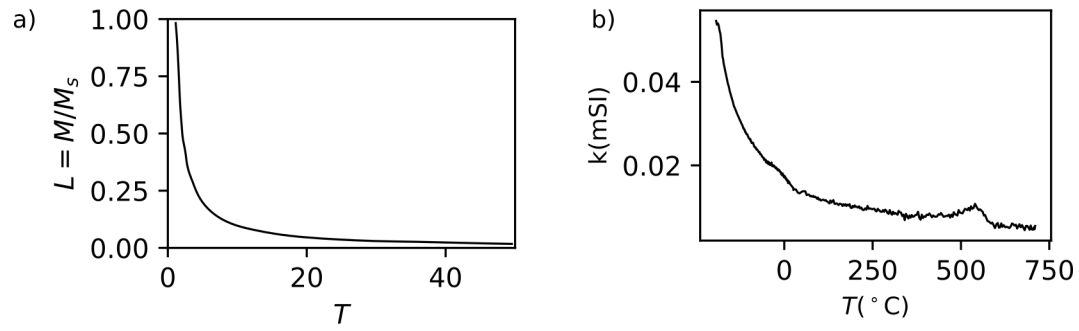

Figura 8 – a) Curva termomagnética teórica calculada segundo a função de Langevin mostrando a magnetização paramagnética em função da temperatura. Adaptado de Tauxe (2005). b) Curva termomagnética experimental para rocha rica em biotita.

magnetização pela função de Langevin $L(a)$, dada por

$$L(a) = M/M_s = \coth(a) - 1/a, \tag{2.2}$$

em que

$$a = m_b \mu_0 H/KT, \tag{2.3}$$

M_s é a magnetização de saturação, m_b é o magnéton de Bohr, μ_0 é a permeabilidade magnética e K é a constante de Boltzmann. A susceptibilidade paramgnética portanto, é, inversamente proporcional à temperatura (Figura 8a). A Figura 8b mostra a curva termomagnética para uma rocha rica em biotita. Em temperatura ambiente campos externos muito elevados (c. 100 T) são necessários para saturar a magnetização (Figura 9). Para silicatos ferromagnesianos comuns a susceptibilidade paramagnética em condições gerais de temperatura ambiente e baixos campos indutores é positiva e da ordem de alguns mSI (c. 2 mSI para biotita e até 9 mSI para anfibólio). Se $KT >> m_b \mu_0 H$, a função de Langevin tem uma aproximação linear (Figura 9) da qual pode ser obtida a lei de Curie para a susceptibilidade paramagnética k, dada por

$$M/H = k = m_b \mu_0 M_s/3KT. \tag{2.4}$$

Os orbitais eletrônicos são dispostos conforme o retículo do mineral e forma das ligações com átomos vizinhos, de forma que o alinhamento dos momentos mangéticos é favorecido em determinadas direções cristalográficas (O'Handley, 2000). Tal variação direcional da energia relacionada à magnetização induzida e da susceptibilidade

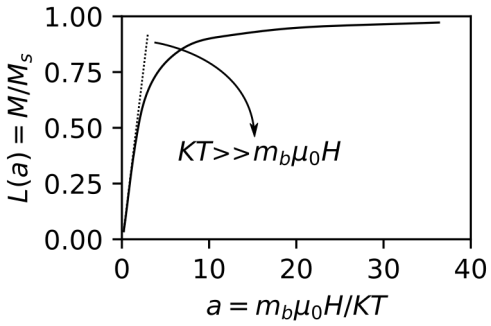

Figura 9 – Curva teórica de aquisição de magnetização calculada segundo a função de Langevin mostrando a saturação da magnetização paramagnética (M/M_s) com o aumento do campo indutor (H). A curva pontilhada mostra a aproximação para a susceptibilidade paramagnética (Equação 2.4) quando $KT >> m_b\mu_0 H$. Adaptado de Tauxe (2005).

magnética de minerais paramagnéticos e diamagnéticos é chamada anisotropia magnetocristalina. Assim, a susceptibilidade magnética k_{ij} é um tensor material de segunda ordem simétrico, que relaciona o campo aplicado $\vec{H}$ à magnetização induzida $\vec{M}$ por $M_i = k_{ij}H_j$ $(i, j = 1,2,3)$. Dado que k_{ij} deve conter no mínimo todos os elementos de simetria macroscópica do cristal (Nye, 1984) as direções principais de susceptibilidade ($k_{max} > k_{int} > k_{min}$) são convenientemente paralelas ou subparalelas aos eixos de maior simetria dos cristais (Figura 10; Borradaile and Jackson 2010). Em anfibólios e piroxênios monoclínicos, por exemplo, k_{int} é subparalelo ao hábito elongado dos cristais (i.e. subparalelo ao eixo c). Em micas, k_{max} e k_{int} são subparalelas ao plano basal e k_{min} é normal a ele. A estrutura trigonal do quartzo confere simetria uniaxial para k_{ij}. Em cristais naturais, a ocorrência de exsoluções a heterogeneidades composicionais leva a ampla variação na orientação e módulo das direções principais de susceptibilidade magnética (Lagroix and Borradaile, 2000).

Em alguns materiais cristalinos, os orbitais de elétrons desemparelhados se interferem para minimizar a energia de átomos de metais de transição suficientemente próximos produzem uma ordem de longo alcance para os momentos magnéticos. Diversos tipos de “interações de troca” ou acoplamentos entre duas órbitas eletrônicas de átomos vizinhos podem ocorrer que são baseados no princípio de exclusão de Pauli. Com o alinhamento dos momentos magnéticos forma-se uma intensa magnetização espontânea que caracteriza materiais ferromagnéticos. Estas interações decaem exponencialmente

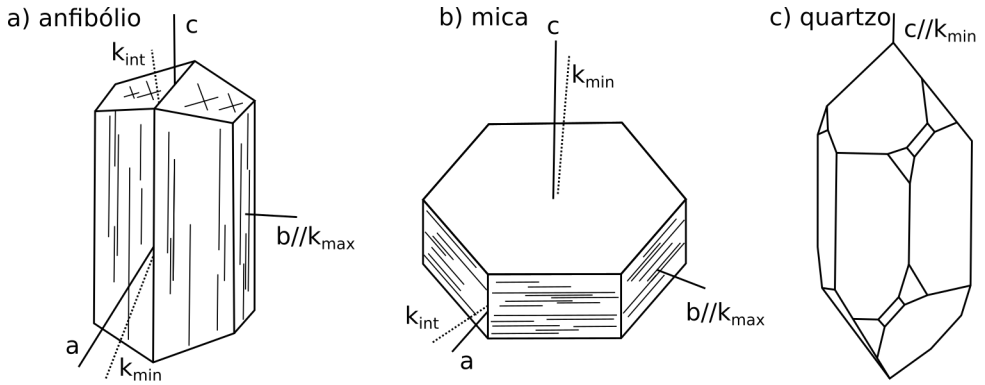

Figura 10 – Direções principais de susceptibilidade magnética em a) anfibólio, b) mica e c) quartzo. Os eixos a, b e c são eixos da cela unitária. Adaptado de Borradaile and Jackson (2010) e Lagroix and Borradaile (2000).

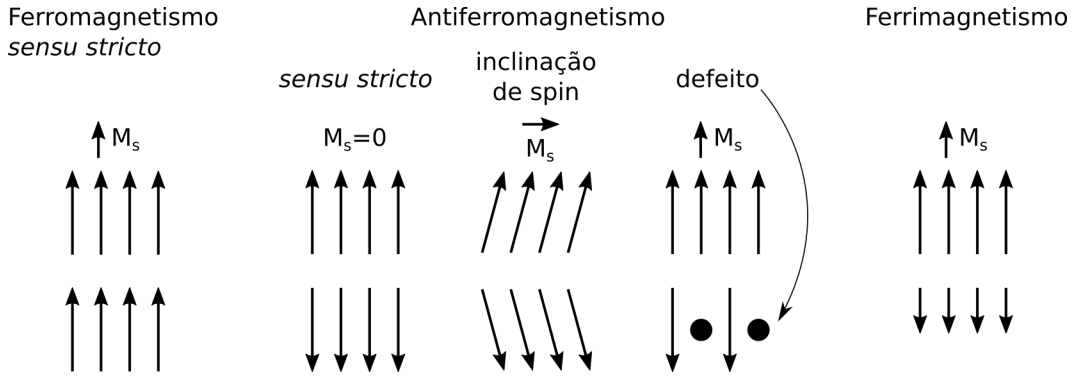

Figura 11 – Tipos de ferromagnetismo com indicação da magnetização espontânea resultante (M_S). As duas camadas de setas de spin representam sub-retículos de momentos magnéticos.

com a distância e se dão a espaçamentos da ordem de 50 Å. Com o aumento da temperatura as distâncias interatômicas aumentam até uma temperatura característica, chamada temperatura de Curie (T_C), em que há o desacoplamento e desorganização dos momentos magnéticos. A magnetização espontânea é removida e a susceptibilidade paramagnética predomina.

Há três tipos principais de comportamento ferromagnético (Figura 11): ferromagnetismo *sensu stricto*, ferrimagnetismo e antiferromagnetismo. Em materiais ferromagnéticos *sensu stricto* (e.g. ferro nativo), átomos estão suficientemnete próximos para gerar interações de troca diretas e os momentos magnéticos de elétrons desemparelhados são

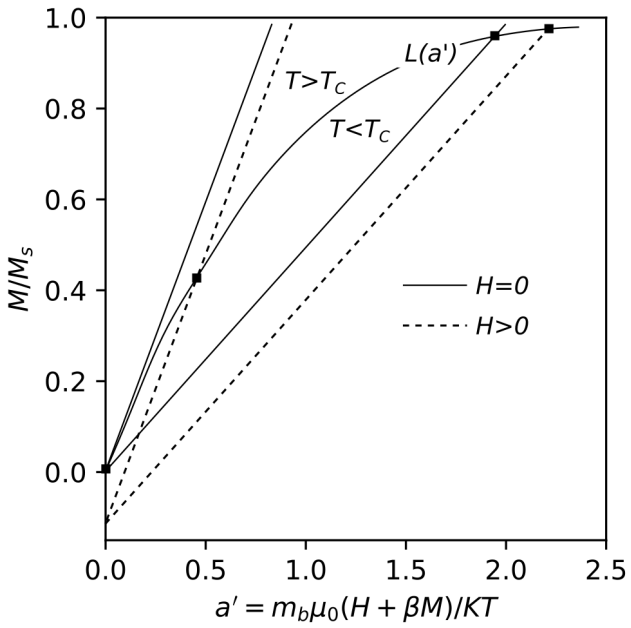

Figura 12 – Magnetização teórica de minerais ferromagnéticos em função de a' conforme a teoria de campo molecular de Weiss. As interseções das funções dadas pelas equações 2.5 e 2.6 é indicada com quadrados. Adaptado de Dunlop and Özdemir (1997)

paralelos. Em compostos diversos, as interações de troca entre os átomos com elétrons desemparelhados se dão por meio de ânions intermediários (e.g. oxigênio). Devido à estrutura cristalina se formam sub-retículos de momentos magnéticos com spins opostos. Se os momentos magnéticos dos sub-retículos opostos são iguais em módulo tem-se um material antiferromagnético, no qual os spins se cancelam e a magnetização resultante é nula (e.g. hematita e ilmenita). Em alguns casos, os momentos magnéticos têm uma leve inclinação; suas componentes antiparalelas se cancelam mas uma magnetização resultante se forma. Defeitos cristalinos também podem provocar uma magnetização não nula em minerais antiferromagnéticos. Em minerais ferrimagnéticos (e.g. magnetita), os sub-retículos antiparalelos não são iguais em módulo e uma intensa magnetização espontânea se forma. Devido à magnetização espontânea, minerais ferromagnéticos têm alta susceptibilidade magnética, na ordem de 10^3–10^1 mSI (Figura 7).

Não há uma relação simples para a dependência da susceptibilidade magnética de minerais ferromagnéticos com temperatura e campo aplicado devido ao desenvolvi-

mento de anisotropia magnetostática e histerese. Segundo a teoria do campo molecular de Weiss a magnetização espontânea pode ser expressa pela suposição de existência de um campo indutor interno $H_w = \beta M$, proporcional por β à magnetização espontânea de forma que o campo total é dado por $H_T = H + H_w = H + \beta M$. Substitutindo H_T em a na função de Langevin (Equação 2.3) obtem-se $a' = m_b \mu_0 (H + \beta M)/KT$. Assim, tem-se o caso geral de magnetização ferromagnética

$$M = M_s L(a'). \tag{2.5}$$

Quando $H = 0$ tem-se a relação do campo molecular de Weiss dada por:

$$M = a' KT / m_b \mu_0 \beta \tag{2.6}$$

A solução do sistema de equações constituído pelas equações 2.5 e 2.6 pode ser encontrada graficamente como mostrado na Figura 12. Para $T < T_C$, a interseção das curvas mostra que a magnetização espontânea, i.e. quando $H = 0$, é próxima da magnetização de saturação, uma propriedade geral de minerais ferromagnéticos. Por outro lado, quando $T > T_C$, não há magnetização espontânea e o comportamento paramagnético predomina. Em baixos campos e $T > T_C$ o campo molecular de Weiss H_w é nulo, e a função de Langevin tem uma aproximação linear semelhante àquela de minerais paramagnéticos (Equação 2.4), e a susceptibilidade ferromagnética pode ser dada por

$$k = M/H = m_b \mu_0 M_S / 3K(T - T_C).$$

O modelo de campo molecular de Weiss é uma boa aproximação para elementos nativos, mas algumas modificações são necessárias para melhor adequação a demais compostos ferromagnéticos (e.g. magnetita, Dunlop and Özdemir 1997).

A magnetização espontânea de minerais ferromagnéticos também se dá preferencialmente em direções energeticamente favoráveis devido à anisotropia magnetocristalina. Em cristais de magnetita, as direções de fácil magnetização (*soft directions*) são normais aos planos octaédricos $\{111\}$, ao passo que as direções de difícil magnetização (*hard directions*) são normais a $\{100\}$. Devido à elevada magnetização espontânea, uma distribuição de "pólos magnéticos" se forma na superfície dos minerais ferromagnéticos. Este conjunto de pólos que simula a mesma magnetização gera no interior do mineral linhas de campo que se opõe aos momentos magnéticos internos. Este campo desmagnetizante é dado por $H_d = -NM$, em que N é o fator desmagnetizante que depende da

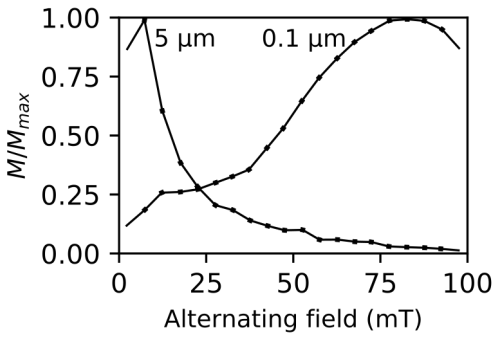

Figura 13 – Espectro de coercividade para agregados sintéticos de magnetita com tamanhos de grão médio de 5 e 0.1 µm. Adaptado de Jackson et al. (1988).

forma do grão. H_d aumenta com a densidade de pólos magnéticos (i.e. $H_d \propto M$) e diminui com a distância (i.e. $H - d \propto 1/d^2$). Em grãos alongados, o fator desmagnetizante é mais alto para a menor dimensão, facilitando a magnetização ao longo do eixo maior (e.g. $N = 1/3$ em todas as direções de um grão esférico). A variação da energia de magnetização associada às diferentes direções de um grão anisométrico é chamada anisotropia magnetostática. Para grãos com uma razão axial acima de 20%, a anisotropia magnetostática supera a magnetocristalina. As barreiras energéticas que as anisotropias magnetocristalina e magnetostática de minerais ferromagnéticos apresentam para a modificação da orientação da magnetização é a característica que garante a estabilidade de magnetizações remanentes naturais (NRM) estudadas em paleomagnetismo e que auxilia na formação de tramas magnéticas.

Com o aumento do volume de partículas ferromagnéticas a energia associada ao campo desmagnetizante aumenta. Para minimizar tal energia, a partir de determinado tamanho de grão formam-se múltiplos domínios com magnetizações internamente consistentes. A magnetização resultante dos diversos domínios é minimizada, assim como a energia magnética interna. O limite que separa grãos monodomínio (SD) de multidomínio (MD) depende da anisotropia magnetocristalina, forma, e magnetização de saturação; para magnetitas, partículas MD se formam a partir de tamanhos de grão de 0.1–1 µm. Em grãos SD, é necessário um elevado campo indutor para fazer a magnetização espontânea superar a barreira energética da anisotropia magnetostática e mudar (reverter) sua direção. Este campo é chamado coercividade microscópica, e é propor-

cional à razão axial do grão SD. Em um agregado de partículas SD, o campo indutor necessário para anular uma magnetização remanente é chamado coercividade total (H_c; Figura 7). O campo necessário para reverter metade dos momentos magnéticos e gerar uma remanência resultante nula é chamado coercividade de remanência (H_{cr}; Figura 7). Em geral, para agregados de magnetita SD, a coercividade total indicada em espectros de coercividade é < 300 mT (Figura 13). Para mover as paredes de domínios e expandir um domínio em detrimento de outro as barreiras energéticas são comparativamente pequenas, e agregados de partículas MD têm coercividades de < 50 mT (Figura 13).

2.3.2 Anisotropia de susceptibilidade magnética

Susceptibilidade magnética de uma rocha tem as mesmas propriedades tensoriais que a susceptibilidade magnética de monocristais. O método universal de determinação de k_{ij} é baseado na medição da magnetização induzida em direções arbitrárias nas quais são aplicados baixos campos externos ($H \leq 200\,\mathrm{A\,m^{-1}}$). Em seguida, o tensor médio é calculado por mínimos quadrados (Jelínek, 1978) a partir da totalidade das medições. Um mínimo de seis medições em direções distintas é necessário para determinar as componentes de k_{ij} devido a sua simetria, mas mais direções são usadas para aumentar a acurácia (Borradaile and Henry, 1997). Para medições de k são usados espécimes de rocha cilíndricos de 2.2 cm de altura e 2.5 cm de diâmetro para aproximar a forma geral de uma esfera e minimizar a anisotropia magnetostática da amostra. As análises deste estudo foram conduzidas usando o Kappabridge KLY5 (AGICO) do Laboratório de Paleomagnetismo do Instituto de Astronomia, Geofísica e Ciências Atmosféricas (IAG - USP).

A susceptibilidade magnética é mais facilmente representada por seu elipsóide de magnitudes, triaxial, no qual os três autovetores ($k_1 > k_2 > k_3$) constituem a trama magnética e são usados para interpretação geológica. Por exemplo, em rochas graníticas a direção principal máxima de susceptibilidade magnética k_1 é a lineação magnética, e a direção principal mínima de susceptibilidade magnética k_3 é o polo da foliação magnética. Dentre os diversos parâmetros utilizados para resumir a forma e magnitude do elipsóide de susceptibilidade magnética, os mais comuns são dados por Jelinek (1981). O grau de anisotropia é dado por $P = k_1/k_3$. Em granitos paramagnéticos o grau de anisotropia é geralmente baixo (c. 5%, i.e. $P \sim 1.05$) e em granitos ferromagnéticos P

tem valores dispersos que tendem a ser comparativamente altos (i.e. entre 10 e 20%; Archanjo et al. 2009). O caráter geométrico do elipsóide é resumido pelo parâmetro de forma dado por $T = [\ln(k_2/k_3) - \ln(k_1/k_2)]/[\ln(k_2/k_3) + \ln(k_1/k_2)]$. T varia entre prolato ($T = -1$, $k_2 = k_3$) e oblato ($T = 1$, $k_1 = k_2$). No caso de um elipsóide triaxial ($T = 0$, $k_1 \neq k_2 \neq k_3$), lineação e foliação magnética podem ser usadas como indicadores da petrotrama.

Se a susceptibilidade magnética dos minerais constituintes é conhecida, assim como seu volume e orientação preferencial, é possível teoricamente prever a ASM resultante, de modo análogo à determinação de anisotropia sísmica de uma rocha a partir de sua microestrutura analisada com EBSD (i.e. *fabric recipes*; Biedermann 2017; Lloyd et al. 2009). Entretanto, devido ao efeito magnetostático de minerais ferromagnéticos é necessário avaliar as tramas de forma e de domínios (*locational fabric*; Stephenson 1994).

Embora um contínuo de composições e susceptibilidade magnéticas exista, com base na mineralogia magnética dominante, Bouchez (1997) separou plútons graníticos entre ferromagnetícos, de alta susceptibilidade, e paramagnéticos, de baixa susceptibilidade. Em granitos paramagnéticos, a ASM é interpretada como o produto de anisotropia magnetocristalina dos silicatos paramagnéticos e de sua orientação preferencial. Em geral, em silicatos paramagnéticos mais comuns, os eixos de maior susceptibilidade são paralelos à elongação dos cristais (e.g. paralello ao plano basal de biotita), de forma que os eixos de maior susceptibilidade da ASM da rocha tendem a ser paralelos à foliação.

Granitos ferromagnéticos são caracterizados por susceptibilidades mais elevadas devido principalmente a alta porcentagem de magnetita. O tamanho de grão de magnetita varia de poucos micrômetros a alguns milímetros, formando grãos com apenas um domínio magnético ou grãos de multi-domínios. Grãos monodomínios podem gerar tramas de ASM inversas devido à saturação da sua magnetização espontânea paralela aos eixos longos dos cristais (Bouchez, 1997). Mesmo em granitos ferromagnéticos, as fases paramagnéticas têm importante contribuição para a trama completa (Archanjo et al., 1995).

2.3.3 Anisotropia de magnetização remanente

Em rochas cuja trama magnética tem forte contribuição de minerais ferromagnéticos pode ser útil determinar a trama magnética portada exclusivamente pela petrotrama

de tais minerais (Trindade et al., 1999). Nestes casos, é possível determinar a anisotropia de magnetização espontânea medindo a variação da mesma após aplicação de uma magnetização remanente em múltiplas direções usando magnetização remanente de saturação isotérmica (SIRM) ou magnetização remanente anisterética (ARM). Para se aplicar uma ARM, é feita uma desmagnetização com campos alternados num vasto intervalo de coercividades (0–100 mT) com um baixo (da ordem de μT) campo de corrente direto superposto para induzir ARM na direção desejada. O campo direto pode ser aplicado em intervalos específicos do campo alternado, que correspondem a coercividades características de frações de tamanho de grão dos minerais ferromagnéticos (Jackson et al., 1988), formando uma magnetização remanente anisterética parcial (pARM). Magnetitas multidomínio têm força de coercividade H_C inferior a 20–30 mT ao passo que magnetitas monodomínio têm coercividades de até 300 mT. Em um material com petrotrama ferromagnética isotrópica a magnetização remanente ($\vec{M}_r$) é proporcional à intensidade do campo alternado no qual o campo direto foi aplicado conforme a susceptibilidade de remanência k_r: $\vec{M}_r = k_r\vec{H}$. Em materiais anisotrópicos (há orientação preferencial de forma dos minerais ferromagnéticos), a susceptibilidade de remanência k_r é um tensor de segunda ordem com propriedades semelhantes à do tensor de susceptibilidade magnética, sendo também representado pelo seu elipsóide de magnitudes (i.e. $k_{r1} > k_{r2} > k_{r3}$). Para as análises de espectro de coercividade e AARM foram usados o desmagnetizador LDA-3A, magnetizador anisterético AMU-1A, e magnetizações remanentes foram medidas com o magnetômetro automático JR-6A (AGICO) do Laboratório de Paleomagnetismo do Instituto de Astronomia, Geofísica e Ciências Atmosféricas (IAG - USP).

2.4 Difração de Elétrons Retroespalhados - *EBSD*

Nas últimas décadas o estudo de microstruturas de deformação em minerais e rochas teve avanços significativos devido ao advento da técnica de Difração de Elétrons Retroespalhados (EBSD, Prior et al. 2009). Com esta técnica é possível fazer uma determinação da orientação cristalográfica *in situ*, i.e., associar a orientação cristalográfica com seu domínio no agregado ou em um grão deformado. Com isso, os parâmetros fundamentais de forma, textura cristalográfica e tamanho de grão são determinados em grande detalhe mesmo em agregados ultrafinos. Em particular, EBSD é o método mais

indicado para a medição de tamanho de grãos recristalizados. Além de permitir a verificação de que ocorreu recristalização dinâmica associada ao fluxo de discordâncias, com EBSD é possível fazer a segmentação de um agregado com base na comparação entre ângulos de desorientação entre pontos adjacentes e valores de desorientação de referência (e.g. aproximadamente 10° para grãos e 3° para subgrãos; Stipp et al. 2010). Com os parâmetros de tamanho de grão para um agregado recristalizado, pode-se estudar os níveis de tensão de fluxo em uma zona de cisalhamento.

Para este tipo de análise, as amostras de rocha devem ter um polimento fino de alta qualidade para garantir a produção de padrões de difração nítidos. Em seções delgadas e polidas das amostras selecionadas é feita uma etapa de polimento mecânico fino, realizado em polidora rotativa com pastas de diamante em granulometrias diversas espalhadas sobre tecido de polimento. As granulometrias usadas decrescem com cada etapa de polimento, de 9 µm até 0.1 µm com o objetivo de reduzir os sulcos gerados pelo próprio polimento da etapa anterior (Figura 14). A última etapa de preparo é o polimento químico-mecânico, no qual se usa uma suspensão de pH elevado com partículas abrasivas de 20 e 70 nm (e.g. sílica coloidal ou alumina).

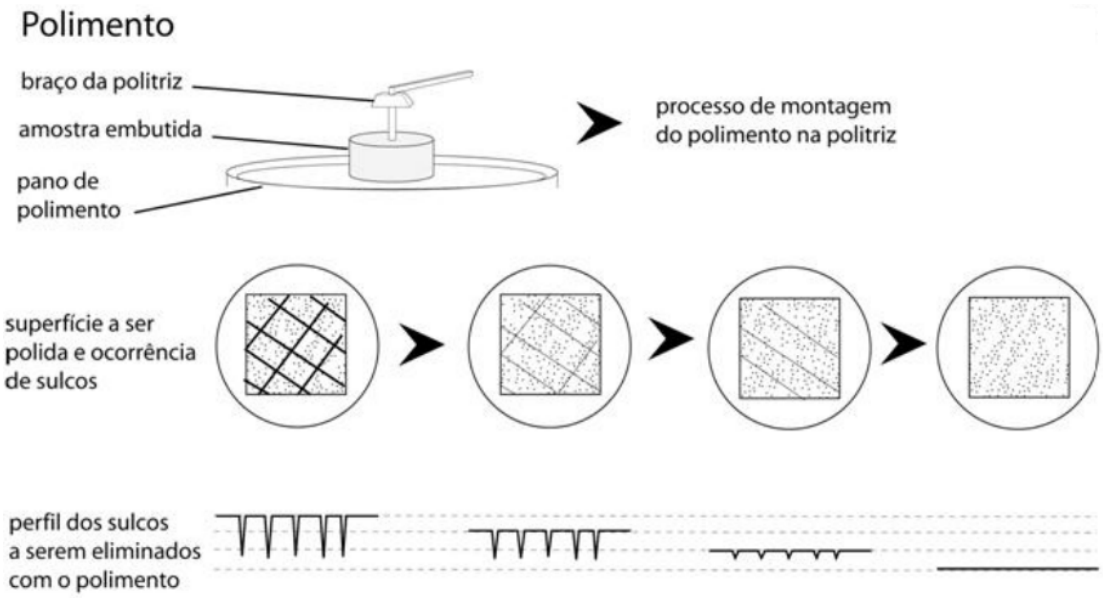

Figura 14 – Esquema das etapas de preparação de amostras para EBSD. Adaptado de Barbosa (2009).

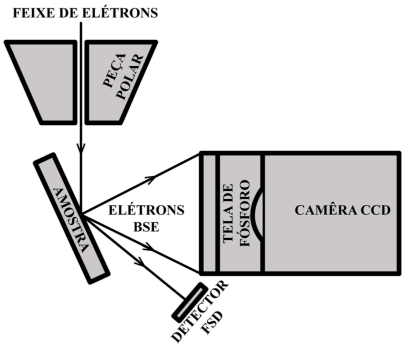

Figura 15 – Ilustração esquemática do sistema de EBSD (*Electron Backscatter Diffraction*) no microscópio eletrônico de varredura (modificado de Reed 2006).

Na análise de EBSD os dados processados são obtidos pela difração de elétrons retroespalhados. Em uma análise de microscopia eletrônica de varredura, os elétrons incidentes na amostra interagem com ela de diversas maneiras. De um pequeno volume na superfície da amostra, uma fração dos elétrons retroespalhados, que incide em planos cristalográficos segundo o ângulo de Bragg θ retroespalhados que sofre difração incidiram em planos cristalográficos segundo o ângulo de Bragg θ, sofre difração. O ângulo de Bragg é dado em $n\lambda = 2d\sin\theta$, em que n é um número inteiro, λ é o comprimento de onda dos életrons incidentes e d é o espaço interplanar de determinado plano cristalográfico. A difração dos elétrons retroespalhados se dá em direções opostas perpendiculares ao plano cristalográfico e gera cones de difração. A amostra é inclinada por 70° para que o sinal gerado seja maximizado. Uma tela de fósforo com uma câmera CCD e um conjunto de diodos de silício é colocada de frente para a amostra inclinada. Este conjunto é interceptado pelos cones de difração formando bandas que registram a simetria e a orientação do cristal presente onde o feixe de elétrons incide. Os diodos de silício também interceptados pelo cone de difração na direção frontal (forward scattered electrons - FSD) produzem imagens de contraste de orientação, composição química e topológicas de acordo com a intensidade das bandas de Kikuchi que os atravessam. A Figura 15 mostra um esquema deste sistema. As bandas formadas na tela de fósforo pelos elétrons retroespalhados difratados são chamadas bandas de Kikuchi, em homenagem a Seishi Kikuchi que observou bandas de difração de elétrons gerados em cristais de mica e calcita em 1928. O conjunto de bandas de Kikuchi forma o padrão de difração (Figura 16) sobre o qual é feita a determinação de simetria e orientação do

cristal analisado.

Sobre o padrão de difração são aplicadas técnicas de processamento digital de imagens para realçar a qualidade e visibilidade das bandas (Figura 17). Um esquema das etapas de processamento do EBSD é dado na Figura 17. As bandas são detectadas pela transformada de Hough, em que cada o padrão de difração é disposto como uma curva no espaço de coordenadas polares. As intensidades das bandas são transformadas em curvas nas quais os pontos de maior intensidade representam arestas. Eixos de zona, fase cristalina e orientação dos cristais no ponto analisado são determinados.

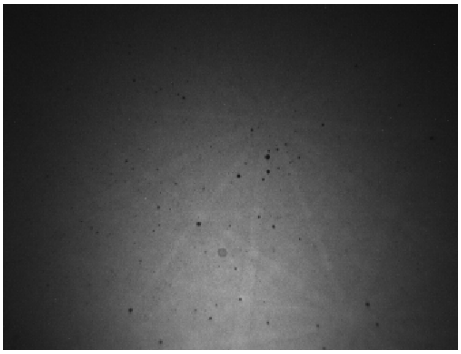

Figura 16 – Padrão de difração de elétrons retroespalhados não processado de um cristal de hematita.

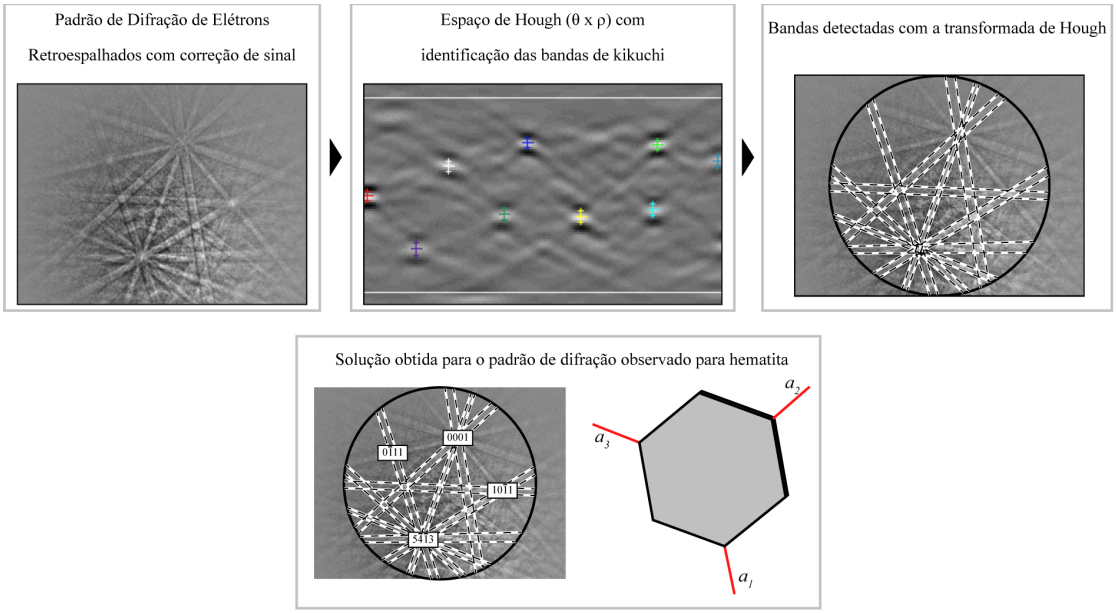

Figura 17 – Etapas de operação de uma análise de EBSD (*Electron Backscatter Diffraction*) até indexação.

3 Geologia Regional

3.1 Resumo da estratigrafia e evolução tectônica

O domínio Ceará Central (CCD - *Ceará Central Domain*) no noroeste da Província Borborema tem uma posição de destaque no entendimento da orogênese Brasiliana que resultou da colisão dos crátons *West Africa* (Oeste Africano), Congo-São Francisco, e Amazônico (Almeida et al., 1981). Avanços significativos foram feitos nas últimas duas décadas no conhecimento da evolução tectônica do CCD, em particular graças ao detalhamento gradativo da cartografia geológica da região, a estudos geocronológicos conduzidos em diversas unidades geológicas, e ao amplo levantamento aerogamaespectrometrométrico realizado na Província Borborema pelo Serviço Geológico do Brasil (CPRM).

A mais antiga unidade do CCD é composta majoritariamente de gnaisses cinzas e migmatitos e data do Neoarqueano (sincrônica com a orogênese Jequié registrada em outras províncias do escudo sul-americano, Alkmim and Marshak, 1998; Almeida et al., 1981). É hoje denominada Complexo Cruzeta (Ganade et al., 2017), foi originalmente reconhecida por Brito Neves (1975) como Maciço de Tróia (Figura 18), e ocupa um pequeno núcleo do embasamento limitado a sudeste pela zona de cisalhamento Senador Pompeu. Uma idade de 2560 Ma, obtida por isócrona de Rb-Sr (Pessoa and Archanjo, 1984), foi a primeira a assinalar esta unidade ao Neoarqueano. Com base em idades U-Pb de cristalização e composição isotópica Sm-Nd, Fetter (1999) separou o Complexo Cruzeta nas unidades Mombaça (basal) e Pedra Branca. A unidade Mombaça é composta de ortognaisses e migmatitos de composição granodiorítica (Fetter, 1999; Ganade et al., 2017), com variações para tonalitos e dioritos, e ocorrências localizadas de metamáficas, metaultramáficas, leucognaisses, pegmatitos e porções gnássicas ricas em granada (Ganade et al., 2017; Martins, 2000). Idades U-Pb variam de 2857 (Fetter, 1999) a 2793 Ma (Ganade et al., 2017). Sua distribuição de elementos traços e terras raras é típica de TTGs Arqueanos (Ganade et al., 2017). A unidade Pedra Branca é também composta de associações gnássicas-migmatíticas, com intercalações complexas de granodioritos, tonalitos e dioritos (Ganade et al., 2017) e supracrustais subordinadas

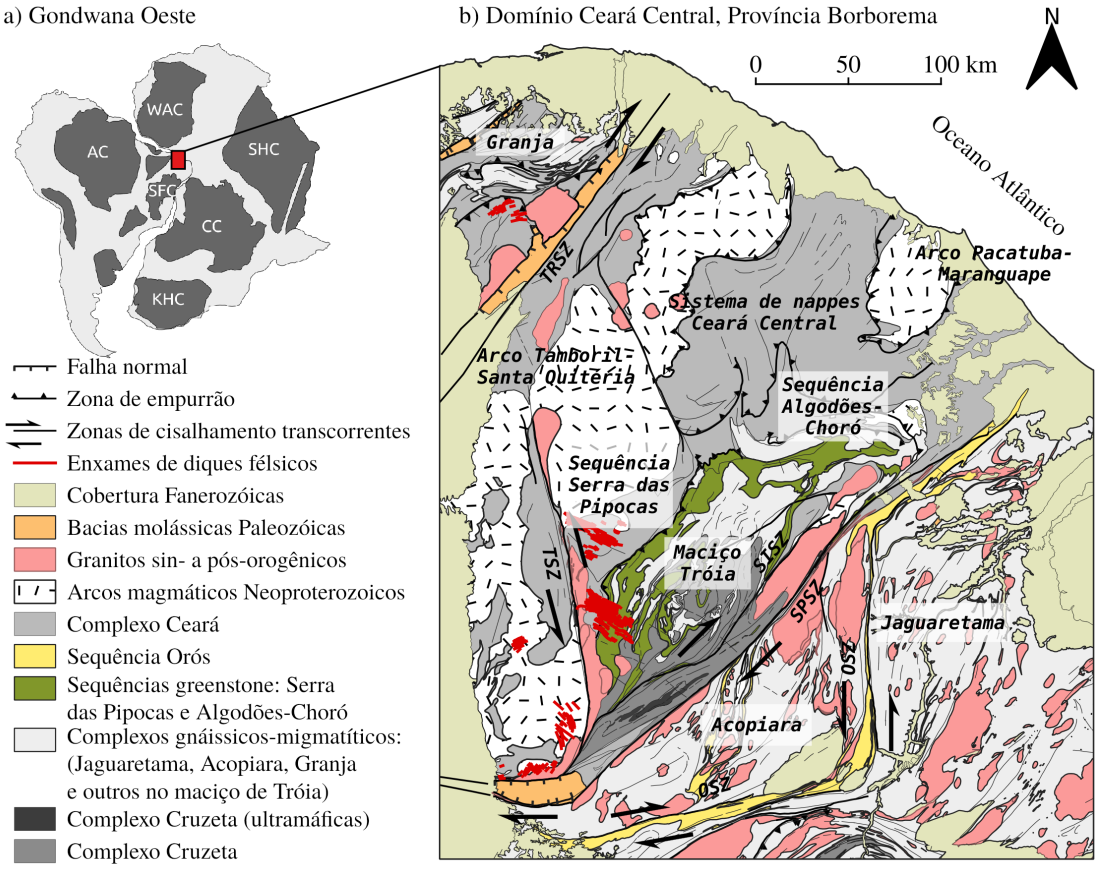

Figura 18 – a) Gondwana Oeste. AC - Cráton Amazônico, SFC - Cráton São Francisco, KHC - Cráton do Kalahari, CC - Cráton do Congo, SHC - Cráton do Saara, WAC - Cráton Oeste África. b) Mapa geológico-tectônico do Domínio Ceará Central. O Maciço de Tróia inclui o Complexo Cruzeta e os complexos gnáissicos-migmatíticos Riacianos.

(Martins, 2000). Fetter (1999) e Ganade et al. (2017) obtiveram idades U-Pb entre 2776 e 2675 Ma. A assinatura geoquímica da unidade Pedra Branca é semelhante à da unidade Mombaça, com indicações de petrogênese levemente distinta (Ganade et al., 2017). Com base nesses dados, Ganade et al. (2017) interpretou que o magmatismo que formou a unidade Mombaça teve origem por fusão de uma crosta oceânica jovem (metamáfica rica em granada) subduzida a baixo ângulo (*flat subduction*), e os magmas que formaram a unidade Pedra Branca formaram-se por fusão de rochas metassomatizadas da cunha do manto. Idades modelo T_{DM} da unidade Mombaça (T_{DM} c. 2780–3040 Ma)

indicam maior grau de contaminação crustal e reciclagem em relação à unidade Pedra Branca (T_{DM} c. 2690–2920, Fetter, 1999). Silva et al. (2002) obteve uma idade U-Pb em zircão de 3270 Ma para um leucossoma associado ao Complexo Cruzeta, porém o significado desta idade ainda é incerto.

Uma associação de gnaisses-migmatitos, sequências metavulcanossedimentares e granitos de idade Riaciana circundam o Complexo Cruzeta a norte, noroeste e oeste. Parte das rochas que compõem esta unidade eram anteriormente agrupadas no Maciço de Tróia (Neoarqueano) e foram depois corretamente separadas com idades entre 2240 e 2030 Ma graças a uma série de estudos geocronológicos (Castro, 2004; Costa et al., 2015b,c; Fetter, 1999; Martins, 2000; Martins et al., 2009). Na parte nordeste, a associação de rochas anfibolíticas, paragnaisses e metassedimentares diversas, e ortognaisses foi definida como Suíte Metamórfica Algodões-Choró (Figura 18; Arthaud et al., 2015; Martins, 2000). A unidade Algodões que ocorre na base da sequência é composta de anfibolitos, granada anfibolitos, hornblenditos, intercalações de metassedimentares, formações ferríferas e metafelsitos (Arthaud et al., 2015; Martins et al., 2009). Algumas estruturas como bandamentos composicionais entre granada-afibolitos e anfibolitos, e nódulos quartzo-feldspáticos estirados ao longo da foliação caracterizam a origem vulcânica da unidade Algodões, e sua assinatura geoquímica indicam afinidade com magmatismo básico de platôs oceânicos, e/ou bacias de retro-arco (Martins, 2000). Uma idade isócrona de Sm-Nd de rocha total de 2240 Ma foi determinada para a unidade Algodões (Martins et al., 2009). As rochas metassedimentares da unidade Choró ocorrem sobre a unidade Algodões e incluem metagrauvacas, quartzitos, metapelitos (predominantemente silimanita-cianita-mica-xistos), metaconglomerados, calcissilicáticas e paragnaisses diversos (Martins, 2000). A população mais jovem de zircões detríticos da unidade Choró, analisados por Costa et al. (2014), formam um pico de idade em 2100–2200. Um conjunto de tonalitos, granodioritos e granitos com idades entre 2190 e 2130 Ma, variáveis graus de deformação e metamorfismo ocorrem associados a sequência *greenstone* Madalena-Choró (Costa et al., 2015b). Os ortognaisses da unidade Cipó (Figura 18) têm composição TTG (tonalito-trondhjemito-granodiorito) variável, predominantemente biotita-metatonalitos, com idade de 2190–2180 Ma; esse magmatismo se originou provavelmente em ambiente de subducção por fusão de crosta oceânica subduzida (Costa et al., 2018, 2015b). Depois de um hiato de cerca de 30 My (milhões de anos), formaram-se os complexos graníticos-granodioríticos-dioríticos das

unidades Serra da Palha (2150 Ma) e Madalena (2150–2130 Ma), estudados por Costa et al. (2015b). A unidade Serra da Palha é composta de *augen*-gnaisses de composição granítica com porfiroclastos de feldspato potássico, com assinatura geoquímica que permite caracterizá-la como granitóides tipo A (Costa et al., 2015b). Os ortognaisses da unidade Madalena têm composição predominantemente diorítica a tonalítica com assinatura geoquímica típica de adakitos de baixa sílica. Os complexos Boa Viagem (2150–2124 Ma, Costa et al., 2015a) e São José da Macaoca (2140–2130 Ma, Fetter, 1999) são constituídos de ortognaisses e paragnaisses diversos; foram interpretados por Costa et al. (2015b) como complexos ígneos e sequências sedimentares de ambiente de arco. Essa associação entre unidades TTG e sequências metavulcanossedimentares similares a *greenstone belts*, intrudidas por magmas graníticos a granodioriticos após um hiato de dezenas de My é característica de terrenos granito-*greenstone*, comuns ao Neoarqueano (Alkmim and Marshak, 1998; Costa et al., 2018).

De forma semelhante, complexos metaplutônicos e sequências metavulcanossedimentares de idade Riaciana ocorrem circundando a parte sul do Complexo Cruzeta (Figura 18). O *greenstone belt* Serra das Pipocas (Costa et al., 2018), análogo à Suíte Algodões-Choró, é constituído de metavulcânicas básicas, metavulcânicas félsicas subordinadas, metagrauvacas e metapelitos, metasilexitos, calcissilicáticas e serpentinitos (Sousa, 2016). Uma idade deposicional máxima de 2200 Ma para os metassedimentos desta unidade foi obtida de zircões detríticos estudados por Costa et al. (2014), e uma camada de metadacito gerou uma idade U-Pb de 2151 Ma (Fetter, 1999). Portanto, a formação da sequência *greenstone* Serra das Pipocas se deu em 2200–2150 Ma, potencialmente em ambiente de retro-arco, como indicado por sua assinatura geoquímica (Sousa, 2016). Ortognaisses da unidade Mirador ocorrem intrudidos nas porções basais da sequência Serra das Pipocas. São constituídos de biotita-hornblenda-metatonalitos com idade U-Pb de 2185 Ma (Costa et al., 2018), e sua assinatura geoquímica adakítica indica origem de seu magma progenitor por fusão parcial de crosta máfica em zona de subducção. A suíte Bananeira, composta de granitos e quartzo-monzonitos, ocorre intrudida entre o Complexo Cruzeta e as demais unidades Riacianas. Costa et al. (2018) encontrou idades U-Pb para esta unidade de 2079 e 2068 Ma que tem assinatura geoquímica shoshonítica e de alto K, indicativa de fusão de crosta máfica rica em K sob pressão intermediária. Um conjunto de rochas metamáficas e metaultramáficas com mineralizações associadas (e.g. cromititos) ocorrem intrudidas nas unidades Neoarqueana

e Paleoproterozóicas na parte sudoeste do CCD e foram agrupadas na unidade Tróia (Costa et al., 2018; Ganade et al., 2017). Esta unidade ocorre como soleiras (*sill* Esbarro) e diques. Uma idade U-Pb de 2028 Ma foi obtida por Ganade et al. (2017) para um dique máfico potencialmente associado à unidade Tróia, e uma idade U-Pb de 2036 Ma para um depósito de EGP (elementos do grupo da Platina) em cromititos da unidade Tróia (Costa et al., 2018).

O Complexo Ceará é uma sequência metavulcanossedimentar que tem importante papel no entendimento da Orogênese Brasiliana na Província Borborema, análogo às faixas Seridó e Cachoeirinha-Salgueiro (Archanjo et al., 2013). Estudos sistemáticos foram conduzidos nas unidades Independência e Canindé do Complexo Ceará, amplamente metamorfizadas em alto grau e em alguns locais registrando assembléias retrometamórficas indicativas de alta pressão ($>$ 10 kbar, Amaral et al., 2012; Arthaud, 2007; Castro, 2004; Ganade de Araujo et al., 2014b; Garcia et al., 2014; Santos et al., 2009). Como notado por Ganade de Araujo et al. (2014a), no mapa geológico do Estado do Ceará de 1983 (Cavalcante, 2003), as unidades Independência e Canindé foram distinguidas com base no grau metamórifco, sendo a segunda caracterizada por intensa migmatização em relação à primeira. Ambas são compostas de quartzitos, metapelitos, metagrauvacas, paragnaisses diversos com variáveis graus de migmatização, diques e soleiras granitóides sin-metamórficos, carbonatos, e metavulcânicas básicas e ácidas (Arthaud, 2007; Arthaud et al., 2015; Garcia et al., 2014). Complicações cartográficas geradas por diferenciação metamórfica da unidade Canindé têm dificultado a identificação de partes da unidade como Paleoproterozóica ou Neoproterozóica. Duas idades U-Pb em metavulcânicas da unidade Independência de 772 Ma (metarriolito Fetter, 1999) e 749 Ma (granada-anfibolito metabásico Arthaud, 2007), interpretadas como idade de cristalização do protólito, confirmam que parte do Complexo Ceará formou-se no Neoproterozóico. Zircões detríticos obtidos na unidade do Complexo Ceará indicam para diversas amostras idades máximas em intervalos tardios (populações entre 700–600 Ma, Ganade de Araujo et al., 2012; Garcia et al., 2014). Zircões detríticos de populações mais jovens, em 900–940 Ma (Ganade de Araujo et al., 2012), indicam que o Complexo Ceará pode ter se formado em sincronicidade com o magmatismo do Arco Tamboril-Santa Quitéria (Ganade de Araujo et al., 2012, 2014a, ver abaixo) no longo intervalo de 900 a c. 600 Ma.

Ocupando um terço de toda a área do CCD ocorrem os complexos anatético-migmatíticos

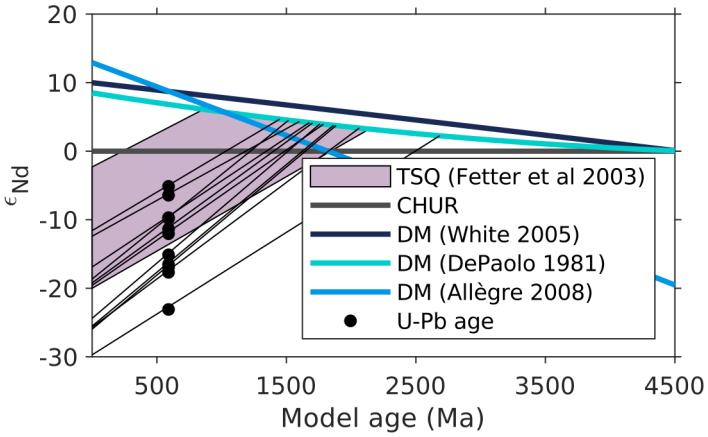

Figura 19 – Diagrama de evolução de neodímio para os batólitos Quixadá-Quixeramobim e Tauá, construído a partir de dados adaptados de Cavalcanti et al. (2012) e Nogueira (2004) após correção para idades U-Pb SHRIMP obtidas por Ávila et al. (2019). DM - manto empobrecido, CHUR - *Chondritic Uniform Reservoir*. TSQ - Tamboril-Santa Quitéria.

Tamboril-Santa Quitéria e Pacatuba-Maranguape. O Complexo Tamboril-Santa Quitéria foi reconhecido em parte inicialmente por Brito Neves (1975, então como Maciço de Santa Quitéria). O Complexo Pacatuba-Maranguape, anteriormente reconhecido como parte do Complexo Tamboril-Santa Quitéria foi estudado por Pitombeira et al. (2021). Quatro unidades principais são reconhecidas atualmente segundo Ganade de Araujo et al. (2014a): (i) Lagoa Caiçara, caracterizada por metatexitos estromáticos granodioríticos, (ii) Boi, composta de metatexitos máficos a intermediários, (iii) Santa Quitéria e (iv) Tamboril, compostas de granitos e diatexitos, respectivamente. Com base na distribuição, idades, assinatura isotópica e características do magmatismo que compõe o Complexo, Fetter (1999) o interpretou como um arco magmático formado num curto tempo (c. 30 My) no Ediacarano inferior (em torno de 620 Ma, Fetter, 1999). Idades modelo (T_{DM}), por exemplo, variam de Mesoproterozóico a Neoproterozóico, indicando mistura de magmas juvenis com material crustal para os complexos Tamboril-Santa Quitéria (Figura 19; Fetter, 1999) e Pacatuba-Maranguape (Pitombeira et al., 2021). Uma série de estudos foram conduzidos recentemente no Complexo Tamboril-Santa Quitéria por Ganade de Araujo et al. (2012, 2014a,b,c) que avançaram significativamente o conhecimento sobre o maciço e sobre a evolução tectônica do CCD. Particularmente, foi mostrado que o arco Tamboril-Santa Quitéria pode ter sido formado a em

torno de 880 Ma (Ganade et al., 2021a) e estado intermitentemente ativo até c. 600 Ma, e que neste intervalo serviu de área fonte para os sedimentos que preencheram a bacia do Complexo Ceará (Garcia et al., 2014). Todas as unidades do Complexo Tamboril-Santa Quitéria têm idades U-Pb de 660–620 Ma, interpretadas como cristalização de protólitos (Ganade de Araujo et al., 2014a). Para granitos e migmatitos do Complexo Pacatuba-Maranguape as idades U-Pb variam entre 675 e 610 Ma (Pitombeira et al., 2021). As unidades Lagoa Caiçara e Tamboril também possuem idades U-Pb de 890 a 830 Ma (Ganade de Araujo et al., 2014a), ao passo que zircões herdados no Complexo Pacatuba-Maranguape têm idades de 880–650 Ma, e 2200–2000 Ma (Pitombeira et al., 2021).

Com o fim da orogênese Brasiliana no CCD seguiu-se um episódio de exumação e distensão crustal responsável por geração de pequenas bacias em proto-riftes de constituição molássica. A bacia de Cococi tem uma espessura de < 3 km (Filho et al., 2021) e a estruturação de seu eixo foi condicionada pela zona de cisalhamento de Cococi (formada pela junção das zonas de cisalhamento Tauá e Senador Pompeu). Consiste principalmente de uma camada basal de conglomerados, brechas e arenitos (formação Angico Torto) seguida de pelitos com pequenas intercalações de arenitos (formação Cococi). Estas representam uma transição de deposição em leque aluvial para ambiente lacustre. Idades de zircões detríticos da Bacia de Jaibaras, correlata à Bacia de Cococi, e de unidades sincrônicas a ela, indicam idade de sedimentação de c. 540 Ma (Ganade de Araujo et al., 2012; Garcia et al., 2018).

3.2 Magmatismo sin-transcorrência

O intenso magmatismo que caracteriza o arco Tamboril-Santa Quitéria e que cessou em 610 Ma (Ganade de Araujo et al., 2014a; Pitombeira et al., 2021) antecede a deformação de transcorrência do CCD. Conforme indicado pelos dados mais recentes (ver capítulos subsequentes, Ávila et al., 2019, 2020), o pico de deformação em alta temperatura das zonas de cisalhamento Senador Pompeu e Tauá ocorreu em c. 584 Ma. Os plútons sin-cinemáticos que ocorrem tanto dentro das zonas de cisalhamento como distante delas, indicam atividade conjugada do par e um sistema de deformação consistente em todo o CCD.

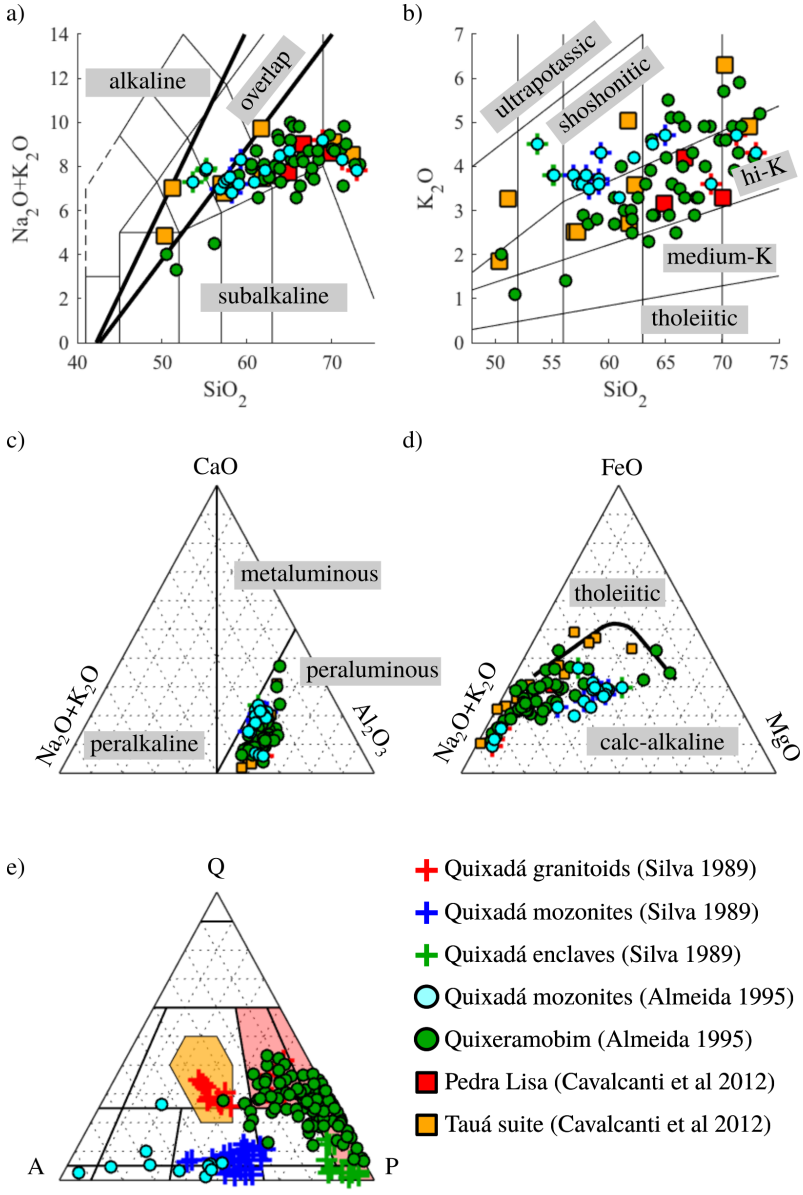

Figura 20 – Compilação de geoquímica de elementos maiores e dados de composição modal para os plutons sin-tectônicos estudados (referências indicadas). a) Diagram TAS (*total alkalis-silica*). Limites dados por Le Maitre (2002). b) Diagrama Harker de K_2O *versus* SiO_2. Limites dados por Peccerillo and Taylor (1976). c) Diagrama de saturação em alumina. d) Diagrama AFM (álcalis, Fe, Mg). Limites dados por Irvine and Baragar (1971). d) Diagrama QAP (quartzo, álcali-feldspato, plagioclásio).

Em sua maioria têm proporções batolíticas. Fazem parte deste conjunto os batólitos Quixeramobim e Quixadá, alojados entre as zonas de cisalhamento Senador Pompeu e Sabonete-Inharé, o batólito *en cornue* Nova Russas e os granitos Pedra Lisa, alojados na margem leste da zona de cisalhamento Tauá e em seu núcleo, respectivamente, e o batólito Tauá (também denominado Suíte Magmática Tauá, Cavalcanti et al., 2012). Entre as zonas de cisalhamento Senador Pompeu e Tauá foram identificados três enxames de diques de composição félsico-intermediária denominados Ematuba, Independência e Marrecas (Figura 18, Almeida 1987). As idades de cristalização destes indicam que eles são sincrônicos aos plútons (Ávila et al., 2019). Poucos estudos sistemáticos geoquímicos-geocronológicos foram conduzidos nas unidades magmáticas mencionadas, com exceção dos batólitos Quixadá e Quixeramobim (Almeida, 1995; Fetter, 1999; Nogueira, 2004). De forma semelhante aos granitos tardi-orogênicos e sin-cinemáticos encontrados por toda a Província Borborema, os batólitos Tauá, Nova Russas-Pedra Lisa e Quixadá-Quixeramobim são granitóides a dioritóides calci-alcalinos shoshoníticos e de alto K (Figura 20, Sial, 1986), alguns caracteristicamente porfiríticos, com megacristais de feldspato potássico de até 20 cm de largura (e.g. Quixadá, Quixeramobim, e granito Pedra Lisa; Figura 5b). Mais descrições detalhadas sobre mineralogia, textura, estruturas e aspectos de campo dos plútons são apresentadas nos capítulos subsequentes.

4 Zippered Shear Zone Model for Interacting Shear Zones in the Borborema Province, Brazil, as Constrained by UPb Dating

Carlos F. Ávila, Carlos J. Archanjo, Haakon Fossen, Maria Helena B.M. Hollanda

4.1 Abstract

Shear zones typically interact to form connected systems or networks to accommodate crustal deformation, but our knowledge of how this happens is fragmentary. Understanding branching and interacting shear zones requires knowledge of timing, deformation kinematics and rheology. The Senador Pompeu, Tauá and Cococi strike-slip shear zones of the Borborema Province (NE Brazil) have a central role and location in the Neoproterozoic assembly of Gondwana, and provide a means to understand shear zone interaction. We apply (i) U-Pb *in situ* SHRIMP analysis of zircons from syntectonic plutons to constrain the timing of shearing, and (ii) vorticity and strain analysis on pluton's megacrystic facies deformed in the magmatic state and during final stages of crystallization. Obtained ages show that the shear zone pair was active under high temperature at 583.5 ± 4.6 Ma while felsic dykes were emplaced in the brittle regime in the wall rocks. Average vorticity estimates of 0.70 indicate a strong component of pure shear in the shear zones. Despite the transpressional character, the dispersion in estimates of thinning and thickening for the Senador Pompeu shear zone highlights variations of offset rate for the interacting branches that leads to localized transtension. We conclude that the kinematic framework of the Senador Pompeu and Tauá conjugate pair involves the formation of a dextrally closing zipper structure involving the trailing Cococi shear zone to the southwest, which in turn caused the northeastward extrusion of the enclosed crustal wedge and possibly activation of the nappe system of the Ceará

Central domain.

4.2 Introduction

Continental-scale shear zones are a most fundamental tectonic feature of orogenic deformation. As such they have been subject to extensive structural and geodynamic investigations and found to play a key role in crustal deformation and in accompanying lithospheric extrusion (Daout et al., 2018; Yakovlev and Clark, 2014). Heterogeneities of shear zones and faults have also been largely regarded as properties favouring such structures as conduits of fluids, including magma (Rosenberg, 2004), as well as representing loci of magma generation (Leloup et al., 1999) and emplacement (Rosenberg, 2004), hence further increasing the importance of shear zones in the development of orogens and most other tectonic settings. Indeed the absence of shear zones as magma pathways may favour deep entrapment of melts (Cavalcante et al., 2016), or their presence may function as an obstacle for flow of melts and crustal masses (Leech, 2008). Earlier studies have highlighted how deep strike slip shear zones can account for the observed aspect of extrusion in collisional orogens (e.g. eastern Tibet and Indochina) by means of very large offsets on a network of splaying faults controlled by upper crustal strength (Tapponnier et al., 1982). Subsequent studies on modern rates of fault slip (Daout et al., 2018) and refinements on long-term geological slip rates (Phillips et al., 2004) have favoured continuous deformation in Tibet with shear zones possibly working as passive markers of mantle or upper-crustal-controlled deformation (England, 1997), and renewed interest in this topic continues to yield support to both models (Daout et al., 2018).

The Neoproterozoic West Gondwana orogen represents such an example of continental collision that involves both extruding lithospheric blocks and orogens built by thrusts, as recently outlined by Ganade de Araujo et al. (2014a). In the context of such orogen the Borborema Province (BP) characterises the extrusion part with its abundant anastomosing strike-slip shear zones connecting with the Nigerian belt and additional correlatives in west Africa (Archanjo et al., 2013), while flat-lying foliations and inverted metamorphic gradients associated with thrusts have tentatively been described as “Himalayan-type” nappes within the fault bounded domains (Caby and Arthaud, 1986). This province is now exposing mid to lower crustal terranes, thence providing an op-

portunity to investigate how shear zone systems change character with depth and over time, how the shear zones may control exhumation during orogeny and how thrusts and strike-slip faults are related; these are key aspects for understanding of active collisional orogens.

In the BP it is possible to constrain the full, time-integrated offset and age of shear zone activity. A common approach involves absolute dating of plutons interpreted as having formed before, during or after shear zone activity (Archanjo et al., 2008; Oriolo et al., 2018). In this study we report the ages of plutons emplaced within or contiguous to a pair of major strike-slip shear zones, synchronous with their shear deformation, in the northwest Ceará Central domain of BP. Magmatic deformation of the syn-kinematic plutons is followed by small solid-state strains, possibly indicating the important role of melt weakening and heat advection to shear zones by magma intrusion. We attempt to establish the structural-kinematic framework of these interacting strike-slip shear zones and the thrusts within the fault bounded block by also using vorticity and strain estimates. A region-wide consistent deformation field which resulted in crustal extrusion, intrusion of plutons and dykes and, possibly, the emplacement of thrust nappes is proposed.

4.3 Geological setting

The Ceará Central domain (CCD) is located in the NW part of the BP, which is a 400000 km^2 orogenic terrane formed in the Neoproterozoic (Brasiliano/Pan-African orogeny) due to collision between the Congo-São Francisco and West African cratons (Figura 21). This domain is characterised by high to medium-T metamorphism and migmatisation, abundant syn- to late-tectonic granitoid plutons and a network of anastomosing strike-slip shear zones (Vauchez et al., 1995). In addition to a few Archean cratonic nuclei most of the basement of the BP is composed of Rhyacian to Orosirian granite-gneiss and greenstone sequences related to the Transamazonian orogeny, and of Neoproterozoic orogenic belts (Costa et al., 2015b). The major shear zones have been interpreted to separate different tectonic domains, the CCD being limited to the southeast by the Senador Pompeu shear zone, and to the northwest by the Transbrasiliano lineament. To the west the CCD is covered by the Paleozoic Parnaíba basin and to the east by the sedimentary cover of the Atlantic coast. In a pre-drift reconstruction

the province is correlated with Pan-African belts of western Africa, with Senador Pompeu and Transbrasiliano lineaments being connected to Ile-Ife and Kandi lineaments, respectively (Figura 21; Archanjo et al. 2013).

Within the CCD (Figura 21b) the Neoarchean Cruzeta Complex is rimmed to the northwest by accreted Rhyacian terranes (Fetter et al., 2003) which, in turn, are interleaved with Neoproterozoic metassedimentary rocks metamorphosed to varying grades (Arthaud et al., 2015). The earliest record of the Neoproterozoic Brasiliano collage starts with the Tamboril-Santa Quitéria magmatic arc in the Late Tonian and proceeds to a collisional setting through to Middle Ediacaran (Fetter et al., 2003). This arc consists mostly of migmatitic rocks intruded by syn-collisional granitoids dated at c. 620 Ma, but may have had its initation as early as 800 Ma (Ganade de Araujo et al., 2014a); it is also believed to be the last manifestation of continental collision in the CCD, which was then followed by pervasive strike-slip tectonics. A variety of granitoid plutons and felsic dykes occur throughout the area and are thought to be syn- to late-tectonic. These include the Nova Russas and Pedra Lisa plutons, Ematuba, Independência and Marrecas dyke swarms, and Quixeramobim and Quixadá batholiths (Figura 21). The plutons are mostly granites, monzonites, granodiorites and tonalites whereas the dykes are composed of porphyritic dacites to rhyolites. These dykes have not yet been found near the shear zones, thus crosscutting relations are not directly seen.

4.4 The Senador Pompeu and Tauá shear zones

Multispectral satellite imagery and airborne magnetic survey data were used to produce maps that highlight significant structures. CBERS high-resolution images at the pancromatic band have revealed the structural grain of both shear zones and particularly of the area where the two shear zones merge. The intepretation is shown in Figura 22. Airborne magnetic survey data (made available by the Brazilian Geological Survey) were processed for the area encompassing most of the length of the shear zones. An amplitude of analytic signal filter processing applied to magnetic data reduced to the magnetic pole and with upwards continuation to 500m from ground level is shown in the inset map of Figura 22. Amongst other applied filters the amplitude of analytic signal was the most effective for showing deeper structures and stronger contrasts, providing additional clues to the structural lineaments map.

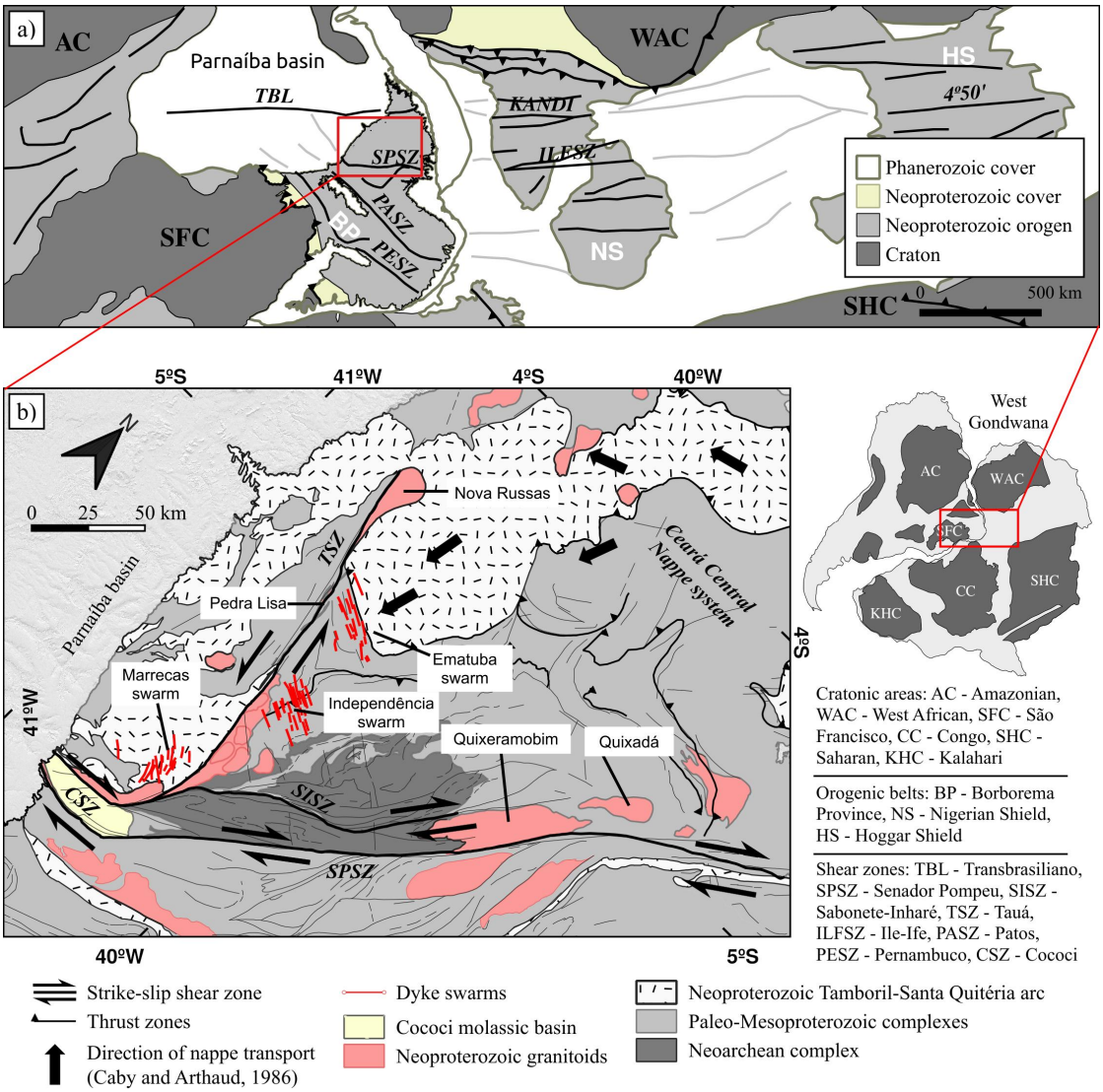

Figura 21 – a) Geological map of the central West Gondwana Orogen. b) Geological map of the Ceará Central domain (CCD). The studied plutons are indicated by their respective names. See Figura 22 for sample locations. Note that all maps have the north rotated 45° clockwise.

The deformation in the CCD is characterised by a system of southwest and south-moving allochtonous units collectively known as the "Ceará Central crystalline nappes" (Caby and Arthaud, 1986), and major strike-slip faults such as the Senador Pompeu (SPSZ) and Tauá (TSZ) shear zones (Figura 22). The SPSZ is a NE trending dextral shear zone measuring c. 350 km in length from its southwest intersection with the TSZ to the NE Brazilian coast. In a pre-drift Gondwana reconstruction, the SPSZ is roughly continuous with the Ilesha-Ifewara shear zone of southwest Nigeria (Archanjo et al., 2013; Caby and Boessé, 2001). It cuts through Archean-Paleoproterozoic basement rocks deformed at various temperatures, including local high-temperature granulite-facies mylonites dominating the northern half and amphibolite to greenschist-facies mylonites occurring along the southern half of the shear zone (Vauchez et al., 1995). Pseudotachylites and breccias occur in the southern segment. Mylonitic foliations are steeply dipping and stretching lineations are mostly subhorizontal. Flat-lying foliations from adjoining areas are transposed by the strike-slip deformation and form upright folds close to the shear zone. Its width ranges from 1–2 km and up to 16 km to the north when it merges with the Orós-Jaguaribe shear zone. No estimates of offset exist for the SPSZ. A crustal scale vertical boundary is revealed in magnetotelluric (Padilha et al., 2017) and gravity data (Oliveira and Medeiros, 2018) beneath the SPSZ. To the northwest of the SPSZ occurs the Sabonete-Inharé shear zone (SISZ). It consists of a dextral discrete mylonite zone cutting through the Neoarchean basement. It is parallel to SPSZ and extends for c. 180 km, from its junction with the Tauá shear zone to the southwest to the Quixadá batholith to the northeast where it probably splays into minor high-temperature zones and becomes indistinct. Gammaspectrometric images of the SISZ indicate it causes only minor displacements within the basement.

The sinistral TSZ extends for c. 220 km in a N10W strike from its intersection with SPSZ to the south, to the Transbrasiliano lineament to the north. It has a thickness of c. 5 km with steeply dipping foliations that are deflected in a sinistral sense on both sides of the fault, while mineral and stretching lineations are mostly horizontal. Neves (1991) has estimated an offset of 30–35 km (thus with an average shear strain of 10) from deflected NW striking structures in agreement with c. 30 km offset of the tail of the *en cornue* Nova Russas pluton (see Figures 21 and 22). The shear zone cuts across migmatites and anatexites of the Tamboril-Santa Quitéria arc (Neves, 1991) and is composed of high-temperature mylonites to cataclasites, the latter often overprin-

ting previous ductile deformation. The core of the TSZ includes a set of anastomosing sheets of porphyritic granitoids (Pedra Lisa suite) which defines a linear magnetic low following most of the length of TSZ (inset of Figura 22), from the Nova Russas pluton southwards. This magnetic low indicates a magma-laden character for the shear zone core at depth, and in addition to gravity data (Oliveira and Medeiros, 2018) reveal how the TSZ causes an offset to the Tamboril-Santa Quitéria arc, juxtaposing it to the schist complex to the E. The TSZ is underlain by east-dipping seismic reflectors with slightly folded geometries (Daly et al., 2014) at fairly shallow depths. In addition to that, magnetotelluric results (Padilha et al., 2017) suggest that the TSZ is a shallow structure rooted at mid-lower crustal detachments dipping east.

The SPSZ and TSZ merge to the southwest and bend into an EW strike direction. Stretching lineations of both TSZ and SPSZ plunge away from that point of convergence (i.e. lineations plunge N for TSZ and NE for SPSZ, Figura 22), whereas farther away from their junction lineations tend to plunge in the opposite direction. The EW dextral shear zone segment that forms from the intersection between TSZ and SPSZ is here termed Cococi shear zone (CSZ). This segment was reactivated at later times under a brittle pull-apart regime during which the Cococi molassic basin was formed. Thus most of the core of the shear zone is buried, and mylonite exposures are scarce on either shoulder of the basin. Such mylonites indicate greenschist facies conditions during dextral shearing.

4.5 Analytical methods

Zircons for U-Th-Pb analysis were recovered after crushing fresh hand samples (2–5 kg) and separating the different grain fractions by hydraulic, magnetic and density methods. The zircon grains were mounted in epoxy resin together with chips of the TEMORA 1 reference zircons (Black et al., 2004). They were polished and imaged with transmitted light and cathodoluminescence (CL). This procedure allows recognition of best grains for analysis; i.e. those with no fractures, inclusions or signs of metamictization. Analyses were focused on areas of pronounced oscillatory zoning typical of primary igneous crystals. *In situ* analyses were conducted in SHRIMP IIe at the Geochronological Research Center of the *Universidade de São Paulo*. The isotopic data were collected in sets of five scans through the masses and the TEMORA standard measured

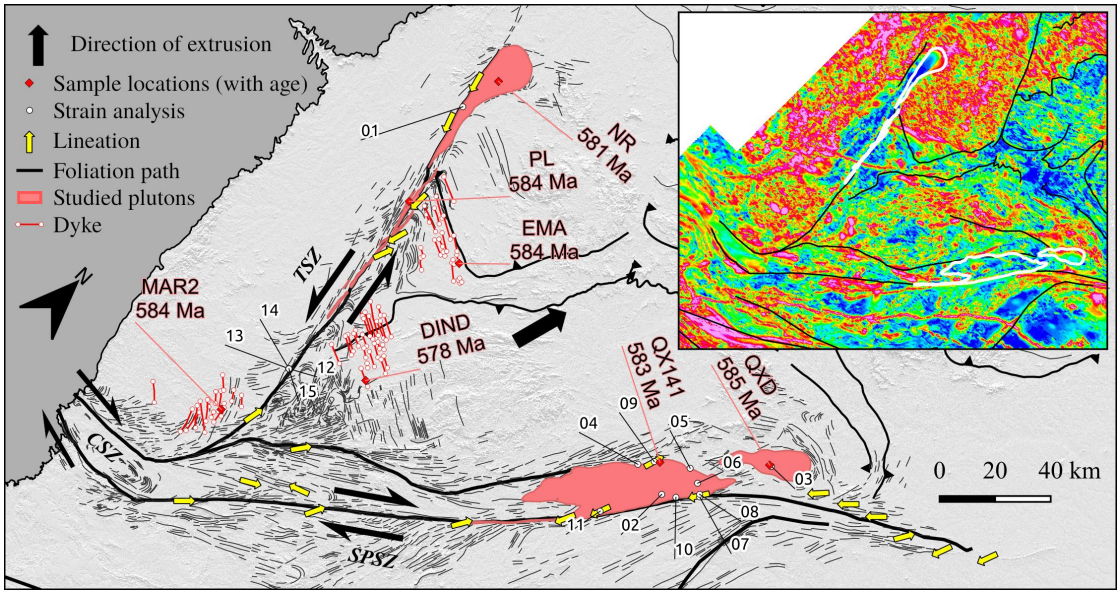

Figura 22 – Structural lineaments interpreted from multispectral CBERS4 images and magnetic anomaly map (inset). Sample locations are shown with mean $^{206}Pb/^{238}U$ ages and their respective codes (QXD - Quixadá, QX141 - Quixeramobim, NR - Nova Russas, PL - Pedra Lisa, EMA - Ematuba, DIND - Independência, MAR2 - Marrecas). Lineation plunges are less than 30°.

after four unknowns (see details in Sato et al., 2014). Data reduction was performed on SQUID 2.5 and statistical assessments calculated using ISOPLOT 2.2 (Ludwig, 2009). The ages calculated are presented with errors of 2σ (95% confidence). The tabulated analysis data, concordia plots and cathodoluminescence images of zircons are given in the Supporting Information[1]. Sample locations are given in Figura 22.

4.6 Results

4.6.1 SHRIMP ages

4.6.1.1 Quixadá and Quixeramobim

The Quixadá sample consists of monzodiorite rocks with alkali-feldspar and plagioclase megacrysts up to 10 cm in size in a dark green coarse-grained biotite and amphi-

[1] Appendix A

bole rich matrix. The Quixeramobim sample consists of a porphyritic granodiorite with feldspar phenocrysts up to 6 cm in size in a coarse grained matrix of quartz, feldspar and biotite. Apatite, magnetite and epidote are accessory phases in both Quixadá and Quixeramobim batholiths. Zircons from the respective granitic samples are similar with average size and aspect ratio of 135 μm and 2:1, respectively. They exhibit conspicuous magmatic oscillatory zoning. The analyses were focused on the inclusion-free oscillatory zoning domains that record crystallization age of the zircon (Figura 23).

For the Quixadá sample most of the single-grain $^{206}Pb/^{238}U$ ages (12 spots) range between 571 and 597 Ma. Three analyses not belonging to the most coherent group and with ages of c. 555 Ma (spot 2.1, see Supporting Information[2]) and c. 606 Ma (spots 8.1 and 15.1) were discarded. The remaining dataset yielded a good concordia age of 585 ± 3 Ma (MSWD=0.39, see Supporting Information[3] for concordia plots) and a weighted average age of 585 ± 5 Ma (MSWD=2.5, Figura 23), thus setting c. 585 Ma as an accurate estimate of age of emplacement for the Quixadá magmas.

Zircons within the Quixeramobim batholith yield a poor concordia age of 584 ± 5 Ma (MSWD = 8.4) and a weighted mean age of 583 ± 4 Ma (MSWD = 1.2, Figura 23) from the most coherent group of analyses (12 spots). Ages were calculated after removal of analyses with high U (spot 3.1) or common ^{206}Pb (spots 2.1 and 6.1), and ages not belonging to the most coherent group (spots 4.1, 5.1 and 10.1).

4.6.1.2 Nova Russas and Pedra Lisa plutons

Coarse-grained, porphyritic and slightly deformed biotite-rich granodiorite samples from the Pedra Lisa suite provided zircons with pronounced oscillatory zoning. Truncated zoning indicates possible inherited xenocrystic or antecrystic cores which were not analysed. Their average size and aspect ratios are 137 μm and 2:1, respectively. The sample from the core of Nova Russas pluton is a coarse grained, aphyric and undeformed hornblende-biotite monzogranite having zircons much like those of Pedra Lisa with smaller grain size (130 μm) and rich in large apatite inclusions (which were also avoided during the analysis).

The ages of the analysed Pedra Lisa zircon grains range from 569–617 Ma. Individual analyses have concordant $^{206}Pb/^{238}U$ and $^{207}Pb/^{235}U$ ages which are scattered over

[2] Appendix A
[3] Appendix A

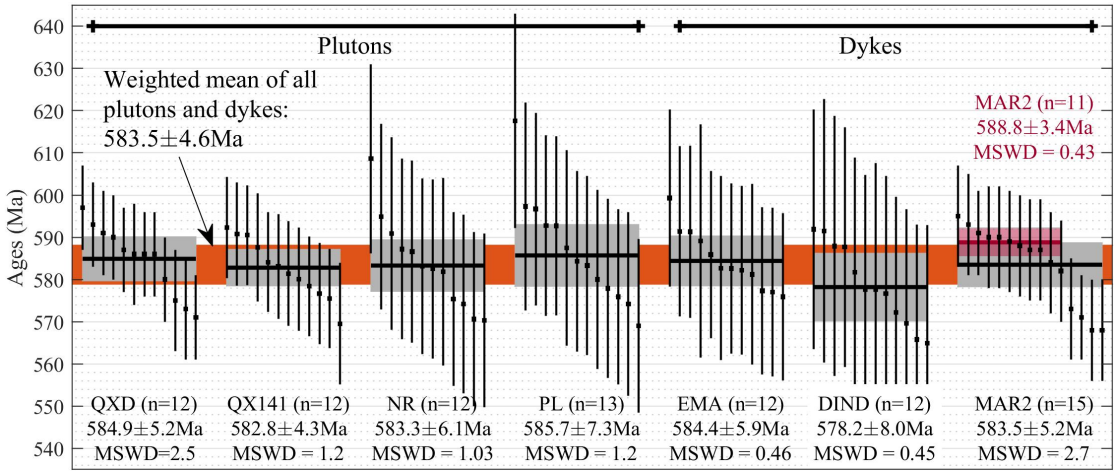

Figura 23 – Weighted average $^{238}U/^{238}U$ ages for the granitoid plutons and felsic dyke swarms. Sample codes are as defined in Figure 2. Vertical lengths are analytical errors at 2σ centred at the age. Grey bars are weighted average ages with 2σ uncertainty. For cathodoluminescence images, concordia plots and data of individual analyses see Supporting Information. Dark red weighted average is calculated for Marrecas sample without the four youngest ages.

the concordia, providing a poorly defined concordia age of 587 ± 6 Ma (MSWD=8.3, 13 spots). One analysis (spot 11.1) with an older age of 626 Ma and very low Th/U compared to other analyses was discarded. The remaining dataset forms the most coherent group with a weighted average age of 586 ± 7 Ma (MSWD=1.2) providing the best estimate of crystallization of the Pedra Lisa suite magmas.

For the Nova Russas pluton, three analyses with comparatively high values of U and ^{204}Pb, and with ages between 548 and 555 Ma were discarded (spots 2.1, 3.1 and 5.1). The remaining zircons form the most coherent group (12 spots) with $^{206}Pb/^{238}U$ ages varying from 570 to 608 Ma. These yield a poor concordia age of 583 ± 6 Ma (MSWD=0.0007). Thus we take the weighted mean age of 583 ± 6 Ma (MSWD=1.03, Figure 3) as best estimate of crystallization of the Nova Russas pluton.

4.6.1.3 Ematuba, Independência and Marrecas dyke swarms

Samples of the Ematuba, Independência and Marrecas dykes show similar composition and texture. They are porphyritic with 0.5–1 cm large biotite, hornblende and plagioclase phenocrysts in a trachytic to rhyolitic aphanitic groundmass. A myriad

of variations to the typical texture include embayed quartz phenocrysts, large magmatic epidote, sagenitic biotite phenocrysts, rapakivi feldspar, anorthosite microenclaves and anthophylite aggregates with biotite corona. Zircons in these rocks obtained from unaltered samples are typically euhedral with pronounced oscillatory zoning, contain a distinctly high amount of apatite inclusions of various sizes, and have an average aspect ratio of 2:1. The dated zircons from Ematuba had average size of 130 μm. The Indenpendência dyke sample had zircons with fewer inclusions and less pronounced oscillatory zoning, with average size of 122 μm. Zircons from Marrecas dykes are very homogeneous with average size of 140 μm. Analyses of all zircons were preferentially focused on well developed zoning sites distant from inclusions and fractures. Homogeneous cores of possibly inherited origin were avoided.

Ematuba zircons forming the most coherent group (12 analyses) had $^{206}Pb/^{238}U$ ages of 575 to 599 Ma, with a poor concordia age of 586 ± 8 Ma (MSWD=11.1). Three discarded analyses (spots 8.1, 10.1 and 13.1) were characterised by large uncertainties and were strongly discordant falling below the concordia (see Supporting Information[4]). Thus the weighted average age of 584 ± 6 Ma (MSWD=0.46) provided by the most coherent group is the best estimate for the age of the Ematuba dykes.

Analyses on 12 spots of the Independência zircons gives a poor concordia age at 579 ± 8 Ma (MSWD = 0.31) and a similar weighted mean age at 578 ± 8 Ma (MSWD = 0.45, Figura 23). These were calculated after discarding four analyses with high ^{204}Pb causing large uncertainties (spots 3.1, 4.1, 5.1 and 7.1).

Zircons from the Marrecas dykes provided the lowest uncertainties with individual ages (15 spots) ranging from 568 to 595 Ma. Two analyses (spots 3.1 and 6.1) with significantly older $^{206}Pb/^{238}U$ ages of 627 and 625 Ma, outliers to the most coherent group, were discarded. The coherent dataset yielded a good concordia age of 584 ± 3 Ma (MSWD=0.79) and an equivalent weighted average age of 584 ± 5 Ma (MSWD=2.7), which we thus take as the age of emplacement for the Marrecas dyke swarm.

4.6.2 Magmatic deformation structures and mylonites

Several structural criteria from macro- to microscale have been adopted to indicate the syn-tectonic emplacement of granitic magmas. In a regional scale the tear

[4] Appendix A

(*en cornue*) shape of deep-seated intrusions records syn-tectonic magmatism and the asymmetry of the pluton's tail has been used to define the emplacement kinematics (Roman Berdiel et al., 1997; Rosenberg, 2004). The Nova Russas is a typical asymmetric tear-shaped pluton in agreement with the sinistral movement of the Tauá shear zone. The Quixadá batholith also has a tear-drop shape in agreement with the dextral movement of the SPSZ (Figure 4a). Roman Berdiel et al. (1997) showed by means of analog modelling of granite emplacement in shear zones that the *en cornue* shape of plutons is formed when the feeder zone for pluton construction is located outside the shear zone core, which then deforms the pluton into a tear-drop shape. A feeder zone for the Quixadá pluton is inferred from both gravity (Lopes de Castro et al., 2002) and magnetic (magnetic high around the NW contact of the batholith, Figura 22) anomalies to be located at its NW margin.

Shape preferred orientation of feldspar phenocrysts in a granitoid where the matrix is not affected by conspicuous solid state deformation (e.g. equant magmatic quartz) is often a reliable indicator of syn-magmatic deformation. The Quixeramobim batholith bounding the SPSZ and Pedra Lisa sheet-like plutons within the TSZ is characterised by syn-magmatic deformation of feldspar megacrystic granitoid facies (Figures 24b and 25a) where a shape preferred orientation is defined by feldspar megacrysts and biotite grains in the matrix. In thin sections these fabrics show equant magmatic quartz, undeformed feldspar and biotite, and epidote-rich shear bands forming after late-magmatic plagioclase alteration (Figura 25b). Similar syn-magmatic deformation of megacrystic facies occurs in the Quixadá batholith whereas for the Nova Russas pluton, which is mostly equigranular to slightly porphyritic, magmatic deformation fabrics are less evident. In addition, mafic and megacrystic facies of the Quixeramobim batholith occurring as sheets and syn-magmatic dykes are deflected towards SPSZ, as are metasedimentary wall rocks (green stripes in SE margin of the Quixeramobim batholith in gammaspectrometric image, Figura 24a). These granitoid facies with feldspar megacrysts are also characterised by SC foliations (dextral shear sense for Quixeramobim batholith and sinistral for Pedra Lisa suite), creep cavitation features, and absence of shear localizations or strong compositional layering. Magmatic deformation was progressively followed by low amounts of sub-magmatic and solid-state strain as shown by megacrystic granitoids of SPSZ that contain deformed quartz lenses wrapping around equant feldspar crystals (Figure 4c).

Mylonites occurring in the SPSZ close to the Quixadá-Quixeramobim complex are mostly comprised of metasedimentary wall-rock slivers and metagranitoids. At the northern SPSZ they are mostly high-temperature mylonites, characterised by feldspar grains with large recrystallized grain sizes (i.e. formed by subgrain rotation rather than bulging recrystallization; Martelat et al., 1999) and quartz ribbons. At the southwestern strand of SPSZ close to the tail of the Quixeramobim batholith, the metamorphic grade is middle amphibolite facies, producing sub-grain rotation recrystallization of quartz to lower grain sizes and *c*-axis fabrics perpendicular to the foliation, suggesting a temperature decreases towards the TSZ. The typical core of the SPSZ is characterised by dm-thick bands of variably deformed and mylonitised granitoids, juxtaposed with ultramylonite layers (Figure 4d). Pseudotachylites occur on the southern segments of SPSZ overprinting ultramylonites and locally associated with thin brecciated layers (Figure 4e). Lithological markers appreciable from gammaspectrometric composition images of SPSZ indicate an offset between 66 and 96 km (see markers on Figure 4a), which for the central segment of SPSZ (width of c. 1.5 km) yields a mean shear strain of 54.

Mylonites in the TSZ are characterised by a range of deformation temperatures and conditions. Where the Nova Russas pluton intersects the shear zone at its northern segment, mineral assemblages record upper greenschist to amphibolite facies conditions with pervasive recrystallization of quartz and feldspar brittle and recrystallization-driven grain size reduction (Figura 25c). Larger strains at similar metamorphic conditions took place at the southern segment of the TSZ close to its intersection with the SPSZ (Figura 25d), where a strong compositional fabric with abundant recrystallization of feldspar and quartz is found. In the middle segment of TSZ cataclastic deformation is found to overprint plastic strain fabrics, occurring as decimeter-thick zones of brittle comminution wrapping around pods of preserved mylonites. In such pods, feldspars show large recrystallized grain sizes and mildly developed quartz ribbons occur (Figura 25e), suggesting high-temperature deformation, whereas smaller grain sizes for quartz in oblique fabrics and epidote-rich shear bands indicate an overprinting greenschist facies deformation. Thus, the cataclastic microstructures wrapping around mylonite pods (Figura 25f) indicate that the shear zone was active during progressive cooling into brittle crustal levels.

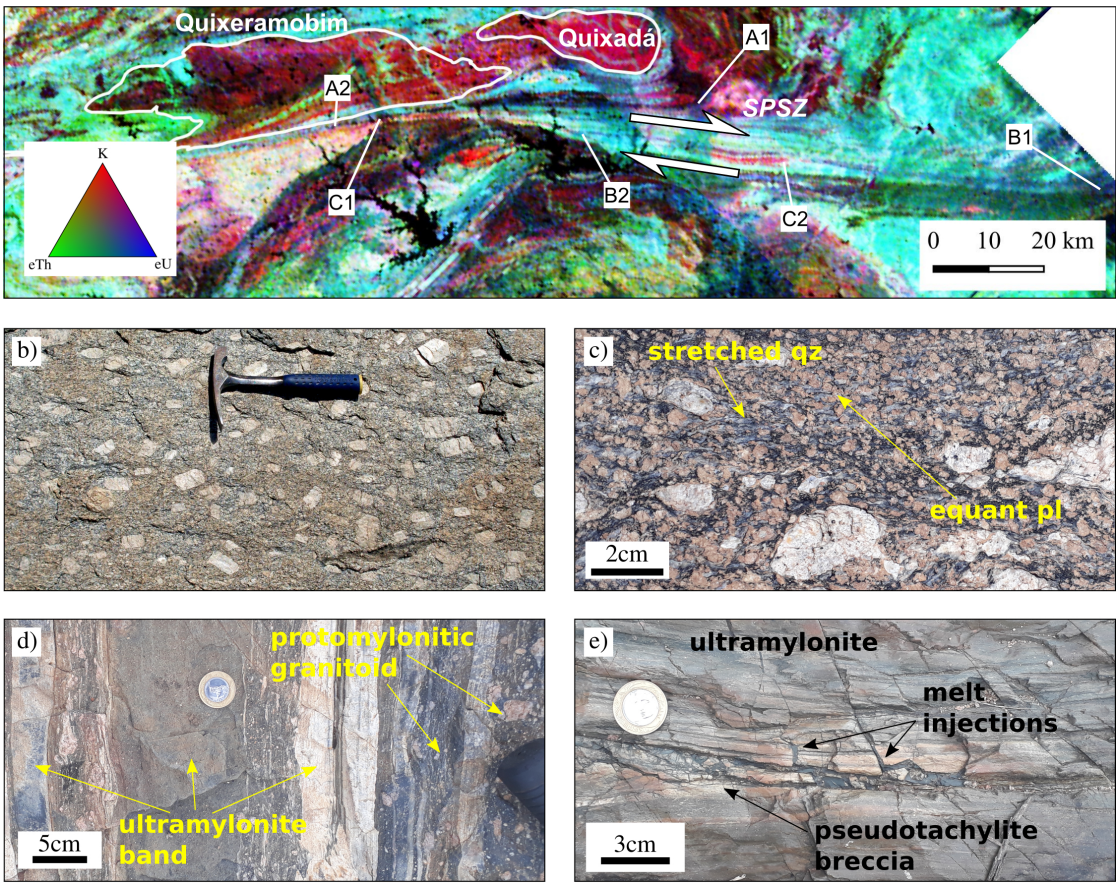

Figura 24 – a) Gamma ray spectrometry map (ternary composition) of Senador Pompeu shear zone (SPSZ). Lithological control points give offset estimates of 66, (A1-A2) 96 (B1-B2) and 68 km (C1-C2). b) Megacrystic facies SPO of the Quixeramobim batholith (magmatic foliation is horizontal). c) Megacrystic Quixeramobim granitoid with solid-state deformation (elongate quartz) overprinting magmatic deformation (strong SPO of equant feldspars), SPSZ. d) SPSZ mylonite zone with banded ultramylonites, protomylonites and lightly deformed porphyritic granites. e) Pseudotachylite in southern segment of SPSZ. All figures have dextral shear sense.

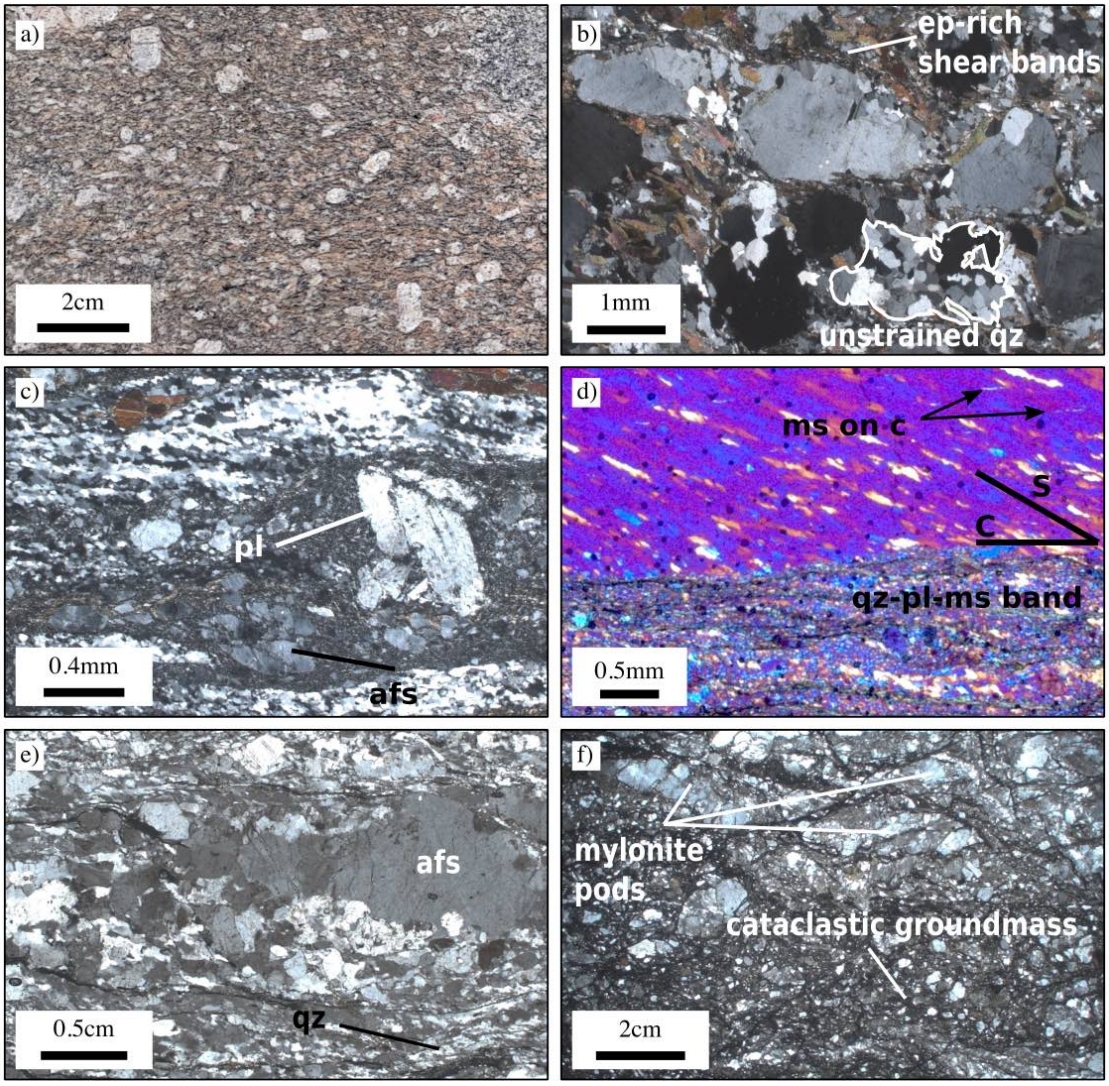

Figura 25 – a) Magmatic fabric of porphyritic facies of Pedra Lisa pluton. Foliation trace is horizontal. b) Microstructure of Pedra-Lisa pluton deformed at sub-magmatic to magmatic conditions. c) Intermediate-temperature quartz-feldspar mylonite at the fault-bounded walls of Nova Russas pluton. d) Low-temperature S-C mylonite of southern TSZ. Note micrometer-sized muscovite laths e) High-temperature mylonite of middle segment of TSZ preserved from cataclastic deformation. f) Cataclastic groundmass formed after brittle deformation overprinting high-temperature mylonites (preserved pods indicated). All figures have sinistral shear sense.

4.6.3 Vorticity and kinematic analysis

It is often challenging to find reliable structures for estimating kinematic vorticity (W_k) of flow, and each method has its own limitations (Fossen and Cavalcante, 2017; Law et al., 2004; Passchier, 1987). Megacrystic facies deformed in the magmatic to sub-magmatic state with low ensuing solid state strain such as those of Pedra Lisa suite and Quixeramobim megacrystic facies provide a good opportunity for W_k estimates by the porphyroclast method, as well as a strain estimate for the same dataset by means of the Fry (1979) method. The strain recorded by these megacrystic granitoid rocks has occurred mostly in the magmatic to sub-magmatic state as attested by recrystallization tails in feldspar and large equant to slightly elongate quartz grains with mild undulose extinction. On those grounds we infer that the amount of solid-state strain following crystallization of the plutons has been low, although it would be difficult to assert its actual contribution since strain occurs continuously through the rheological transitions of a crystallizing magma. Evidently strain estimates from magmatic deformation structures of the granitoids represents only a snapshot of their full strain history, mostly recording only the last increment of deformation. We have attempted to estimate strain by Delauney triangulation of nearest neighbours according to a modification of the Fry (1979) method by Mulchrone (2003) using the PolyLX toolbox for Matlab (`https://petrol.natur.cuni.cz/~ondro/oldweb/polylx:home`; Lexa, 2003). Results are shown in Figures 26 and 27 for SPSZ and TSZ respectively.

Sequences of photographs were taken from well exposed surfaces of granitoids where the feldspar megacrysts were clearly visible for subsequent tracing of outlines in GNU Image Manipulation Program (GIMP, Version 2.10.12). As much as possible the photos were taken of surfaces perpendicular to the magmatic foliation plane and parallel to the lineation. Images of outlined megacrysts were then processed using MATLAB (Version R2019a Update 3) for identification of best fit ellipses and their geometrical parameters (e.g. aspect ratio and orientation). Orientations of ellipses (ϕ) fit to megacrysts were plotted against axis ratio (R) in Figura 26 for megacrystic facies rocks of the Quixeramobim batholith. Kinematic vorticity is calculated according to Passchier (1987) where $W_k = (R_c^2 - 1)(R_c^2 + 1)$, and R_c is the critical aspect ratio in ϕ–R plots, which is selected as a mean value between minimum and maximum of the uncertainty region. Mean R_c values obtained for the Quixeramobim range in 1.61–3.54. W_k values

	W_k	PS%	R_f	θ	a
01 (TSZ)	0.64	56	1.12	100°	1.25
12 (TSZ)	0.77	44	1.40	87°	1.41
13 (TSZ)	0.69	52	1.54	92°	1.18
14 (TSZ)	0.71	50	1.55	84°	1.22
15 (TSZ)	0.67	53	1.19	34°	1.26
04 (SPSZ)	0.69	52	1.30	74°	1.26
03 (SPSZ)	0.82	39	1.58	66°	1.53
02 (SPSZ)	0.79	42	1.74	84°	1.37
05 (SPSZ)	0.82	39	1.24	95°	1.64
06 (SPSZ)	0.62	57	1.41	86°	1.11
07 (SPSZ)	0.44	71	1.52	81°	0.92
08 (SPSZ)	0.75	46	1.10	79°	1.46
09 (SPSZ)	0.68	52	2.66	90°	0.95
10 (SPSZ)	0.45	70	1.73	86°	0.87
11 (SPSZ)	0.85	35	1.18	100°	1.82

Tabela 1 – Kinematic vorticity (W_k), percentage of pure shear (PS%), aspect ratio of strain ellipsoid (R_f), angle of ellipsoid long axis to foliation (θ) and thinning estimates (a) for megacrystic magmas occurring in the Senador Pompeu (SPSZ) and Tauá (TSZ) shear zones.

for the Quixeramobim megacrystic facies fall in the range of 0.44–0.85, with an average W_k of 0.69 and standard deviation of 0.148. The percentage of pure shear relative to simple shear (Figura 28; Law et al. 2004) for that range is between 44 and 71 with a mean of 50. The strain ellipse for the same data set has a strain aspect ratio (X/Z of the strain ellipse) of 1.10–2.66 with a mean of 1.55. Estimated strain parameters are summarized in Table 1.

ϕ–R plots and strain analyses for megacrystic granitoids of the Pedra Lisa suite in southern TSZ are shown in Figura 27. R_c values ranged between $\sim$ 2.12 and 2.79. The resulting W_k falls in the range of 0.64–0.77, with an average W_k of 0.70 and standard deviation of 0.049. Percentage of pure shear relative to simple shear is between 44 and 56 with a mean of 51 (Figura 28). The calculated strain ellipses have an aspect ratio range of 1.12–1.55 with a mean value of 1.42. Strain parameters are given in Table 1.

By combining vorticity (W_k) and shape ratio of the strain ellipsoid (R_f) it is possible to estimate the thinning (a) of the deforming layer (Festa, 2014), which for plane strain

is given (Wallis et al., 1993) by

$$a = 0.5\sqrt{(1-W_k^2)}[R_f + R_f^{-1} + 2\frac{1+W_k^2}{1-W_k^2} + \sqrt{R_f + R_f^{-1} - 2}].$$

Often one has to use a strain gauge or marker different from the structure used for vorticity estimates, which may introduce an error due to strain partitioning and heterogeneity. Thus using the megacrystic facies SPO for both is a good opportunity for a reliable estimate of thinning, albeit such structures represent a fraction of the deformation history and thinning-thickening values may be underestimated. For the deformed Pedra Lisa suite the initial shear zone was calculated to have been 1.18 to 1.41 times thicker than the active shear zone width at the final increment of deformation (Festa, 2014), i.e. a thinning of 15–30%. Estimates for the Quixeramobim batholith have a much wider range, from 1.82 to 0.87 (45% thinning to 15% thickening).

An independent gauge for kinematic vorticity of the deformation affecting the TSZ is tentatively offered by the synchronous dyke swarms (Ematuba and Independência). If assumed to be pure extension fractures these dykes have maximum extension directions at $\approx 38^\circ$ to the TSZ, yielding a vorticity ($W_k = (90 - 2\theta)$, where θ is the angle between shear plane and extension direction of fractures) of ≈ 0.97 (Fossen and Cavalcante, 2017). This estimate , which is from the walls of the TSZ, is different from the one estimated within the shear zone, indicating that the pure shear component is higher within the shear zone than in the wallrocks. Additionally, magmas can be affected by strain due to some inflating component during emplacement. However, we believe that the plutons were already constructed prior to the deformation which was recorded and the strain related to episodic accretion of magmas was likely overprinted.

4.7 Discussion: a kinematic model for the TSZ-SPSZ interaction

4.7.1 Timing of shear zone activity

U-Pb isotope ratios for samples from the Marrecas dyke swarm (and to some extent the Quixadá sample) exhibit a distinct dispersion (seen from error ellipses of concordia

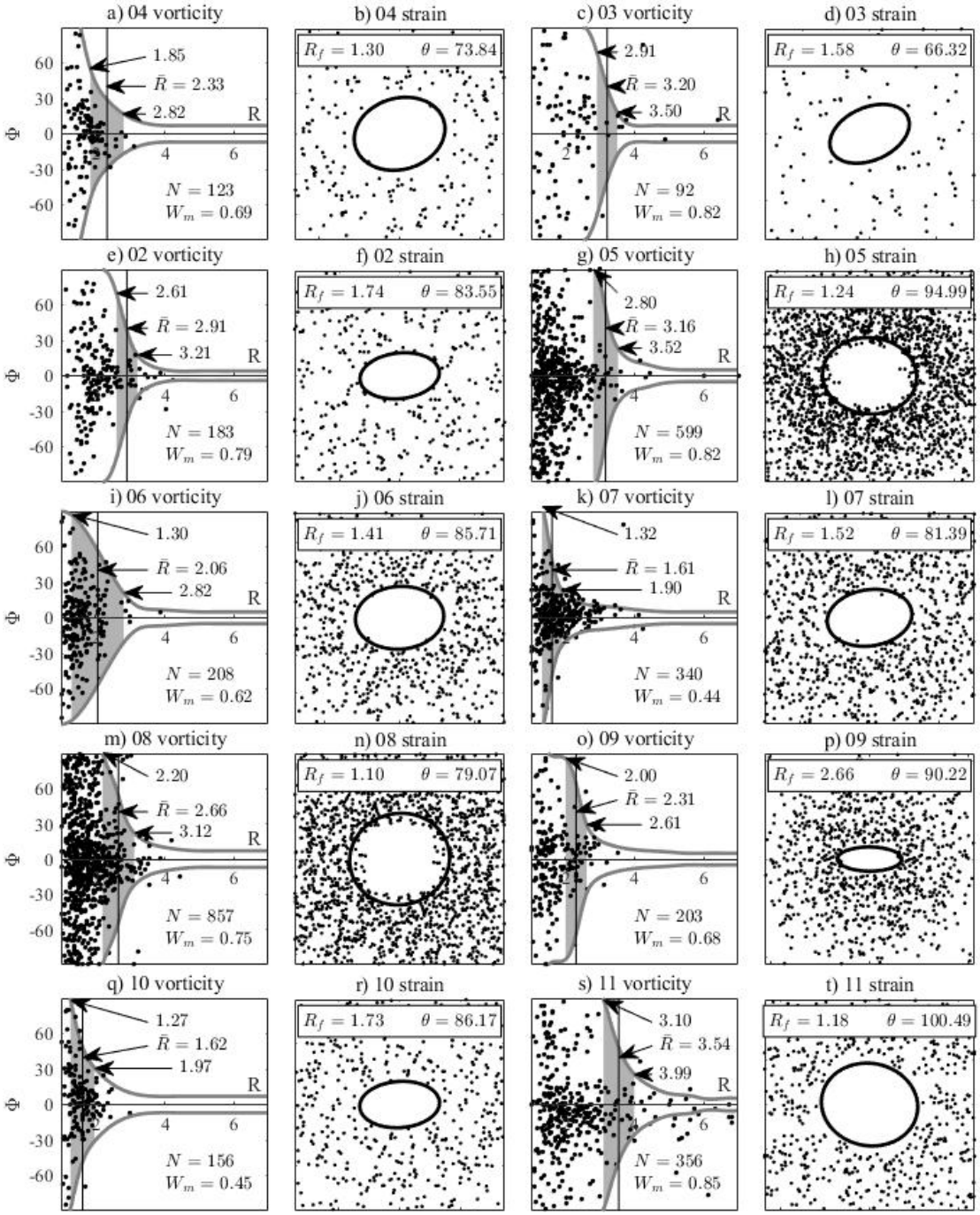

Figura 26 – Kinematic vorticity and strain ellipsoid estimates of megacrystic facies of the Quixeramobim pluton deformed by the Senador Pompeu shear zone (SPSZ). Left charts show shape ratio of feldspar porphyroclasts (R) versus angle between feldspar long axis and the foliation plane (ϕ). $\bar{R}$ is the estimate of mean critical ratio (R_c). Right charts are strain estimates according to Fry (1979), where R_f is ellipsoid aspect ratio and θ is the clockwise angle between ellipsoid long axis and foliaton pole (chart north). In all cases the foliation plane is horizontal.

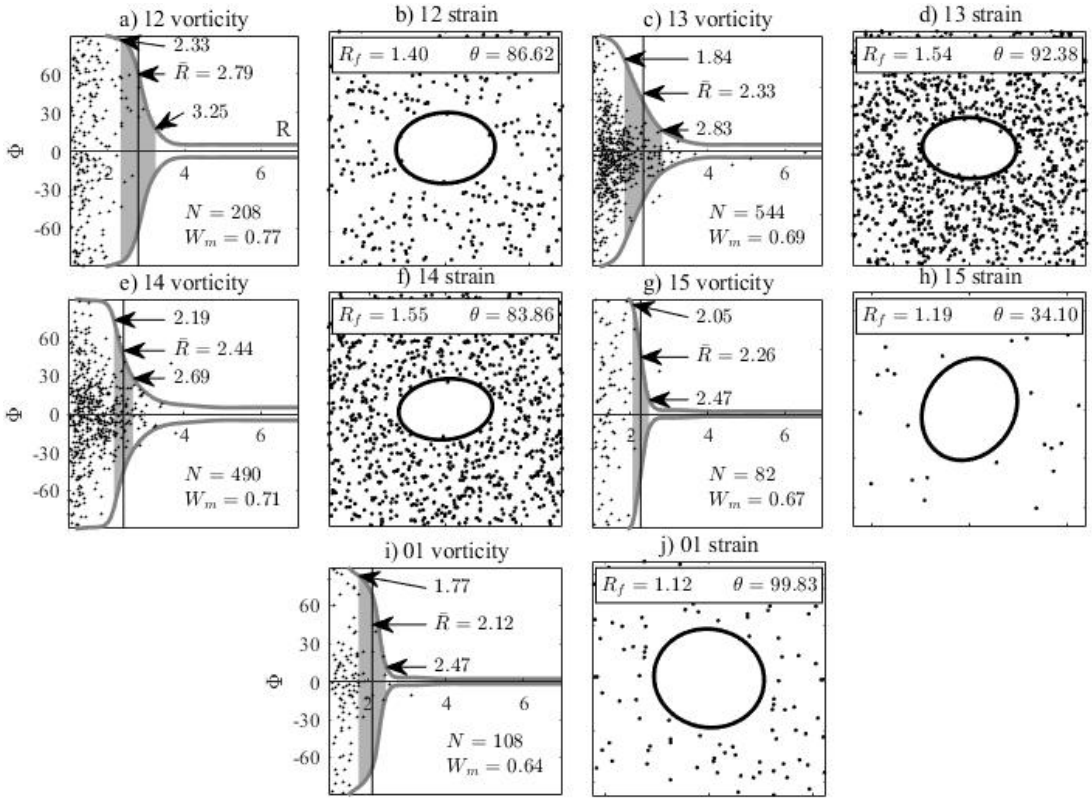

Figura 27 – Kinematic vorticity and strain ellipsoid estimates of megacrystic facies of the Pedra Lisa and Nova Russas plutons deformed by the Tauá shear zone (TSZ). Left charts show shape ratio of feldspar porphyroclasts (R) versus angle between feldspar long axis and the foliation plane (ϕ). $\bar{R}$ is the estimate of mean critical ratio (R_c). Right charts are strain estimates according to Fry (1979), where R_f is ellipsoid aspect ratio and θ is the clockwise angle between ellipsoid long axis and foliaton pole (chart north). In all cases the foliation plane is horizontal.

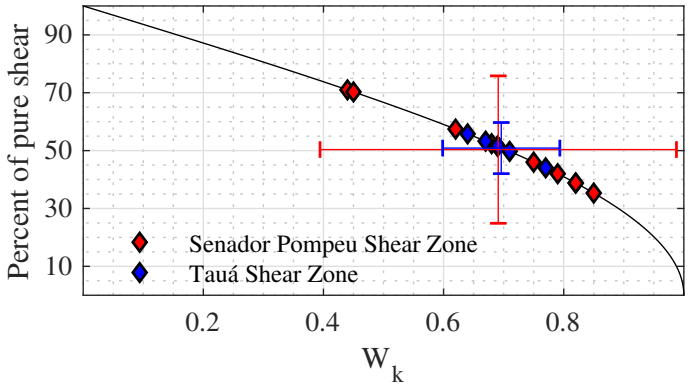

Figura 28 – Relationship between percentage of pure shear relative to simple shear and kinematic vorticity (W_k). Red and blue error bars at two standard deviations centered at the means for estimates of Senador Pompeu shear zone (SPSZ) and Tauá shear zone (TSZ).

diagrams; see Supporting Information[5]) along the concordia. This dispersion from older to younger ages may well be due to the presence of an earlier population of antecrystic zircons (Leuthold et al., 2012), as it might be due to ^{238}U loss affecting to different extent zircons of the same population (Schoene, 2014), in which case the ages for the Marrecas dykes may indicate emplacement as early as 589 Ma if the four youngest ages (spots 11.1, 12.1, 14.1 and 15.1) are disregarded (weighted average age plotted in magenta in Figura 23). However, compositional and textural characteristics of these younger zircons are indistinct from those of the main population and provide no reliable grounds to discard them. Moreover, these processes are unresolvable at the available precision since they lead to variations of isotope ratios that lie within the uncertainties, and since weighted average ages do not differ from concordia ages we take the former to be the most reasonable estimate of peak magmatism. The ages we obtained for the syn-kinematic Quixadá, Quixeramobim, Nova Russas and Pedra Lisa plutons, and for the dyke swarms emplaced away from shear zones, indicate their formation at about 583.5 ± 4.6 Ma (weighted mean age). This confirms synchronous high-temperature activity of SPSZ and TSZ while the internal blocks had high brittle strength.

[5] Appendix A

4.7.2 Shear zone interaction

From the age constraints presented above we are now set to evaluate the synchronous activity of the strike-slip shear zones of the CCD. A model for this tectonic evolution is presented in Figure 9. The magnetic anomaly map (Figure 2) shows that SPSZ is bent from a NE to EW orientation after merging with TSZ to form the Cococi shear zone (CSZ). Detailed observation of high-resolution CBERS4 multispectral satellite images reveal that a set of structures syntaxial with the Marrecas dykes north of the Cococi basin undergo dextral-sense deflection from a starting orientation probably equal to that of Ematuba and Independência swarms. This is in agreement with the dextral shear of the CSZ, and places a maximum shortening direction at about N60W (assuming a tension fracture origin for the dykes) that is consistent throughout the whole domain (Figure 9a). The immediate interpretation is that of northeastwards extrusion of the CCD internal block, which is interpreted to be stronger than the shear zones. At the trailing end of the block, the conjugate shear zones are zippered together forming the CSZ, which has a net dextral shear (dextral closing zipper; Passchier and Platt, 2017; Figure 9b). This requires large internal deformations in the Acaraú (west of TSZ) and Banabuiú (southeast of SPSZ) blocks. Net displacement on the zippered segment is a result of the summation of slip vectors of the interacting shear zones (Passchier and Platt, 2017). Thus CSZ has a net dextral shear which must be a result of the SPSZ having a higher slip rate than the TSZ during their synchronous activity. Representative relations between length (L) and maximum displacements (D) for shear zones ($D = 0.017L^{1.56}$; Fossen and Cavalcante, 2017) indicate a maximum offset for TSZ of c. 80 km. A sinistral deflection of structures syntaxial with the Ematuba and Independência dyke swarms close to the TSZ has been used by Neves (1991) to estimate a total offset of 30–35 km, consistent with the minimum estimate apparent from the sheared tail of Nova Russas pluton. Therefore we believe synkinematic pluton emplacement occurred in late stages of shear zone activity in the CCD (Figure 9a). Also, minimum estimates of diplacement on SPSZ (Figure 4) are of about 66–96 km, thereby supporting the dextral closing zipper model for the CSZ (estimated values from length-displacements relations would be significantly higher). At this stage magmatism in shear zones was at its peak and the suite of synchronous magmas of SPSZ and TSZ was emplaced (Figure 9b). Lastly, brittle reactivation (Figure 4e) of the southern segments of TSZ and SPSZ led

to a NE-SW oriented pull-apart at the CSZ on which the Cococi basin was formed, probably in the Cambrian as a precursor to the Parnaíba basin to the west (Figure 9c).

Whether these synchronous shear zones maintain the different blocks contiguous (i.e. without transverse displacements) during deformation depends on their slip rates and relative orientation. At any point it may be assumed that differential uncompensated slip rates on faults or shear zones would generate transverse deformation. A pull-apart room-making process was interpreted for the Quixadá batholith by Lopes de Castro et al. (2002) on geophysical grounds, assuming a transtensional jog with NE-SW opening. We propose ductile transtension takes place at the SPSZ as a result of slip on the TSZ (illustrated in y-y' cross-section of Figure 9c) while an uncompensated dextral shear continues on the SPSZ, therefore causing floor subsidence that facilitates emplacement of magmas to construct the Quixeramobim batholith. On a crustal scale it follows that transtension-related floor subsidence due to relative motion of shear zone-bounded terranes implies a strong spatial correlation between shear zones and plutons with emplacement favoured outside fault cores rather than within (Schmidt and Paterson, 2000). The vorticities and strain ellipsoid shape ratios that were estimated in this study support this kinematic model. Because the SPO fabrics of megacrystic granitoid facies record only a snapshot of the deformation kinematics we expect a variety of situations to emerge from interacting shear zones. The TSZ is characterised by a narrow range of W_k and thinning, with a low amount of strain being recorded at about 50% simple shear (average W_k of 0.7, Figura 28). On the other hand the SPSZ has similar average values of W_k and thinning, and is distinguished by its broader range of estimated deformation parameters, including thinning and thickening, as well as percentages of simple shear varying from approximately 65 to 30%. Hence the TSZ and SPSZ reveal a typically transpressive character of the deformation at the setting of CCD, whereas the varying character of SPSZ is related to the geometrical arrengement of the shear zone network. Expeditious Fry method strain analysis conducted by Almeida (1995) using the megacrystic facies of the Quixeramobim batholith has also shown that although most areas are consistent with the NW-SE shortening there has been some N-S or NW-SE stretching. Further structural investigations on the Neoarchean Mombaça unit (lying southwest of the Quixeramobim pluton and bound by SPSZ and SISZ) are needed to characterise strain patterns that might hint to this hypothesis such as folding of boudinaged layers and superposed folds (inset of Figure 9c). As a first approximation

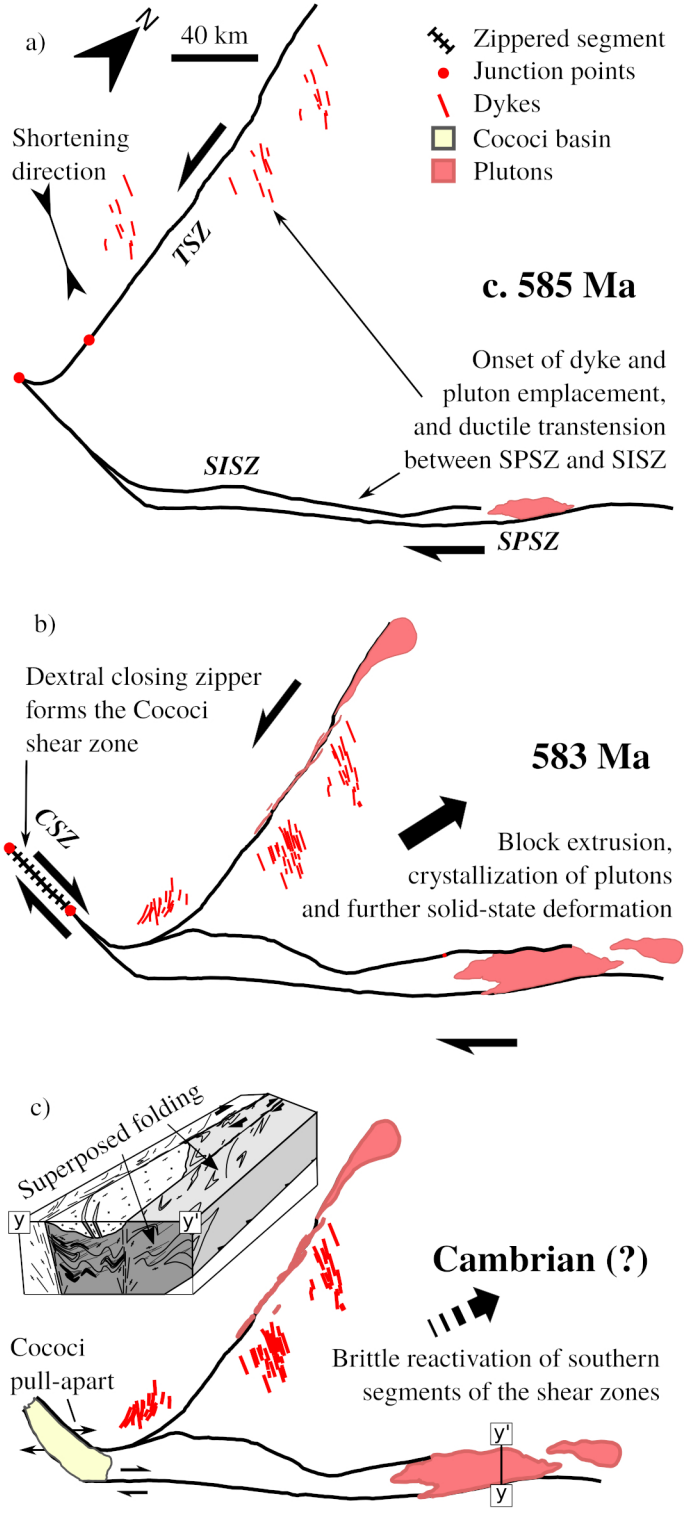

Figura 29 – Model describing the geometrical framework and kinematic interactions between the Senador Pompeu (SPSZ) , Tauá (TSZ), Sabonete-Inharé (SISZ) and Cococi (CSZ) shear zones in the Ceará Central Domain (CCD). See text for discussion.

however it may be said that structures resulting from this process may be elusive since the transtension is a transient event (or several) in a dominantly transpressive setting.

4.7.3 Tectonic implications

The intrusion of dyke swarms around 584 Ma in the central part of CCD (Ematuba and Independência) and to the west of TSZ (Marrecas swarm) at mid-crustal depths (c. 4.5–5.5 kbar, Nogueira, 2004) suggest a high strength of the fault-bounded blocks as compared to the plastically deforming shear zones. Considering that the SPSZ and TSZ are both abundantly permeated by magmas during their activity, with granite sheets occurring along most of their length (Figures 2 and 4c), the role of melt weakening (Hollister & Crawford, 1986) must have been substantial. Due to their low viscosity, magmas can localize a significant amount of strain in short periods (Tommasi et al., 1994; Davidson et al., 1992). Neves et al. (1996) has propposed that the weakening induced by the presence of magma in the TSZ is the enabling factor for shear zone nucleation. Various geophysical and geological evidence indicate that the SPSZ (Padilha et al., 2017) is a pre-existing (relative to late Brasiliano strike-slip deformation) geological discontinuity in the Borborema. However it is also affected by shear zone-concordant granite sheets, some which display only weak solid-state deformation features, possibly as a result of shear zone arrest after full magma crystallization, as described by Tommasi et al (1994).

The development of this shear zone pair and extrusion of the internal block of the CCD is currently believed to shortly succed the continental collision that followed long-lived arc magmatism (Ganade de Araujo et al., 2014a). According to Caby and Arthaud (1986), the formation of the Ceará Central nappe system (Figura 21) would be synchronous with such an extrusion tectonics which, in turn, would place the Tamboril-Santa Quitéria arc as an allochtonous unit over the Rhyacian basement. The initial hypothesis of Caby and Arthaud (1986) about the existence of large nappes transported to SSW over long distances required the SPSZ and TSZ to act as lateral ramps, which would imply an opposite sense of shear. Geophysical evidence that the TSZ is a relatively shallow structure in the present day crust possibly indicates that it merges with a middle-lower crustal detachment. Such deeper detachment structures are likely synchronous with the development of the CCD nappes and may be related to their formation by the extrusion

of the internal block. Caby and Boessé (2001) have also outlined nappe-like structures in the Nigerian belt next to the Ifewara-Ilesha shear zone, with NE-plunging stretching lineations and top to the NE (i.e. extensional) movement. Additional investigations of both provinces, however, are necessary to set the chronology and kinematic compatibility between deep-seated nappe structures and lateral strike-slip shear zones.

4.8 Conclusions

Interpreting the kinematic, rheological and geochronological characteristics of interacting shear zones in the middle crust is necessary to understand the evolution of shear zone networks. In this work we have demonstrated how a zippered shear zone model applies to large-scale shearing and extrusion of crustal blocks. This approach is also essential for the understanding of processes of continental collision and orogen exhumation. Specifically, constraining timing of fault activity and their strain kinematics hint into processes ranging from pluton emplacement to transport of crustal blocks. By applying in situ U-Pb dating to dykes and syn-kinematic plutons of the Senador Pompeu and Tauá shear zones we determined their synchronous activity at 583.5 ± 4.6. Rheological heterogeneities at this level are marked by syn-kinematic plutons that cause melt weakening, enhanced viscous flow and later crustal welding, while felsic dyke swarms are emplaced in brittle extensional fractures. Furthermore, the arrangement of the Senador Pompeu and Tauá shear zones has formed a dextral closing zipper (Cococi shear zone) trailing the extrusion of the strong confined crustal block to the east. Such a framework agrees with the wider range of vorticity and thinning estimates recorded in the high-temperature Senador Pompeu dextral shear zone, which are thought to result from varying offset rates of the interacting shear zones and could serve as a local transtension mechanism allowing emplacement of the Quixeramobim batholith. The post-collisional deformation of the northwest part of the Borborema Province is consistent therefore with lateral escape to the north of the Ceará Central domain, pluton emplacement along a conjugate set of a bulk transpressive shear system and, in the intervening stiffer crustal fragments, brittle fracturing and emplacement of dykes.

4.9 Acknowledgements

The authors would like to thank Ernst Willingshofer, Gustavo Viegas and an anonymous referee for their thorough and constructive reviews. We thank Antomat Macedo Filho, Alisson Oliveira and Daniel Do Valle Lemos-Santos for assistance with SHRIMP analyses. C. Ávila and C. Archanjo would like to thank the financial sponsorship from São Paulo Science Foundation (FAPESP, grants 2016/22226-9 and 2017/21440-0). C. Ávila is also thankful to the free software community of developers and users and in particular to the QGIS Geographic Information System Development Team. SHRIMP analysis data used in this study are available in Supporting Information[6], airborne geophysical survey data are available in the Brazilian Geological Survey database (http://geosgb.cprm.gov.br/), and CBERS4 stallite imagery are available at the database of the National Institute for Space Research of Brasil (http://www.cbers.inpe.br/).

[6] Appendix A

5 Shear zone cooling and fabrics of synkinematic plutons evidence timing and rates of orogenic exhumation in the northwest Borborema Province (NE Brazil)

Carlos F. Ávila, Carlos J. Archanjo, Maria Helena B.M. Hollanda, Antomat A. de Macêdo Filho, Daniel do V. Lemos-Santos

5.1 Abstract

Ediacaran convergence and collision resulting from amalgamation of West Gondwana are documented in the Borborema Province by high-pressure units, contractional tectonics and anatexis. Thermochronological (zircon U-Pb and amphibole-biotite Ar-Ar) and structural (Anisotropy of Magnetic Susceptibility) constraints from shear zone-bounding synkinematic plutons in the Ceará Central domain provide timing and rates of the subsequent post-collisional evolution in the northwest Borborema Province that characterises the orogenic collapse. Our results show that: (i) U-Pb ages of zircons of 585–571 Ma record magma crystallisation and a protracted history of assembly for the Tauá batholith, synchronous with deformation in the bounding trascurrent shear zone junction; (ii) AMS fabrics document chamber construction processes and the effect of long-lived shear zone deformation due to fast acquisition of structures in hybridized magmas; and (iii) $^{40}Ar/^{39}Ar$ plateau ages of amphibole and biotite from the synkinematic plutons at 577–562 and 559–554 Ma, respectively, yield cooling rates of 20–40 $^{\circ}C$/My characterising distinct cooling paths in the northwest Borborema Province. Integration of various thermochronometers available for the strike-slip shear zones and the internal high-pressure domain reveals a fast isothermal decompression episode (long-

term unroofing rate of 1.5–4.5 mm/y), which exhumed high-pressure rock units. Subsequently, fast, nearly isobaric cooling (20–40 °C/My) occurred in the whole terrane until 590 Ma, with temperatures falling below 320°C. Due to enhanced magmatic activity and deformation, the shear zones were kept at much higher temperatures at that same depth at 584 Ma, and later experienced fast cooling (20–40 °C/My) to temperatures below 320 °C at 560 Ma. These final cooling episodes were accompanied by slow unroofing at an estimated rate of 0.4–0.9 mm/y, sufficient to bring these rocks to the surface by 540 Ma, when molassic sequences were deposited.

5.2 Introduction

Deep cores of Precambrian orogens are thought to be exhumed to the surface by pervasive extension and thinning, ensuing from the gravitational collapse of mountain chains (Dewey, 1988). This process may be accelerated by erosional unroofing (Beaumont et al., 2001) and results in exhumation of high-pressure terranes of as much as 40000 km^2 (Kylander-Clark et al., 2012). In numerous Precambrian orogenic belts, the control of specific extensional structures in tectonic exhumation is difficult to ascertain (Mahan et al., 2003), and the history of orogenic collapse has a poor geological record. However, these processes leave a distinct temporal record in the P-T paths of rock units (Flowers et al., 2006) which are critical to understanding the timing and rates of continental shortening, tectonic unroofing and cooling (England and Molnar, 1990). Clockwise P-T-t histories, occasionally showing pulses of isothermal decompression followed by isobaric cooling, are typical of collisional settings, in which the final stages of orogenic deformation are dominated by major transcurrent shear zone deformation (Hollister et al., 1987). Therefore, shear zones that were active during unroofing and granitic plutons emplaced at that time are invaluable proxies to the operating deformation field during crustal extension (Archanjo et al., 2002; Paterson et al., 1998). The northwest Borborema Province is well suited to shed light on these unroofing mechanisms and histories, since it contains an association of transcontinental late-orogenic strike-slip shear zones, high-pressure terranes and the first record of deep continental subduction to the ultrahigh-pressure realm, along with its central African correlatives (Ganade de Araujo et al., 2014b).

Classically known for its major Ediacaran strike-slip shear zone network (Vau-

chez et al., 1995), the Borborema Province is part of a Neoproterozoic set of orogenic belts of Himalayan proportions formed during subduction and later amalgamation of Gondwana. Ávila et al. (2019) showed that the high-temperature strike-slip shear deformation in northwest Borborema province is well constrained at 584 ± 5 Ma under pressures of c. 5 kbar, while the internal high-pressure terrane was already a coherent strong unit. This internal domain is characterised by peak temperatures of 700–900°C at pressures of 8–13 kbar (Amaral et al., 2012; Arthaud, 2007) over more than 20000 km^2, with local occurrences of retrogressed eclogites that had peak metamorphic conditions of 17.3 kbar and 770°C, formed at c. 620 Ma (Ganade de Araujo et al., 2014b; Santos et al., 2009). The relation between the deformation within thrusts of the internal nappe system and the deformation of bounding strike-slip shear zones have been widely treated as synchronous (Caby and Arthaud, 1986). However, the mechanisms and rates of exhumation which allowed these contrasting metamorphic conditions to be arranged at the same structural level (i.e. how different terranes have been juxtaposed) are still unknown. A synthetic interpretation of the post-collisional evolution of the terrane has not been presented thus far.

In this study, we report a coupled structural-geochronological study of a late-collisional batholith and bounding strike-slip shear zones in the Ceará Central domain of northwest Borborema Province. U-Pb zircon dating of granitoids record a protracted history of pluton assembly at a shear zone junction setting, shown to be synchronous with deformation by a magnetic anisotropy survey (Anisotropy of Magnetic Susceptibility - AMS). $^{40}Ar/^{39}Ar$ data of mineral concentrates from syn-tectonic plutons reveal distinct cooling paths for different terranes. A thorough assessment of this new data set and existing knowledge allows us to better constrain the timing of shear zone activity and its relation to magmatism, the history of cooling and unroofing of the high-pressure nappe domain, and the origin of the structural architecture of this setting.

5.3 Geological setting

5.3.1 The Ceará Central domain

Formed in the Brasiliano orogeny due to diachronous collision between the São Francisco, West African and Amazonian cratons (Almeida et al., 1981; Ganade de

Araujo et al., 2014b), the Neoproterozoic Borborema Province of northeast Brazil occurs at a central location of West Gondwana (Figura 30). The Borborema Province is set in a mostly Transamazonian (Rhyacian) migmatitic-gneissic basement, surrounding a few Meso- to Neoarchean nuclei, and locally overlain by Late Proterozoic metasedimentary sequences (Ganade de Araujo et al., 2012; Hollanda et al., 2015; van Schmus et al., 2008). It is a widely known Ediacaran transcurrent shear zone system with profuse syn- to late-tectonic granitoid magmatism and high-temperature metamorphism (Vauchez et al., 1995), continuous with the Nigerian and Dahomeydes belts of western Africa (de Wit et al., 2008) in a pre-drift reconstruction and therefore forming shear zones with over 1000 km in length. Recent evidence also suggests the importance of the Borborema Province as being possibly the first instance where subduction of cold continental lithosphere leads to the formation of a Himalayan-style orogen (Ganade de Araujo et al., 2014b).

At the northern section of the Borborema Province, two major northeast-trending shear zones (Senador Pompeu and Transbrasiliano shear zones) occur enclosing the Ceará Central Domain (CCD, Figura 30). The Transbrasiliano lineament is part of a major suture zone extending to West Africa where several ultramafic complexes, eclogites and linear gravity anomalies occur (El-Hadj Tidjani et al., 1993). The oldest unit of the Ceará Central domain is composed of a Neoarchean greenstone-TTG association (Fetter, 1999). It is rimmed by supracrustal sequences of Paleo to Neoproterozoic ages (Arthaud et al., 2015; Costa et al., 2018; Santos et al., 2008). Subduction-related arc magmatism preceding the Brasiliano collision is recorded by the large Tamboril-Santa Quitéria arc, composed of migmatites, granites and calc-silicate enclaves (Ganade de Araujo et al., 2014a). A set of southwest-verging thrusts cut through the Proterozoic units and the base of the Tamboril-Santa Quitéria arc and forms the Ceará Central nappe system (Caby and Arthaud, 1986). These thrusts are characterised by high-temperature shear zones with flat-lying foliations. High-pressure granulites (over 700°C and c. 10 kbar) occur over large areas of the Proterozoic supracrustal sequences (indicated in Figura 30; Amaral et al., 2012; Arthaud, 2007; Silva, 2017) with a range of metamorphic ages averaging at 610 Ma (Amaral et al., 2012; Arthaud, 2007; Castro, 2004). Pods of retrogressed eclogites with pressure estimates of 17 kbar and relict textures indicating previous stable coesite (Amaral et al., 2012; Santos et al., 2009) occur within the high-pressure granulite belt of Cariré. Metamorphic ages of about 620 Ma for the retrogressed eclogites are

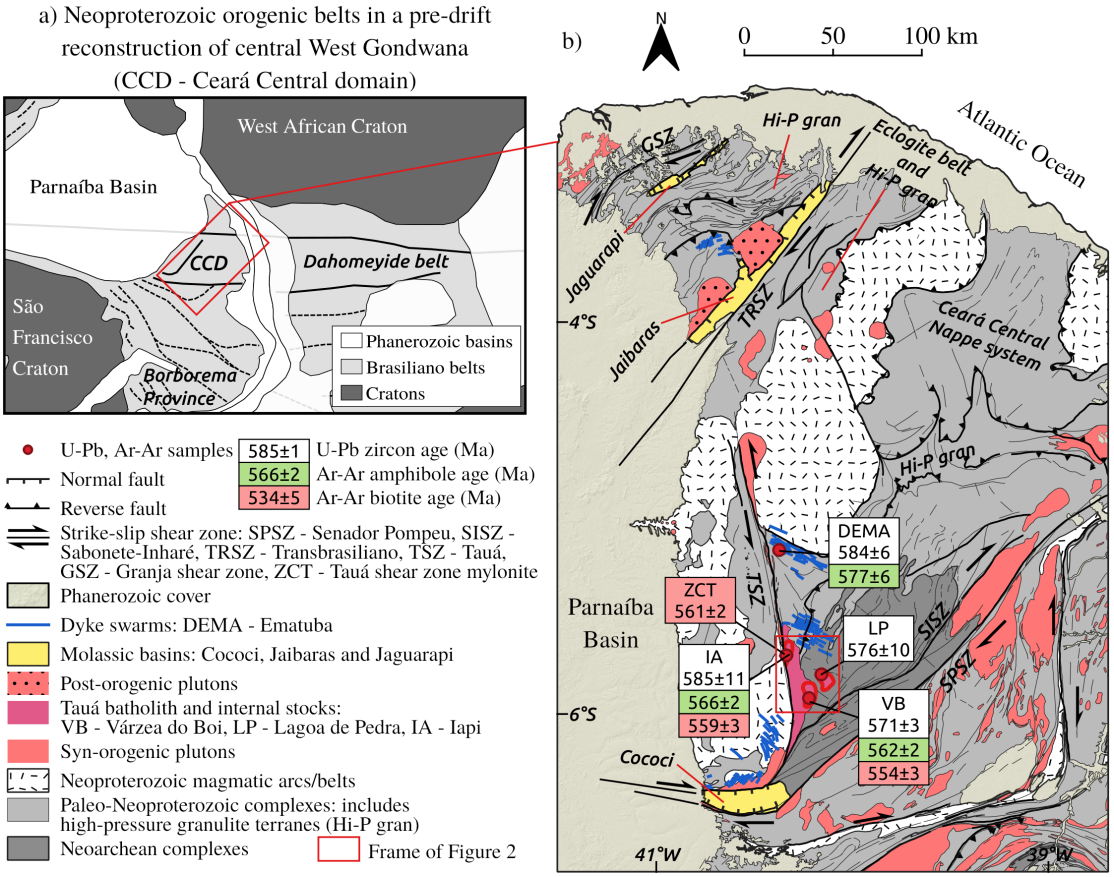

Figura 30 – a) Central West Gondwana. Red frame gives location of b). Note that the map is rotated c. 45° clockwise relative to the true north of b). b) Geological map of the Northwest Borborema Province. Red inset shows location of Figura 31.

thought to mark continental collision within the northwest Borborema Province, and the west African correlatives (Ganade de Araujo et al., 2014).

5.3.2 The interacting Senador Pompeu and Tauá shear zones

In the Ceará Central Domain, late-collisional strike-slip deformation occurred in the interacting Senador Pompeu (SPSZ), Tauá (TSZ) and Transbrasiliano shear zones (Figura 30), which cross-cut all the Precambrian basement. High temperature deformation at 584 Ma is recorded for both shear zones by the syn-kinematic emplacement of granitoid plutons (Ávila et al., 2019) and hypabyssal dykes, indicating their conjugate

character. Flat-lying foliations of the internal terranes are transposed and form progressively tighter upright folds approaching the strike-slip shear zone segments. The crustal-scale dextral SPSZ strikes NE for some 300 km and is possibly continuous with the Ile-Ife shear zone of the Nigerian belt. Vertical foliations and mostly horizontal lineations occur at the core of SPSZ. High temperature gneissic mylonites are prevalent at the northern segments and are gradually overprinted by low-temperature deformation to the south. The dextral Sabonete-Inharé shear zone (SISZ) occurs northwest of SPSZ and at the same orientation, merging with the sinistral Tauá shear zone (TSZ) at its southern termination. The TSZ strikes NNW for 100km until its abrupt northwards termination on the Transbrasiliano lineament. The vertical foliations and horizontal lineations of TSZ occur on rocks deformed at various conditions, from high-temperature mylonitisation to cataclastic deformation. The TSZ is also characterised by abundant syn-kinematic granitoid sheets occurring in most of its length and at depth as indicated by geophysical evidence (Oliveira and Medeiros, 2018). At the intersection of the SPSZ and TSZ the Tauá diorite-granite magmatic suite occurs, containing the Várzea do Boi and Lagoa de Pedra stocks in addition to other concentric intrusions. At the trailing end of the SPSZ-TSZ junction, a dextral closing zipper is formed by their interaction (Ávila et al., 2019). Due to the unique relation of the Tauá batholith and its internal stocks with the conjugate shear zone junction of TSZ, SISZ and SPSZ, they provide a proxy to the characteristics of deformation at the time of its emplacement. This zippered shear zone, called the Cococi branch, is buried by the Paleozoic pull-apart Cococi basin (Figura 30).

5.4 Results

5.4.1 Field relations and petrography

The Tauá magmatic suite consists of a north-elongated 650 km^2 granite-diorite association sharply bound to the west by the Tauá shear zone and limited to the southeast by the Sabonete-Inhará shear zone (Figura 30). The batholith tapers to the south approaching the shear zone junction. It intrudes mostly metasedimentary and gneissic sequences of Proterozoic age, locally interleaved with greenstone associations of the Neoarchean basement to the south. Separate stock-sized plutons occur within the batholith as revealed by concentric layering and structures (red outlines within the Tauá suite

in Figura 30b). The Várzea do Boi stock (Figura 31) located at the eastern margin of the suite displays a mostly bimodal distribution of dark grey aphyric fine-grained diorites and coarse-grained syenogranites, with an off-centre concentric layering. Contacts may be abrupt between two large areas of either facies or may occur as decimetre-scale intercalations. Frequently, the contacts are compositionally gradational and occur as a hybridized facies characterized by the porphyritic texture of 1-2 mm rapakivi feldspar, biotite-hornblende phenocrysts and glomerocrysts, and quartz ocelli set in an aphanitic granodioritic matrix (Figura 32a). The western margin of the stock is also gradational into the Tauá diorite, whereas the eastern margin contains significant amounts of gneiss xenoliths from the country rocks to the east.

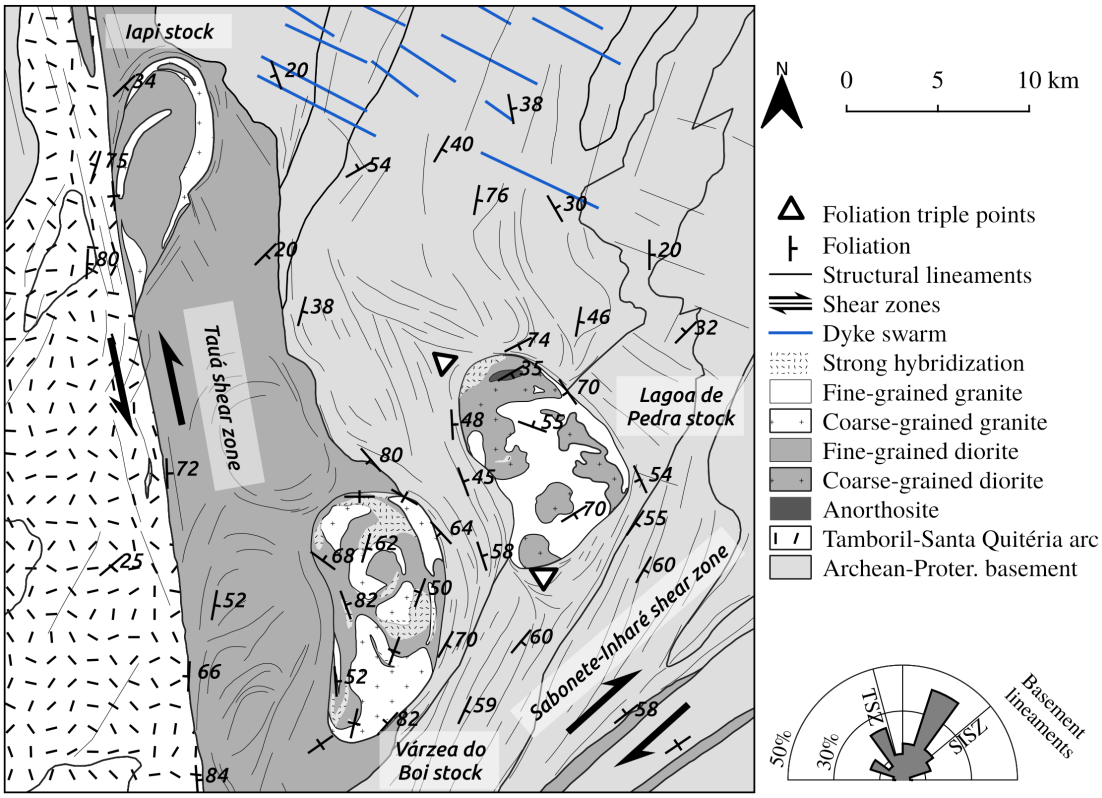

Figura 31 – Geological map of Várzea do Boi (VB) and Lagoa de Pedra (LP) stocks within the Tauá magmatic suite. Polar histograms are given for the different subsets of structural lineaments. Strike of Tauá (TSZ) and Sabonete-Inharé (SISZ) are given for reference. See location in Figura 30b.

Outside of the suite occurs the cogenetic Lagoa de Pedra stock. It similarly displays

a bimodal facies distribution, though mostly between coarse-grained diorites and fine-grained muscovite-bearing leucogranites. Contacts between the facies are also variable but hybridization is less intense relative to Várzea do Boi stock. Migmatitic gneiss enclaves occur in variable sizes (up to 100m long). The largest xenoliths occur at the centre of Lagoa de Pedra stock and strike northeast with a large dip, concordant with the surrounding basement. Coarse-grained anorthosites (c. 85% plagioclase, An_{47}) also occur at the northern Lagoa de Pedra, with adcumulus texture of a euhedral plagioclase framework surrounded by pyroxene with tiger-symplectitic intergrowths with oxides (Figura 32b). Anorthosites grade laterally through coarse-grained gabbro to coarse-grained diorite.

All facies in both stocks are aphyric and massive (i.e. with very weakly developed mineral alignment foliations), except for local occurrences of trachytic texture, where feldspar and hornblende crystals have a prominent shape preferred orientation (Figura 32c). Feldspar is euhedral to subhedral with well-developed zoning, whereas quartz is anhedral and equant, with only incipient undulose extinction. Kinking in biotite is rare and hornblende forms euhedral to subhedral stubby prisms. Measurements of foliation were possible in only a few sites, revealed by preferred elongations of the granitic veinlets around diorites or of cusps in corrugated contacts that are more prominent in one specific direction. Furthermore, the exposure of the stocks lies in a low-relief erosion surface with poor 3-dimensional information, increasing the importance of Anisotropy of Magnetic Susceptibility as a reliable proxy for the magmatic fabric. For the Várzea do Boi and Lagoa de Pedra stocks foliations and structural lineaments (interpreted from satellite imagery) are also concentric and only locally cross-cut layering. Basement structures around the stocks are oriented parallel to the Tauá and Sabonete-Inharé shear zones, and wrap around the plutons, forming foliation triple points (Brun and Pons, 1981, Figura 31).

Hybridization is a ubiquitous feature of this suite and occurs either as comingling of contrasted magmas, or as partial mixing and homogenization forming an intermediate facies (Figura 32d, Bateman, 1995). Since one facies usually predominates, the lithological map of Figura 31 presents areas of intense hybridization as a stippled pattern overlay. The fine-grained diorite suite occurs frequently as pillows surrounded permeated by granitic veinlets (Figura 32e, Wiebe, 2016), though the same outcrops may show stockworks of the granite magma through the diorite facies (Figura 32f). Comagmatic

granite-diorite relations are exhibited by small-scale diapirism emerging from the walls of granitic veins (Figura 32g) and corrugated contacts (Figura 32h). Where the coarse-grained syenogranite dominates, hybridization features are subordinate, mainly occurring as decimetre-sized enclaves of the porphyritic hybrid granodiorite (Figura 32i). Coarse-grained diorites may present mingling relations with both fine-grained diorite and granite, but is more frequently found as angular metre-scale blocks amidst the mingled diorite-granite association (Figura 32j). The anorthosites are comparatively homogeneous and free of enclaves.

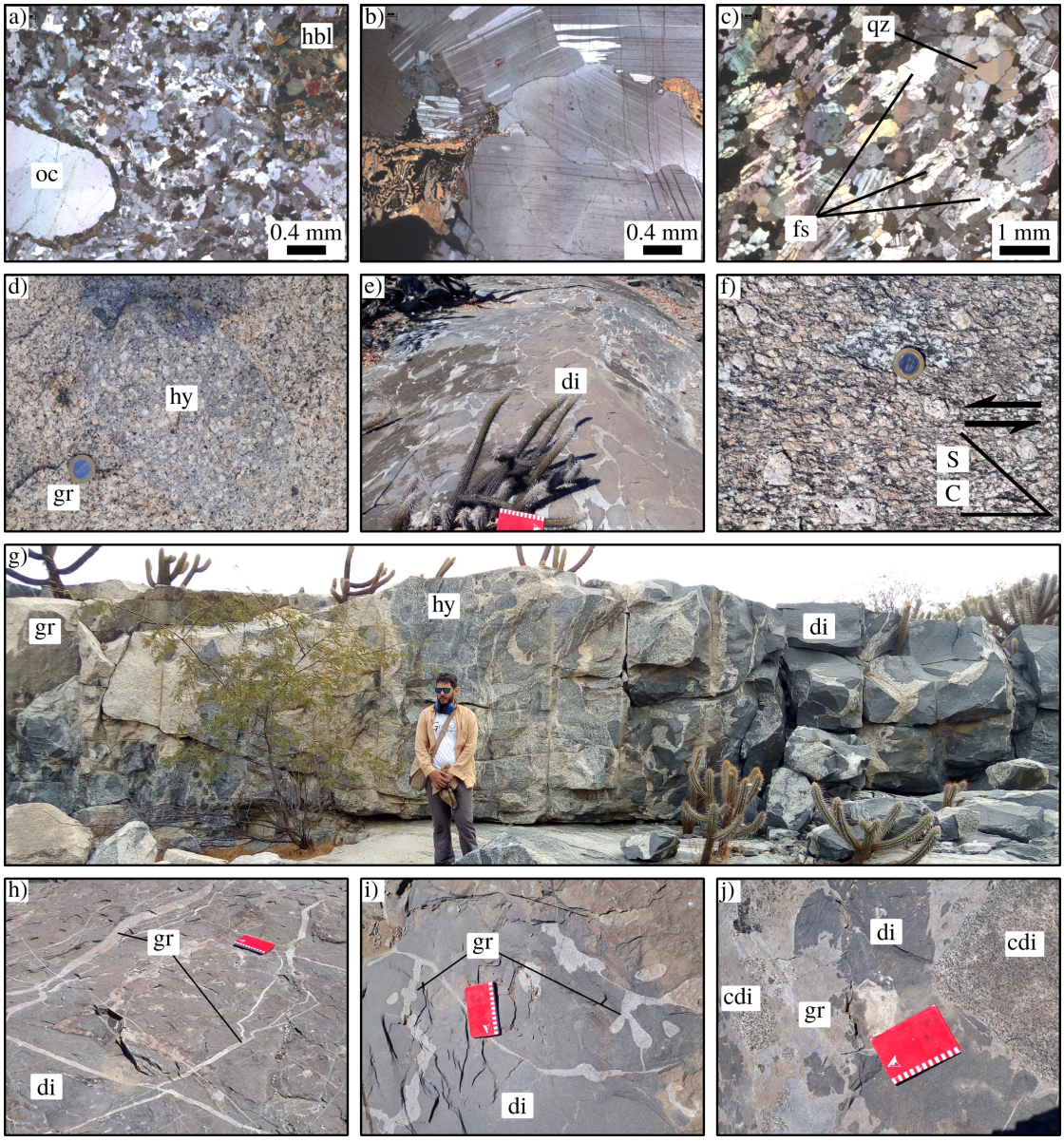

Figura 32 – Field relations in the Várzea do Boi and Lagoa de Pedra stocks and micrographs. a) Micrograph of fine-grained diorite facies showing pronounced trachytic texture of feldspar laths (fs) and oriented hornblende while quartz (qz) is equant and undeformed. b) Micrograph of hybrid facies showing hornblende clot (hbl) and ocellar quartz (oc) with hornblende reaction rim. c) Micrograph of anorthosite showing adcumulus texture with tiger-symplectite in pyroxene. d) Comingling of diorite (di) and granite (gr) facies with a vertical zone of hybridization (hy) in between. e) Intramagmatic flow of diorite (di) in granite (white seams). f) Fracture stockwork within diorite (di) filled with granite melt (gr). g) Microdiapirism of granitic melt (gr) frozen in its dioritic substrate (di). h) Small-scale convolutions in contact between mingled granite (gr) and diorite (di). Compass for scale. i) Hybrid (hy) enclave within coarse-grained granite (gr). Coin for scale. j) Coarse-grained diorite (cdi) blocks enclosed in comingled fine-grained granite (gr) and diorite (di).

5.4.2 Magnetic fabrics

5.4.2.1 Magnetic mineralogy

We extracted oriented cores in 54 sites in the Várzea do Boi and 35 in the Lagoa de Pedra stocks (Figura 33) using a gasoline powered mechanical drill. The number of drills per site varied but an average of four was sought, each drill being about 8 cm long. An even distribution of sites was not possible due to restricted access to some areas. Specimens of standard size (2 cm high by 2.2 cm in diameter) were then cut yielding about 10 oriented specimens per site (total of 1005).

Analyses of Anisotropy of Low-Field Magnetic Susceptibility (AMS) was conducted on a MFK1 automated Agico Kappabridge under low inducing field (A/m) operating at a frequency of 900 Hz. The distribution of bulk susceptibility (K) in the stocks is shown in Figura 33. For the Várzea do Boi stock a rough correlation can be seen between areas of high K and coarse-grained granites mostly at pluton margins. This facies has a large range of K values with a mode of 0.25 mSI. The fine-grained diorite, however, shows a lower spread around a mode of 0.55 mSI. In the Lagoa de Pedra stock, the highest K values occur for the coarse-grained diorite (mode of 0.65 mSI), whereas the fine-grained granite has a mode of 0.05 mSI. Hybridized facies have a K distribution similar to that of the coarse-grained granite. The anorthosite has a K of 34 mSI.

Magnetic mineralogy is interpreted from the dependence of susceptibility with temperature (K-T) and Isothermal Remanent Magnetisation (IRM) acquisition curves, shown in Figura 34. Three groups were then arranged from measurements carried out for two samples of the six different facies. Facies characterized by a mostly low susceptibility ($K < 0.25$ mSI; hybrids, coarse-grained and fine-grained granites) display a prominent Verwey transition (Moskowitz et al., 1998) at about -150°C, and a distinct drop in K at 580°C, typical of pure stoichiometric magnetite. The smooth bell-shaped curve of decreasing susceptibility on heating following the magnetite Curie point at 585°C is attributed to low amounts of Ti-poor titanohematite. A progressive increase in susceptibility on heating above c. 400°C and the higher susceptibilities of the cooling curve indicate formation of new magnetite due to high-temperature alteration of Fe-bearing silicates. Over 95% of IRM is acquired at fields below 200 mT, indicating low coercivity magnetite, but full saturation is not reached until 2.5 T.

In thermomagnetic curves for coarse and fine-grained diorites (Figura 34), low-

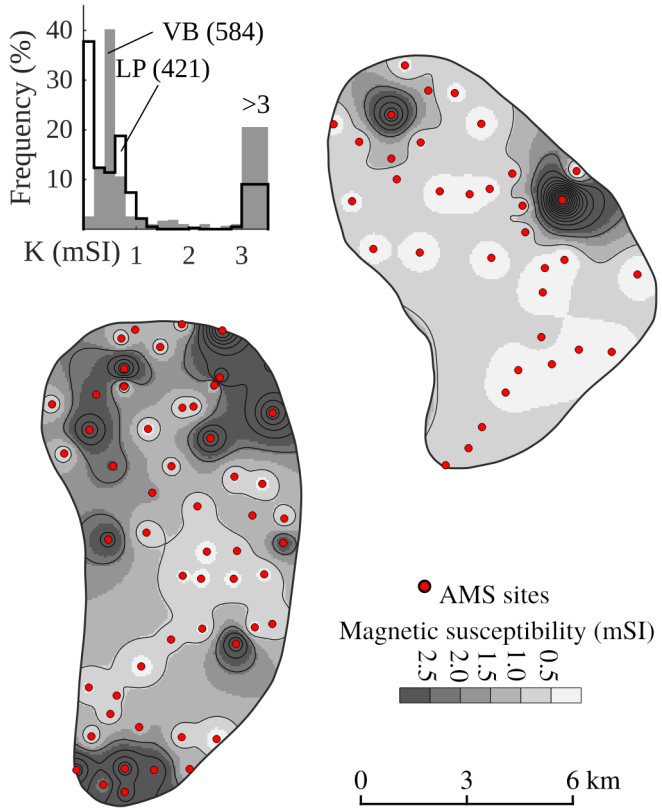

Figura 33 – Locations of Anisotropy of Magnetic Susceptibility (AMS) sites for Várzea do Boi (VB) and Lagoa de Pedra (LP) stocks and distribution of bulk susceptibility. Inset shows susceptibility histogram.

temperature transitions are absent. The peak in susceptibility just before the magnetite Curie point (580°C), where there is a full drop, is due to the formation of magnetite on heating. The high-temperature curve is irreversible. At room temperature the susceptibility is higher than the initial susceptibility on heating. About 95% of IRM is acquired by 300 mT but full saturation is not reached until 2.5 T. The high field part of the IRM curve for granites has is steeper, suggesting that diorites have higher amounts of coercive phases.

The anorthosite shows a subdued low-temperature transition around -150°C, possibly due to non-stoichiometry of magnetite (Özdemir et al., 1993). Susceptibility is decreased to nearly zero at the magnetite Curie point. IRM acquisition curve is similar to that of granites, with nearly full saturation at 300 mT and a shallow increase in IRM

up to maximum applied field (2.0 T).

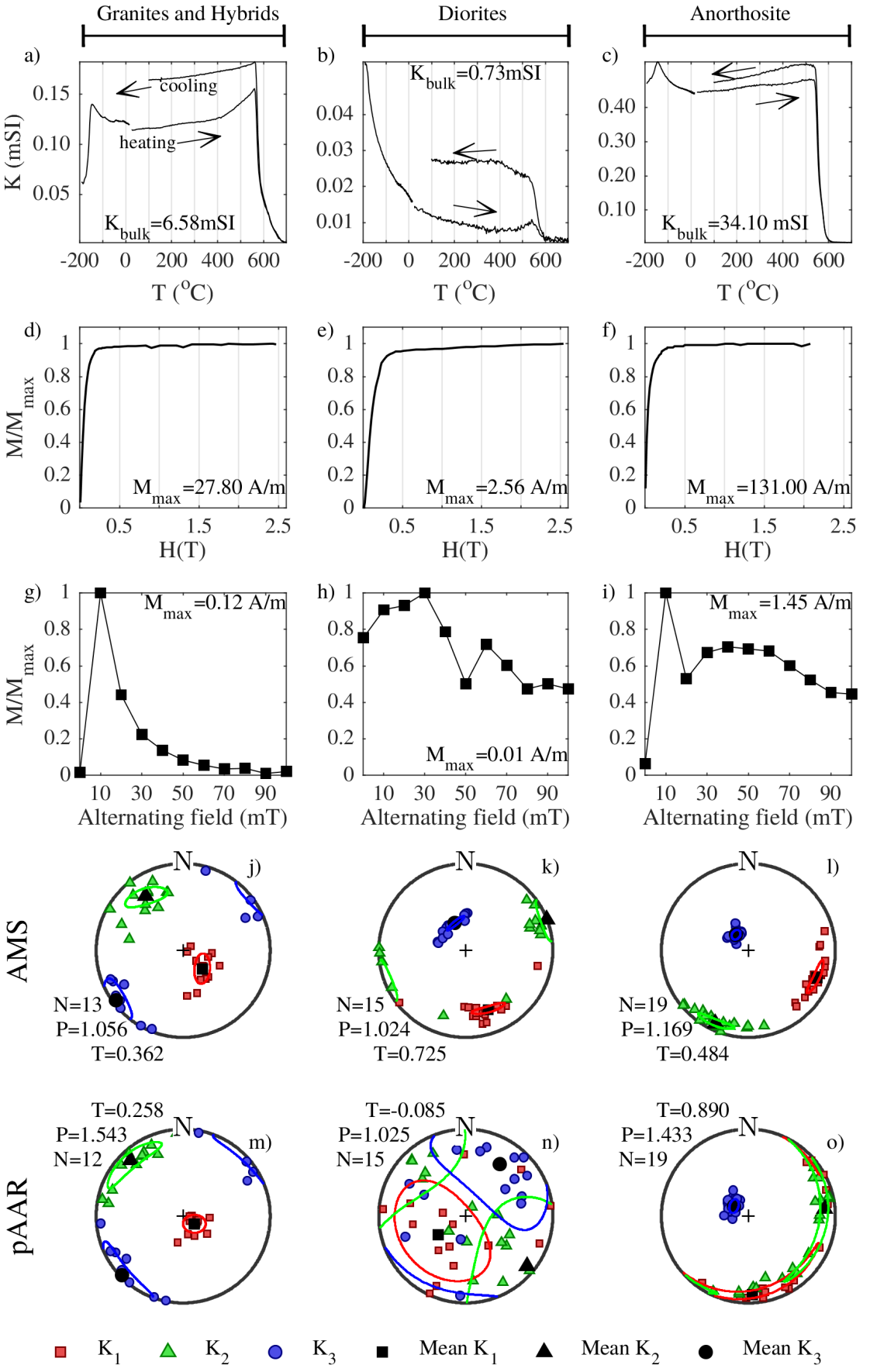

Figura 34 – Representative rock magnetic properties and fabrics for the Várzea do Boi and Lagoa de Pedra plutons.

5.4.2.2 Anisotropy of magnetic susceptibility (AMS) and Anhysteretic Remanence (AAR)

Principal directions of low-field AMS were determined following the (Jelínek, 1978) procedure. The second-rank AMS tensor has three principal directions of susceptibility ($K_1 > K_2 > K_3$) where K_1 is the magnetic lineation and K_3 is the pole to the magnetic foliation (Figura 35). The 2σ angular uncertainty around either K_1 or K_3 is lower than 10° for 67% of all sites, and is below 20° for 85%. Geometrical characteristics of the AMS tensor can be described by an ellipsoid and summarised by the degree of anisotropy $P = K_1/K_3$, and shape parameter $T = (\ln K_2/K_3 - \ln K_1/K_2)/(\ln K_2/K_3 + \ln K_1/K_2)$, where $0 < T \leq 1$ for oblate and $-1 \leq T < 0$ for prolate ellipsoids, respectively. P is lognormally distributed for both stocks, with a mean of 5.9% for the Várzea do Boi and 4.8% for the Lagoa de Pedra. T values show two peaks for the Várzea do Boi stock at 0.3 and -0.3, with a mean of 0.2 (triaxial to slightly oblate). The Lagoa de Pedra stock has a unimodal distribution of T around a mean of 0.4. Variations of P and T between facies are of lesser significance but diorites generally have higher average degrees of anisotropy (by up to 3%) relative to granites. Examples of representative AMS tensors are given in Figura 34. The data table is given in the Supplementary Material[1].

Magnetic foliations for the Várzea do Boi stock mimic its concentric structure. This is matched by a moderately defined horizontal girdle in stereographic projections of Figura 35. A distinct foliation pole maximum can be identified that indicates a steep subset of foliations (dips above 60°) with a mean NNE strike and dips to ESE. A secondary near-vertical foliation pole maximum corresponds to flat-lying foliations (dips less than 20°) which occur at the centre of concentric layering with outwards radial dips. The strikes of foliations are mostly concordant with granite-diorite contacts, particularly in the northern end of the stock. In the southern end of the stock, magnetic foliations cross-cut the magmatic contacts and are concordant with basement structures. Magnetic lineations also vary gradually between different sites, and exhibit a more distinct bimodality, with one steeply plunging subset and a gently plunging NE-trending subset that cross-cuts magmatic contacts. Hence the variations of lineations do not resemble a concentric distribution.

Magnetic foliations for the Lagoa de Pedra stock are more disperse, with K_3 maxima

[1] Appendix B

at various orientations. Most foliation strikes are approximately concordant with magmatic contacts and stock-basement contacts in the plutons northern half and are often discordant in the southern half. Lineations for the Lagoa de Pedra also form a maximum close to vertical and a NNE trending girdle, though more disperse relative to the Várzea do Boi stock. A few sites at which mingled granite and diorite were sampled showed differences in orientations of K_1 or K_3 between the facies, but overall there is no facies-specific preferred orientation.

Anisotropy of magnetic remanence was investigated in selected representative sites of all facies in order to resolve composite fabrics and investigate the contribution of fine-grained single-domain magnetite (Potter and Stephenson, 1988). Samples demagnetised in alternating fields of up to 100 mT were imparted with low anhysteretic remanent magnetisations (ARM) in appropriate windows of coercivity (pARM; Jackson, 1991). Windows of coercivity over which the bias field of 100 µT was applied were determined after inspection of coercivity spectra (Figura 34; Jackson et al., 1988). Most remanence carrying grains of granites and the hybrid facies have maximum coercivities within 30 mT, above which remanence was minor. For anorthosites, a similar set of grains occurs within the 0–30 mT range, but a distinct increase of ARM occurs after 40 mT forming a plateau up to 80 mT. Coercivity spectra vary strongly for diorite sites, often showing multiple peaks of magnetisation, or a single flat curve. In most cases, the most important grain population has coercivities of up to 40 mT, followed by other subpopulations. Therefore partial Anisotropy of Anhysteretic Remanent Magnetisation (pAAR) was carried out for different facies on the 0–30 mT range of coercivity.

pAAR was imparted and measured in 6 different directions following standard procedures and resulting tensors are given in Figura 34. Principal directions of pAAR tensors of granite and anorthosite sites are closely coaxial with principal directions of AMS (Figures 34j and l) discarding, therefore, the effect of inverse fabrics in AMS results (Rochette et al., 1999). Degrees of anisotropy are increased by up to 50% for granite sites and about 30% for the anorthosite site, while the shape parameter is changed slightly. In contrast, the diorite site has a poorly constrained pAAR tensor not coaxial with the corresponding AMS tensor (Figura 34k). The diorite differs from granite and anorthosite by its lower mean susceptibility and absence of Verwey transition suggesting, therefore, that the magnetocrystalline anisotropy of the paramagnetic silicates dominate AMS.

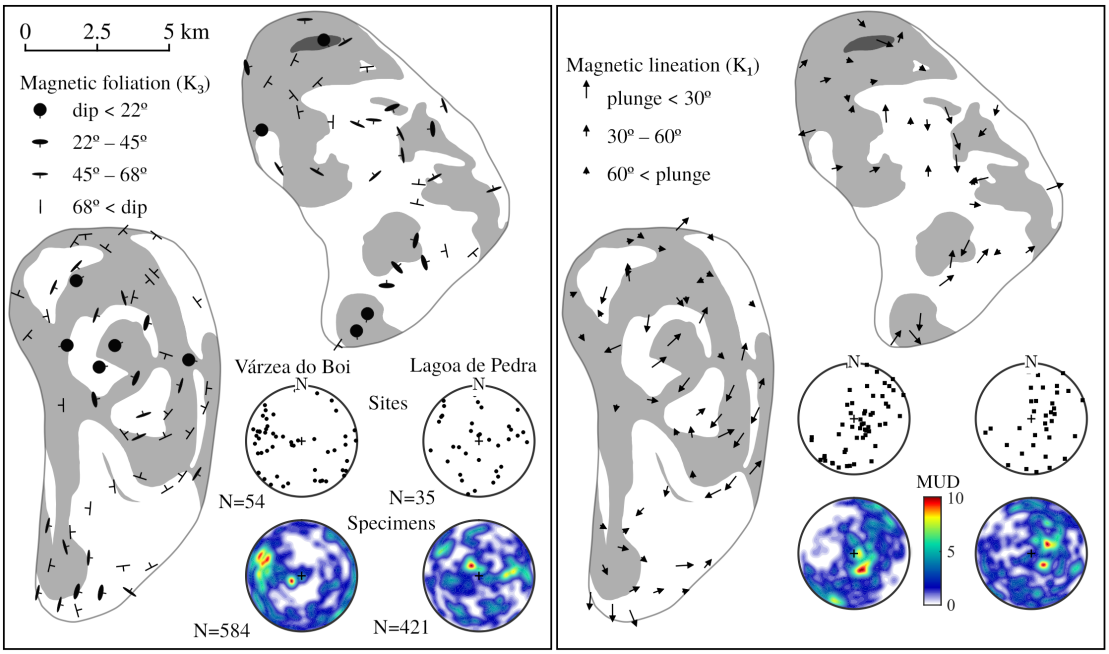

Figura 35 – Map of magnetic foliation (normal to K_3) and lineation (K_1) for the Várzea do Boi (VB) and Lagoa de Pedra (LP) stocks. Stereographic projections are equal area and lower hemisphere. Data for sites are plotted as scatter, whereas full set of measured specimens is plotted as density contouring (in multiples of uniform distribution, MUD).

5.4.3 U-Pb SHRIMP geochronology

Zircons crystals for geochronological analyses were recovered from crushed 2-5 kg fresh samples after standard procedures of magnetic, hydraulic and density separation methods. The crystals were then mounted in epoxy resin and polished for cathodoluminescence imaging. From such images, appropriate crystals with magmatic zoning were targeted for analysis to obtain crystallization age. Zircons with inclusions, fractures, recrystallization textures, cores or signs of metamictization were avoided. U-Pb analyses were conducted in Sensitive High-Resolution Ion Microprobe (SHRIMP) at the SHRIMP IIe facility of *Universidade de São Paulo*. Isotopic data were collected in five sets of scans through the masses and TEMORA 1 reference zircons (Black et al., 2004) were analysed after every four unknowns (details in Sato et al., 2014). Data reduction was performed in SQUID 2.5 (Ludwig, 2009). The ages calculated are presented with 2σ uncertainties. Data tables and cathodoluminescence images of zircons are given in

the Supplementary Material[2].

Two analytical experiments were carried out on zircons extracted from the fine-grained dioritic facies of the Várzea do Boi stock. The first experiment was carried out on zircons from the sample VB1A resulting in a large scatter of concordant ages, a reason that led us to perform a second experiment with zircons extracted from the sample CA-124, collected within the same petrographic facies. Both samples have a mineral assemblage and textures equivalent to those described in the previous section for the diorite facies. Their extracted zircons have an average grain size (long axis) of c. 150 μm and an aspect ratio of 2.3–2.6:1. Cathodoluminescence images reveal that zircon crystals from sample VB1A are euhedral to subhedral, have pronounced concentric oscillatory zoning and a moderate amount of apatite inclusions. Fractures, areas of convoluted zoning, xenocrystic cores, and areas of overgrowth or recrystallization (Corfu, 2003) are rare. Spots were focused on areas of strong concentric zoning closer to grain margins and away from areas of irregular zoning, fracturing or recrystallization. Zircons from sample CA124 are subhedral and mostly characterised by sector zoning parallel to the long dimension. They may also contain convolute zoning or unzoned homogeneous domains. The spot analyses were focused in crystals with stronger oscillatory zoning, mostly near grain margins and away from areas of convolution, recrystallization or fracturing.

Single grain $^{206}Pb/^{238}U$ ages corrected for ^{204}Pb for sample VB1A range between 557 and 616 Ma, with three disparate ages of 637, 652 and 653 Ma. A concordia age cannot be calculated from the main range of ages, in which two coherent subsets are identifiable, one between 557 and 585 Ma, and another between 589 and 616 Ma (see Kernel probability distribution in Figura 36a). Th and U contents were fairly homogeneous, and a few analyses showed high content in common Pb though no correlation with ages is apparent. Sample CA124 has single grain $^{206}Pb/^{238}U$ ages ranging between 567 and 604 Ma, from which a concordia age could not be calculated. For sample CA124, Th, U and common Pb contents were homogeneous. Despite the significant textural differences described from cathodoluminescence images, sample CA124 displays a bimodal age distribution similar to that of VB1A, with one younger coherent group having ages between 567 and 576 Ma and an older coherent group with ages between 586 and 604 Ma (Figura 36a).

[2] Appendix B

A sample collected from the fine-grained granite facies of the Lagoa de Pedra stock provided zircons with an average grain size of 157 μm and an aspect ratio of 2:1. These zircons are euhedral with some broken pyramidal terminations (see cathodoluminescence images in Supplementary Material[3]), and also exhibit pronounced oscillatory concentric zoning, with minor overgrown rims. Irregular inclusion, xenocrystic or metamict cores, and domains of convoluted zoning are common; these were avoided during spot analysis, which was focused on domains of oscillatory zoning. This zircon population (15 spots) have $^{206}Pb/^{238}U$ ages ranging between 544 and 606 Ma, with a concordia age of 576 ± 10 Ma (MSWD 2.7, Figura 36c), concordant with a weighted average age of 573 ± 10 Ma (MSWD = 0.70). No analysis showed spurious values of Th, U or common Pb.

The Iapi stock sample consists of unaltered diorite containing accessory apatite, magnetite and zircon. Zircons retrieved have an aspect ratio of 2.5:1 and an average grain size of 164 μm. Cathodoluminescence images reveal oscillatory zoning domains parallel to their long dimensions most prominently developed towards the rims, whereas the cores are fairly unzoned and homogeneous. No abrupt transition or truncated zoning exist between cores and rims. Fractures, inclusions, xenocrystic cores and domains of convoluted zoning or recrystallization are scarce. Single grain $^{206}Pb/^{238}U$ ages for Iapi zircons range between 547 and 617 (15 spots), and the concordia age calculated is 585 ± 11 Ma (Figure 7). This is concordant with a weighted average age of 584 ± 11 Ma (MSWD = 0.87), taken as a reliable estimate of magma crystallization. Spurious values of Th, U or common Pb do not occur.

[3] Appendix B

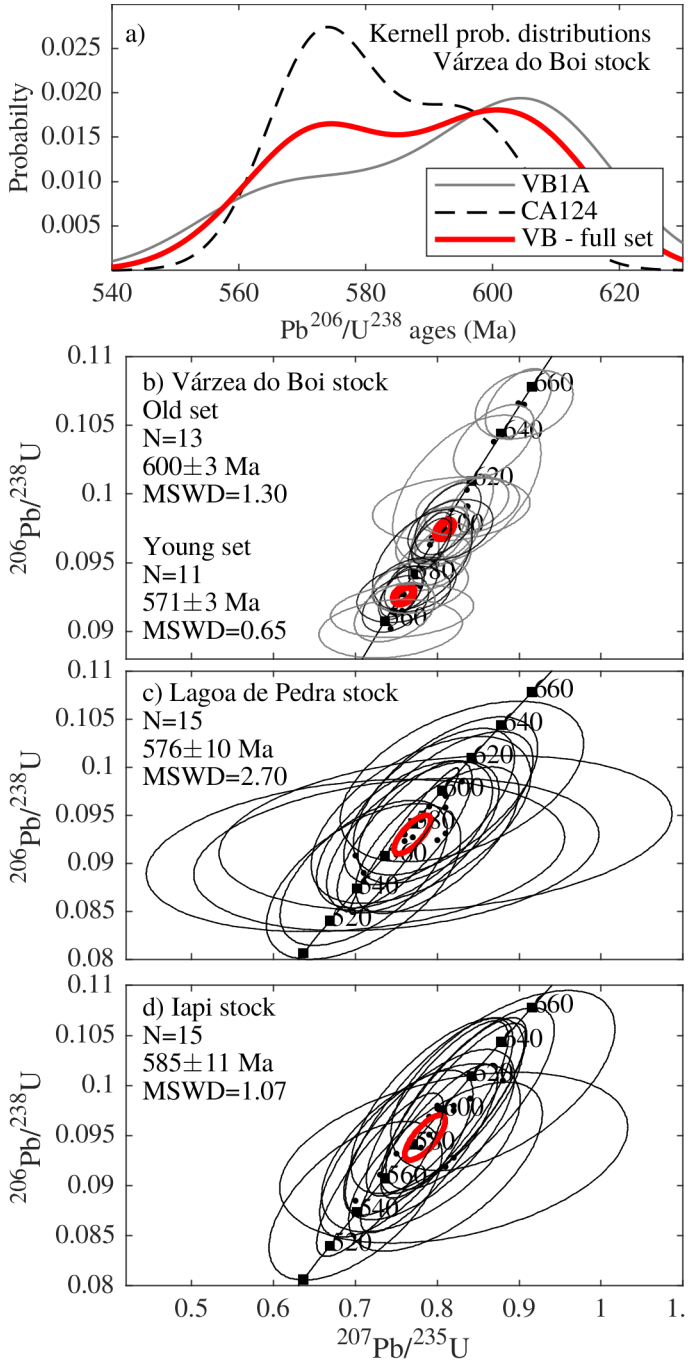

Figura 36 – a) Kernel probability distribution of $^{206}Pb/^{238}U$ for two replicate U-Pb SHRIMP analyses (samples VB1A and CA124) of the diorite facies from Várzea do Boi stock, and their combined distribution. b) U-Pb concordia diagram for the two combined replicate analyses of the Várzea do Boi stock. Legend as in a). c) U-Pb concordia diagram for the Lagoa de Pedra stock. d) U-Pb concordia diagram for the Iapi stock. All ellipses and ages at 2σ uncertainty. Concordia ages in red.

5.4.4 $^{40}Ar/^{39}Ar$ thermochronology

Multigrain concentrates of hornblende and biotite for $^{40}Ar/^{39}Ar$ dating were irradiated along with the Fish Canyon sanidine in the TRIGA nuclear reactor using the CLICIT facility at Oregon State University (OSU). The analytical experiments were performed by incremental heating gas extraction using a solid state Nd-YVO4 laser (532 nm) coupled to a ARGUS VI mass spectrometer (Thermo Scientific) at the *Laboratório de Geocronologia de Gases Nobres* (*Centro de pesquisas em Geocronologia e Geoquímica Isotópica, Universidade de São Paulo*). Gas purification before mass spectrometry is made through a commercial prep system equipped with Zr-Al getters. All masses were simultaneously measured in Faraday detectors equipped with amplifiers that are fitted with 1011 ohm (for ^{40}Ar) and 1012 ohm (for ^{39}Ar, ^{38}Ar, ^{37}Ar, ^{36}Ar) resistors. The ArArCALC v2.6e software package (Koppers, 2002) was used for data reduction including corrections for interference nucleogenic reactions, atmospheric contamination and mass discrimination. All $^{40}Ar/^{39}Ar$ ages were measured relative to the flux monitor standard FC-1 sanidine by assuming the age of 28.01 ± 0.04 Ma (Phillips and Matchan, 2013) with J values given in the Supplementary Material[4]. Plateau ages are the weighted (by inverse variance) means of at least three sequential and concordant (at 2σ level) apparent ages that represent $\geq 50\%$ of the total ^{39}Ar released during the heating experiment. $^{40}Ar/^{39}Ar$ results are given in the Supplementary Material[4] and age spectra are presented in Figura 37.

One hornblende $^{40}Ar/^{39}Ar$ analysis was carried out for the Ematuba dykes. In thin sections, hornblende from those samples occurs as inclusion-free dark green and euhedral phenocrysts in an aphanitic dacitic matrix. Biotite is an accessory phase. A broadly flat age spectrum was obtained for the intermediate temperature range, while a distinct saddle shape is evident from the low temperature steps (Figura 37a). The shape of the age spectra match K/Ca spectra (not shown), with high values in low temperature steps that fall and flatten through the intermediate temperature steps, indicating compositional variations control changing isotope ratios. A plateau age of 577 ± 6 Ma (MSWD = 1.2, Figura 37a) can be calculated for 75% of the released gas (total gas age of 583 ± 4 Ma). The discordant (older) total fusion ages and a saddle-shaped plateau for the lower temperature steps is likely a result of excess Ar and places this as a maximum cooling

[4] Appendix B

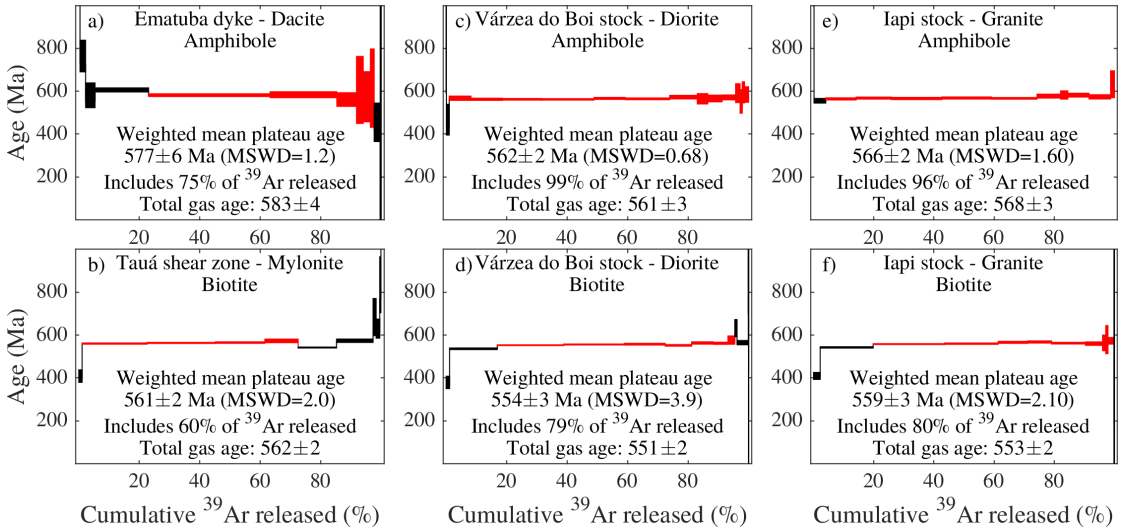

Figura 37 – Ar-Ar ages for amphibole and biotite mineral separates for the studied plutons. a) Ematuba dyke, amphibole, b) Tauá shear zone mylonite, biotite, c) Iapi stock, amphibole, d) Iapi stock, biotite, e) Várzea do Boi stock, amphibole, f) Várzea do Boi stock, biotite. Height of bars and uncertainty are given at 2σ level. Steps forming a plateau are highlighted in red.

age estimate.

One biotite concentrate from protomylonitic rocks of the Tauá shear zone was also analysed. It yielded a flat age spectrum for nearly 90% of the released ^{39}Ar in the mid-temperature range (Figura 37b), with a plateau age of 561 ± 2 Ma (MSWD = 2.0) calculated for 60% of the released gas. This age is concordant with total fusion and isochron ages. Given the very homogeneous K/Ca spectrum, younger ages in the low-temperature steps are likely a result of minor Ar loss. Thus 561 ± 2 Ma is considered a reliable cooling age of biotite.

Hornblende and biotite multigrain concentrates were extracted from the dioritic facies of the Várzea do Boi stock. The hornblende concentrate produced flat age and K/Ca spectra with a well-constrained plateau age of 562 ± 2 Ma (MSWD = 0.7) calculated for 99% of released ^{39}Ar (Figura 37c), concordant with total fusion and isochron ages. The biotite concentrate for the same sample yielded a flat age spectrum, except for the slight saddle shape of the low-temperature heating steps (Figura 37d). This spectrum is not matched by the corresponding highly irregular K/Ca spectrum. However, 79% of released ^{39}Ar in the intermediate and high-temperature steps produced a reliable plateau age

of 554 ± 3 Ma (MSWD = 3.9), concordant with ages obtained from both total fusion and normal isochron plots. Thus given the possibility of some Ar loss this provides a minimum estimate of cooling age of biotite.

The hornblende concentrate from Iapi displays a saddle-shaped K/Ca spectrum, particularly for the low-temperature steps, despite yielding a remarkably flat age spectrum (Figura 37e). Total fusion and normal isochron ages are concordant, with a plateau age of 566 ± 2 Ma (MSWD = 1.6) calculated from 96% of ^{39}Ar released, taken as a reliable estimate of cooling age. The biotite concentrate from the same sample produces a flat K/Ca spectrum, broadly matching the age spectrum for which lower ages were obtained in the low-temperature heating steps. A plateau age of 559 ± 3 Ma (MSWD = 2.1) was calculated for the intermediate to high-temperature steps with 80% of released ^{39}Ar (Figura 37f). Lower ages were obtained from total fusion (553 ± 2 Ma) and the normal isochron plot (550 ± 7 Ma) and indicate Ar loss, placing the age of 559 ± 3 Ma as a minimum estimate of cooling age.

5.4.5 Argon closure temperatures and cooling rates

Mineral ages obtained from argon isotopic data are traditionally viewed as the last cooling event through the mineral closure temperature (T_C) with respect to argon diffusion. Provided that the bulk of the cooling history was steadily slow and linear, T_C can be calculated with the model of (Dodson, 1973) as a function of the mineral-specific diffusion parameters, grain size and cooling rate (dT/dt). We have used Ar diffusion parameters determined experimentally for amphibole by (Harrison, 1982), and for biotite by (Harrison et al., 1985). Starting cooling rates were obtained from ages of amphibole-bitotite pairs of a given sample, considering the nominal closure temperatures of 550 and 300 °C for amphibole and biotite, respectively. Since the Ematuba dykes have no biotite age we used the zircon-amphibole pair assuming a starting nominal temperature of 750°C for the zircon U-Pb age. For samples having U-Pb zircon, Ar-Ar amphibole and Ar-Ar biotite ages, we have approximated the cooling path by iterating a polynomial through the three age-temperature pairs in order to avoid underestimating cooling rates through the amphibole closure temperature due to Ar loss in biotite. Subsequently, dT/dt and T_C were calculated by iterating over both with a precision of 1%. No more than five iterations were necessary. Effective diffusion radii of 80 (Harrison, 1982) and

150 µm (Hanson and Gast, 1967; Harrison et al., 1985) were used instead of grain sizes where these were observed to have greater mean values in thin section in order to avoid overestimates of T_C. In order to minimise covariances of the parameters input to the model we have performed Monte Carlo simulations as outlined by (Scibiorski et al., 2015). 20000 trials were conducted with all parameters having some inferred probability distribution, while T_C and dT/dt were calculated. Trials starting with negative values of dT/dt (i.e. heating) are more common for samples with larger differences in the bounding ages and were not disregarded from the total percentage of trials. The full set of simulations, input parameters and their respective distributions, iteration methods and a Python sample script are given in the Supplementary Material[5].

Histograms of simulated T_C are typically bell-shaped and are reported here by a mean with a 2σ uncertainty. Histograms of dT/dt are right-skewed and are reported here as medians with differences to their first and third quartiles (e.g. $26^{+3.0}_{-2.4}$ °C/My). Simulation results are given in Tabela 2, including estimates made to data of Castro (2004) for the central nappe system, and Monié et al. (1997) for transcurrent shear zones, within the Ceará Central domain. Most amphibole and biotite closure temperatures are of c. 515 and 315 °C, respectively, whereas cooling rates are consistently between 40 and 20 °C/My. As expected from the positive correlation between T_C and dT/dt, the more elevated closure temperatures (524 ± 43 and 327 ± 26 °C for amphibole and biotite, respectively) are associated with faster cooling (40^{+32}_{-13} °C/My).

[5] Appendix B

Tabela 2 – Calculated cooling rates (2σ uncertainty) and closure temperatures (with differences to first and third quartiles). * Inferred temperature ranges for metamorphism. ** No mineral pair available.

Sample	Mineral	Age (Ma)	Closure temperature (°C)	Cooling rate (°C/My)
	Strike-slip shear zones of the Ceará Central domain			
Ematuba dykes – TSZ	Zircon	584.4 ± 5.9	750 ± 50*	$31^{+15}_{-7.9}$
	Amphibole	577 ± 6	517.9 ± 32.6	$31^{+15}_{-7.9}$
Várzea do Boi – TSZ	Zircon	571 ± 3	750 ± 50*	$28^{+7}_{-6.1}$
	Amphibole	562 ± 2	513.3 ± 22.3	$26^{+3}_{-2.4}$
	Biotite	554 ± 3	321.4 ± 26.2	$21.6^{+6.4}_{-5.8}$
Iapi – TSZ	Zircon	585 ± 11	750 ± 50*	$15.6^{+6.4}_{-4.1}$
	Amphibole	566 ± 2	511.5 ± 22.9	$21.7^{+3.3}_{-2.7}$
	Biotite	559 ± 3	322.0 ± 25.8	$23.8^{+4.2}_{-3.8}$
Mylonite – TSZ	Biotite	561 ± 2	**	
SPSZ – Monié et al. (1997)	Amphibole	572.7 ± 5.6	524.2 ± 43.4	$39.6^{+32.4}_{-12.9}$
	Biotite	568.6 ± 5.5	327.4 ± 36.4	$39.6^{+32.4}_{-12.9}$
TRSZ – Monié et al. (1997)	Amphibole	574.7 ± 6.1	505.3 ± 28.5	$16.5^{+5.5}_{-3.3}$
	Biotite	563 ± 5.4	312.6 ± 26	$16.5^{+5.5}_{-3.3}$
	Ceará Central nappe system - high-pressure granulites			
Castro (2004)	Zircon	611 ± 2.5	750 ± 50*	$32.6^{+7.4}_{-6.5}$
	Amphibole	603 ± 4	514 ± 22.1	$27.3^{+2.7}_{-2.1}$
	Biotite	594.8 ± 2.8	320.8 ± 26.1	$20.1^{+4.4}_{-5.5}$
	Zircon	603 ± 3	750 ± 50*	$24.4^{+1.6}_{-1.3}$
	Amphibole	595.4 ± 3.2	515 ± 21.9	$17.4^{+1.6}_{-1.2}$
	Biotite	569.6 ± 1.6	283.4 ± 37.4	$0.8^{+1.2}_{-0.5}$
	Amphibole	599.7 ± 3.8	496.6 ± 23.4	$10.9^{+1.1}_{-1.0}$
	Biotite	582.2 ± 1.6	306.0 ± 22.6	$10.9^{+1.1}_{-1.0}$
	Biotite	597.6 ± 1.6	**	
	Biotite	592.8 ± 1.4	**	

5.5 Discussions

5.5.1 Timing of pluton emplacement

Replicate U-Pb SHRIMP analysis of zircons from samples (VB1A and CA124) from the Várzea do Boi stock have both yielded a bimodal distribution of ages, centred at c. 571 Ma and 600 Ma, with a gap at c. 580 Ma. Given the remarkable similarity in age distribution between the samples and their concordant maxima and minima, their ages may be grouped to compose two subsets centred about the two age maxima (see Kernel probability distribution of the combined population in Figura 36a), forming two groups of coherent ages. A concordia age of 571 ± 3 Ma (MSWD = 0.7) can be calculated for the younger set, with a concordant weighted average age of 571 ± 5 Ma (MSWD = 2.1). The older set has the concordia age of 600 ± 3 Ma (MSWD = 1.3) and a concordant weighted mean of 599 ± 4 Ma (MSWD = 1.6). Having been focused on zircon areas that have homogeneous texture or pronounced oscillatory zoning, these analyses likely point to the crystallization age of their host magma. This is in agreement with the absence of significant variations in U, Th and Pb content, and with all ellipses lying on the concordia, without resolvable Pb loss. Hence, we estimate that the younger population (571 ± 3 Ma) records the final pulse of magmatism at the Várzea do Boi stock and the Tauá magmatic suite. It is unlikely that the older zircon population (600 ± 3 Ma) is comprised by xenocrysts eroded from country rocks during upwelling and emplacement as they would not form such a tightly constrained age distribution, or this would have been made evident by textural and compositional differences; i.e. these older zircons do not have overgrown rims nor were their ages obtained from xenocrystic cores. Instead they probably comprise zircon antecrysts (Davidson et al., 2007) formed within the magmatic plumbing system that feeds the Tauá magmatic suite that were captured during the upwelling of the last magma batch. No magmatism dated at 600 Ma is known within the Ceará Central Domain. This is well within the period of magmatic quiescence in the Northern Borborema Province which is used to separate an earlier magmatic-tectonic phase characterised by emplacement of nappes and arc magmatism (thought to have ended around 620–610 Ma, Ganade de Araujo et al., 2014c), from the final stage of orogenesis encompassing development of transcurrent shear zones and shear zone related granite emplacement at 590 Ma and onwards (Ávila et al., 2019).

Since the SHRIMP data for the two replicate analysis are unequivocal, we interpret that the existence of a long-lived magmatic system at and below the present structural level of the Tauá suite does not reflect regional tectonic aspects, and is a result of the processes taking place at the unique conditions of the shear zone junction between the Tauá and Senador Pompeu shear zones. Hence the fine-grained diorite at the Várzea do Boi stock records at 571 ± 3 Ma the final magmatic pulse within the suite, whereas the magmatic system may have started developing as early as 600 Ma.

The Iapi diorite, bound to the west by the Tauá shear zone, has a unimodal straightforward zircon age distribution that records magma emplacement and crystallization of at 585 ± 11 Ma. This age is concordant with that of all other synkinematic, shear zone-bounded plutons of the Ceará Central Domain, emplaced at 584 ± 5 Ma (Ávila et al., 2019). Thus, the Iapi stock in synchronous with deformation in the Tauá shear zone. The Lagoa de Pedra has a similar unimodal age distribution recording crystallization at 576 ± 10 Ma, concordant with the 571 ± 3 Ma age of the Várzea do Boi pluton, with which many field and petrological characteristics are shared. It seems likely that a sense of "younging" of magmas within the Tauá suite exists away from the shear zone junction. Older magmas are emplaced during and as a result of shear zone activity, whereas younger magmas are emplaced farther to the east, possibly in stages of waning shear zone deformation.

5.5.2 Magnetic fabrics, magma emplacement and relation to shear zone

K-T and IRM results (Figura 34) indicate that the granitic facies and anorthosite of the Várzea do Boi and Lagoa de Pedra stocks have their rock magnetic properties dominated by multi-domain (MD) low-Ti magnetite attested by net drop of susceptibility at 580 °C, a well developed Verwey transition, and prevalence of low coercivity phases (< 40 mT) in coercivity spectra. This ensures high ferromagnetic susceptibilities for granites, hybrids and anorthosite, with the exception of a few fine-grained granites with low susceptibility (< 0.05 mSI) in which the contribution of paramagnetic silicates (biotite, amphibole) to the bulk susceptibility must be important. Both soft (coarse magnetite) and minor hard magnetic phases (hematite) are also recorded in IRM of the granites of the Tauá batholith. Fine and coarse-grained diorites have much higher

contributions from hornblende and pyroxene to the susceptibility as indicated in *K-T* curves. However, some magnetite and a low amount of hematite must occur in the diorite samples as indicated by its IRM that does not saturate at induced fields as high as 2.5 T, and flat coercivity spectra (Figura 34). Their AMS fabrics are thus dominated by paramagnetic minerals.

Comparison between AMS and AARM fabrics (Figura 34) confirms that ferromagnetic grains dominate the magnetic fabric, except for diorites where more coercive populations could not be demagnetised. AMS has degrees of anisotropy between 5 and 6% (mean P of 1.048–1.059), which are fairly low compared to other shear zone-bounded plutons of the Borborema Province that have anisotropies of 11–20% (Archanjo et al., 2009, 2002). This suggests that the plutons have been affected by only incipient amounts of strain that produced a weak preferred orientation of ferro- and paramagnetic minerals. Such strain occurred entirely in the magmatic state since microstructures indicating solid-state or even sub-magmatic deformation are absent of all facies. Plagioclase and hornblende occur as euhedral crystals, whereas quartz forms equant and anhedral crystals with absent to incipient undulose extinction (even where shape preferred orientation of feldspar and hornblende is strong, e.g. Figura 32c). On average the shape parameter is slightly oblate for both the Várzea do Boi and Lagoa de Pedra stocks, therefore providing geological significance for both magnetic foliation (K_3) and lineation (K_1).

Most magnetic foliations and lineations in the Várzea do Boi are parallel to facies contacts, therefore, setting the timing of pluton fabric acquisition at least partly to magma emplacement and chamber construction processes (Fowler and Paterson, 1997; Paterson et al., 1998). This is somewhat expected given the distinct bimodality between dioritic and felsic magmas, and partial hybridization features, which imply quick cooling and "stiffening" of the diorite facies. This low magmatic strain allowed many primary magmatic structures related to the hybridization to be preserved (Figura 32). Primary magmatic structures include pillow-like flows of diorites surrounded by felsic seams and veins, corrugated diorite-granite contacts and silicic pipes (Snyder and Tait, 1995). Diorite magma is cooled rapidly after the intramagmatic flow (Figura 32e) and fracture stockworks may form locally (Figura 32f). Rates of cooling are decreased and hold the magmas at a condition of low viscosity; thermal instabilities allow for the formation of silicic microdiapirs rising into the diorite crystal mush (Figura 32g). All such features are believed to result from intramagmatic flows of intermediate-mafic magmas

into a silicic chamber (Wiebe, 2016). It is also apparent that magnetic lineations of diorites are steeply plunging where adjacent to nearly horizontal lineations of the granites (Figura 35), perhaps indicating the gravitational settling of denser dioritic magmas after their emplacement atop a felsic chamber, a process expected in chambers formed by intramagmatic flows (Wiebe, 2016).

The eccentric circular structure of the Várzea do Boi stock is revealed by the concentric steep facies layering and magnetic foliations alike. Flat-lying foliations occur in such centre and dip outwards, whereas most other foliations are steeply dipping and distributed about the centre. This type of fabric has been attributed to ballooning as a result of magma being fed through the centre of the pluton (Ramsay, 1989). In this scenario, the flat-lying foliations would be formed at the roof of the chamber and the concentric foliations likely reflect the gradual accretion of dioritic magma (Fowler and Paterson, 1997) through the granitic chamber centre with subsequent lateral spreading.

Internal structure and magnetic fabrics are less evident in the Lagoa de Pedra stock. At the northern half, magnetic foliations are contact-parallel, and a pluton centre is indicated by steep contact orientations and inwards dipping foliations. EW foliations separate this from the southern half where foliations have lower dips and lie at high angles to internal and basement contacts. This magnetic fabric distribution reveals that ballooning-like body forces have been effective for only the northern half, to which the southern half might have been subsequently accreted through a different feeder zone. Steeply plunging lineations are also more common on diorites relative to granites, and smooth variations in orientation are not present. Such heterogeneity can thus be viewed as resulting from very local processes of magma accretion.

Several lines of evidence are necessary for a reliable assessment of the role of regional tectonics on the formation of magmatic fabrics (Paterson et al., 1998). Unambiguous determination of the relative timing of pluton emplacement and fault activity, and therefore the correlation between regional deformation fields and pluton body forces, can only be provided by combined structural and geochronological methods (Archanjo et al., 2008; Ávila et al., 2019; Oriolo et al., 2018; Paterson et al., 1989). It is clear from field relations that the Tauá magmatic suite is either pre- or synkinematic to the Tauá shear zone. The entire batholith is sharply bound by the shear zone to the west and tapers to the south towards the junction as it is tightened by the Sabonete-Inharé shear zone. The Iapi stock itself has a left-lateral *en cornue* shape and magmatic fo-

liations become progressively more intense westwards. U-Pb zircon ages of the Iapi (585 Ma) and Lagoa de Pedra (576 Ma) are concordant within uncertainty with the age determined for synchronous activity of the Tauá-Senador Pompeu zipper system (584 ± 5 Ma, Ávila et al., 2019) and thus confirm that the batholith was built during shear deformation. Well preserved magmatic fabrics reflecting mostly chamber construction processes in the Várzea do Boi and Lagoa de Pedra stocks are then a result of shear deformation being strongly partitioned in the shear zones and the quick cooling of magmas after mingling. Nonetheless, some aspects of the magnetic fabrics of the Várzea do Boi stock cannot be explained by body forces alone and must be the effect of external strain field (Archanjo et al., 2002, 1994). Evidence comes from foliations that systematically cross-cut magmatic contacts at the southern margin of the Várzea do Boi stock, whereas lineations are distributed in a NE-SW girdle parallel to basement lineaments (see polar plots in Figura 31). Furthermore, wall-rock foliation triple junctions surrounding the stocks (Figura 31) indicate the interference of regional strike-slip shear deformation and that due to body forces that shaped the inner part of the plutons (Brun and Pons, 1981). Hence, the emplacement of the Tauá suite is likely to have occurred during synchronous shear zone activity. In this scenario, the well developed concentric structures occurring in both stocks indicate a strong mechanical decoupling from the basement (Paterson et al., 1998), which is undergoing major strike-slip shear deformation. Further evidence is provided by basement rock slivers of up to 100 m in length that occur in the central portion of the Lagoa de Pedra stock at structural continuity with the pluton walls. Radiometric composition images from airborne geophysical surveys also show these slivers are continuous from the pluton walls and are probably *in situ* and still rooted at the basement. Such degree of decoupling is characteristic of the brittle upper crust (Fowler and Paterson, 1997).

5.5.3 Cooling and exhumation of the Ceará Central domain

Cooling ages of biotite and amphibole through their respective Ar blocking temperatures reported in this study record the last episode of cooling and exhumation of the Tauá magmatic suite and Tauá shear zone. Robust hornblende plateau ages for Iapi and Várzea do Boi stocks are of 566 and 562 Ma, respectively, while the slightly older plateau age of 577 Ma of the Ematuba dykes may be due to a cryptic form of excess

Ar (Kuiper, 2002). Thus 577 ± 6 Ma is a maximum estimate. Amphibole from the granulites bounding the northeast-trending Senador Pompeu shear zone and Transbrasiliano lineament have Ar-Ar ages of 573 ± 6 and 575 ± 6 Ma determined by Monié et al. (1997), broadly similar to those determined in this study for the synchronous Tauá shear zone. Better concordance is found amongst biotite plateau ages of 554 ± 3 (Várzea do Boi stock), $559 \pm 3Ma$ (Iapi stock) and 561 ± 2 Ma (Tauá shear zone mylonite). Senador Pompeu and Transbrasiliano lineaments have biotite Ar-Ar ages of 569 ± 6 and 563 ± 5 Ma, respectively (Monié et al., 1997). Taken at face value these mineral cooling ages of the different shear zones may seem largely discordant, but they form very distinct T-t paths when compared to nearby tectonic domains of the Borborema Province. Most strikingly, the Ceará Central Domain, which is bound by the Tauá, Senador Pompeu and Transbrasiliano shear zones (Figura 30) has a range of amphibole and biotite cooling ages systematically older by c. 20 My (Castro, 2004). Amphibole Ar-Ar ages determined by Castro (2004) for the high-pressure granulite rocks of the Ceará Central nappe system (areas of occurrence indicated in Figura 30) range between 603 and 593 Ma, whereas biotite ages range mainly between 598 and 570 Ma. What these contrasted ages highlight is that cooling ages of minerals are controlled by very local thermal regimes, and only by comparing large datasets from nearby terranes can the general T-t path be revealed, as shown in Figura 38.

Closure temperatures (T_C) were calculated under the linear cooling path assumption with the model of (Dodson, 1973), by applying Monte Carlo simulations. T_C values were determined for the data in this study, and also for those of Castro (2004) for the Ceará Central nappe system, and Monié et al. (1997) for the Senador Pompeu and Transbrasiliano lineaments. Amphibole closure temperatures are generally 520–510 °C, whereas for biotite it is in the range of 320–310 °C. These low variations are a consequence of very similar cooling rates found amongst all samples (T-t paths, Figura 38). Most calculated cooling rates range between 20 and 40 °C/My (Tabela 2) for the shear zones and for the internal nappe domain. The lower cooling rates (0.8 and 10.9 °C/My) found for two samples from the Ceará Central nappe system analysed by Castro (2004) are a consequence of the polynomial fitting to a set of younger biotite (570 and 582 Ma) cooling ages which were affected by Ar loss. This is the purpose of not fitting the cooling path with a straight line, which would not allow an accurate estimate to be made to the cooling rate at the amphibole closure temperature. Within the transcurrent

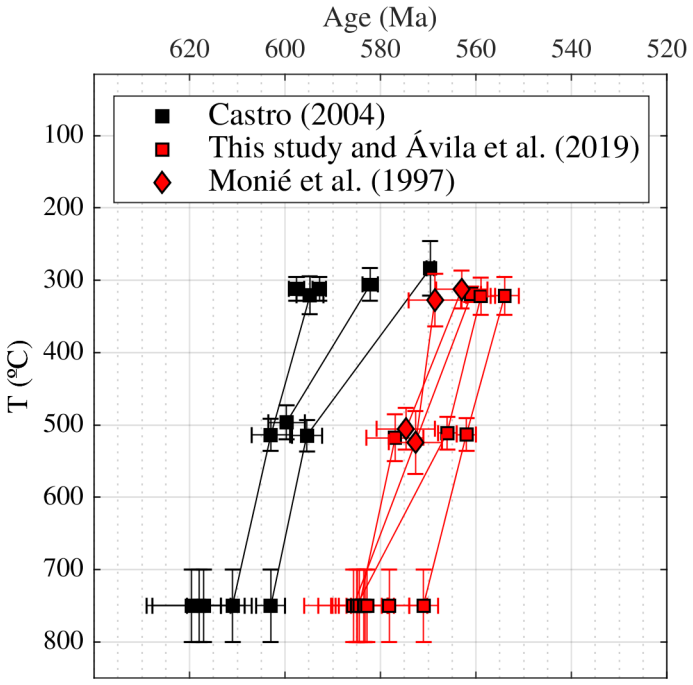

Figura 38 – U-Pb and Ar-Ar ages plotted against closure temperature of their respective isotopic systems. Lines connect ages obtained from the same sample (for Ar-Armineral ages) or from samples collected from the same outcrop or geological unit (zircon U-Pb and amphibole Ar-Ar). The equivalent depth of a normal continental geotherm is given in the right axis for reference.

shear zones, simulated cooling rates range between 40 and 17 °C/My, whereas within the internal nappe system, cooling rates range between 33 and 17 °C/My.

For the Ematuba dyke, a cooling rate of 31^{+15}_{-8} °C/My was calculated from the zircon-amphibole pair assuming a temperature of 750 °C for the zircon crystallisation. To do so, we considered that the plutons from which these minerals were samples have cooled to their ambient temperatures at timescales of 10^{-1}–10^{-3} My (Stüwe, 2007), much shorter than the tectonic processes under investigation. It is widely established that many of the late-orogenic granitoids of the Borborema Province were emplaced during transcurrent shear deformation at high temperature (Archanjo et al., 2002). This observation is also supported by field evidence for the Tauá shear zone (Ávila et al., 2019) and we, therefore, take the zircon U-Pb ages of plutons to indicate the timing for peak metamorphism of country rocks during strike-slip deformation. Syn-deformational garnet, kyanite, rutile and Zn-spinel, found in Senador Pompeu shear zone mylonites in-

dicate temperatures as high as 650–800 °C and pressures of c. 6 kbar, whereas kyanite-rutile-biotite inclusions in garnet evidence earlier pressures as high as 10 kbar (Monié et al., 1997). Similar upper amphibolite-lower granulite facies conditions are recorded for the Tauá shear zone (Neves, 1991). Abundant granitic plutons within and straddling the Senador Pompeu and Tauá shear zones were emplaced during high-temperature shear deformation at 584 ± 5 Ma (Ávila et al., 2019), and therefore constrain the peak metamorphic temperature of strike-slip deformation to that age. These intrusions have likely been emplaced at pressures of c. 5 kbar (Nogueira, 2004). Calculated cooling rates for zircon-amphibole pairs of samples which have also biotite cooling age estimates is broadly constant through the whole interval of temperature, from c. 750 to less than 320 °C (Figura 38). This provides confirmation of the applicability of the used simulations to calculate closure temperatures.

A similar argument can be made for the use of U-Pb ages of metamorphic zircons and monazite from high-pressure granulites of the nappe system of the Ceará Central Domain to calculate cooling rates. Arthaud (2007) and Castro (2004) determined U-Pb ages of zircon metamorphic rims and monazite of c. 620–600 Ma. These minerals form upon cooling from peak metamorphic temperatures and grow, either from the melt or by recrystallization, well below their closure temperatures (Cherniak et al., 2004; Rubatto, 2017). Within the high-pressure granulite units, metamorphic assemblages stable during melt crystallization indicate temperatures of c. 700–900 řC and pressures of c. 8–14 kbar at several areas of occurrence, including the Granja granulites to the northwest (Silva, 2017), Cariré high-pressure granulite belt (Amaral et al., 2012), and Independência nappes (Arthaud, 2007). U-Pb ages of metamorphic zircons from Castro (2004), which had Ar-Ar ages for amphibole and biotite from the same sample, were thus plotted against a temperature of 750 ± 50 °C (assumed to have a uniform frequency distribution, Figura 38). As in the case of *T*-*t* paths of shear zones, calculated cooling rates for zircon-amphibole pairs of samples from the internal nappe system are in the range of 20–30 °C/My, thus very similar to the subsequent cooling rate down to the closure temperature of biotite.

From geochronological and thermobarometric estimates available for the Ceará Central nappe system and the bounding strike-slip shear zones, we can synthesise a well-constrained *P*-*T*-*t* path (Figura 39). The general history starts conceivably with pods of eclogitic rocks found in the high-pressure granulite belt of Cariré (Santos et al., 2009).

Original pressure estimates are as high 22 GPa (Santos et al., 2009), which indicate these rocks were uplifted from over 100 km depths to the base of the crust due to buoyancy of surrounding material (Platt, 1993). Afterwards, these pods were retrogressed under high-pressure granulite conditions, with pressures of c. 17 kbar and peak temperature of 770 °C at c. 620 Ma (peak pressure in Figura 39; age from Ganade de Araujo et al., 2014a). Subsequently, the internal terrane was prevalently metamorphosed under conditions transitional between granulite and high-pressure granulite (8–14 kbar with an average of 10 kbar) at similar temperatures of 750–850 °C (Amaral et al., 2012; Arthaud, 2007). Zircon and monazite formed during cooling and crystallization of partial melts in such granulites record ages averaging at 610 Ma (Amaral et al., 2012; Arthaud, 2007; Castro, 2004, Figura 39). This characterises an episode of broadly isothermal decompression, bringing lower crustal terranes to the middle crust in a clockwise P-T-t trajectory as conceived by Arthaud (2007). Considering the range of metamorphic ages and geobarometric estimates outlined (8–14 kbar), a long-term unroofing rate of 1.5–4.5 mm/y can be calculated. This rate compares favourably with those of many collisional orogens of varying ages. Hollister (1993) has ascribed unroofing rates of more than 1 mm/y, observed in the Late Cretaceous Coast Mountains of British Columbia, to the process of isobaric decompression during melt-assisted extensional collapse. At this order of magnitude, unroofing has been observed to result from increased erosion rates in the Himalayan front at 1.1–1.4 mm/y (Thiede et al., 2004), or as a result of normal faulting such as in the Tauern window in the Alps, at c. 3.6 mm/y (von Blanckenburg et al., 1989). In the 1.8 Ga Snowbird Tectonic Zone of the Canadian shield, unroofing at 1.5–2.0 mm/y is also attributed to extensional deformation by (Flowers et al., 2006). We thus believe that such rates of 1.5–4.5 mm/y must represent the extensional collapse of the thickened crust at the northwest Borborema Province.

Once emplaced in the middle crust, the high-pressure granulite terrane cooled at a rate of 20–40 °C/My below the biotite closure temperature at 590 Ma (Figura 38). From this age onwards, the Ceará Central internal domain must have developed a very elevated strength and behaved as a coherent stable crustal unit. At 584 Ma, strike-slip shear zones were deforming under pressure and temperature conditions of about 5–6 kbar and c. 750 °C (Ávila et al., 2019). Since dip-slip components are not found in the shear zones, no significant vertical displacements of their cores relative to the internal nappe system must have occurred, setting them to the same structural level. Thus, considering

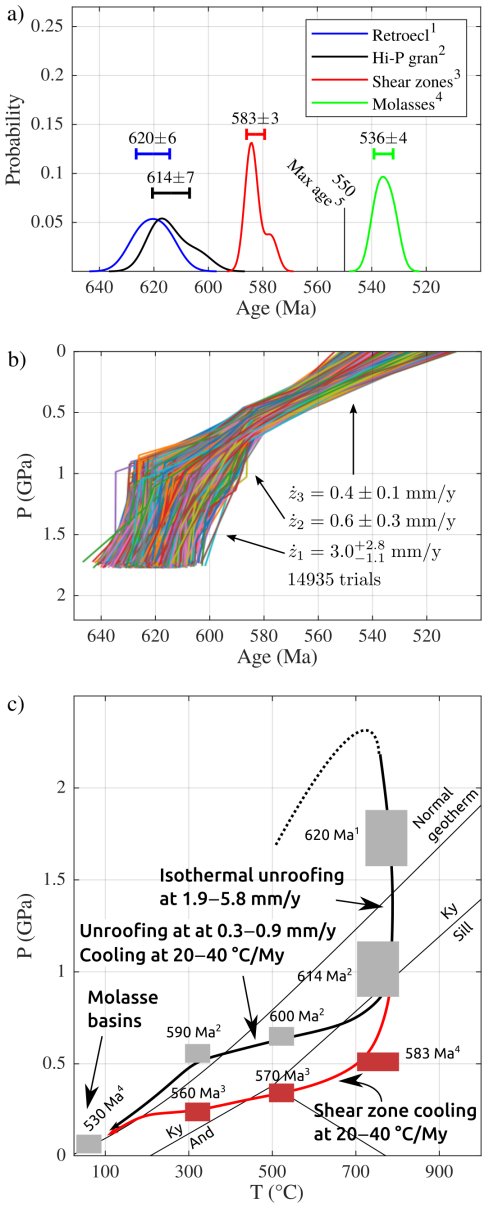

Figura 39 – P-T-t path for the Ceará Central domain and bounding transcurrent shear zones. Filled boxes indicate the general P-T range constrained by thermochronological, geochronological and thermobarometric data. Ages shown are approximate according to 1) Ganade de Araujo et al. (2014b), 2) Castro (2004), 3) this study, 4) Ávila et al. (2019) and 5) Garcia et al. (2018). For further details refer back to text.

the uncertainties in ages and pressure estimates, a long-term unroofing rate of c. 0.4–0.9 mm/yr can be estimated from the end of the isothermal decompression path of the internal terrane at c. 10 kbar and 610 Ma to the present crustal section at 584 Ma. Furthermore, it is thought that the post-orogenic molassic basins of Cococi, Jaibaras and Jaguarapi formed at c. 540 Ma. Provenance studies in the Jaibaras basin constrain a maximum deposition age of c. 550 Ma (Ganade de Araujo et al., 2012), whereas rhyolites occurring in intermediate strata have an age of 536 ± 9 Ma (Garcia et al., 2018). From the time of peak activity in shear zones at 584 Ma until final exhumation to the surface at c. 540 Ma, an unroofing rate of 0.4–0.7 mm/y can be calculated, in agreement with that calculated for the interval between 610 to 584 Ma. Given the low temperature of the internal domain, we believe a long-term unroofing rate of 0.4–0.9 mm/y prevailed from the end of the extensional collapse of the orogen at 590 Ma until the formation of molassic basins at 540 Ma, mainly driven by erosion. Although rates of unroofing calculated in this study are not meant as strict determinations of true rates, they serve as order of magnitude estimates that clearly correspond to distinct processes of exhumation.

The shear zones later cooled through the amphibole and biotite closure temperatures at very similar cooling rates of 20–40 žC/My, with a temperature below c. 300 °C at 560–550 Ma. This similarity in cooling rates is surprising since while the Ceará Central nappe system has certainly experienced cooling as a result of unroofing in a first stage, the shear zones may have cooled essentially isobarically after the whole domain was already exhumed to the middle-upper crust. Furthermore, since the shear zones and internal domain must have been at the same structural level, the younger mineral cooling ages of the shear zones reflect strong lateral variations in thermal regimes, a possible consequence of heat advection and radioactive heat production enhanced by the intense granite magmatism within shear zones. These cooling rates of 20–40 °C/My are also in agreement with those found in various orogens, such as the Mesoproterozoic Albany-Fraser orogen of Australia (10–30 °C/My, Scibiorski et al., 2016), the Cretaceous McLaren metamorphic belt of Alaska (12–24 °C/My, Hollister, 1993), the Karakoram metamorphic complex in the southern Tibet (30 °C/My, Krol et al., 1996) and the Pennine nappes in the Western Alps (c. $>$ 25 °C/My, Barnicoat et al., 1995). More extreme rates of unroofing (10–50 mm/y) and cooling (over 100 °C/My) are found in specific tectonic settings due to extrusion in syntaxes (e.g. Himalayan syntaxes, Pa-

lin et al., 2015) or transpressive jogs (Batt et al., 2000). The evidence for a tectonic origin of the magmatic fabrics in the Várzea do Boi stock also indicate that deformation in the interacting transcurrent shear zones of the Ceará Central domain has occurred at least from 584 to 571 Ma. This time span covers the fast isobaric cooling episode (20–40 žC/My). As a consequence, the Senador Pompeu and Tauá shear zones experienced deformation under decreasing metamorphic grade. This led to formation of early high-temperature mylonitic gneisses which were then overprinted by low-temperature mylonitization and cataclastic deformation.

5.6 Conclusions

Crustal thickening due to shortening and nappe stacking followed by extensional collapse and prominent shear zone deformation characterise the Ediacaran orogenic history in the northwest Borborema Province. The extension was achieved by reactivation of lower crustal *décollements* and newly forming strike-slip shear zones, allowing fast decompression of high-pressure rocks at an unroofing rate of 1.5–4.5 mm/y. $^{40}Ar/^{39}Ar$ ages indicate that the internal terranes of the Ceará Central domain were below 300 °C at c. 590 Ma, and following the isothermal decompression, exhumation of the entire domain continued at a long-term unroofing rate of 0.4–0.9 mm/y. In contrast, at 584 Ma, the transcurrent shear zones (Senador Pompeu and Tauá) record high-temperature conditions including partial melting. This lateral variation in thermal regime at the same structural level is likely due to magmatic activity leading to intense heat advection to and through the shear zones. Fast cooling at approximately 20–40 °C/My continued through 520 °C and 320 °C at 570 Ma and 560 Ma, respectively, at the Tauá shear zone. The Tauá magmatic suite, in turn, records a protracted history of pluton construction from 585 to 571 Ma. AMS of concentrically zoned stocks records magmatic fabrics shaped by internal processes of magma accretion and by deformation in nearby shear zones, as a result of strain being progressively more localized due to fast cooling. Additionally, the magnetic fabrics of the late Várzea do Boi stock indicate that the shear zones were still active by 571 Ma. The unroofing rate of 0.4–0.9 mm/y was maintained until the terrane was exhumed to the surface at the Ediacaran-Cambrian transition, when the molassic sequences of Cococi and Jaibaras transtensional basins were deposited

5.7 Acknowledgements

C. Ávila and C. Archanjo thank São Paulo Science Foundation (FAPESP) for financial sponsorship (grants 2016/22226-9, 2017/21440-0 and 2019/10167-6). M. H. B. M. Hollanda thanks CNPq for the research fellowship no. 303201/2019-3. U-Pb SHRIMP, Ar-Ar and Anisotropy of Magnetic Susceptibility (AMS) analyses data used in this study are available in further detail in the Supplementary Material[6]. Airborne geophysical survey data that aided in geological mapping are available in the Brazilian Geological Survey database (http://geosgb.cprm.gov.br/). Maps for this study were created in QGIS (QGIS.org, 2020. QGIS Geographic Information System. Open Source Geospatial Foundation Project. http://qgis.org).

[6] Appendix B

6 Rheology, shear zone width, microstructural evolution and tectonics of a zippered strike-slip shear zone: the Senador Pompeu shear zone, northern Borborema Province, Brazil

6.1 Abstract

Studies of the Borborema Province have broadly elicited the important role of its abundant strike-slip shear zones in accommodating relative motion of crustal blocks during the Brasiliano orogeny, but seldom quantitatively addressed key aspects of shear zone deformation such as longevity, slip rate, total offset, kinematics and rheology. To provide unprecedented level of detail regarding the Senador Pompeu shear zone of northern Borborema Province, we have conducted a complete structural study using detailed geological mapping, deformation microstructures, Electron Backscatter Diffraction (EBSD), geobarometry, and shear zone width modelling. Our results show that: (i) shear zone width decreases systematically along strike from its northern segment, monotonously comprised of high-temperature penetrative mylonitic gneisses, towards the south, comprised by low-temperature ultramylonites, cataclasites and pseudotachylytes; (ii) quartz deformation microstructures change consistently from high-T grain boundary migration recrystallization and $\{m\}\langle c\rangle$ slip in the northern segment, to subgrain rotation/bulging recrystallization, mixed-$\langle a\rangle$ slip and cataclasis in the southern segment; (iii) geobarometry of synkinematic shear zone-bounded plutons indicate a depth difference of c. 10 km over a length of 200 km of the Senador Pompeu shear zone; (iv) shear zone width modelling indicate that slip rates must have been at least 10 mm/yr; (v) geolo-

gical units show a total offset of 50–75 km; (vi) three dextral closing zipper segments found along the length of the shear zone juxtapose mylonites with opposing kinematics. From the consistent decrease in shear zone width and deformation temperature towards the southwest and the difference in emplacement depth of synkinematic granites we interpret that the northern segment is up-tilted by a few degrees (c. 3°) relative to the southern segment, exposing the strength profile, the brittle-ductile transition and the relation between depth and width of the shear zone. The width simulation carried out on that basis allowed the long-term slip rate to be constrained at >10 mm/yr, from which we interpret that the Senador Pompeu had a short-lived activity of c. 10 Myr (584–574 Ma).

6.2 Introduction

Investigations on the rheology of continental shear zones, on an empirical basis, established a broad correlation between the width of shear zones and deformation temperatures (Oriolo et al., 2015; Sibson, 1977, 1986; Tommasi et al., 1994; West and Hubbard, 1997). It is well known that deformation tends to progressively localize in narrow shear zones with decreasing temperature, until no more than a discrete fault zone (potentially made thicker by its associated damage zone) materializes the boundary between two sliding blocks under brittle (sub-greenschist facies, $<300\,^{\circ}C$) conditions (Sibson, 1986). As seen in many ancient and deeply eroded orogens, the deep crustal roots of shear zones which were formed under high (up to melting) temperatures, may be up to 30 km thick (Hoffman, 1987; Leloup et al., 1995; Norris and Cooper, 2003; Vauchez and Tommasi, 2003), as is the northern Senador Pompeu shear zone and eastern Patos shear zone of the Borborema Province (Figura 40). This general width-temperature correlation has been attributed to thermal softening of the continental crust that occurs with depth. However, few attempts have been made to systematically assess the relation between the width of shear zones and rock rheology (Behr and Platt, 2011; Platt and Behr, 2011a; Platt, 2015a).

Alternatively, extensive research on deformation mechanisms and microstructures of diverse shear zone rocks allowed for continuous improvement in our understanding of the strength profile of the continental lithosphere (Burov and Watts, 2006; Jackson, 2002; Wallis et al., 2013). In particular, a recent hypothesis regarding how the rheology

of a shear zone affects its width was proposed by Platt and Behr (2011c), and subsequently elaborated on by Behr and Platt (2011), Lusk and Platt (2020), Platt and Behr (2011a) and Platt (2015a,b) Platt (2015a, 2015b). In exhumed deep shear zones, no actual evidence is available regarding its corresponding shallow crustal extension (Norris and Cooper, 2003). The difficulty in constraining how crustal strength varies with depth in a single consistent deformation zone is worked around by studying the progressive exhumation of a shear zone core, mostly in dip-slip deformation zones (Behr and Platt, 2011; Imber et al., 2001; West and Hubbard, 1997). Only rarely do tilted sections expose large depth ranges (Cook and Crawford, 1994; Stipp et al., 2002b). Therefore, strike-slip shear zones that exhibit deformation structures formed at different depths, either by progressive exhumation or crustal tilting, should provide further constraints on the interplay between shear zone width and the strength profile of the crust.

Strike-slip deformation under multiple conditions is recorded by high-T and locally low-T shear zones with widely variable geometric properties in the Borborema Province of NE Brazil (Figura 40). These form a system of transcurrent shear (Vauchez et al., 1995), often interpreted to have facilitated block extrusion or escape tectonics (Archanjo et al., 2021; Ganade de Araujo et al., 2014c). While correct on kinematic grounds, this interpretation must be tested by asking "how much escape?" Lack of estimates of offset and slip rate, and the speculative shear zone longevity of as much as 50–100 Myr (Ganade de Araujo et al., 2014c; Miranda et al., 2020; Vauchez et al., 1995) hinder our understanding of the overall magnitude of crustal movements and of the origin of low-T deformation within the framework of rheology and tectonics. This study is intended as a preliminary test of the hypothesis of crustal extrusion in the Borborema Province and also as groundwork for constraining shear zone-related deformation parameters that hint to the tectonic significance of the shear zone system. We present a structural analysis and microstructural study of the strike-slip Senador Pompeu shear zone of northern Borborema Province that allows plausible estimates of deformation temperatures and depths at several strands of the shear zone, minimum shear zone widths, minimum offset, and overall rheology. Several zippered sections (Ávila et al., 2019) with reverse kinematics have been observed. We interpret that the shear zone exposes a tilted crustal section that displays the brittle-ductile transition, and the theory regarding the association between width and rheology allows for reasonable approximations to be made of the longevity of shear deformation.

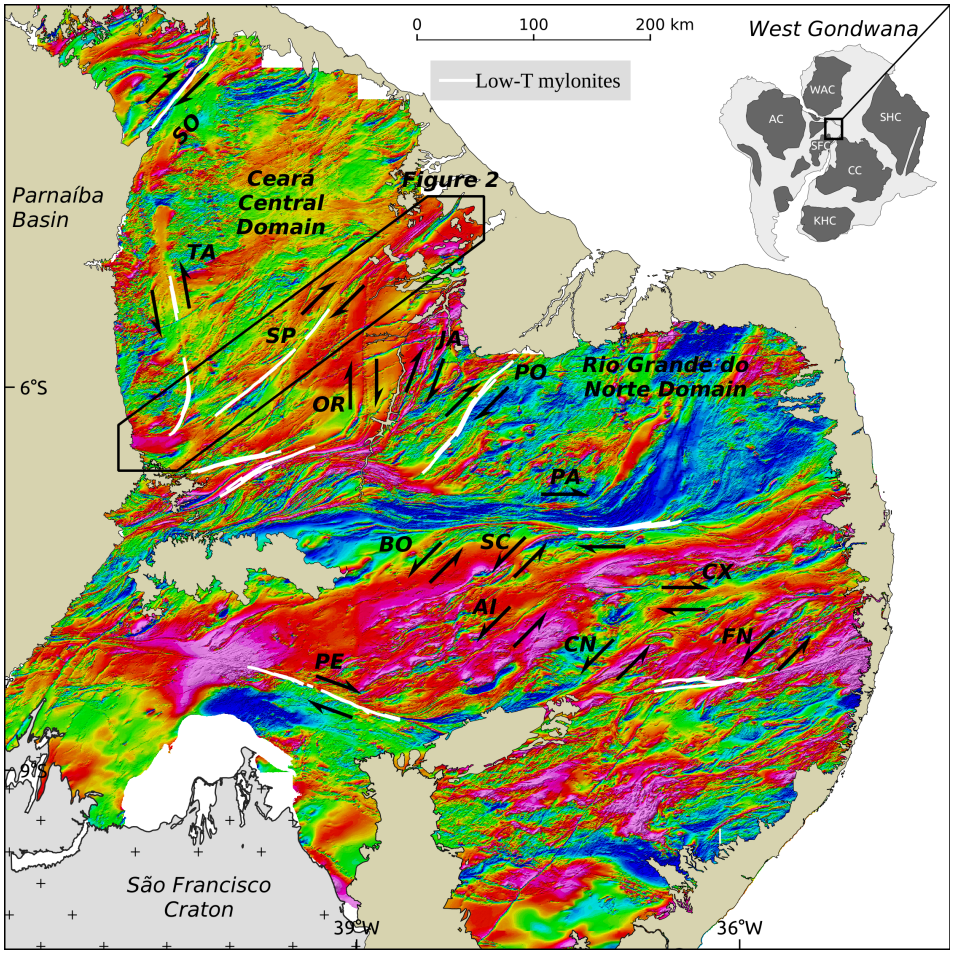

Figura 40 – Total magnetic anomaly map of the Borborema Province, reduced to pole. White lines show occurrences of low-temperature mylonite zones. Shear zones from northwest to southeast: SO - Sobral-Pedro II, TA - Tauá, SP - Senador Pompeu, OR - Orós, JA - Jaguaribe, PO - Portalegre, PA - Patos, BO - Boqueirão dos Cochos, SC - Serra do Caboclo, AI - Afogados da Ingazeira, CX - Coxixola, CN - Cruzeiro do Nordeste, FN - Fazenda Nova, PE - Pernambuco. Inset shows location of the map frame in West Gondwana, in which dark grey areas are cratons and light grey areas are orogens. AC - Amazonian Craton, WAC - West Africa Craton, SFC - São Francisco Craton, SHC - Saharan Craton, CC - Congo Craton, KHC - Kalahari Craton.

6.3 Geological setting

Covering over 400 000 km^2 in northeast Brazil, the Borborema Province (Figura 40) is a Neoproterozoic orogenic belt originated from the amalgamation of several cra-

tonic blocks in the Brasiliano/Pan-African orogenesis, leading to formation of West Gondwana (Almeida et al. 1981; see inset in Figura 40). Its basement comprises geological units from the Neoarchean to the Neoproterozoic, but is somewhat dominated by Paleoproterozoic gneiss-migmatite complexes and Neoproterozoic metasedimentary sequences. Continental collision is thought to have occurred in the northern Borborema Province at 620–610 Ma (Ganade de Araujo et al., 2014b). Subsequently, a kinematically coherent network of transcurrent shear zones developed with broad synchronicity (for the most important shear zones) at 590–570 Ma, and with a strong genetic link with high-K and shoshonitic granitoid magmatism (Vauchez et al., 1995). This tectonomagmatic association is coeval with high-T metamorphism and migmatization, so that throughout the Borborema Province shear zones are constituted of high-T mylonites. Low-T mylonites of uncertain origin form narrow and comparatively short strands within the major shear zones (Figura 40).

The Senador Pompeu shear zone is the most prominent structural feature that cuts through the northern Borborema Province (Figura 40), separating the Ceará Central domain (northwest) from the Rio Grande do Norte domain (southeast). A TTG gneiss terrane of Neoarchean age (Cruzeta Complex, 2.68–2.78 Ga; Fetter 1999; Ganade et al. 2017) comprises the core of this region, about which several Rhyacian Paleoproterozoic metaplutonic and metavolcanosedimentary terranes are accreted (Rhyacian gneiss-migmatite and greenstone complexes in Figura 41). In the northeast of this area, the metavolcanosedimenary greenstone belt-like sequence (named Algodões-Choró metamorphic suite; Martins 2000) is composed primarily of amphibolites, garnet-amphibolites and paragneisses which have an age of 2240 Ma (Martins et al., 2009). A range of metaplutonic terranes with ages of 2190–2130 Ma surround the older units (Costa et al., 2015a, 2018). A Neoproterozoic (Arthaud et al., 2015; Fetter, 1999; Ganade de Araujo et al., 2012; Garcia et al., 2014; Mendes et al., 2021) metasedimentary sequence of passive and active margin sediments termed the Ceará Complex roughly occupies a large portion of the Ceará Central domain. It is composed of high-grade paragneisses, metapelites, quartzites, calc-silicates and minor felsic and mafic metavolcanics (Arthaud et al., 2015), with the lower unit generally presenting significantly higher (up to migmatization) metamorphic grade (Ganade de Araujo et al., 2014a; Mendes et al., 2021). All the above-mentioned units are deformed by the Senador Pompeu shear zone, some serving as an offset marker (Figura 41). Further to the northwest,

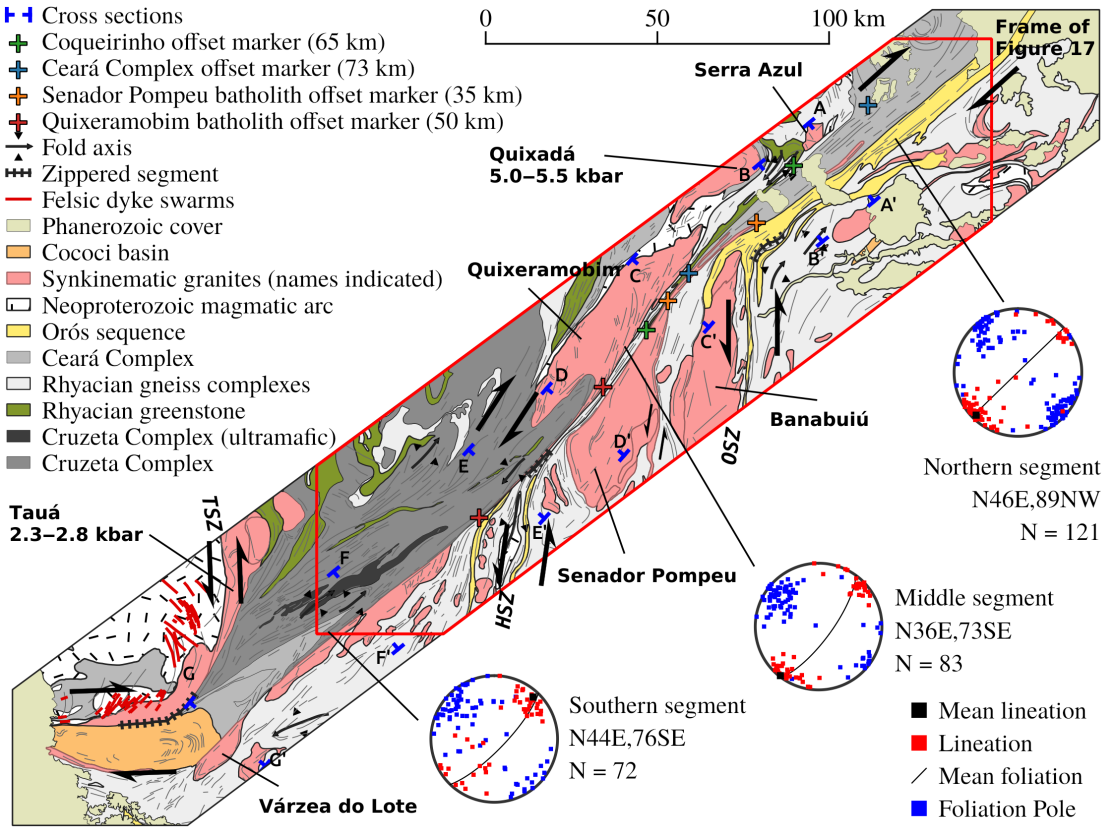

Figura 41 – Geological map of the Senador Pompeu shear zone. Geological cross sections (AA' to GG') are given in Figura 42. TSZ - Tauá shear zone, OSZ - Orós shear zone, HSZ - Hebrón shear zone. Stereographic projections show foliation poles (blue), stretching lineations (red), mean lineation (black) and the mean foliation (black line) is indicated by their strike and dip (e.g. N44E,76SE).

the Tamboril-Santa Quitéria magmatic arc (Ganade de Araujo et al., 2014a) and the Pacatuba-Maranguape magmatic arc (Pitombeira et al., 2021) record long-lived subduction (c. 800–600 Ma) in the Ceará Central domain, synchronous with deposition of the Ceará Complex sediments. Southeast of the Senador Pompeu shear zone, the Paleoproterozoic basement is represented by the poorly studied gneiss-migmatite Jaguaretama and Acopiara complexes. These are separated by the volcanosedimentary Statherian Orós-Jaguaribe sequence which follows along the Orós shear zone (Figura 41; Parente and Arthaud 1995).

Flat-lying foliations in the central parts of the Ceará Central domain characterize

its earlier Neoproterozoic deformation, when the Ceará Central nappes were emplaced (Caby and Arthaud, 1986). Precise estimates of the age of nappe emplacement are lacking. Stretching lineations in key thrusts are defined by high-temperature minerals (Arthaud, 2007) which, according to thermochronological integrations, indicates that nappe emplacement was completed somewhat earlier than 600 Ma (Ávila et al., 2020). High-temperature strike-slip deformation on the Senador Pompeu and Tauá shear zones dominated late orogenic deformation. This thermokinematic regime is accompanied by shear zone-related plutons and by dykes formed in the intervening block at 584 ± 5 Ma (Ávila et al., 2019). Surrounding the Senador Pompeu shear zone, the Quixadá, Quixeramobim and Senador Pompeu batholiths are noticeably offset and affected by shear (Figura 41). After the emplacement of granite batholiths at 584 Ma, slow exhumation of the northwest part of the Borborema Province took place at rates of 0.3–0.9 mm/yr (Ávila et al., 2020), causing the present crustal section to be exposed at 530 Ma when molassic basins have been formed with strong structural control of major shear zones (Archanjo et al., 2009; Ganade de Araujo et al., 2012; Garcia et al., 2018). Lastly, the synchronous activity of the SPSZ and TSZ pair led to the formation of a dextral closing zipper (Platt and Passchier, 2016) at their junction (Cococi shear zone).

The temperature of deformation decreases from NE to SW along the SPSZ (Ávila et al., 2019; Vauchez et al., 1995); high-temperature mylonitic gneisses of amphibolite facies conditions occur to the NE, and narrow strands of greenschist facies ultramylonites with pseudotachylitic breccias occur to the SW. The Senador Pompeu shear zone extends for 350 km from its SW termination at the Cococi dextral closing zipper to the northeastern coast of Brasil, showing a general increase in width from less than 1 km in the southwest to over 20 km in the northeast. It strikes c. 40° clockwise and is subvertical (Figura 41). Previous offset estimates range between 66 and 96 km (Ávila et al., 2019). Kinematic vorticities for syntectonic intrusions deformed by the Senador Pompeu and Tauá shear zones are somewhat variable but centered at 0.7 (i.e. c. 50% simple shear; Ávila et al. 2019). Flat-lying basement foliations are gradually transposed towards the shear zone where upright folds occur. Pre-drift reconstructions of west Gondwana show that the Senador Pompeu shear zone is continuous with the Ile-Ife shear zone of the Nigerian belt (Archanjo et al., 2013; Caby and Boessé, 2001), indicating its full length as an original shear zone may exceed 800 km. Indeed, a crustal-scale discontinuity is revealed beneath the Senador Pompeu shear zone by gravity and mag-

netotelluric surveys (Oliveira and Medeiros, 2018; Padilha et al., 2017) with a steep to vertical southeast dip.

6.4 Methods

6.4.1 Electron Backscatter Diffraction (EBSD)

Electron Backscatter Diffraction (EBSD) analyses were conducted on fine-grained quartz-rich bands in low-temperature mylonites on a JEOL 7001 FEG-SEM equipped with an EDAX-TSL EBSD-EDS system. No conductive coating was applied. Specimens were mounted on sample holder with conducting tapes and the analyses were conducted under low vacuum (19 Pa) to minimize sample charging. The FEG-SEM was operated with an accelerating voltage of 20 kV, working distance of 15 mm and sample tilt of 70° towards the EBSD detector screen. The step size was varied between 0.5 and 2 µm. The system operates with the EDAX OIM Data Collection software suite. Most analyses were carried out with a speed of approximately 40–50 indexed patterns per second, with full maps having around 250 thousand points.

6.4.2 Standard procedure of noise reduction and segmentation of EBSD data

In order to determine paleopiezometry values from recrystallized aggregates, accurate estimates of grain sizes need to be conducted. Grain reconstruction from raw EBSD follows a standard procedure of removal of data points with a poor diffraction pattern (EBSP) that results in a low Confidence Index (CI) for the solution (Field, 1997). One commonly recommended approach is removing EBSD grains reconstructed from the raw data that have a very high ratio of grain boundary to grain area (Hielscher et al., 2019; Mainprice et al., 2015), a proxy for areas at grain boundaries and defects, where CI is low. Segmentation was carried out considering a misorientation threshold of 10° and a subgrain threshold of 3° (Shigematsu et al., 2006). One and two-point grains were removed and grain reconstruction carried out again. In the new grain microstructure, we removed both quartz and non-indexed (i.e. no phase) grains with a large surface area, estimated by $\log(D/P)$, where D is grain size and P is grain boundary length. Visual

inspection of each map allowed optimal values of $\log(D/P)$, generally around -0.3, to be determined, separating grains from areas of grain boundary, where the overlap of neighbouring EBSPs may lead to a low CI. Grain reconstruction was repeated allowing for new grains to "grow" over previously deleted areas. The mean recrystallized grain size D is then obtained from root mean squares (RMS) of the diameter of the circle with equivalent area (given by $D = [\sum(2\sqrt{A/\pi})^2/n]^{0.5}$, where is grain area and is the number of reconstructed grains) The grain reconstruction method described above is appropriate for use of the piezometer calibration of Stipp and Tullis (2003).

6.4.3 Cross et al. (2015) procedure

A paleopiezometry calibration appropriate for EBSD data was created by Cross et al. (2017) (details in the following sections) which uses a method of grain reconstruction developed by Cross et al. (2015). It consists of removing initially grains which are consisted of 4 pixels or less, assumed to be produced by misindexing (low CI solutions). Instead, an extrapolation of neighbouring grains into these areas is allowed to occupy the EBSD map fully. The newly constructed grain population will then contain grains that are well constrained by a large amount of high CI pixels, and grains that have a large number of pixels previously disregarded (for comprising small grains). They can be weighted according to $f = (nd_{step}^2/A_{grain})$, where n is the number of pixels which were not removed from the dataset (i.e. comprised grains larger than 4 pixels), d_{step} is the step size, and A_{grain} is the area of the newly reconstructed grains. This weighting parameter can be plotted in a histogram, where a cutoff value is found separating well constrained grains (high f) from poorly constrained grains (low f; for details see Cross et al. 2017). Grain size histograms for both datasets do not reveal appreciable differences in distribution and central tendency estimates, but grains reconstructed using the Cross et al. (2015) appear smoother since they are allowed to fill grain boundaries completely; this may be useful in studies of correlated misorientation of EBSD data.

6.4.4 Electron Microprobe Analysis (EMPA)

Major and minor elements of plagioclase and amphibole in polished thin sections of dioritoids from the Tauá batholith were quantified by Electron Microprobe Analyses (EMPA) with a JEOL JXA-8600S equipped with five WDS (Wavelength Dispersive

Spectrometry) detectors automated by the Thermo-Noran Voyager 4.3.1 system at the GeoAnalitica lab of Universidade de São Paulo. Operating conditions were kept at 15 kV acceleration voltage, 5 µm beam size, and 20 nA for beam current. Standards used are in accordance with their respective mineral or diffracting crystals standards using the Kαline (Gualda and Vlach, 2007): TAP for Si(wollastonite and microcline), Al (hornblende), Mg (diopside), Na (albite), F (fluorite); LiF for Ti (rutile), Fe (olivine), Mn (olivine), Zn (ZnO); and PET for Zr (zircon), Ba (barite), Sr (Sr-anorthite), K (microcline).

6.5 Results

6.5.1 Field relations, structural architecture and microstructures

Most protoliths of the Senador Pompeu shear zone (SPSZ) are granites and granodiorites derived from the Paleoproterozoic and Archean basement units, or from late orogenic plutons that intruded slightly pre- or syn-shear zone deformation (Ávila et al., 2019). As a result, widely varying deformation microstructures and degrees of mylonitization occur along its strike. For the sake of discussion, we will refer to the northern, middle, and southern segments of the SPSZ individually due to their distinct features.

The northern segment extends for c. 150 km from the northeastern coast of Brazil to the southwest. In its southwest termination, it gets squeezed between the Senador Pompeu and Quixeramobim batholiths to a thickness of less than 1.5 km, whereas north of this point it has a thickness of c. 10 km (AA' and BB' in Figura 42). Furthermore, it merges with the Orós shear zone further north forming a shear zone with a minimum thickness of 15 km. Foliations are vertical in the shear zone core and dip away from it in the less deformed wall rocks to the southeast and northwest. Plunges of stretching lineations vary from horizontal to slight southwest (see stereogram of Figura 41). Protoliths in the northern segment of the SPSZ are mostly granodioritic gneisses that derive from the Neoproterozoic Canindé unit of the Ceará Complex and have been sheared to the southwest. They form mylonitic gneisses with millimetre scale penetrative compositional banding (Figures 43a, 43b and 43f) and a strong stretching lineation (Figura 43d). Leucosome filled foliation boudins collecting melt from within the compositional bands are local features, as well as strongly deformed and transposed

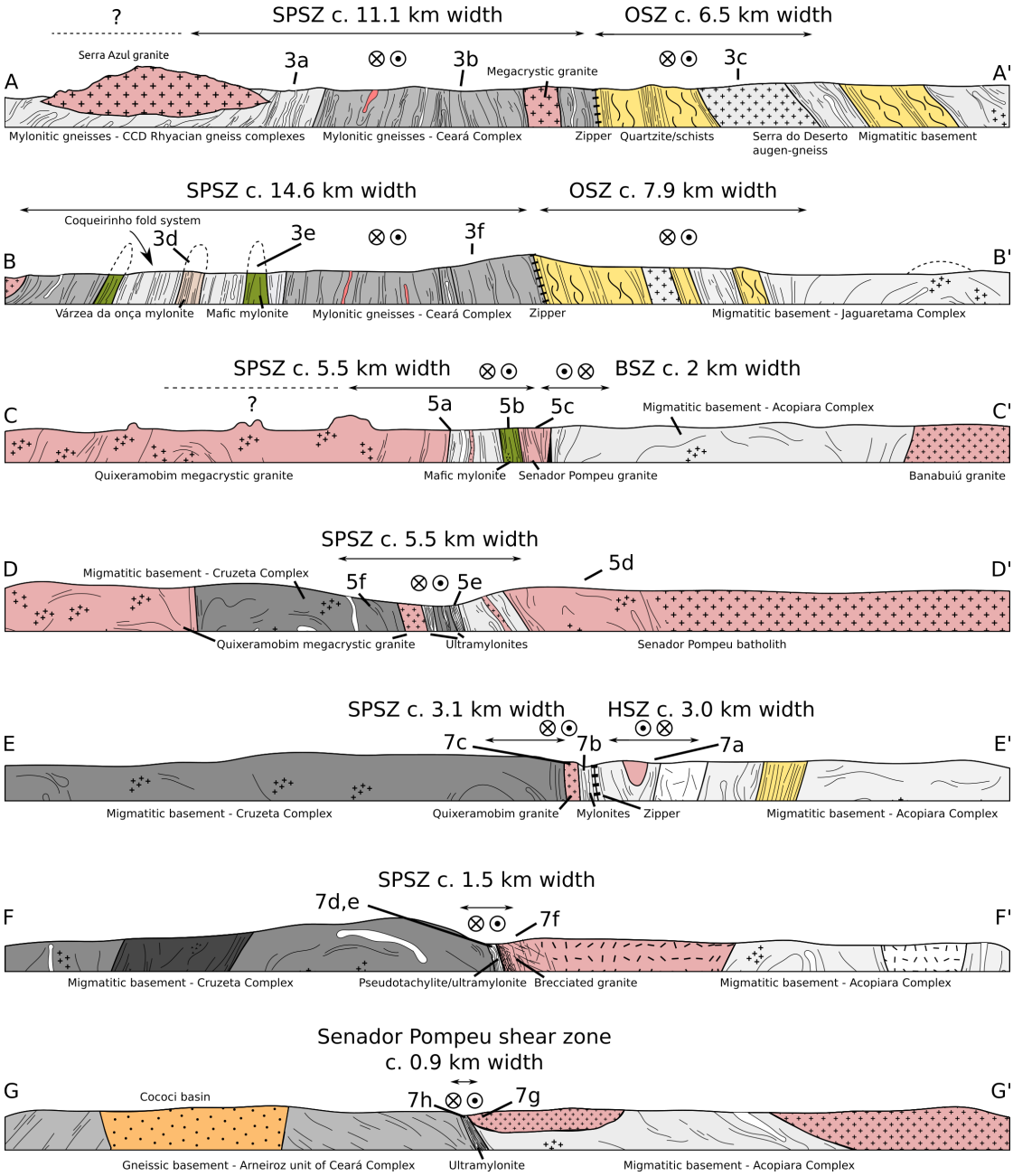

Figura 42 – Geological cross sections of the northern segment of the Senador Pompeu shear zone. Represented dips of units and strucures are true (from field measurements) but vertical dimensions are not to scale. a) AA'. b) BB'. Symbology of geological units is similar to that of Figura 41.

garnet-bearing leucosome bands. Shear band boudins, rotated porphyroclasts, and S, C and C' foliations (Figuras 43a, 43b and 43af) consistently indicate right-lateral shear. Biotite and hornblende may form thin laminae but are mostly dispersed in the matrix. A sheet of megacrystic granitoid (similar to the Quixeramobim megacrystic facies) occurs in the northern segment and displays syn-magmatic deformation with negligible solid-state strain and is thought to have formed at the last stages of deformation of the Senador Pompeu shear zone (Figura 42 AA'). The hornblende-rich Serra Azul stock is characterised by flat-lying foliations even close to contacts with the basement, indicating post-kinematic emplacement (Figura 42 AA'). Metagreywacke and metamafic rocks of the Paleoproterozoic Algodões-Choró metamorphic suite (Rhyacian greenstone and gneiss complexes surrounding the Quixadá batholith in Figura 41) constitute the southwest-plunging Coqueirinho fold system (northeast of the Quixadá batholith; Figura 42 BB'), with mylonitised amphibolites interlayered with metagreywackes (Figura 43e) and overlain by the Várzea da Onça mylonitic gneisses (the typical mylonite of the northern strand of the Senador Pompeu shear zone; Figura 43d). In the southeast half of the Senador Pompeu shear zone, rock units are comprised by those "zippered together" from the left-lateral northern strand of the Orós shear zone (Figura 41), particularly dominated by the Statherian quartzites of the Orós sequence. Right-lateral criteria such as S-C fabrics are displayed by the augen-gneiss of the Serra do Deserto unit (Figura 43c).

Except for local occurrences of late-kinematic porphyritic-megacrystic granitoid lenses, the northern segment of the Senador Pompeu shear zone is monotonously composed of aphyric mylonitic gneisses with incipient grain-scale compositional banding (Figura 44a). Quartz and feldspar occur as equant grains thoroughly mixed in layers of c. 0.5–1 mm in grain size. Foliation is defined by occasional quartz ribbons, subtle compositional layering (Figura 44b) and oriented biotite, muscovite, hornblende (Figura 44c). In phase-mixed layers, quartz is found also as c. 0.1 mm round "droplets" (Figura 44a) that can locally be traced back to dismembered myrmekitic feldspar porphyroclasts. Quartz in ribbons have sutured and irregular grain boundaries, left over grains, undulose extinction and prismatic subgrains. Pinch-and-swell and cuspate grain boundaries parallel to the stretching lineation are found at quartz-feldspar contacts around ribbons (Figura 44b). Subgrain microstructure and mechanical twinning can be observed in relict feldspar porphyroclasts (Figura 44c).

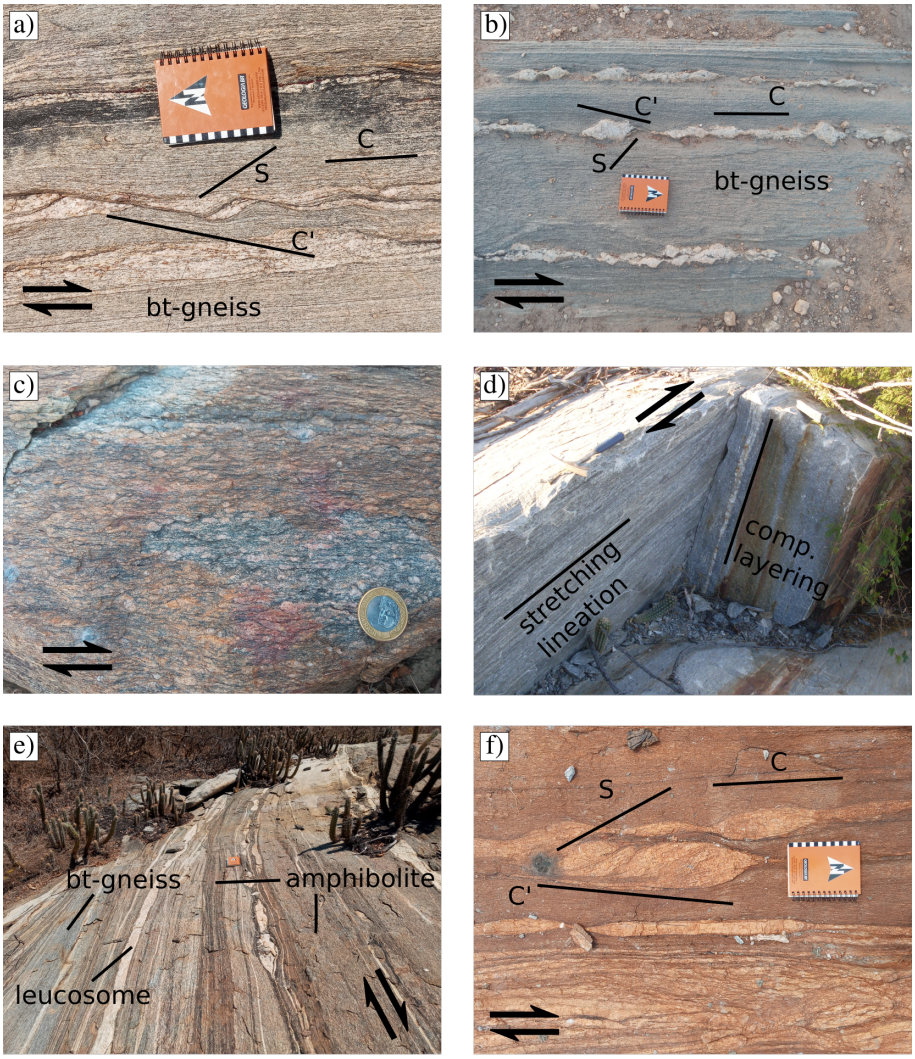

Figura 43 – a) Mylonitic biotite-gneiss showing S, C and C' foliations, and (right-lateral) boudinaged quartz-feldspar layer. b) Mylonitic biotite-gneiss with hyper-extended pegmatite dykes, S, C and C' foliations. c) Protomylonitic Serra do Deserto augen-gneiss with right-lateral σ-type porphyroclasts. d) Várzea da Onça mylonitic biotite-gneiss showing pronounced foliation (mm-scale compositional layering) and stretching lineation. Elsewhere in the same unit right-lateral σ-type porphyroclasts are found in hyper-extended pegmatite dykes. e) Interlayered amphibolitic mylonites and metagreywacke biotite-gneiss with leucosome from the Algodões-Choró metamorphic suite at the Coqueirinho fold system. f) Mylonitic biotite-gneiss with S, C and C' foliations showing right-lateral shear.

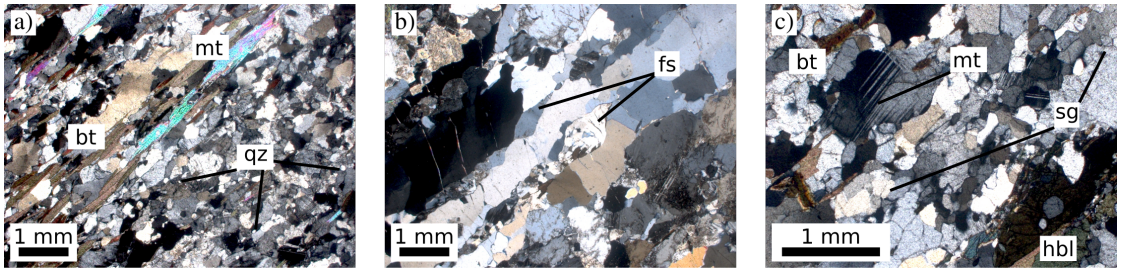

Figura 44 – Micrographs of mylonitic gneisses of the northern segment of the Senador Pompeu shear zone, displayed from north (a) towards the south (c). a) Aphyric biotite (bt)-muscovite (mt) mylonitic gneiss of metagreywacke that occurs north of the AA' cross section of Figura 42. Microstructure is dominated by mixed quartz and feldspar with average grain size of c. 0.5 mm. Quartz may form ribbons locally, and rounded quartz "droplets" of < 0.1 mm (qz) that occur mixed in quartz-feldspar layers are the product of dismembered myrmekites. b) Biotite mylonitic gneiss (sample from mylonite shown in Figura 43d). Quartz and feldspar occur in mixed layers as in a), but cuspate feldspar-quartz boundaries (fs) and feldspar pinch-and-swell structures are visible around quartz ribbons. Quartz grain boundaries are irregular to lobate, indicating grain boundary migration recrystallization. Note coarse grained quartz (c. 1 mm) in quartz ribbons. c) Biotite (bt)-hornblende (hbl) mylonitic gneiss formed from deformed amphibolite of the Algodões Choró suite (sample from mylonite shown in Figura 43e). Remaining feldspar porphyroclasts have incipient undulose extinction, subgrain microstructure (sg) and mechanical twinning (mt). Hornblende in lower right corner

Bound between the Quixeramobim and Senador Pompeu batholiths, the middle segment of the SPSZ extends for 70 km and has strong foliations consistently dipping steeply to the southeast, while stretching lineations are horizontal (see stereograms in Figura 41). The thickness of the middle segment is reduced to the south, from c. 4 km to c. 2.5 km (compare cross sections CC and DD in Figura 42). Wider lithological variations distinguish the middle segment of the SPSZ. To the northwest, it is bound by the Quixeramobim batholith (583 ± 4 Ma) which exhibits abundant syn-magmatic deformation structures (Figura 45a; Ávila et al. 2019). Garnet-bearing metagreywackes and metabasites of the Coqueirinho fold system are sheared 65 km from the northern to the middle segment (minimum offset, Figura 41), and show strong mylonitization, with right-lateral SC foliations and σ-type feldspar porphyroclasts (Figura 45b). Muscovite-

bearing leucogranites of the Senador Pompeu batholith (Figura 41) are also sheared c. 36 km into the SPSZ, and are characterized by mylonitic fabrics with distinct quartz-feldspar compositional banding (Figura 45c).

Varying degrees of mylonitization characterise strong mm to dm-scale banding in mylonites and ultramylonites of the core of the shear zone (Figura 45d), which show consistent right-lateral shear criteria. Melanocratic aphanitic layers a few centimetres thick occur within stepped openings of the host rock resembling small-scale sidewall ripouts (Figura 45e; Swanson 1989). These are characterised by the absence of compositional banding and porphyroclasts, except for a few captured from recrystallizing clasts occurring at the contacts, and are interpreted as recrystallized pseudotachylytes. At the southern parts of the middle segment, no more than 2 km from the shear zone core, basement rocks exhibit no deformation. Migmatitic gneiss of the Mombaça unit is characterised by strong steep-dipping lineations and strongly variable foliations (Figura 45f), whereas the Senador Pompeu batholith is characterised by massive and isotropic texture, indicating lack of deformation.

Although deformation microstructures vary widely at outcrop scale, mylonitic gneisses such as those in the northern segment are absent in the middle segment. Porphyroclastic schists (Figura 46a) and mylonites (Figura 46b and c) occur more commonly to the northeast. Quartz shows lobate, sutured and irregular grain boundaries and internal subgrain microstructures (Figura 46a, b and c). Through the entire length of the middle segment, however, sheared quartz veins and quartz laminae are fully recrystallized to grain sizes of 20–50 µm, dominated by straight grain boundaries, undulose extinction, subgrain microstructures and strong crystallographic textures (Figura 46d). Feldspar shows poorly developed subgrain microstructures, recrystallization and flame perthites (Figura 46b and c). Late deformation in ultramylonites where cataclasis and fracturing are observed causes quartz to recrystallize to grain sizes of c. 10 µm (Figura 46e), similar to the size of grain boundary bulges. Aphanitic striped ultramylonites occur more commonly to the southwest. Except for a small percentage of rounded feldspar porphyroclasts, all phases are fully recrystallized and comprise a mixed groundmass (Figura 46f).

An essentially discrete boundary characterises the southern segment of the SPSZ for 170 km as it bends to an EW orientation along the Cococi basin (Figura 41). It has a broadly constant thickness of c. 1 km through most of its length (EE', FF' and GG'

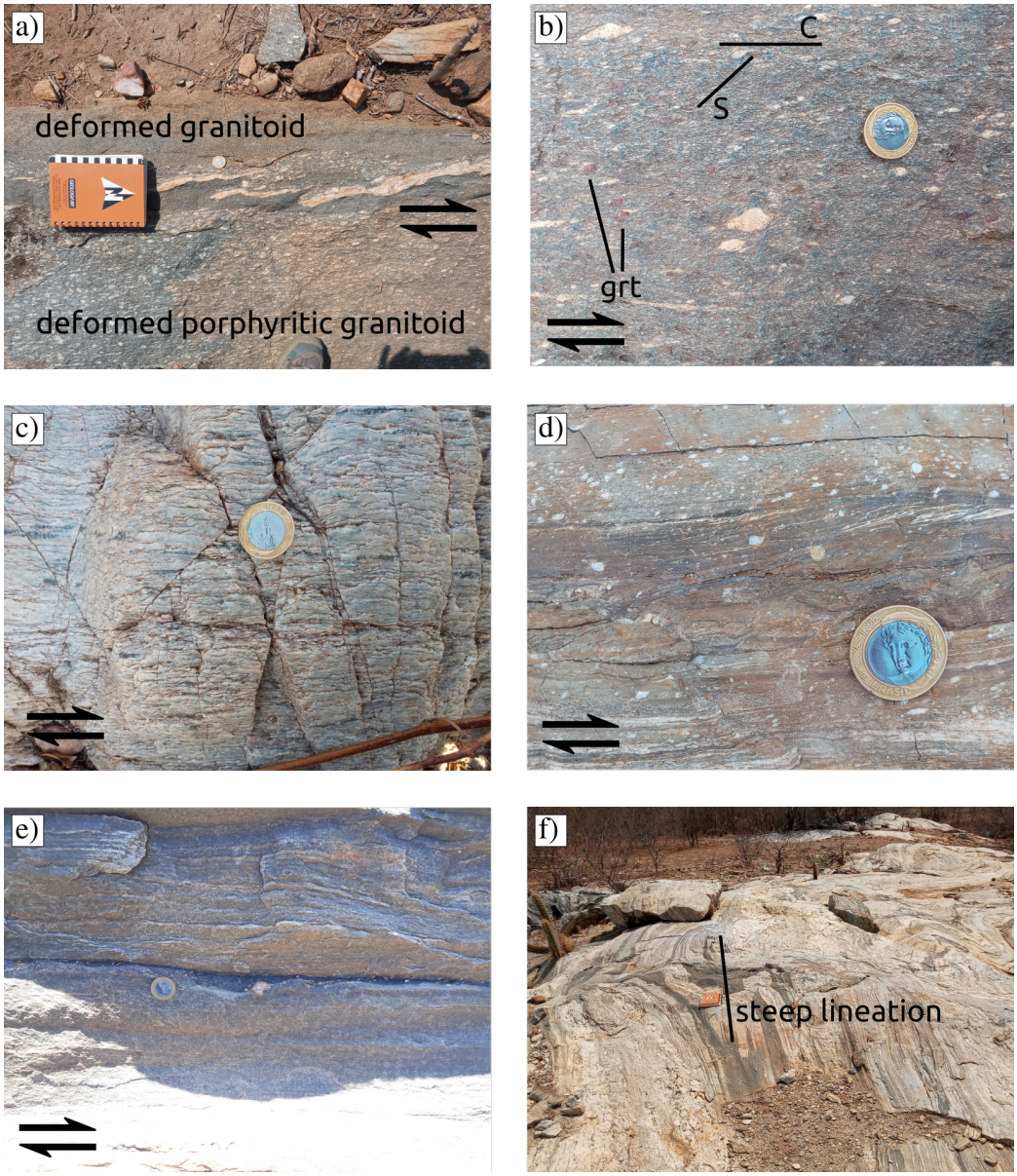

Figura 45 – a) Deformed porphyritic granitoid of the Quixeramobim batholith. b) Mylonitic garnet amphibolite of the Algodões-Choró metamorphic suite with right-lateral SC structure and σ-type feldspar porphyroclasts. c) Strongly deformed muscovite-leucogranite of the Senador Pompeu batholith. d) Ultramylonite of the core of the middle segment of the Senador Pompeu shear zone with right-lateral σ and δ-type porphyroclasts. e) Sidewall-ripout with incipient recrystallization. f) Stromatic migmatite of the Mombaça unit.

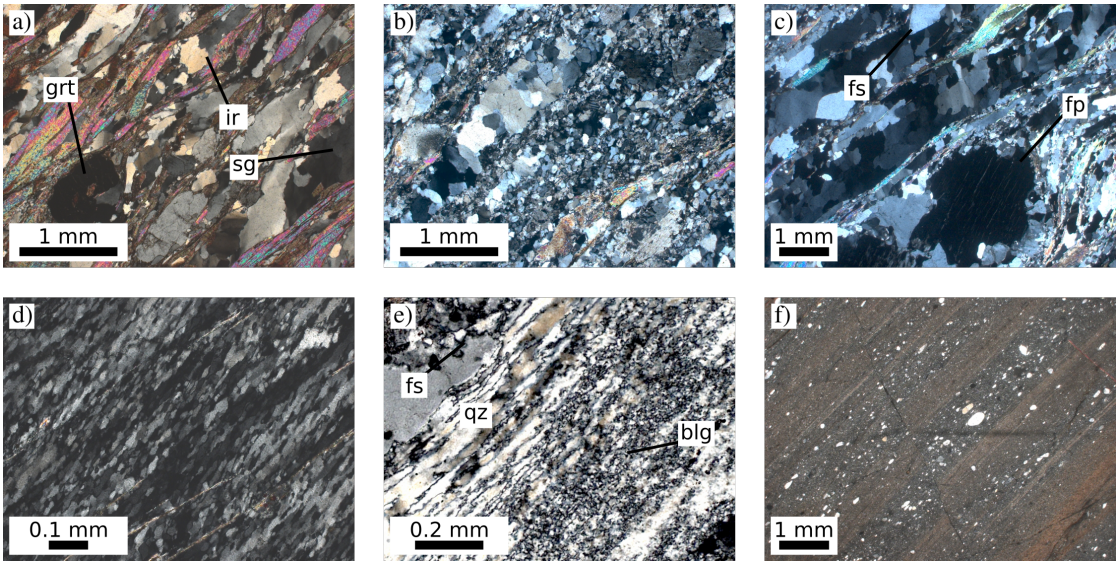

Figura 46 – Micrographs of mylonites from the middle segment of the Senador Pompeu shear zone, displayed from north (a) towards the south (f). a) Muscovite-biotite-garnet (grt) schist from metagreywacke of the Algodões-Choró unit (sample from Figura 45b). S-C foliation and asymmetric feldspar porphyroclasts show right-lateral shear. Quartz shows subgrain microstructure (sg) and sutured/irregular grain boundaries (ir). b) Muscovite bearing mylonite from the sheared Senador Pompeu batholith (sample from Figura 45c). Dynamic recrystallization affects quartz, feldspar and muscovite. c) Porphyroclastic muscovite-biotite mylonite with compositional banding. Feldspar porphyroclasts have abundant flame perthites (fp) and subgrain microstructures, and occur as fish in quartz ribbons (fs). Quartz displays sutured and lobate grain boundaries, and undulose extinction. d) Quartz vein in mica-schist showing straight grain boundaries, subgrain microstructures and right-lateral grain elongation fabric. Quartz grain size c. 15 µm. e) Quartz layer in muscovite-biotite mylonite (sample from Figura 45d). Relict quartz of 50–100 µm is elongated parallel to foliation (qz) and grain boundary bulges are c. 15 µm (blg). Feldspar shows bulges (fs). f) Striped ultramylonitic granitoid with feldspar porphyroclasts in fully mixed quartz-feldspar-mica groundmass with grain size of c. 10 µm.

cross sections in Figura 42), with foliations consistently dipping steeply to the southeast. Stretching lineations are generally horizontal or slightly northeast plunging (Figura 41). The shear zone core is composed mainly by ultramylonites, synkinematic granites, pseudotachylytes, cataclasites and breccias (Figura 42). A well-developed dextral closing

zipper is formed by the junction of the Hebrón shear zone (HSZ) with the Senador Pompeu shear zone (Figura 42 EE'). Numerous left-lateral criteria are found in porphyroclastic gneiss of the HSZ (Figura 47a). Such criteria switch abruptly to right-lateral in the core of the SPSZ, where mylonites and ultramylonites (Figura 47b) are sharply bound to the northwest by a sheared tail of the Quixeramobim batholith composed of synkinematic megacrystic granitoid (Figura 47c), thus indicating 50 km offset. Pseudotachylyte and pseudotachylitic breccias are found discontinuously in the southern strand formed within ultramylonites (Figures 47d and 47e) showing right-lateral criteria as well. Shear zone walls at this level show no sign of synchronous ductile deformation; the migmatitic basement of the Mombaça unit to the northwest shows discordant foliation and poorly developed compositional banding whereas the alkali-feldspar granite to the southeast is pervasively brecciated and chloritized (Figura 47f), but otherwise isotropic. Ultramylonites and mylonites constitute the narrow core of the shear zone towards the southwest termination (Figura 47g) where the dioritic-granitic Várzea do Lote stock occurs with deformation fabrics that indicate synkinematic emplacement (Figura 47h).

Microstructures of mylonites in the southern segment are similar to those of the mylonites in the middle segment, except for more intense recrystallization and quartz recrystallized grain sizes of $< 50\,\mu m$. Full recrystallization/comminution and thorough mixing generated aphanitic ultramylonites of various compositions (Figura 48a). Microfracturing causes segmentation of feldspar porphyroclasts and subsequent boudinage. Incipient recrystallization to grain sizes of 10–20 µm at microfractures smooths off fragments to a rounded lozenge shape. Flame perthites are abundant (Figura 48b), and quartz-rich layers mostly exhibit full recrystallization with strain-free new polygonized grains (Figura 48b). Relict quartz that may locally be preserved from recrystallization show internal subgrain microstructure and intense bulging at grain boundaries (Figura 48c).

6.5.2 Crystallographic fabrics

EBSD analyses carried out on fine-grained mylonites and ultramylonites from the middle and southern segments of the Senador Pompeu shear zone provide a direct correlation between microstructures and crystallographic orientation. Mylonitic gneisses occurring in the northern segment are coarse-grained (c. 1000 µm grain size) allowing

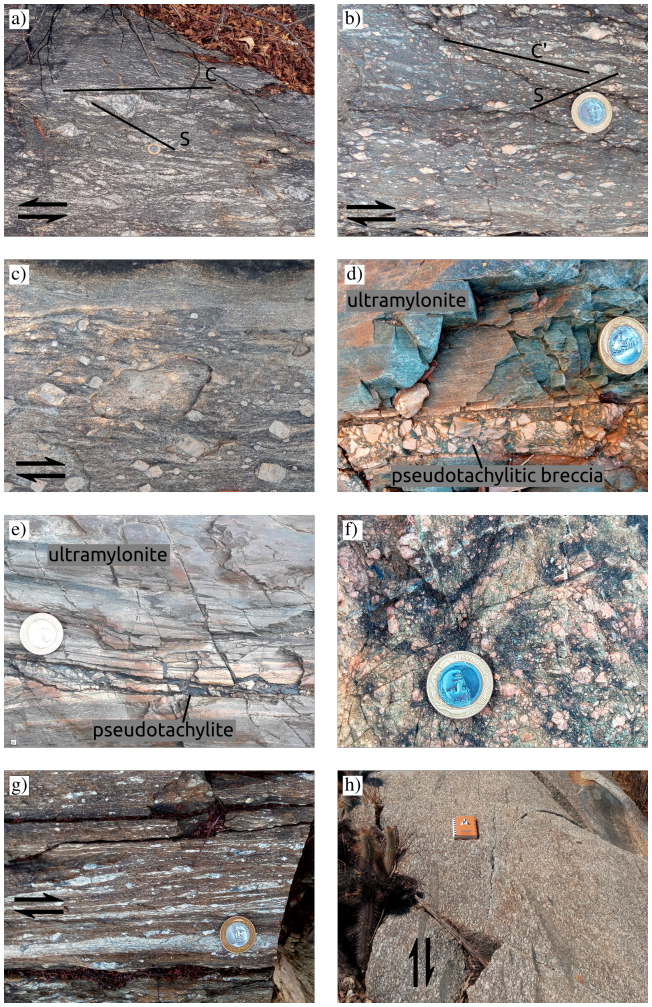

Figura 47 – Gneiss of the Hebrón shear zone with left-lateral SC foliation and σ-type porphyroclasts. b) Mylonites and ultramylonites of the Senador Pompeu shear zone with right-lateral σ-type feldspar porphyroclasts. c) Megacrystic granitoid of the Quixeramobim batholith with shape preferred orientation of feldspar megacrysts indicating magmatic deformation. d) Ultramylonite and pseudotachylitic breccia of the core of the Senador Pompeu shear zone. e) Ultramylonite and pseudotachylite of the core of the Senador Pompeu shear zone. f) Brecciated chloritized granitoid southest of the Senador Pompeu shear zone; no structures indicate ductile deformation. g) Mingled diorite and granodiorite of the Várzea do Lote granitoid showing magmatic deformation. h) Ultramylonite with σ-type porphyroclasts. See locations in Figura 42.

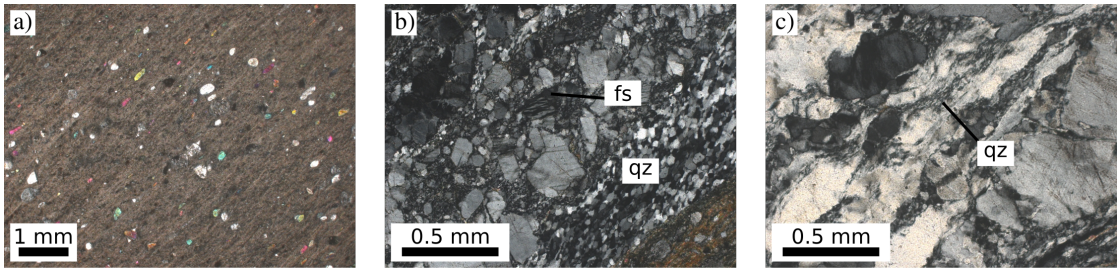

Figura 48 – Micrographs of mylonites from the southern segment of the Senador Pompeu shear zone, displayed from north (a) towards the south (f). a) Ultramylonite of intermediate-mafic composition. Feldspar and hornblende occur as rounded porphyroclasts in mixed groundmass. b) Quartz-feldspar mylonite. Feldspar porphyroclasts are intensely fractured and boudinaged, and rich in flame perthites (fs). Quartz (qz) laminae are recrystallized fully to a grain size of c. 30 µm, grain boundaries are straight and polygonal, and relict porphyroclasts have subgrain microstructures. c) Deformed quartz-feldspar gneiss. Quartz is strongly elongated to large axial ratios and has incipient recrystallization by local development of grain boundary bulges of c. 10 µm (qz). Feldspar is comminuted by microfracturing and subsequent boudinage.

⟨c⟩-axis orientations of quartz crystals to be quickly obtained with a universal stage. Figura 49 shows a representative ⟨c⟩ axis pole figure with X, Y and Z sample directions as the frame of reference where X is the lineation and Z is the pole to the foliation. While a broad XZ girdle can be distinguished, a clear ⟨c⟩ maximum exists at a low clockwise angle to X and a secondary maximum is found along Z. Fabrics of quartz in the analysed ultramylonites are represented in pole figures and inverse pole figures of the relevant directions, given in Figura 50 (arranged from southwest to northeast as left to right). The simplest crystallographic fabric found is that of CA154 in the middle segment of the SPSZ (Figures 50d and 50i), characterised by a maximum of ⟨c⟩ parallel to Z with a streak of a ZY girdle. ⟨a⟩ and ⟨m⟩ form a YX girdle with principal maxima along X and secondary maxima at the symmetrical positions (i.e. at 60° intervals). Inverse pole figures of CA154 (Figures 50n and 50s) show that Z and X, in turn, form strong single maxima parallel to ⟨c⟩ and ⟨a⟩, respectively. Samples CA155 (middle segment of SPSZ, Figures 50e and 50j) and CA159 (southern segment of SPSZ, Figures 50c and 50h) have very similar textures with a ⟨c⟩ maximum centered on Y and elongated towards Z, possibly representing a transition between a simple Y-maximum

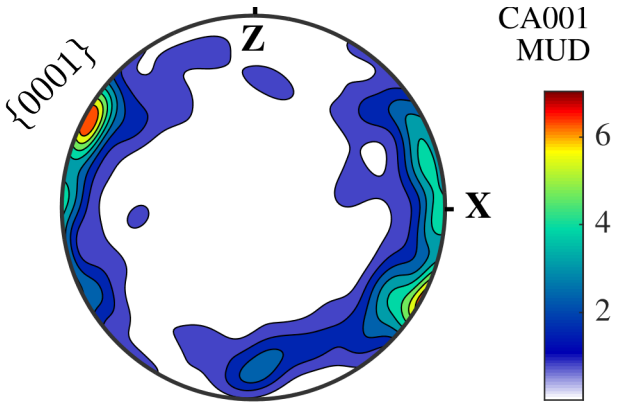

Figura 49 – Quartz ⟨c⟩ axis pole figure for sample CA001 from a mylonitic gneiss of the high-temperature segment of the Senador Pompeu shear zone (SPSZ). ⟨c⟩ axis measurements were carried out with a universal stage. Scale in multiples of uniform distribution (MUD).

and a YZ girdle (Schmid and Casey, 1986). Inverse pole figures of Z (Figures 50m and 50o) forms a very broad maximum around ⟨a⟩ and ⟨m⟩, while inverse pole figures of X (Figures 50r and 50t) show maxima at ⟨m⟩. Samples CA146 (Figures 50a and 50f) and CA148 (Figures 50b and 50g), both from the southern segment, have ⟨c⟩-axis type I crossed girdles (Schmid and Casey, 1986). They display an asymmetry concerning the fabric strength of the girdles (i.e. the girdle with a clockwise slant to X is better defined than the other). ⟨a⟩ develops a single maximum at a low clockwise angle to X, as also seen in samples CA155 and CA159. Inverse pole figures of Z (Figures 50k and 50l) show broad maxima around {r}. The X-direction for these samples (Figures 50p and 50q) have a broad maximum around ⟨a⟩ and {m}.

6.5.3 Recrystallized grain size paleopiezometry

Various piezometer calibrations for recrystallized grain size of quartz have been proposed from theoretical arguments (Twiss, 1977) and experimental data (Mercier et al., 1977). The most widely used calibration for quartz, determined by (Stipp and Tullis, 2003), is given by $D = 10^{3.56\pm0.27}\Delta\sigma^{-1.26\pm0.13}$, where $\Delta\sigma$ is the differential stress (MPa) and D is grain size (μm). This calibration was obtained from experimental deformation of quartz aggregates in which steady state flow stress was achieved. For the SPSZ, calculated grain sizes range from 5 to 21 μm, with equivalent differential stres-

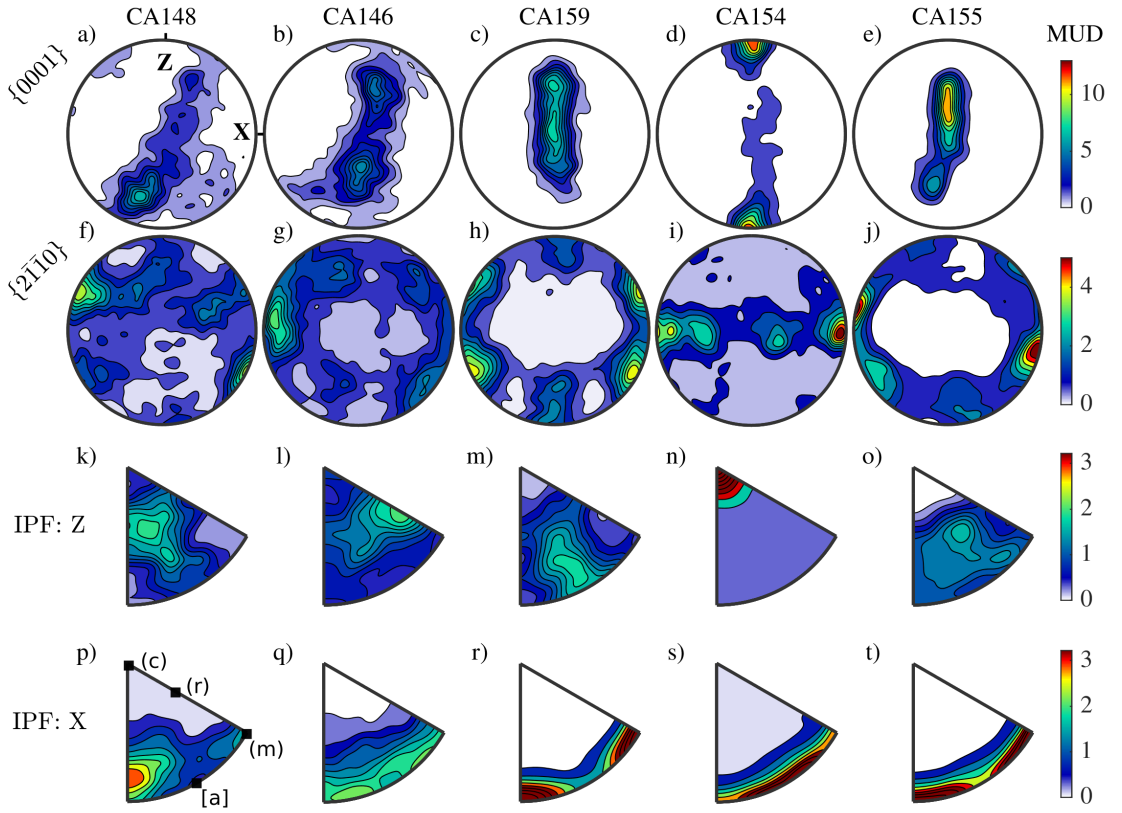

Figura 50 – Pole figures (a–j) and inverse pole figures (k–o) for quartz from mylonites from the middle and southern segments of the Senador Pompeu shear zone (SPSZ), obtained from EBSD analyses. Figures a) to e) are for ⟨c⟩ axes and f) to j) for ⟨a⟩ axes. Inverse pole figure plots the X sample direction. Samples are arranged from southwest (left) to northeast (right) along the shear zone. Scale in multiples of uniform distribution (MUD).

ses of 203 to 61 MPa (Tabela 3). Samples 148 and 146, which occur in the southern segment of the SPSZ and have grain sizes of 21 and 19 µm, respectively, yielding differential stresses of 61 and 66 MPa. Samples CA159 and CA155, from the southern and middle segments of the SPSZ, respectively, have grain sizes of 11 and 18 µm, with equivalent flow stresses 107 and 68 MPa. Sample CA154 (middle segment of SPSZ), characterised by a strong ⟨c⟩-axis fabric parallel to Z, has the lowest grain size of about 5 µm, with an equivalent calculated differential stress of 203 MPa. Although we did not conduct EBSD analyses on quartz grains from the mylonitic gneisses, grain sizes were grossly estimated from optical microscopy around 100 µm, which yields flow stresses

Sample	D_{full} [μm]	D_{recr} [μm]	D_{relict} [μm]	σ_{full} [MPa]	σ_{recr} [MPa]	σ_{relict} [MPa]
CA155	17.82 ± 9.96	12.29 ± 4.90	26.32 ± 14.40	68.02 ± 30.17	100.07 ± 28.30	58.31 ± 22.62
CA154	4.50 ± 3.54	4.62 ± 2.58	15.64 ± 10.36	202.76 ± 126.59	200.30 ± 79.33	84.35 ± 39.62
CA159	10.08 ± 7.24	5.29 ± 2.78	18.80 ± 12.85	106.90 ± 60.94	181.95 ± 67.82	74.03 ± 35.33
CA146	18.52 ± 9.84	15.91 ± 7.67	26.67 ± 11.25	65.97 ± 27.82	83.33 ± 28.50	57.78 ± 17.28
CA148	20.58 ± 12.36	14.84 ± 8.69	25.78 ± 10.45	60.67 ± 29.07	87.55 ± 36.36	59.18 ± 17.01

Tabela 3 – Recrystallized grain sizes obtained from EBSD and the corresponding estimates of flow stress according to the piezometer law of Stipp and Tullis (2003), i.e. $D = 10^{3.56\pm0.27}\sigma^{-1.26\pm0.13}$. Averages of grain sizes obtained by root mean squares (RMS). D_{full} is RMS of full population of grains reconstructed from the standard method. D_{recr} and D_{relict} are RMS of recrystallized and relict fraction of grains according to the method of Cross et al. (2017), for which the piezometer law used was $D = 10^{3.91\pm0.41}\sigma^{-1.41\pm0.21}$.

of 15–20 MPa.

A paleopiezometry calibration for quartz specific for EBSD data was developed by Cross et al. (2017) using data on recrystallized grain sizes and flow stress from the experiments of Stipp and Tullis (2003) and Stipp et al. (2006). This calibration was based on the consideration that recrystallized grains have a minimum of dislocation strain energy (this being the mechanism for softening in deforming polycrystalline materials; Doherty et al. 1997), and can thus be distinguished from relict grains on the basis of internal deformation/misorientation. A threshold value of Grain Orientation Spread (GOS) may be found that separates recrystallized from relict grains. To apply the method of Cross et al. (2017), a specific procedure of noise reduction is necessary prior to grain reconstruction as given in detail by Cross et al. (2015). Their recalibration using the data from Stipp and Tullis (2003) and Stipp et al. (2006) yields the relation $D = 10^{3.91\pm0.41}\Delta\sigma^{-1.41\pm0.21}$. This method is particularly useful for samples where there may be different population of quartz grains which have only a slight difference in grain size and cannot be distinguished in a grain size histogram, but affects the estimate of mean recrystallized grain size. Furthermore, inspection of EBSD grain maps of samples CA159, CA154 and CA155 (Figura 51) reveals possible occurrence of distinct populations of grain sizes. Recrystallized and relict grain sizes obtained via this method are given in Tabela 3. Recrystallized grain sizes are most different from those determined using the standard method for coarser grain sizes, but overall they are reduced by up to

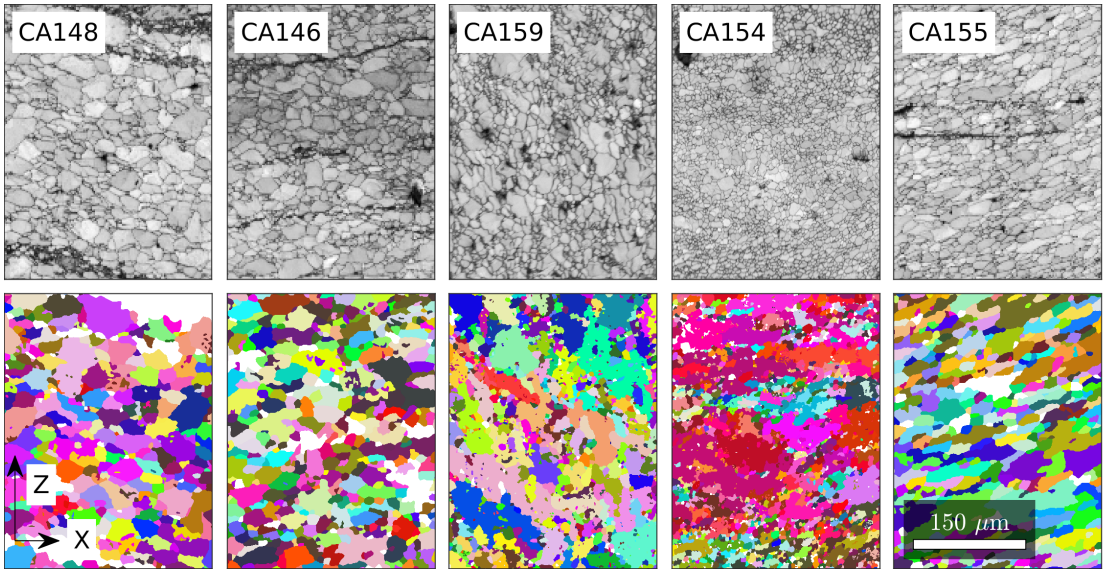

Figura 51 – EBSD maps showing CI (confidence index, top row) and reconstructed grain maps colored by orientation (bottom row).

50%. Samples CA148 and CA146 yield stresses of 79 and 74 MPa respectively. Samples CA159 and CA155 were the ones which showed a larger difference in estimated stress, with values increased to 198 and 71 MPa. Sample CA154, which had the lowest recrystallized grain size, had its differential stress estimate marginally reduced to about 199 MPa.

6.5.4 Geobarometry of syn-tectonic intrusions

Mylonites from the full length of the Senador Pompeu shear zone are monotonously granodioritic in composition and have poor quartzo-feldspathic mineral assemblages with subordinate biotite and amphibole. They are, therefore, of little use in attempts at applying geobarometry to a large set of samples. In order to further constrain the conditions of shear zone deformation we instead used Al-in-hornblende (Hammarstrom and Zen, 1986) geobarometric estimates of synkinematic plutons (Ávila et al., 2019, 2020) emplaced at positions along the Senador Pompeu shear zone as depth proxies. Hornblende is a major phase in the monzonitic Quixadá batholith located at the northern segment of the SPSZ (Figura 41). It may present occurrences of magmatic epidote (Almeida, 1995), suggesting pressure above 5 kbar (Zen and Hammarstrom, 1984). Ge-

obarometric estimates for this pluton were obtained by Nogueira (2004) and indicate crystallization at pressures of c. 5–5.5 kbar (19–20 km depth for a geobaric gradient of 0.27 kbar/km).

Hornblende is also a major phase in the dioritic facies of the Tauá batholith, located at the junction between the Senador Pompeu and Tauá shear zones (Ávila et al., 2020), in addition to the remaining components of the buffering assemblage necessary for application of the Al-in-hornblende barometer (alkali-feldspar, plagioclase, amphibole, quartz, biotite, titanite and magnetite). Electron Microprobe Analyses (EMPA) were conducted in hornblende and plagioclase from diorite sampled from the tapered SW termination of the batholith. Locations of the Quixadá and Tauá batholith samples are indicated in Figura 41.

Amphibole formulas were then calculated from EMPA data on a 23 oxygen basis, using the stoichiometric constraints outlined by Leake et al. (1997). To fill the formula ($^{X-XII}A^{VI-VII}_{0-1}B^{VI}_{2}C^{IV}_{5}T_8O_{22(OH,F,Cl)_2}$), where roman numerals indicate coordination numbers and letters indicate cation types), the all ferrous iron assumption was used initially, and then corrected with mean normalization factors to establish Fe^{3+}/Fe^{2+} values that place the formula within site occupancy limits (Leake et al., 1997). All calculated formulas plot as magnesiohornblendes, as do amphiboles for the Quixadá monzonite (Nogueira, 2004). The Al-in-hornblende calibration of Hammarstrom and Zen (1986) indicate a mean (from all the analysis points to a precision of $\pm$3 kbar) pressure of 2.3 kbar (equivalent to c. 8.5 km depth). To account for the potential effect of temperature in elevating tetrahedral Al content in amphibole due to edenite substitution (Blundy and Holland, 1990), we have applied a temperature correction within the Al-in-hornblende barometer of Anderson and Smith (1995). Using the pressure calculated with the calibration of Hammarstrom and Zen (1986), we applied the plagioclase-hornblende thermometer of Blundy and Holland (1990). Plagioclase formulas were calculated on an 8 oxygen basis, yielding mostly an andesine-oligoclase composition. Calculated temperatures range between 650 to 730 °C, with average of 675$\pm$30 °C, in good agreement with the ternary feldspar solvus of 700 °C (simulated from activity matching between plagioclase and alkali-feldspar, Figura 52; Benisek et al. 2010). With the temperature correction, the Anderson and Smith (1995) calibration indicates mean pressures of 2.8 kbar (c. 10 km depth) to an uncertainty of c. $\pm$1 kbar.

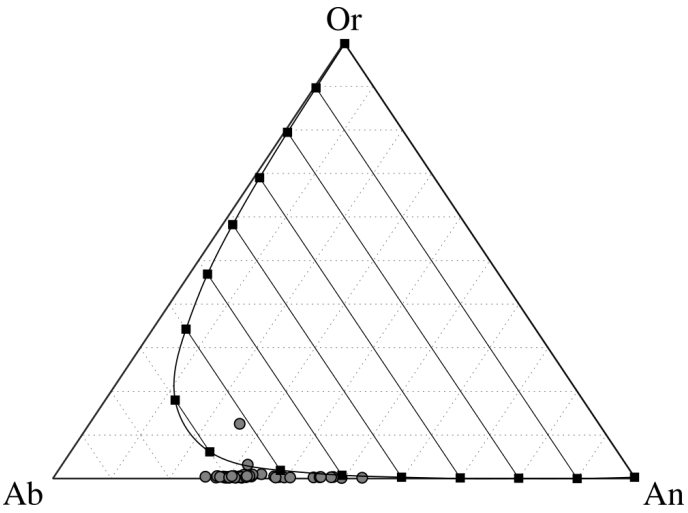

Figura 52 – Ternary feldspar diagram with 700 °C solvus calculated by activity matching between plagioclase and alkali-feldspar (Benisek et al., 2010). Grey circles are feldspar compositions calculated from Electron Microprobe Analyses of the diorite facies of the Tauá batholith. Tie lines connect exsolution compositions (black squares).

6.6 Discussions

6.6.1 Microstructures, active slip systems and deformation temperatures

Deformation mechanisms are the result of a complex interplay of temperature, strain rate, water fugacity, bulk composition, confining pressure and flow stress, such that no isolated microstructural feature should be taken as an accurate geothermometer. Nonetheless, using a range of microstructural temperature gauges from quartz, feldspar and other minerals has proven to be a successful tool in constraining conditions of deformation (Carosi et al., 2020; Mendes and Lagoeiro, 2012; Parsons et al., 2016; Pryer, 1993; Zulauf, 2001). In the Senador Pompeu shear zone, deformation mechanisms vary widely, from discrete cataclasis and seismic slip in the southern segment, to bulk plastic flow in wide regions of mylonitic gneisses in the northern segment. We have attempted to further constrain the deformation conditions of the SPSZ by using known ranges of temperature in which common deformation microstructures of quartz and feldspar are found. Below we briefly review the nature of quartz and feldspar deformation mecha-

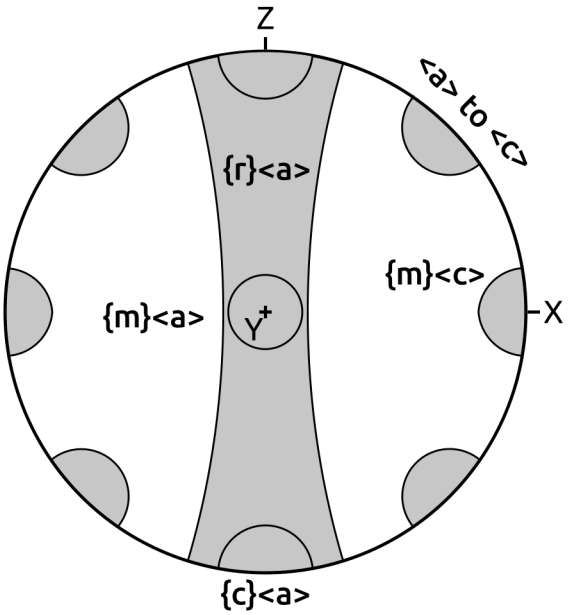

Figura 53 – Typical crystallographic preferred orientation types found in naturally deformed quartz aggregates and their corresponding dominant slip system (Schmid and Casey, 1986; Toy et al., 2008).

nisms and their temperature ranges.

Quartz recrystallization regimes as described by Stipp et al. (2002a) have become a popular guide to interpreting ranges of deformation temperature under common shear zone strain rates (10^{-13}–10^{-14} s^{-1}). Recrystallization by small-scale bulging of grain boundaries is thought to occur at the lowest temperatures, at 270–400 °C (corresponding to creep regime 1 of Hirth and Tullis, 1992), driven by differences in internal strain energy of deforming grains. At higher temperatures, dislocation climb is facilitated by increased energy for internal diffusion, and grains mostly recrystallize by the development of subgrain walls and subsequent increase in the subgrain misorientation angle. Subgrain rotation recrystallization is dominant at 400–500 °C and corresponds broadly to dislocation creep regime 2 of Hirth and Tullis (1992). At temperatures above 500 °C, grain boundary mobility is high enough that recrystallization operates by pervasive grain boundary migration (regime 3 of Hirth and Tullis, 1992).

Crystallographic preferred orientations (CPO) are the product of dislocation creep

which is controlled by specific slip systems dominating at different temperatures (Morales et al., 2014). For instance, deformation experiments on quartz single crystals have been somewhat inconclusive regarding the relative activity of slip systems at variable temperatures (Baëta and Ashbee, 1969; Hobbs, 1968). While it is clear that a shorter Burgers vector of ⟨a⟩-slip dislocations makes these more prevalent at lower temperatures, experiments showed that the critical resolved shear stress (CRSS) for the basal plane is only marginally less than that of rhomb and prism planes (Baëta and Ashbee, 1969; Bouchez and Pecher, 1981). There is also mounting evidence that transitions between typical fabric patterns can result as a function of finite strain (Heilbronner and Tullis, 2006; Muto et al., 2011; Toy et al., 2008). However, countless studies of crystallographic preferred orientations in deformed quartz aggregates have also revealed a tendency for fabric types to occur at specific temperature ranges (Wenk et al., 2019). Notably, {m}⟨c⟩ slip in quartz requires high temperatures (c. 650 °C) to be dominant and produce its distinctive fabric type, characterised by a maximum along the lineation (X axis of finite strain; Blumenfeld et al., 1986; Mainprice et al., 1986; Zulauf, 2001). Presence of sub-basal subgrain boundaries, chessboard extinction patterns, and dislocations with ⟨c⟩ Burgers vectors confirm the strong activity of this slip system under high temperatures (Blumenfeld et al., 1986; Kruhl, 2003; Mainprice et al., 1986). {c}⟨a⟩ is the dominant slip system at the other end of the temperature range for quartz plasticity, occurring in semi-brittle conditions of 270 °C (Stipp and Kunze, 2008; Zulauf, 2001), up to mid-greenschist facies conditions (Kirschner and Teyssier, 1991; Wenk et al., 2019). A strong single ⟨c⟩ maximum perpendicular to the foliation is the resulting CPO (Schmid and Casey, 1986). Comprising a temperature range between mid-greenschist facies to upper-amphibolite facies, a complex set of fabrics occurs, with broad transitions amongst them. ZY single girdles, type-I crossed girdles and type-II crossed girdles are the most common CPOs in naturally deformed quartz aggregates (Wenk et al., 2019). They result from several ⟨a⟩ slip systems being simultaneously active, dominated by {r}⟨a⟩ (Schmid and Casey, 1986). Gradual ⟨c⟩-fabric transitions are found from the typical Z maximum, through girdle fabrics, to a single Y-maximum, with a range of studies showing a tendency for the Y-maximum CPO to occur at higher, amphibolite facies temperatures (Ishii et al., 2007; Klaper, 1988; Mancktelow, 1987; Parsons et al., 2016; Schmid and Casey, 1986; Toy et al., 2008; Wenk et al., 2019; Wilson, 1975). Therefore, similar to Parsons et al. (2016), we attribute the girdle fabrics to a temperature range

of 400–500 °C, and Y-maximum fabrics to the range of 500–650 °C. The CPO types discussed above are illustrated in Figura 53. Small circles are not included here since they are generally attributed to coaxial strain (Schmid and Casey, 1986).

Cross-girdle fabrics are also conceivably sensitive to rising temperature, with Z-maxima that transition to girdles, then to peripheral conjugate c-axis maxima and finally to X-maxima (see Figura 53; Cavalcante et al. 2018; Lister and Dornsiepen 1982) This is the general basis for the c-axis opening angle (α) geothermometer (Law, 2014), which results from the progressive activation of $\{m\}\langle c\rangle$ slip, from $\{c\}\langle a\rangle$ and $\{r\}\langle a\rangle$. Fabric simulations performed by Morales et al. (2014) show that such correlation exists in a non-linear and non-predictable pattern, and the difficulties in modelling the effects of strain state and kinematics on the α led to some skepticism regarding the technique. Nonetheless, empirical data show good correlations, as shown by the latest calibration by Faleiros et al. (2016), given by $T = 6.9\alpha + 48$ (where T is temperature in degree Celsius and α is the opening angle in degrees) for $250 < T < 650$, and $T = 4.6\alpha + 258$ for $650 < T$.

Feldspar minerals however have more elusive behaviour under deformation due to metamorphic breakdown, specially at low temperatures (Stünitz, 1998). Overall, they are dominated by brittle behaviour up to 450 °C, and microfracturing is the main deformation mechanism often producing asymmetric boudins from feldspar porphyroclasts (Goscombe and Passchier, 2003). This brittle comminution may form interconnected weak layers in which the small grain size causes a switch to grain size sensitive creep (Viegas et al., 2016). Flame perthites are a common feature of feldspars deforming under greenschist facies conditions (Hippertt, 1998; Pryer and Robin, 1996; Pryer, 1993), potentially serving as indicators of paleostress directions (Pryer and Robin, 1996). Strain induced myrmekite as described by Simpson and Wintsch (1989), has been found to occur more frequently under amphibolite facies conditions (Passchier and Trouw, 2005; Pryer and Robin, 1996).

Microstructures related to dislocation creep and dynamic recrystallization in feldspar do not entirely resemble the analogues of quartz. Due to lower diffusivities, the strain threshold for the beginning of recrystallization in feldspar is lower, meaning that feldspar grains need not get severely strained for recrystallization to begin (Tullis, 1983). Still, dislocation glide in feldspar becomes active under amphibolite facies conditions. The associated recrystallization by bulging (BLG) at these temperatures (450–650 °C)

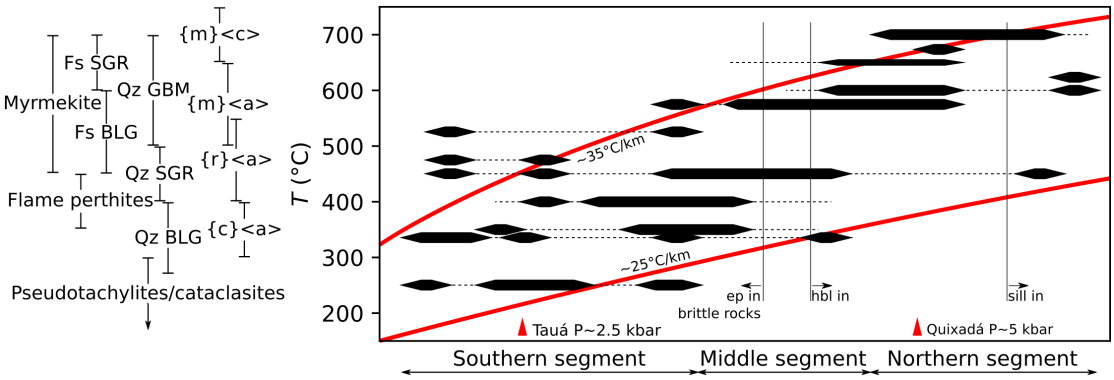

Figura 54 – Range diagram constructed from deformation microstructures of mylonites from the Senador Pompeu shear zone (SPSZ) as approximate microstructural temperature gauges. Red triangles indicate the location of normal projections of the Quixadá and Tauá batholiths on the SPSZ. Red lines are continental geothermal gradients for a "normal" crust (c. 25 °C km^{-1}) and orogenic crust (c. 35 °C km^{-1}; Vanderhaeghe 2012) placed to match the depth profile indicated by the emplacement depths of the Quixadá and Tauá batholiths.

produces typical core-and-mantle microstructures, with subordinate recrystallization by subgrain rotation. At temperatures of >650 °C, subgrain rotation (SGR) is the dominant recrystallization mechanism, accompanied by grain boundary migration (GBM). Studies of CPO of feldspar show that its lowest temperature slip system is $\{010\}\langle001\rangle$ (Egydio-Silva and Mainprice, 1999; Kruse et al., 2001).

In the SPSZ, the study of microstructural evolution along its strike was carried out with optical microscopy observations of thin sections. Results are displayed as a range diagram (Figura 54) where the thickness of ogives correspond to more pronounced deformation mechanisms in the given temperature range. The wider and longer ogives show a clear gradual increase in deformation temperature from the southern segment to the northern segment. In the southern segment, brittle deformation structures indicate deformation temperatures of less than 300 °C (displayed schematically as an ogive at 250 °C). Epidote- and chlorite-bearing ultramylonites and mylonites (Figures 47d and 4711e) on which brittle structures are developed indicate deformation temperatures of 300 to 500 °C. We attribute this range of plastic strain to earlier deformation in the southern strand, occurred at a deeper level. In the middle segment, brittle structures have not been found and deformation is accommodated by plastic flow of quartz at tempera-

tures that increase gradually from c. 300 to 500 °C, while feldspar is deformed mostly by microfracturing. Stable hornblende forms foliations in the upper half of the middle segment. Finally, in the northern segment deformation is accommodated by plastic flow and pervasive dynamic recrystallization of quartz and feldspar. Fibrolite is found locally in the far north of this segment indicating temperatures of >550 °C.

6.6.2 Flow stress

Different theoretical models have been proposed to explain the relation between flow stress and recrystallized grain size (De Bresser et al., 2001; Derby, 1991; Twiss, 1977). They are equally based on a balance between the internal strain energy of crystals due to dislocations, which drives formation of grains at a (smaller) stable grain size, and the grain boundary energy. De Bresser et al. (2001) argue that a small temperature dependence may exist in the relations of grain size piezometry, but this still requires broader confirmation. Stipp et al. (2006) concluded that water fugacity does not affect the paleopiezometric relations. However, it has become apparent that some difference in the piezometric laws may occur that is reflected in changes of recrystallization mechanism (Stipp et al., 2010). Stipp and Tullis (2003) found that aggregates in which recrystallization operated by low-temperature grain boundary migration (bulging), piezometer exponents were less than 1 (i.e. $D = 78\Delta\sigma^{-0.61}$). Grain microstructures exhibited by our samples however are characterised by straight grain boundaries, homogeneously recrystallized grains and subgrain microstructures, typical of subgrain rotation recrystallization (Stipp et al., 2002a).

Well defined crystallographic fabrics found for ultramylonite samples analysed with EBSD confirm that dominant ⟨a⟩ dislocation creep was their prevalent deformation mechanism, occurring in basal, rhomb and prism planes. The fine recrystallized grain sizes, their polygonal shapes and microstructures indicate that post-deformation static recrystallization has not largely modified grain sizes. Application of the recrystallized grain sizes paleopiezometers is thus warranted to these samples. A simple pattern of stress variation along strike is not evident. We note that the highest stress levels of 100–200 MPa are found at the transition between the southern and middle segments of the SPSZ. In the southern and middle segments, flow stress ranges between 60 and 70 MPa (70–90 MPa under the method of Cross et al. 2017). In mylonitic gneiss of the northern segment

of the SPSZ, grain sizes are very large (c. 1000 µm) and strong crystallographic fabrics provide support for deformation dominantly by dislocation creep on $\{m\}\langle c\rangle$. Such coarse grain sizes would yield flow stresses of 15–20 MPa. Thus, inferred flow stresses along the strike of the SPSZ broadly decrease away from the boundary between the middle and southern segments. Because there is consistent evidence that recrystallized grain size is independent of amount of strain and degree of recrystallization (Heilbronner and Kilian, 2017; Xia and Platt, 2018), we assume that recrystallized grain size is constant across the strike of an active shear zone, provided all other deformation conditions are constant. Thus, multiple different recrystallized grain sizes found in mylonites of a given position of the shear zone length are a record of progressive exhumation and strain localization (Behr and Platt, 2011). The estimates of flow stress using the piezometers of Stipp and Tullis (2003) and of Cross et al. (2017) are given in autoref Supplementary Material[1]. For the SPSZ grain sizes vary from 20.58 to 4.50 µm and the flow stress from 203 MPa to 61 MPa. The size of grains of the recrystallized fraction (method of Cross et al. 2017) is equal to or up 50% lower than their equivalents of the full population and gives flow stress estimates ranging from 199 to 74 MPa. Variations in average grain sizes are roughly correlated to the changes in deformation temperatures estimated from crystallographic fabrics of quartz (see previous section), i.e. samples with higher deformation temperatures have larger grain sizes. For our stress estimates, no clear monotonous variation of flow stress with distance along the SPSZ exists.

6.6.3 Pluton emplacement depth and crustal tilting

Several T-independent Al-in-hornblende barometry calibrations have been made (Hammarstrom and Zen, 1986; Hollister et al., 1987; Johnson and Rutherford, 1989; Schmidt, 1992), generally based on largely overlapping magmatic hornblende compositions across different plutons, narrow range of solidus temperatures of most felsic magmas, and low P sensitivity of solidus above 2 kbar (Anderson and Smith, 1995; Hammarstrom and Zen, 1986). However, Anderson and Smith (1995) showed a distinct modification of Al content in hornblende due to T-dependent edenite substitution and f_{O_2}-dependent Fe^{3+} exchange, and found that the barometer is most applicable for $Fe_{tot}/(Fe_{tot}+Mg)$ composition (a proxy for f_{O_2}) in the range of 0.4–0.65 and anorthite

[1] Appendix C

content of plagioclase of 0.25–0.35. Both conditions are satisfied for the Tauá batholith (see Supplementary Material). For the sake of thoroughness, we applied both barometers, but no appreciable difference was found. Crystallization pressures of 2.3 and 2.8 kbar were calculated with the barometer of Hammarstrom and Zen (1986) and Anderson and Smith (1995), respectively (an emplacement depth of 8.5–10 km).

Al-in-hornblende analyses carried out by Nogueira (2004) showed that the Quixadá batholith located at the NE end of the SPSZ was emplaced under a pressure of 5.0–5.5 kbar (i.e. a depth around 18 km). The Quixadá-Quixeramobim complex indeed has a variety of deformation structures indicating strong coupling with the wall rocks, a characteristic of magmas emplaced in a deforming lower crust (Archanjo et al., 2002), a feature of deep-seated plutons (Zen and Hammarstrom, 1984). The Tauá suite is composed mostly of fine-grained dioritic facies weakly coupled to the wall rocks that overall indicate a shallow emplacement. If that can be confirmed it may be argued that the present section of the crust exposed in the area of study is tilted, exposing higher depths to the NE (e.g. Quixadá batholith) and lower depths to the SW, as revealed by the c. 10 km difference in emplacement depth. This depth interval comprises conditions of plastic deformation of quartz in the mid-lower crust, through the viscous-frictional transition (c. 10–15 km; Bürgmann and Dresen 2008; Wallis et al. 2013), to very shallow brittle deformation in the seismogenic layer of the crust.

Two trivial interpretations can be drawn for the systematic variation of deformation temperature and mechanisms along the strike of the Senador Pompeu shear zone, as well as the difference in emplacement depth of synchronous batholiths: i) post-orogenic tilting of the crust and subsequent erosion/exhumation brought the deeper crust to the north to the same exposure level as the shallower crust to the south (e.g. “hinged” uplift; Cook and Crawford 1994); ii) gradual “flat” exhumation of the Ceará Central domain and low-T/brittle strike-slip reactivation of only the southern segment. On a structural/microstructural basis, the former is more likely due to the gradual variations along strike. Furthermore, it was shown that all shear-zone bounded plutons related to the Senador Pompeu and Tauá shear zones are synchronous within the uncertainty (Ávila et al., 2019, 2020). Extreme examples of crustal sections tilted by as much as 30° have been found elsewhere on the basis of depth of emplacement of synchronous plutonic complexes obtained through geobarometry (Butler et al., 1989; Cook and Crawford, 1994; Zulauf, 2001). A 3° tilt can explain the 10 km difference in depth of emplacement for

the Quixadá and Tauá batholiths, which are distant by c. 195 km. It would have affected the orientation of the subhorizontal stretching lineation, but the variability is too large and the tilt too low for any such effect to be detected (see stereograms in Figura 41), giving no false indication of a dip-slip component. Tilted sections of the crust may thus be more common than expected but go largely unrecognised due to the absence of sufficient data coverage and studies focused specifically on this issue (Axen et al., 1998). Interpreting the features outlined here as a product of "flat" exhumation would require that the deformation of the southern segment be a product of later reactivation. This would cause the northern segment to be essentially and abruptly disconnected, with structures of strain transfer and dissipation (e.g. horstail splays and shear zone terminations) present in between. Such structures do not occur, and instead the transition between fabrics of the southern segment to those of the middle segment are penetrative and continuous. Furthermore, if flat exhumation were the case, the northern, 15–20 km wide shear zone would also have existed in the southern segment prior to low-temperature reactivation which would be evident as a form of progressive strain localization (West and Hubbard, 1997). Instead, the c. 1 km wide shear zone of the southern segment is found between migmatitic basement rocks with unrelated fabrics (e.g. flat-lying foliations), in no way similar to mylonitic gneisses of the northern segment.

It is unclear what might have caused post-orogenic crustal tilting. Flexure of the lithosphere due (i) to the overburden of the Paleozoic Parnaíba basin to the SW, (ii) margin uplift to the NE due to opening of the Atlantic Ocean (Gilchrist and Summerfield, 1990; Peulvast et al., 2008), and (iii) regional uplift related to Meso-Cenozoic Mecejana (Fernando de Noronha hostspot in northern Ceará) and Macau magmatisms in the NNE Borborema Province (e.g., Knesel et al., 2011; Mizusaki et al., 2002) are all mechanisms that may cause differential uplift of the northeast continental margin. Indeed, despite being in the same erosional surface (i.e. same altitude), apatite fission-track ages of the Ceará Central domain increase away from the shoreline, from Meso-Cenozoic (130–90 and 30 Ma; Cavalcante 2006) in the northern segment, to Early Carboniferous–Late Triassic (c. 350–230 Ma; Godoy 2010) in the south. Margin uplift modelling and empirical data (Gallagher et al., 1994; Gilchrist and Summerfield, 1990; Sacek et al., 2019), however, show that differential denudation towards the margin is generally from a few hundred meters to c. 2 km. Thus, these processes of lithosphere flexure in the Phanerozoic probably had their contribution, but we argue that most of the apparent crustal

tilt revealed in the Senador Pompeu shear zone was created soon after orogenesis and prior to formation of the Cococi basin at 530 Ma (Ganade de Araujo et al., 2012; Garcia et al., 2018).

6.6.4 Simulating shear zone width as a function of depth

Supported by the systematic decrease in deformation temperature and width of the Senador Pompeu shear zone to the southwest, and by the difference in structural level indicated by the Al-in-hornblende barometry of the synchronous Quixadá and Tauá batholiths (found c. 195 km apart horizontally and c. 10 km vertically; Ávila et al. 2020), we attempted to implement a simulation of shear zone width variation with depth that fits the general aspect of the Senador Pompeu shear zone.

This simulation is grounded on a hypothesis of constant stress elaborated by Platt and Behr (2011c) which we briefly describe here. For a deep transcurrent shear zone bounding lithospheric blocks that move with a relative velocity of V, the total width w of the active shear zone is given by $w = V/\dot{\gamma}$, where $\dot{\gamma}$ is the shear strain rate. Tensor strain rate of viscous flow is given by the Dorn creep equation $\dot{\varepsilon} = A f_{H_2O}^m \sigma^n \exp(-Q/RT)$, where A is the pre-exponential constant, f_{H_2O} is the water fugacity, m is the fugacity exponent, σ is the flow stress, n is the stress exponent, Q is the activation energy, R is the gas constant and T is deformation temperature. If we assume the flow stress to be buffered at the yield stress of intact crust (σ_y) at a given depth, and by making $C = A f_{H_2O} \exp(-Q/RT)$, we may substitute the Dorn creep equation for the shear strain rate and obtain $w = V/2C\sigma_y^n$. If flow stress in the shear zone overcomes σ_y (by e.g. post-seismic stress transfer; Wright et al. 2013), the width relation would yield a transient drop in w since a higher stress would cause the wall rocks to deform, thereby increasing the width back to the buffered value. Weakening as a result of transition of deformation mechanisms should lead to localization, i.e. to reduction in w. If V is assumed to be fixed, the yield stress which buffers the width of shear zones can be found by means of characterizing a local strength profile of the crust (Behr and Platt, 2011).

By calculating a frictional criterion for the seismogenic top layer of the crust (Imber et al., 2001; Sibson, 1974), and using widely known and applied experimentally determined flow law parameters for dominant phases in the crust (Hirth et al., 2001; Paterson and Luan, 1990; Rutter and Brodie, 2004; Tokle et al., 2019), typical strength-

depth profiles for quartzofeldspathic crust can be constructed (Bürgmann and Dresen, 2008; Burov and Watts, 2006). Since we are primarily concerned with the top 30 km of the crust we do not address potential rheological stratification (i.e. transition between quartz-dominated to feldspar-dominated; Janecke and Evans 1988). In our implementation of the Dorn creep we use quartz flow parameters determined by Hirth et al. (2001). Theoretical solutions for the dependence of on depth are fairly difficult to implement and we instead repeat the approach of Shinevar et al. (2015) by which a depth profile is interpolated through a dataset of created at different values of pressure and temperature using the Withers' fugacity calculator (based on the equation of state of Pitzer and Sterner 1995; https://www.esci.umn.edu/people/researchers/withe012/fugacity.htm; see Figura 55a). A normal geotherm (Figura 55a) is calculated by solving steady state crustal heat transfer and the resulting strength profile is shown in Figura 55b for strain rates of 10^{-16} s^{-1} to 10^{-13} s^{-1}. The frictional criterion shown in Figura 55b follows Byerlee's law (internal friction of 0.85; Byerlee et al. 1978) for a pore fluid pressure ratio of 0.4 in transcurrent and thrust regimes (Sibson, 1974), and the frictional-viscous transition occurs at 10 km for a strain rate of 10^{-16} s^{-1} and 15 km for 10^{-13} s^{-1}.

For the Senador Pompeu shear zone, we plot stress estimates from the paleopiezometers (Tabela 3) assuming depths at the shear zone by projecting those measured for the Tauá and Quixadá batholiths transversely from the shear zone midline. Paleopiezometer uncertainties are calculated taking into account only grain size uncertainties, as done by Behr and Platt (2011). Because progressive exhumation may have affected the shear zone throughout, at a given depth, only the maximum stress (minimum temperature) estimate is valid for the last prominent deformation episode. Thus, the paleopiezometer estimates that best fit the correct flow stress profile should be the deepest. If our hypothesis regarding the projected depth of the Quixadá and Tauá batholiths is correct, it can be seen that the paleopiezometer estimates best fit flow stress profiles for strain rates between 10^{-14} s^{-1} and 10^{-15} s^{-1}. Dynamic recrystallization is now widely regarded as the primary mechanism by which strain localization occurs (De Bresser et al., 2001; Tullis and Yund, 1985; White et al., 1980). After a narrow region of intact rock starts deforming in the middle crust and recrystallization takes place, the bulk rheology is affected by the deformation mechanism of the finely recrystallized material and becomes grain size sensitive (Platt, 2015a). Platt and Behr (2011b) derived a recrystallization-accommodated creep law (DRX) which is appropriate for middle crus-

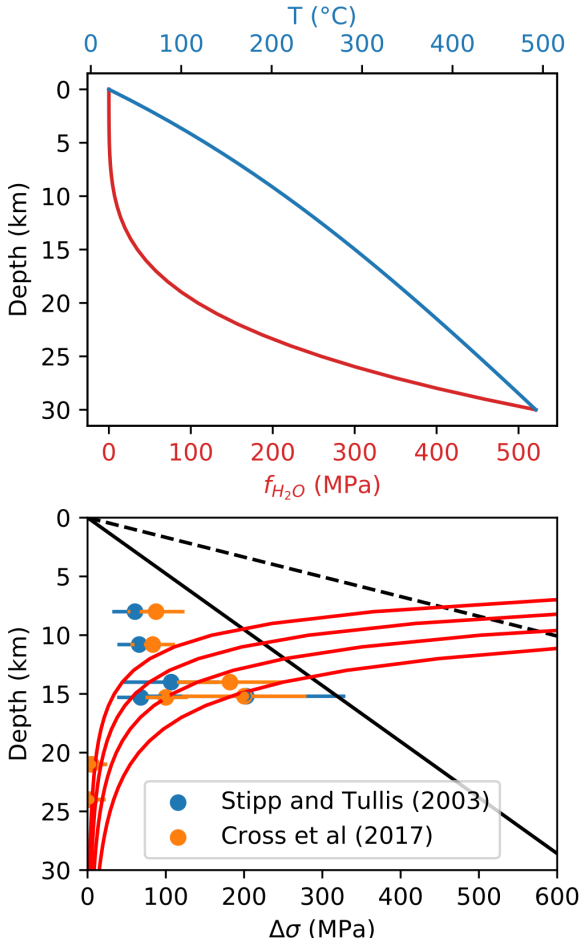

Figura 55 – a) Water fugacity (red) is interpolated through a dataset of f_{H_2O} created at different values of pressure and temperature using the Withers' fugacity calculator (based on the equation of state of Pitzer and Sterner 1995; https://www.esci.umn.edu/people/researchers/withe012/fugacity.htm. A normal geotherm is calculated by solving a steady state geotherm for the crust ($T = T_s + [(zq_m)/k] + [(q_s - q_m)h_r/k][1 - \exp(-z/h_r)]$), similar to that shown in Figura 54 at a gradient of c. 25 °C km^{-1}. b) Black lines show frictional criteria using Byerlee's law (internal friction of 0.85; Byerlee et al. 1978) for wrench (solid black line) and thrust (dashed black line) faults (Sibson, 1974). The viscous flow curves are calculated with quartz flow parameters determined by Hirth et al. (2001) and strain rates of 10^{-16} s^{-1} (with the shallowest brittle-ductile transition), 10^{-15} s^{-1}, 10^{-14} s^{-1}, 10^{-13} s^{-1} (with the deepest brittle-ductile transition).

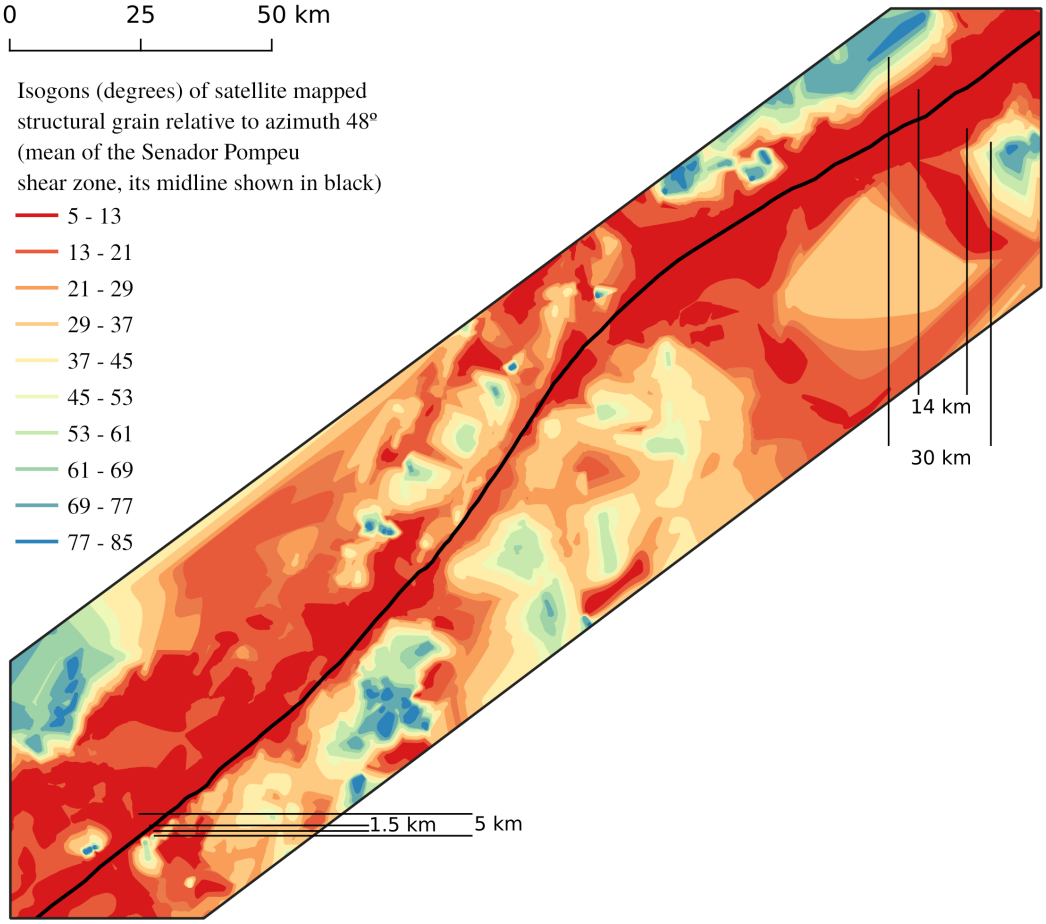

Figura 56 – Fabric isogon map around the Senador Pompeu shear zone, extracted from structural grain in satellite imagery. See map location in Figura 41.

tal levels in which quartz is the dominating phase. With this modification, cumulative shear zone widths for variable slip rates (V, Figura 57) were calculated by $w = VD/2\dot{\varepsilon}$, where D is recrystallized grain size (flow parameters for the DRX law can be found in Platt and Behr 2011c).

In theory, measuring the width of a shear zone can be a simple matter of determining the width in which basement rock units become deflected. It is often difficult to unequivocally map a geological unit that straddles the shear zone to the necessary scale for the purpose of measuring width, and this is complicated further by typical strain gradients. Fabric isogon maps show the deflection of pre-existing wall rock fabrics towards the shear zone, from a "far field" value (Ramsay and Graham, 1970; Ramsay and Huber,

1983), and can be used to indicate shear zone width. In Figura 56 a fabric isogon map is constructed around the Senador Pompeu shear zone, where basement fabrics were extracted from the structural grain mapped from satellite imagery. In this procedure, the three-dimensional orientation of fabric is reduced to its trace at the surface. This leads to ambiguities since basement fabrics may be near-horizontal with a similar strike to that of the shear zone core (e.g. see Figura 42 DD'). Thus, fabric isogon maps can only be used as a rough indication and regarded as useful where basement fabrics are steep. For instance, in the northern part of the Senador Pompeu shear zone, deflection of basement fabric towards the shear zone can be identified from the isogon map (Figura 56) in a width of 30 km, whereas an easily identifiable (from satellite imagery) shear corridor with parallel penetrative foliations occurs in a width of as much as 14 km. Furthermore, the active width of a shear zone at a given stage may be lower than the total width of the shear zone. In the southern segment, low-temperature mylonites (Figura 47d), which comprise a narrow width (1.5 km in Figura 56), transition rapidly to migmatitic wall rock with flat-lying foliation (beyond the wider shear zone-parallel high-temperature tectonite zone of 5 km in Figura 56). Therefore, our measurements of width, however approximate, take into account deflection of basement fabric, and the temperature of deformation that characterizes the active width through a consistent length.

Figura 57 shows the simulated widths compared with the width of the Senador Pompeu shear zone measured using satellite imagery (minimum) and fabric isogon maps (maximum). For simplicity, we extrapolated simulated shear zone widths to the surface in Figura 57, despite the frictional-viscous transition being at about 12 km depth. Figures 57a and 57b show that the cumulative shear zone widths for strain rates of 10^{-13}–10^{-14} s^{-1} are in general too low and at any structural level much less than minimum shear zone widths measured for the Senador Pompeu shear zone, even at very high slip rates (50 mm/yr). On the other end, a strain rate of 10^{-16} s^{-1} (Figura 57d) is too low to begin with for a shear zone. For the more appropriate strain rates of 10^{-14} s^{-1} (Figura 57b) and 10^{-15} s^{-1} (Figura 57c) the slip rate of 50 mm/yr produces a width profile that best fits the minimum width of the Senador Pompeu shear zone. For a demonstration of reproducibility of the simulation compare the 50 mm/yr curves of Figura 57 with those in Platt and Behr (2011c).

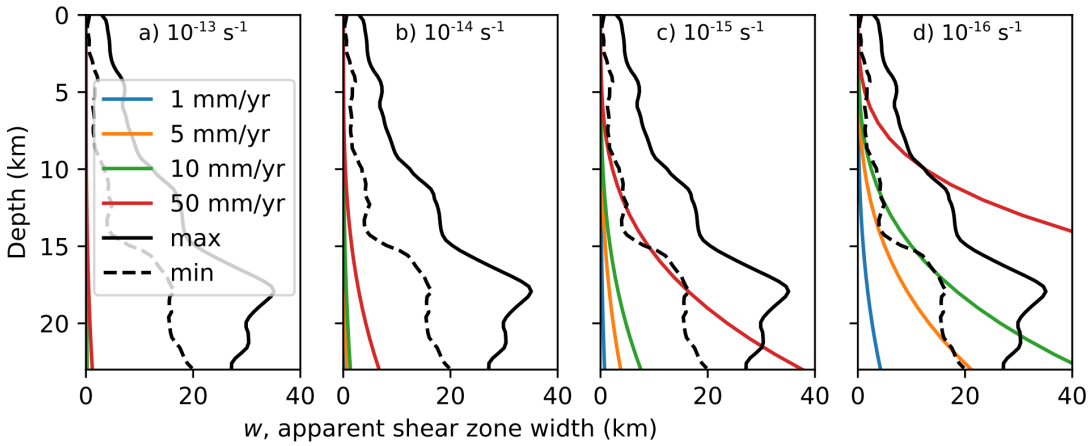

Figura 57 – Cumulative shear zone widths for variable strain rates (a - 10^{-13} to d - 10^{-16} s^{-1}) and slip rates (1 - blue, 5 - orange, 10 - green to 50 mm/yr - red). Solid black line is the maximum width of the Senador Pompeu shear zone (SPSZ) measured in GIS using fabric isogon maps. Dashed black line is the minimum width of the most distinct shear corridor of the SPSZ measured with satellite imagery and field relations. Notice that while we extrapolate shear zone widths up to the surface, the frictional viscous transition is located at around 12 km depth (Figura 55b), above which the true shear zone will not be much wider than just the discrete zone of brittle damage.

6.6.5 Zippered segments and reversed kinematics

From detailed geological mapping and careful observation of kinematic criteria in mylonites, zippered shear zone segments (Ávila et al., 2019; Fossen et al., 2014; Froitzheim et al., 2006; Passchier and Platt, 2017; Platt and Passchier, 2016) have been identified through the length of the SPSZ (Figura 41). On the basis of considerations of total offset and geometry of the conjugate Senador Pompeu and Tauá shear zones, Ávila et al. (2019) concluded that the Cococi shear zone (the core of which is currently buried beneath the Cococi basin) formed as a dextral closing zipper, causing the internal Ceará Central domain to be extruded to the northeast. The left-lateral Hebrón shear zone merges into the SPSZ at the transition between the southern and middle segment. No more than 1 km SE of the SPSZ, numerous left-lateral kinematic criteria were observed in sheared gneisses of the Acopiara Complex in the Orós-Jaguaribe terrane, including rotated σ-type porphyroclasts, S-C foliation and shear band boudinage (Fi-

gura 47a). Kinematic criteria change abruptly to right-lateral towards the core of the SPSZ (Figures 47b and 47c). A dextral closing zipper is therefore formed NE of the junction between the Hebrón and Senador Pompeu shear zones, despite the poor overall expression of the Hebrón shear zone in a map scale (i.e. no strong deflection of rock units is exhibited about it). Similarly, a dextral closing zipper formed to the NE of the junction between the Senador Pompeu shear zone and the north-striking and Orós shear zone (Figura 41). These branching shear zones interacting with the Senador Pompeu shear zone indicate that when investigating the kinematics of a shear zone system, it is fundamental to carry out sufficiently detailed structural mapping in order to identify reversed kinematics that can mark zippered segments, where deformation structures that indicate opposing shear senses (Dutta and Mukherjee, 2019) have been juxtaposed. Reversed kinematics (left-lateral kinematic indicators) have indeed been found locally at the Senador Pompeu shear zone. Hippertt and Tohver (1999) attributed it to marked rheological contrasts between layers that cause extreme strain localizations and departure from the dominating kinematics, whereas Almeida (1995) has interpreted two distinct phases of deformation in the Senador Pompeu shear zone, the first being left-lateral and necessary for generating tension fractures that allowed the emplacement of the Quixadá and Quixeramobim batholiths.

6.6.6 Tectonic implications

Due to lack of broader datasets on cooling rates throughout the Borborema Province, or determinations of deformation temperature that comprise the full length of the Senador Pompeu shear zone, our model outlined above regarding a potential slight tilt of the crust and exhumation of the fault zone profile cannot be used as a specific measure of slip rates or strain rates. However, it allows us to impose plausible upper and lower limits to these parameters that can serve as constraints on timing and longevity of the shear zone. Calculating shear zone widths in order to strengthen the underlying theory may be a goal in itself but in this study, we are particularly interested in using the model to impose the first constraints to longevity of shear zones in the Borborema Pronvince. From what could be interpreted in Figura 57, it is clear that a slip rate of 50 mm/yr for the Senador Pompeu shear zone can only be taken as an upper limit, while a slip rate of 1 mm/yr is exceptionally low. Indeed, slip rates as high as 30–50 mm/yr

are mostly typical of plate boundary continental transform shear zones such as the San Andreas fault (35–50 mm/yr; van der Woerd et al. 2006), the Alpine fault zone (c. 35 mm/yr; Norris and Cooper 2003; Sutherland 1994) and the Oligo-Miocene Ailao Shan-Red River shear zone (29–53 mm/yr; Sassier et al. 2009). Intracontinental shear zones have generally lower slip rates (Vauchez et al., 1995). In Tibet, for example, the most prominent shear zones have plate boundary magnitudes (e.f. >1500 km in length), and their slip rate estimates are generally lower than 30 mm/yr (Tapponnier et al., 2001). The most prominent shear zones may have slip rates of up to 30 mm/yr, but measurements may vary widely (e.g. 5–30 mm/yr for the Altyn Tagh and Karakoram faults; Daout et al., 2018; Searle et al., 2011). Shorter and more internal shear zones of Tibet have lower slip rates of 5–10 mm/yr (Taylor and Peltzer, 2006; Thatcher, 2007).

Longevity, total offset and long-term slip rates of the shear zones in the Borborema Province have not yet been determined with accuracy. However, even broad estimates of these parameters are fundamental to tectonic interpretations. For example, in the Borborema Province, crustal evolution studies indicate a significant longevity for the regional transcurrent shear zone system of 50–100 Myr (Ganade de Araujo et al., 2014c; Miranda et al., 2020; Vauchez et al., 1995). These studies are often based on the ages and cross-cutting relations of large tectonic units and don't account for the actual deformation of the shear zones. Tectonic reconstructions of the pre-drift West Gondwana (Archanjo et al., 2013) show that the Pernambuco, Patos and Senador Pompeu shear zones are potentially continuous with major shear shear zones of the Nigerian Province and Dahomeyan Belt (Arthaud et al., 2008; Caby, 1989), and have been acknowledged as the most prominent terrane-bounding lineaments of the Borborema Province from which the highest long term slip rates can be expected. Geological units deformed by the Senador Pompeu shear zone, as seen in the detailed map of Figura 41, show total offsets ranging from 50 to 73 km. For instance, the Quixeramobim batholith has a tail offset by c. 50 km composed of megacrystic granitoid with strong magmatic deformation structures (megacrystic shape preferred orientation) and only incipient solid state deformation. The banded amphibolites and metagreywackes of the Rhyacian greenstone that occur at the Coqueirinho fold system are offset by 65 km. The grey gneisses of the Ceará Complex are offset by 73 km (see offsets in Figura 41). These fairly high offsets make the Senador Pompeu the most prominent strike-slip discontinuity of the Northern Borborema Province. Considering the total offset measured from the sheared geological

units (50 to 73 km), the longevity of the Senador Pompeu shear zone is less than 15 Myr for an average slip rate of 5 mm/yr, whereas for a slip rate of 50 mm/yr total offset could have accumulated in 1 Myr. For the most reasonable slip rate of 10 mm/yr, slip must have occurred in 5 to 7.3 Myr. Alternatively, if the shear zone profile exposed today is the product of deformation occurring during flat exhumation, Ar-Ar cooling ages of biotite (through c. 315 °C) should constrain the minimum age of low-temperature deformation and therefore the longevity of the shear zone. Existing thermochronology data suggests (Ávila et al., 2020) that biotite cooling in the transcurrent shear zones of the Ceará Central domain occurred around 560 Ma. Shear deformation would therefore be constrained between 584 and 560 Ma, yielding a minimum average slip rate of 3 mm/yr.

Ages of crystallization of shear zone bounded plutons (Quixadá and Quixeramobim batholiths) emplaced during shear deformation were determined by (Ávila et al., 2019) at 584 ± 5 Ma. This was interpreted as a timing constraint of high-temperature deformation that formed mylonitic gneisses of the northern segment. In light of the data presented here, it is probable that deformation in the Senador Pompeu shear zone occurred in an interval of c. 10 Myr, probably between 585 and 575 Ma. The Várzea do Boi stock, which intrudes the Tauá batholith, has an ambiguous crystallization age of 571 Ma and magnetic fabrics that indicate emplacement under a stress field consistent with that of deformation in the Tauá-Senador Pompeu shear system (Ávila et al., 2020). This age, although uncertain, indicates that emplacement of the Várzea do Boi stock magmas occurred during a very weak waning stage of strike-slip deformation, as already suspected by Ávila et al. (2020).

Although some of the discussions made here remain conjectural due to the lack of data, it outlines several large-scale structural features of the Senador Pompeu shear zone, and those shear zones that interact with it, into a consistent framework. Most importantly, it constrains the shear zone longevity to 584–574 Ma, with accumulated offset of 50–75 km. This model would largely benefit from comprehensive geochronological data on brittle deformation and thermobarometric studies of shear deformation through a significant length of the shear zone. Also, further investigations of the shear zones of the Borborema Province should not overlook the value of detailed field work and geological-structural mapping as these reveal many hidden complexities of the evolution of these domain boundaries. Nonetheless, our study can be equally well applied to other large-scale lineaments of the Borborema Province such as the Patos and Per-

nambuco shear zones with the intent of bracketing their longevities. This may prove an important detail in tectonic interpretations; the Borborema Province is often treated as an analogue of tectonic escape (Archanjo et al., 2021; Ganade de Araujo et al., 2014c). As outlined here for the Senador Pompeu shear zone, its total offset falls significantly short of that of the dominant shear zone boundaries of the Himalayan orogenic system (over 100 km for the active Karakoram and Altyn Tagh faults, and up to 700 km for the Oligo-Miocene Ailao Shan-Red River shear zone; Sassier et al. 2009; Searle et al. 2011). Despite the pronounced development of the Borborema shear zone network, in its northern domains the results presented here suggest that it has only accommodated a small amount of orogenic deformation. However, the Borborema Province is well known for diachronous and very diverse tectonic histories. While extreme metamorphic pressures and fast cooling rates are found in the Ceará Central Domain, extensive records are found for low-P/high-T metamorphism and low cooling rates in the eastern Patos lineament (Archanjo et al., 2013; Ávila et al., 2020; Corsini et al., 1998). Ganade et al. (2021b) interpreted an offset of 200 km for the Pernambuco lineament based on displaced lithological units. Age patterns of units deformed by the Patos shear zone also point to significant offsets (Archanjo et al., 2021). Further structural evolution studies are required in the Patos and Penambuco lineaments to constrain their offset and longevities.

6.7 Conclusions

A clear systematic along-strike variation that exists in the style of mylonitization, dominant shear zone rocks and shear zone width in the right-lateral Senador Pompeu shear zone warranted a study of its rheology and deformation processes to an unprecedented level of detail in the Borborema Province. In particular, we were able to identify three distinct structural domains/shear zone segments: i) the northern segment, characterised by a width of more than 15 km and by the ubiquitous presence of mylonitic gneisses, dominated by quartz and feldspar which undergo high-temperature plastic strain and intense recrystallization, ii) the middle segment, bound on either side by syn-kinematic batholiths, has a shear zone thickness of 10–5 km, and is composed both of high-temperature mylonitic gneisses (to its northeast end) and low-temperature ultramylonites (to its southwest end), both exhibiting deformation microstructures that

broadly indicate amphibolite facies temperatures, and iii) the southern segment, with a shear zone width that decreases gradually from 5 km to essentially a discrete boundary in which low-temperature ultramylonites, pseudotachylites and m-thick granite synkinematic dykes occur. On the basis of field relations, detailed geological mapping and microstructural study along the identified shear zone segments, we drew the following conclusions:

- Microstructures indicate a systematic increase in deformation temperature towards the northeast.

- Al-in-hornblende geobarometry applied to magmatic hornblende that occurs in the synkinematic Quixadá and Tauá batholiths reveal a c. 10 km difference in depth of emplacement of magmas occurring at different locations along the shear zone, which we interpret as evidence of post-kinematic tilting of the presently exposed crustal section by c. 3°, bringing the deeper northern segment of the Senador Pompeu shear zone to the same level as the shallower southern segment, and exposing the shear zone strength profile centered at roughly the brittle-ductile transition.

- Offset geological units indicate of a minimum offset of 50 (Quixeramobim batholith tail) to 75 km (mafic mylonites of Coqueirinho fold system).

- By using recrystallized grain size paleopiezometry and the tilted section assumption we simulated a strength profile for the crust at the time of shear deformation which is best fit by a strain rate of 10^{-14}–10^{-15} s^{-1}. The estimated flow stresses also fit the expected shape of the strength profile, further supporting the tilted crust hypothesis.

- Simulated shear zone widths seem to favour a very high slip-rate (50 mm/yr), but considering slip rates in active intra-orogenic transcurrent shear zones, a slip rate of c. 10 mm/yr is more plausible. We interpret that the “excess” measured shear zone width is a result of progressive exhumation of the entire domain, prior to tilting.

- With the slip rate constraints placed by simulated shear zone widths, we interpret that the Senador Pompeu shear zone accumulated its total offset of 50–75 km in c. 10 Myr, approximately at 585–575 Ma.

- Despite the somewhat uncertain slip rate constraint (50–10 mm/yr), the results presented here provide a means to place limits to shear zone longevity in the Borborema Province, challenging common interpretations drawn thus far that several shear zones may have been active for 10s of Myr, and up to 100 Myr.

- Several north-trending left-lateral shear zones (Cococi, Hebrón and Orós) branch into the Senador Pompeu shear zone forming dextral closing zippers. Mylonites with opposing kinematics can be found juxtaposed within the zippered segment, but get progressively transposed into the dominant right-lateral shear sense of the Senador Pompeu shear zone. Sorting out opposing kinematic criteria in shear zone networks requires detailed geological-structural mapping.

7 Considerações finais e conclusões

Os estudos que compõem esta tese têm o objetivo de caracterizar as propriedades e evolução tectônica das zonas de cisalhamento transcorrentes Senador Pompeu e Tauá e o plutonismo associado no Domínio Ceará Central. Para este fim, foi utilizada uma abordagem multidisciplinar envolvendo geocronologia U-Pb e Ar-Ar, anisotropia magnética (ASM e AARM), caracerização microestrutural com EBSD e geobarometria, fundamentada em análise estrutural e estudos de campo de detalhe. Os dados obtidos sobre a deformação tardi-orogênica servirão para refinar modelos da história geológica da zona setentrional da Província Borborema. Além disso, foram feitas observações pioneiras sobre interações e o papel mecânico de zonas de cisalhamento. As principais conclusões são descritas abaixo.

7.1 Interação de zonas de cisalhamento, magmatismo sincrônico e extrusão de bloco

Corpos plutônicos que ocorrem nos núcleos ou ombreiras das zonas de cisalhamento transcorrentes Senador Pompeu (batólitos Quixadá e Quixeramobim) e Tauá (batólito Nova Russas e diques Pedra Lisa), e na sua junção (batólito Tauá), têm feições estruturais que corroboram alojamento sincrônico com o cisalhamento de alta temperatura, a mais marcante sendo orientação preferencial de forma de megacristais porfiroclásticos em matriz com fraca deformação em estado sólido. Idades de cristalização são concordantes em 584 Ma para tais plútons e para os enxames de diques hipo-abissais Ematuba, Independência e Marrecas que ocorrem no embasamento preservado do cisalhamento. Dado o arranjo geométrico, idade do magmatismo e cinemática conjugada, conclui-se que:

- As zonas de cisalhamento Senador Pompeu e Tauá formam um par conjugado, com idade de deformação em 584 Ma, que causa uma extrusão para nordeste do

bloco interno do Domínio Ceará Central.

- A direção de encurtamento para esse sistema é paralela à orientação unimodal dos enxames de diques, bissectando o ângulo obtuso entre as zonas de cisalhamento, e retratando um ambiente consistente de deformação durante alguns Myr.

- Por efeito da extrusão do bloco interno do Domínio Ceará Central, forma-se um zíper que justapõe as zonas de cisalhamento Senador Pompeu e Tauá na sua junção. Este zíper, por sua vez, forma a zona de cisalhamento destral de Cococi, configurando um zíper de fechamento destral (também chamado falha de extração mista destral).

7.2 Tramas magnéticas em plútons circulares tardi-cinemáticos

O batólito Tauá que ocorre no ponto de junção das zonas de cisalhamento conjugadas é também sincrônico com a transcorrência em 584 Ma (dada pelo stock Iapi), mas possui uma prolongada história de cristalização até 571 Ma (i.e. c. 15 Myr). Sua construção incremental se deu a partir de centros de alimentação que formaram stocks individuais internos levemente elípticos, de composição bimodal granítica-diorítica.

Os stocks mais jovens (Várzea do Boi e Lagoa de Pedra) se encontram mais distantes da zona de cisalhamento Tauá. Eles possuem formas circulares, disposição localmente anelar das litologias, mistura física (*mingling*) de magmas granítico e diorítico, textura maciça e relações de *stoping* e desacoplamento com o embasamento. Portanto, em escala mesoscópica, os stocks Várzea do Boi e Lagoa de Pedra não registram influência da deformação do embasamento. Neste cenário, tramas magnéticas obtidas de ASM (anisotropia de susceptibilidade magnética) e AARM (anisotropia de magnetização remanente anisterética) revelam texturas crípticas que permitem concluir que:

- A injeção de magma diorítico em uma câmara granítica, ambos com baixa porcentagem de sólidos, é seguida de rápido resfriamento e cristalização garantindo preservação de estruturas de *mingling* e inclui neste intervalo o *timing* de formação da foliação magmática colocada em evidência com ASM e AARM.

- Granitos e dioritos têm tramas magnéticas consistentes entre si. Para os granitos, magnetita é a principal fase portadora do sinal magnético e controla ASM e AARM, e para os dioritos, ASM é controlada por anfibólio e biotita.

- O baixo grau de anisotropia *P*, em torno de 5%, indica que a foliação magmática incipiente se deve a acumulção de pequena quantidade de deformação inteiramente no estado magmático.

- O stock de Várzea do Boi possui uma trama magnética concordante com a estrutura concêntrica do corpo. O stock Lagoa de Pedra exibe tramas magnéticas concêntricas em sua metade norte e tramas heterogêneas em sua metade sul. Tais tramas se devem a forças de corpo resultantes da construção incremental dos stocks em torno do seu ponto central.

- Foliações magnéticas que truncam contatos litológicos e são concordantes com o embasamento na parte sul do Stock de Várzea do Boi e a guirlanda de lineações magnéticas concordantes com lineamentos do embasamento registram a influência incipiente da deformação regional no batólito.

- Esta fraca influência se deve ao rápido tempo de aquisição de tramas, à forte localização da deformação no núcleo das zonas de cisalhamento, e à diminuição da intensidade da deformação em suas fases finais.

Para resolver as questões e imprecisões remanescentes da Suíte Magmática de Tauá, futuras investigações devem ser dedicadas à geoquímica, petrologia e geocronologia de alta resolução das litologias principais. A ocorrência de mistura física de magmas com incipiente hibridização, e núcleos de composição máfica a ultramáfica, indicam processos de diferenciação magmática com tempos de duração distintos. Particularmente, é necessário detalhar o prolongado período de cristalização e como se insere em tal cenário a mistura de magmas contrastantes, supostamente consolidada abruptamente. Uma expansão de levantamentos de tramas magnéticas por todo o batólito poderá então servir como um registro estrutural longevo da deformação do embasamento.

7.3 Resfriamento e exumação do Domínio Ceará Central

Idades Ar-Ar obtidas para os plútons sin-tectônicos de Várzea do Boi, Iapi e Ematuba indicam fechamento para difusão em anfibólio em 577–562 Ma. Para concentrados de biotitas dos plútons Várzea do Boi, Iapi e milonitos de alta temperatura da zona de cisalhamento Tauá, idades Ar-Ar são c. 561–554 Ma. Considerando a trajetória tempo-temperatura que inclui as idades de cristalização U-Pb e de resfriamento Ar-Ar (que compreendem o intervalo de temperatura c. 700–300 °C), são calculadas temperaturas de fechamento de c. 510 °C e 310 °C para anfibólio e biotita, respectivamente. Rápidas taxas de resfriamento para estas unidades associadas à zona de cisalhamento Tauá foram determinadas entre 40 e 20 °C/Myr. O resfriamento se deu de c. 700 °C em 580 Ma, para menos de 300 °C em 560 Ma. Registros geobarométricos do Complexo Ceará que constitui o sistema de nappes do Ceará Central e das zonas de cisalhamento inserem as rápidas taxas de resfriamento no contexto de uma trajetória *P-T-t* horária. Com base na comparação entre taxas de resfriamento e exumação do Domínio Ceará Central conclui-se que:

- Idades de resfriamento em biotita (c. 590 Ma) e anfibólio (600 Ma) no bloco interno são c. 20 Myr mais jovens que as idades de resfriamento equivalentes nas zonas de cisalhamento. As trajetórias tempo-temperatura para o domínio interno que incluem idades do metamorfismo de fácies granulito-anfibolito caracterizam resfriamento a taxas de 20 a 40 °C/Myr.

- Um episódio de rápida exumação isotérmica provocado pela colocação das nappes do Ceará Central ocorreu antes de 610 Ma a taxas de 1.9–5.8 mm/yr, dando origem ao rápido resfriamento subsequente (20–40 °C/Myr), virtualmente isobárico.

- Após colocação das nappes em torno de 610 Ma, as zonas de cisalhamento transcorrentes e o bloco interno, como um domínio coeso, sofreram uma exumação lenta a taxas de 0.3–0.9 mm/yr, até alcançarem a superfície em c. 530 Ma, quando se formaram as bacias molássicas (e.g. bacia de Cococi).

- No mesmo intervalo, o resfriamento diferencial das zonas de cisalhamento se deve a um regime térmico próprio, relacionado a advecção de calor por magmatismo e geração de calor por cisalhamento.

- A deformação de alta temperatura que se dá no núcleo das zonas de cisalhamento em sincronicidade com a formação de enxames de diques (Ematuba, Independência e Marrecas) em fraturas extensionais no interior do Domínio Ceará Central é a expressâo mecânica-estrutural do resfriamento diferencial entre zonas de cisalhamento e o bloco interno.

- Não há relação tectônica aparente entre o sistema de nappes do Ceará Central, colocado sob altas temperaturas em torno de 610–600 Ma, e a transcorrência cujo pico de atividade se deu em 584 Ma.

7.4 Reologia, cinemática e evolução estrutural de zonas de cisalhamento

Importantes heterogeneidades cinemáticas, deformacionais e reológicas ocorrem em relação às zonas de cisalhamento e ao longo de seu comprimento. O ambiente de transcorrência do par sincrônico Senador Pompeu-Tauá é em resultante transpressivo com contribuições semelhantes de cisalhamento puro e simples, em torno de 50% cada. Durante a evolução da estrutura interna e geometria das zonas de cisalhamento ocorrem variações significativas nos valores de vorticidade associadas a episódios de espessamento e afinamento do volume de cisalhamento, de forma que ocorram sítios locais de transtensão, oferencendo condições para geração de espaço para alojamento de magmas. Tais variações são registradas em granitos sin-tectônicos, e podem ser devido à partição de deformação causada por forças de corpo, não relacionadas ao cisalhamento. Estudos de maior detalhe com múltiplos medidores de vorticidade são necessários para separar as diferentes contribuições.

Segmentos com cinemática oposta à cinemática dominante da zona de cisalhamento Senador Pompeu (i.e. destral) ocorrem de forma anastomosada em seu comprimento. Em sua junção, formam-se zíperes (e.g. zonas de cisalhamento Cococi, Hebrón e Orós) de fechamento destral em que cinemáticas sinistrais são encontradas justapostas com a

cinemática destral. Estas estruturas salientam a importância de mapeamento estrutural de detalhe para a identificação da cinemática de zonas de cisalhamento em sistemas de transcorrência como a Província Borborema uma vez que o sentido de cisalhamento muitas vezes é usado para interpretar direções de encurtamento regionais.

Deflexão de unidades geológicas principais indicam um rejeito mínimo entre 50 e 75 km para a zona de cisalhamento Senador Pompeu. Este valor é consistente com o modelo de zipper de fechamento destral para com a zona de cisalhamento Tauá da qual se espera um rejeito inferior (c. 30–35 km).

A distribuição de rochas de falha, microestruturas de deformação e arquitetura estrutural caracterizam uma zonação da zona de cisalhamento Senador Pompeu ao longo de 350 km de comprimento. Com base em tal zonação, são separados três principais segmentos:

- Segmento norte, amplamente composto de gnaisses miloníticos sincrônicos com o plutonismo em 584 Ma. Este corredor de cisalhamento tem uma largura de 20–30 km. Mecanismos de deformação e assembléias minerais indicam pleno fluxo viscoplástico de quartzo e feldspato em fácies anfibolito superior a granulito. Grãos recristalizados de quartzo em *ribbons* monominerálicos têm tamanhos de grãos c. 1000 μm indicando tensões de fluxo <10 MPa.

- Segmento sul, composto de pseudotaquilitos e cataclasitos, a ultramilonitos da transição rúptil-dúctil e milonitos de alta temperatura. O vasto intervalo de temperatura de deformação implícito na variedade de tectonitos indica exumação deste segmento. Expresso por um limite discreto, neste segmento a zona de cisalhemento possui uma largura inferior a 2 km. Tamanhos de grãos recristalizados variam largamente entre c. 10 e 500 μm.

- O segmento médio é composto principalmente de milonitos de fácies xisto verde a anfibolito com fluxo viscoplástico de quartzo e deformação rúptil de feldspato. Pseudotaquilitos e ultramilonitos finos são escassos. A largura deste segmento aumenta gradativamente de c. 2 km para mais de 10 km de sudoeste para nordeste. Grãos de quartzo recristalizados em milonitos e ultramilonitos têm tamanhos em torno de 10 μm indicando tensões de fluxo de até 200 MPa.

Os batólitos sincrônicos Quixadá e Tauá foram alojados a profundidades de c. 18 e 9 km respectivamente. A projeção normal destas profundidades na zona de cisalhamento Senador Pompeu é consistente com o aumento da temperatura de deformação de sudoeste para nordeste. Onde ocorre deformação dúctil, mecanismos de fluxo de discordância assistidos por recristalização dinâmica são dominantes e controlam as leis de reologia. Uma simulação de largura da zona de cisalhamento baseada nestas condições é coerente com o aumento da largura mínima da zona de cisalhamento Senador Pompeu e indica uma taxa de cisalhamento de c. 10 mm/yr ou superior. Para a zona de cisalhamento Senador Pompeu conclui-se que:

- Uma inclinação pós-orogênica estimada de cerca de 3° expôs um perfil de profundidade na zona de cisalhamento Senador Pompeu, aumentando de sudoeste para nordeste.
- No segmento médio, o perfil mostra a transição rúptil-dúctil com o feixe de resistência máxima (200 MPa).
- As diferentes temperaturas de deformação nos segmentos são consistentes com uma deformação transcorrente contínua progressiva.
- A transcorrência se deu no intervalo aproximado de 584 a 570 Ma.

Apêndices

APÊNDICE A – Supporting Information: Zippered Shear Zone Model for Interacting Shear Zones in the Borborema Province, Brazil, as Constrained by UPb Dating

A.1 Introduction

This supporting information provides the results of SHRIMP U-Pb zircon analysis, concordia plots from the most coherent group, and cathodoluminescence images of zircons with their analysed spots tagged.

												Ages (Ma)			
Spot	$^{206}Pb_c$ (%)	U (ppm)	Th (ppm)	$\frac{Th}{U}$	$\frac{^{206}Pb}{^{238}U}$	error (%)	$\frac{^{207}Pb}{^{235}U}$	error (%)	ρ^2	$\frac{^{207}Pb}{^{206}Pb}$	error (%)	$\frac{^{206}Pb}{^{238}U}$	1σ	$\frac{^{207}Pb}{^{206}Pb}$	1σ
1.1	-0.186	201	126	0.63	0.093	0.88	0.77	1.6	0.5	0.0605	1.3	571	5	622	29
2.1*	0.096	306	223	0.73	0.090	1.10	0.73	1.6	0.7	0.0586	1.2	555	6	553	25
3.1	0.029	184	108	0.59	0.096	0.90	0.79	1.4	0.6	0.0597	1.1	590	5	592	24
4.1	0.038	149	86	0.58	0.097	0.92	0.80	1.6	0.6	0.0596	1.3	597	5	589	28
5.1	0.076	142	52	0.37	0.094	0.93	0.76	1.7	0.6	0.0589	1.4	580	5	564	31
6.1	0.19	223	165	0.74	0.093	1.05	0.76	1.7	0.6	0.0591	1.3	575	6	571	29
7.1	0.038	239	168	0.70	0.095	0.86	0.78	1.3	0.7	0.0594	0.9	587	5	582	20
8.1*	0	192	161	0.84	0.099	0.89	0.81	1.4	0.6	0.0595	1.0	606	5	587	22
9.1	0	101	64	0.63	0.095	0.98	0.78	1.7	0.6	0.0592	1.4	586	6	574	30
10.1	-0.063	190	111	0.58	0.096	0.89	0.78	1.5	0.6	0.0593	1.2	591	5	578	27
11.1	-0.055	197	98	0.50	0.095	0.89	0.79	1.4	0.6	0.0603	1.1	586	5	615	24
12.1	0	227	137	0.60	0.093	1.06	0.77	1.5	0.7	0.0600	1.0	573	6	604	22
13.1	-0.041	149	79	0.53	0.095	0.93	0.78	2.3	0.4	0.0594	2.1	586	5	583	46
14.1	-0.109	168	93	0.55	0.096	0.90	0.79	1.7	0.5	0.0596	1.4	593	5	588	31
15.1*	0	168	93	0.55	0.099	0.90	0.80	1.4	0.6	0.0591	1.1	606	5	572	24

Tabela 4 – U-Pb analysis data for Quixadá batholith. * discarded. Errors are 1σ.

												Ages (Ma)			
Spot	$^{206}Pb_c$ (%)	U (ppm)	Th (ppm)	$\frac{Th}{U}$	$\frac{^{206}Pb}{^{238}U}$	error (%)	$\frac{^{207}Pb}{^{235}U}$	error (%)	ρ^2	$\frac{^{207}Pb}{^{206}Pb}$	error (%)	$\frac{^{206}Pb}{^{238}U}$	1σ	$\frac{^{207}Pb}{^{206}Pb}$	1σ
1.1	0.18	724	223	0.31	0.0962	1.1	0.78	1.5	0.721	0.0591	1.0	592.3	6.0	570	22
2.1*	0.86	814	323	0.40	0.0856	1.1	0.71	2.5	0.426	0.0604	2.2	529.7	5.4	618	48
3.1*	8.00	1319	365	0.28	0.0502	1.2	0.48	15.2	0.081	0.0689	14.9	316.0	3.8	896	313
4.1*	0.33	496	32	0.06	0.0909	1.1	0.76	1.9	0.574	0.0605	1.5	560.6	5.8	622	33
5.1*	0.42	249	115	0.46	0.0919	1.1	0.76	2.6	0.435	0.0602	2.4	567.0	6.2	609	51
6.1*	2.32	391	105	0.27	0.0814	1.1	0.67	5.6	0.199	0.0598	5.4	504.6	5.4	598	120
7.1	0.10	625	170	0.27	0.0948	1.1	0.78	1.4	0.740	0.0596	1.0	584.1	5.9	589	21
8.1	-0.01	415	101	0.24	0.0960	1.1	0.80	1.3	0.813	0.0607	0.8	590.8	6.1	627	17
9.1	0.10	186	81	0.44	0.0924	1.3	0.76	2.0	0.663	0.0595	1.5	569.5	7.2	587	32
10.1*	0.10	571	151	0.26	0.0978	1.1	0.80	1.4	0.772	0.0590	0.9	601.2	6.1	567	19
11.1	0.87	497	153	0.31	0.0934	1.1	0.78	2.6	0.415	0.0607	2.3	575.5	5.9	627	51
12.1	0.22	247	139	0.56	0.0954	1.1	0.77	1.9	0.597	0.0588	1.5	587.6	6.4	558	33
13.1	-0.01	550	76	0.14	0.0939	1.1	0.78	1.3	0.828	0.0603	0.7	578.4	5.9	614	16
14.1	-0.04	319	162	0.51	0.0942	1.1	0.78	1.5	0.754	0.0603	1.0	580.1	6.1	615	21
15.1	0.19	718	221	0.31	0.0959	1.1	0.78	1.4	0.735	0.0589	1.0	590.5	5.9	564	21
16.1	-0.03	306	10	0.03	0.0947	1.1	0.78	1.4	0.766	0.0599	0.9	583.1	6.2	599	20
17.1	-0.01	323	57	0.18	0.0944	1.1	0.80	1.4	0.780	0.0611	0.9	581.4	6.2	643	19
18.1	0.19	788	325	0.41	0.0936	1.1	0.77	1.5	0.746	0.0596	1.0	576.7	6.0	588	21

Tabela 5 – U-Pb analysis data for Quixeramobim batholith. * discarded. Errors are 1σ.

												Ages (Ma)			
Spot	$^{206}Pb_c$ (%)	U (ppm)	Th (ppm)	$\frac{Th}{U}$	$\frac{^{206}Pb}{^{238}U}$	error (%)	$\frac{^{207}Pb}{^{235}U}$	error (%)	ρ^2	$\frac{^{207}Pb}{^{206}Pb}$	error (%)	$\frac{^{206}Pb}{^{238}U}$	1σ	$\frac{^{207}Pb}{^{206}Pb}$	1σ
1.1	0.53	503	232	0.46	0.0925	1.9	0.75	2.7	0.707	0.0586	1.9	570.3	10.3	551	41
2.1*	0.18	696	104	0.15	0.0888	1.9	0.72	2.5	0.755	0.0586	1.7	548.5	10.0	554	36
3.1*	0.82	480	142	0.30	0.0897	1.9	0.73	3.5	0.533	0.0590	3.0	553.9	10.0	568	65
5.1*	0.08	542	144	0.27	0.0900	1.9	0.73	2.1	0.896	0.0591	0.9	555.8	10.0	570	20
6.1	0.59	345	289	0.84	0.0946	1.9	0.78	3.2	0.588	0.0596	2.6	582.5	10.6	590	57
7.1	0.28	300	85	0.28	0.0953	1.9	0.77	2.7	0.719	0.0588	1.8	586.6	10.8	561	40
8.1	0.1	211	135	0.64	0.0960	2.0	0.79	2.5	0.807	0.0594	1.5	590.9	11.4	581	32
9.1	0.08	251	55	0.22	0.0967	1.9	0.80	2.4	0.809	0.0601	1.4	594.9	11.0	609	30
10.1	0.25	739	255	0.35	0.0947	1.9	0.77	2.3	0.814	0.0590	1.3	583.1	10.4	569	29
11.1	0.23	469	131	0.28	0.0934	1.9	0.76	2.3	0.815	0.0588	1.3	575.4	10.3	558	29
12.1	0.12	345	65	0.19	0.0926	1.9	0.75	2.3	0.810	0.0590	1.4	570.6	10.3	568	30
14.1	0.05	179	50	0.28	0.0990	1.9	0.83	2.4	0.817	0.0606	1.4	608.6	11.2	625	29
15.1	0.23	153	20	0.13	0.0944	2.0	0.77	3.1	0.649	0.0593	2.3	581.8	11.1	580	51
16.1	0.27	333	121	0.36	0.0932	1.9	0.76	2.8	0.695	0.0590	2.0	574.2	10.6	565	44
17.1	0.17	397	69	0.17	0.0954	1.9	0.79	2.2	0.855	0.0602	1.1	587.2	10.7	610	25

Tabela 6 – U-Pb analysis data for Nova Russas batholith. * discarded. Errors are 1σ.

												Ages (Ma)			
Spot	$^{206}Pb_c$ (%)	U (ppm)	Th (ppm)	$\frac{Th}{U}$	$\frac{^{206}Pb}{^{238}U}$	error (%)	$\frac{^{207}Pb}{^{235}U}$	error (%)	ρ^2	$\frac{^{207}Pb}{^{206}Pb}$	error (%)	$\frac{^{206}Pb}{^{238}U}$	1σ	$\frac{^{207}Pb}{^{206}Pb}$	1σ
1.1	0.13	482	78	0.16	0.1006	2.2	0.84	2.7	0.802	0.0602	1.6	617.6	12.7	612	35
2.1	0.56	529	142	0.27	0.0932	2.0	0.75	2.9	0.683	0.0585	2.1	574.2	10.9	549	46
3.1	0.14	487	246	0.51	0.0935	1.9	0.77	2.2	0.856	0.0600	1.1	575.9	10.4	602	25
4.1	0.19	347	88	0.25	0.0941	1.9	0.78	2.4	0.786	0.0599	1.5	580.0	10.6	599	33
5.1	0.10	530	178	0.34	0.0938	1.9	0.78	2.1	0.888	0.0606	1.0	577.9	10.6	626	21
6.1	0.29	551	149	0.27	0.0923	1.9	0.77	2.5	0.752	0.0604	1.6	569.0	10.3	619	36
7.1	0.05	366	83	0.23	0.0949	1.9	0.78	2.4	0.794	0.0598	1.5	584.3	10.7	595	32
8.1	-0.06	961	363	0.38	0.0970	2.0	0.81	2.2	0.903	0.0602	1.0	596.7	11.4	612	21
9.1	0.18	432	186	0.43	0.0954	2.1	0.78	2.5	0.826	0.0591	1.4	587.5	11.6	570	31
10.1	0.19	514	202	0.39	0.0947	1.9	0.78	2.5	0.772	0.0595	1.6	583.3	10.6	584	34
11.1*	0.04	423	21	0.05	0.1020	1.9	0.86	2.1	0.891	0.0613	1.0	625.9	11.2	650	21
12.1	-0.05	305	141	0.46	0.0971	2.2	0.81	2.6	0.845	0.0604	1.4	597.3	12.3	617	30
13.1	-0.06	404	154	0.38	0.0963	1.9	0.80	2.4	0.784	0.0599	1.5	592.8	10.7	601	32
14.1	0.03	544	172	0.32	0.0963	1.9	0.81	2.1	0.901	0.0610	0.9	592.7	10.6	638	19

Tabela 7 – U-Pb analysis data for Pedra Lisa plutons. * discarded. Errors are 1σ.

												Ages (Ma)			
Spot	$^{206}Pb_c$ (%)	U (ppm)	Th (ppm)	$\frac{Th}{U}$	$\frac{^{206}Pb}{^{238}U}$	error (%)	$\frac{^{207}Pb}{^{235}U}$	error (%)	ρ^2	$\frac{^{207}Pb}{^{206}Pb}$	error (%)	$\frac{^{206}Pb}{^{238}U}$	1σ	$\frac{^{207}Pb}{^{206}Pb}$	1σ
1.1	0.00	390	152	0.39	0.0951	1.8	0.83	2.5	0.719	0.0636	1.7	585.9	9.9	728	36
2.1	0.07	298	110	0.37	0.0937	1.8	0.76	2.8	0.644	0.0588	2.1	577.3	9.9	560	46
3.1	0.11	250	63	0.25	0.0961	1.8	0.83	2.8	0.647	0.0624	2.1	591.3	10.2	686	46
4.1	0.00	306	89	0.29	0.0961	1.8	0.83	2.6	0.690	0.0625	1.9	591.4	10.1	691	40
5.1	0.09	275	94	0.34	0.0936	1.8	0.75	3.0	0.612	0.0578	2.3	577.0	10.0	521	51
6.1	0.20	291	195	0.67	0.0946	1.8	0.79	3.2	0.575	0.0608	2.6	582.6	10.1	631	56
7.1	0.00	358	133	0.37	0.0943	1.9	0.79	2.7	0.711	0.0608	1.9	581.2	10.7	631	41
8.1*	1.22	280	167	0.60	0.0969	2.0	1.13	9.6	0.209	0.0848	9.4	596.2	11.3	1312	182
9.1	0.21	332	119	0.36	0.0946	1.8	0.78	3.0	0.591	0.0600	2.4	582.5	10.0	605	53
10.1*	0.48	564	529	0.94	0.0983	1.9	0.91	3.8	0.488	0.0669	3.3	604.4	10.8	834	70
11.1	0.31	272	67	0.25	0.0974	1.8	0.78	3.3	0.560	0.0578	2.7	599.3	10.5	524	59
12.1	0.26	348	171	0.49	0.0935	1.8	0.80	3.7	0.490	0.0619	3.2	575.9	9.9	670	68
13.1*	0.00	290	124	0.43	0.0973	2.3	0.98	3.0	0.749	0.0730	2.0	598.3	12.9	1014	40
14.1	0.21	234	91	0.39	0.0946	2.0	0.80	4.1	0.476	0.0615	3.6	582.7	10.9	657	78
15.1	0.41	221	66	0.30	0.0957	2.5	0.81	4.9	0.497	0.0614	4.3	589.1	13.8	652	92

Tabela 8 – U-Pb analysis data for Ematuba dykes. * discarded. Errors are 1σ.

												Ages (Ma)			
Spot	$^{206}Pb_c$ (%)	U (ppm)	Th (ppm)	$\frac{Th}{U}$	$\frac{^{206}Pb}{^{238}U}$	error (%)	$\frac{^{207}Pb}{^{235}U}$	error (%)	ρ^2	$\frac{^{207}Pb}{^{206}Pb}$	error (%)	$\frac{^{206}Pb}{^{238}U}$	1σ	$\frac{^{207}Pb}{^{206}Pb}$	1σ
1.1	1.15	193	90	0.47	0.0961	2.8	0.81	6.5	0.428	0.0615	5.8	591.5	15.6	656	125
3.1*	9.77	238	139	0.58	0.0862	2.9	0.73	25.7	0.112	0.0615	25	532.8	14.7	657	548
4.1*	6.05	732	568	0.78	0.0877	2.9	0.73	14.7	0.200	0.0604	14.1	541.9	15.3	617	311
5.1*	24.2	200	170	0.85	0.0661	5.0						412.9	19.5		
6.1	0.42	406	371	0.91	0.0917	2.5	0.74	6.1	0.408	0.0584	5.6	565.8	13.6	546	123
7.1*	4.88	350	138	0.39	0.1179	3.3	0.98	18.1	0.182	0.0605	17.5	718.2	22.3	619	384
8.1	1.91	240	153	0.64	0.0916	2.6	0.76	8.6	0.302	0.06	8.1	564.9	14	602	177
9.1	0.6	459	395	0.86	0.0924	2.5	0.76	3.9	0.633	0.06	3	569.6	13.5	605	65
10.1	0.81	443	258	0.58	0.0937	2.5	0.78	4.8	0.515	0.0603	4.1	577.6	13.6	613	88
11.1	0.43	323	247	0.76	0.0928	2.5	0.76	4.4	0.564	0.0596	3.6	572.2	13.7	590	79
12.1	0.85	469	328	0.70	0.0944	2.5	0.78	5.3	0.464	0.0599	4.7	581.7	13.6	599	101
13.1	1.93	344	311	0.90	0.0962	2.5	0.82	6.8	0.370	0.0616	6.2	591.9	14.2	659	135
14.1	0.98	373	268	0.72	0.0937	2.7	0.76	7.8	0.347	0.0586	7.3	577.6	15	553	160
15.1	0.88	268	180	0.67	0.0955	2.7	0.77	6.8	0.403	0.0585	6.2	587.9	15.4	549	136
16.1	0.79	320	85	0.27	0.0936	2.5	0.76	5.6	0.447	0.0589	5	576.7	13.9	565	110
17.1	0.51	374	255	0.68	0.0955	2.5	0.78	5.0	0.509	0.0595	4.3	587.7	14.2	587	92

Tabela 9 – U-Pb analysis data for Independência dykes. * discarded. Errors are 1σ.

												Ages (Ma)			
Spot	$^{206}Pb_c$ (%)	U (ppm)	Th (ppm)	$\frac{Th}{U}$	$\frac{^{206}Pb}{^{238}U}$	error (%)	$\frac{^{207}Pb}{^{235}U}$	error (%)	ρ^2	$\frac{^{207}Pb}{^{206}Pb}$	error (%)	$\frac{^{206}Pb}{^{238}U}$	1σ	$\frac{^{207}Pb}{^{206}Pb}$	1σ
1.1	0.4	167	58	0.34	0.0958	1.1	0.795	3	0.4	0.06015	2.8	590	6	609	60
2.1	1.26	199	72	0.36	0.0958	1	0.802	4.1	0.3	0.06073	4	590	6	630	85
3.1*	0.73	207	101	0.49	0.1021	1.1	0.865	4	0.3	0.0614	3.9	627	6	653	84
5.1	0.74	207	73	0.35	0.0948	1	0.776	2.5	0.4	0.05936	2.3	584	6	580	50
6.1*	2.09	249	91	0.36	0.1018	1.1	0.852	4.4	0.2	0.06071	4.2	625	6	629	91
7.1	0.46	231	91	0.39	0.0967	1	0.793	2.1	0.5	0.05945	1.8	595	6	583	39
8.1	0.19	246	107	0.44	0.0955	1	0.789	1.6	0.6	0.05993	1.3	588	6	601	29
10.1	1.04	248	86	0.35	0.0954	1	0.782	2.9	0.3	0.05947	2.8	587	6	584	60
11.1	0.58	193	81	0.42	0.0921	1	0.758	3	0.3	0.0597	2.8	568	6	593	60
12.1	0.38	206	84	0.41	0.093	1	0.766	2	0.5	0.05978	1.8	573	6	596	39
13.1	2.66	364	323	0.89	0.0961	1	0.797	4.1	0.2	0.06016	4	591	5	609	87
14.1	0.46	176	79	0.45	0.092	1	0.766	2.3	0.5	0.06035	2	568	6	616	44
15.1	2.62	301	125	0.42	0.0926	1	0.77	3.4	0.3	0.06034	3.3	571	5	616	71
16.1	1.92	192	69	0.36	0.0946	1	0.78	4.3	0.2	0.05984	4.2	582	6	598	91
17.1	0.4	158	53	0.34	0.0952	1	0.778	2.9	0.4	0.05921	2.7	587	6	575	58
18.1	1.39	183	78	0.42	0.0964	1.1	0.791	6.4	0.2	0.05956	6.3	593	6	588	136
19.1	0.56	249	115	0.46	0.0958	1	0.784	2.1	0.5	0.05938	1.9	589	6	581	41

Tabela 10 – U-Pb analysis data for Marrecas dykes. * discarded. Errors are 1σ.

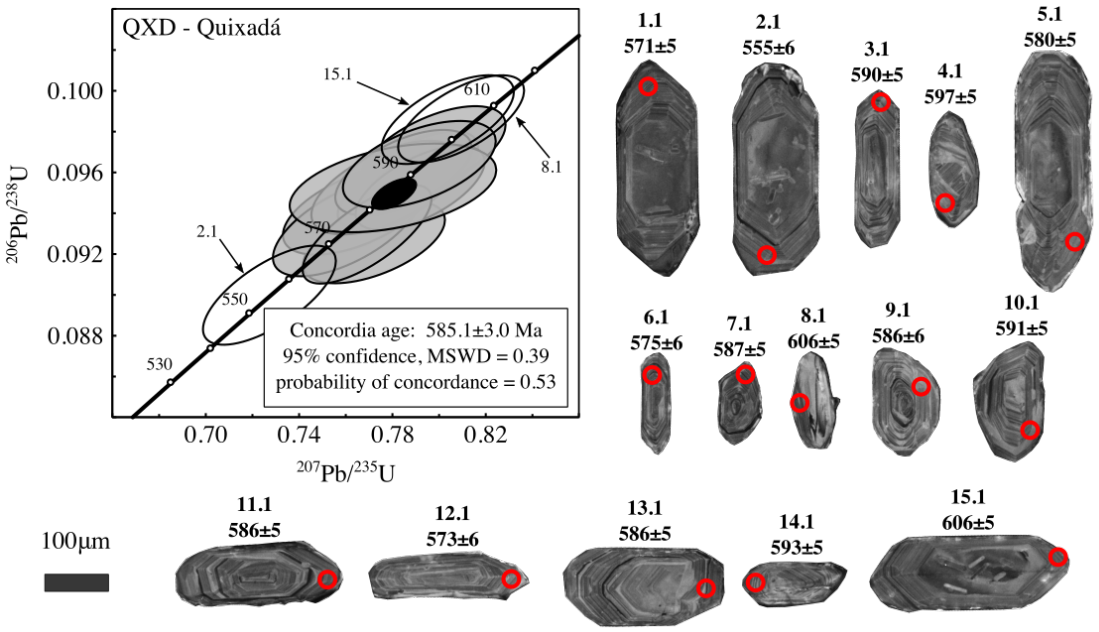

Figura 58 – U-Pb concordia diagram and cathodoluminescence image for Quixadá (QXD sample) zircons. Analysed spots are tagged with $^{206}Pb/^{238}U$ ages at 1σ errors.

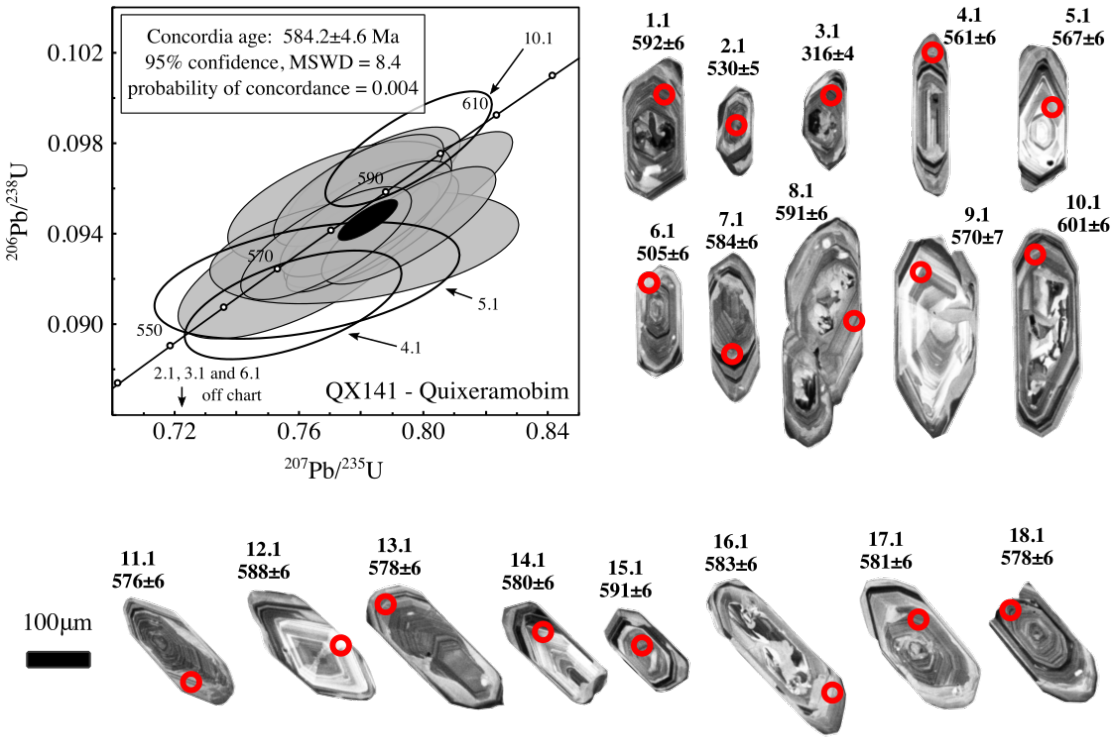

Figura 59 – U-Pb concordia diagram and cathodoluminescence image for Quixeramobim (QX141 sample) zircons. Analysed spots are tagged with $^{206}Pb/^{238}U$ ages at 1σ errors.

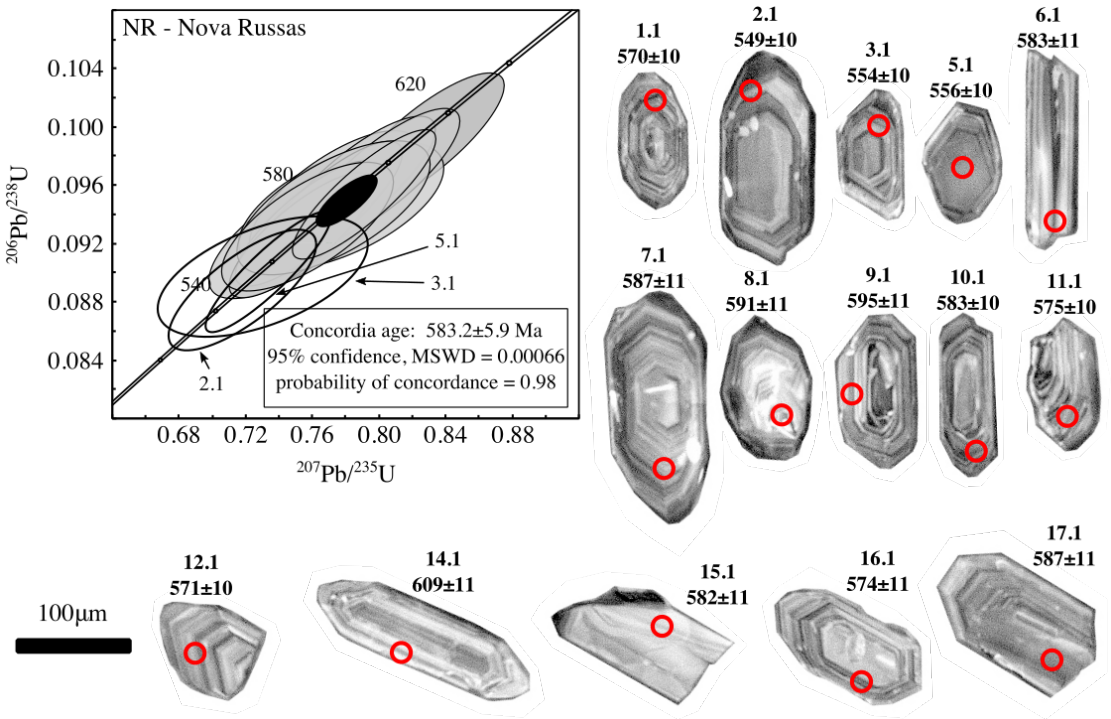

Figura 60 – U-Pb concordia diagram and cathodoluminescence image for Nova Russas (NR sample) zircons. Analysed spots are tagged with $^{206}Pb/^{238}U$ ages at 1σ errors.

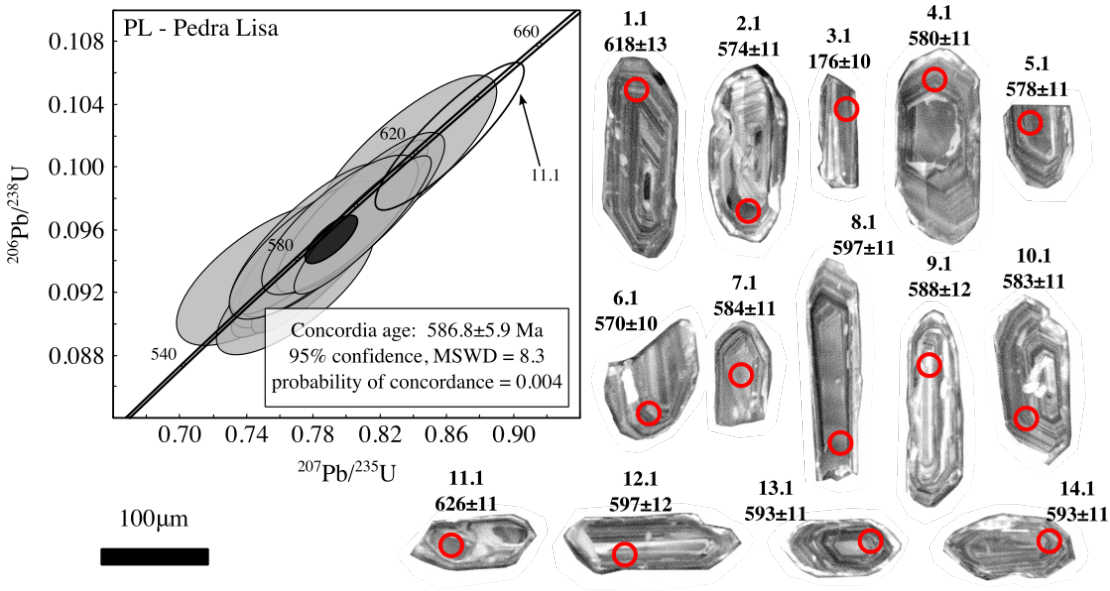

Figura 61 – U-Pb concordia diagram and cathodoluminescence image for Pedra Lisa (PL sample) zircons. Analysed spots are tagged with $^{206}Pb/^{238}U$ ages at 1σ errors.

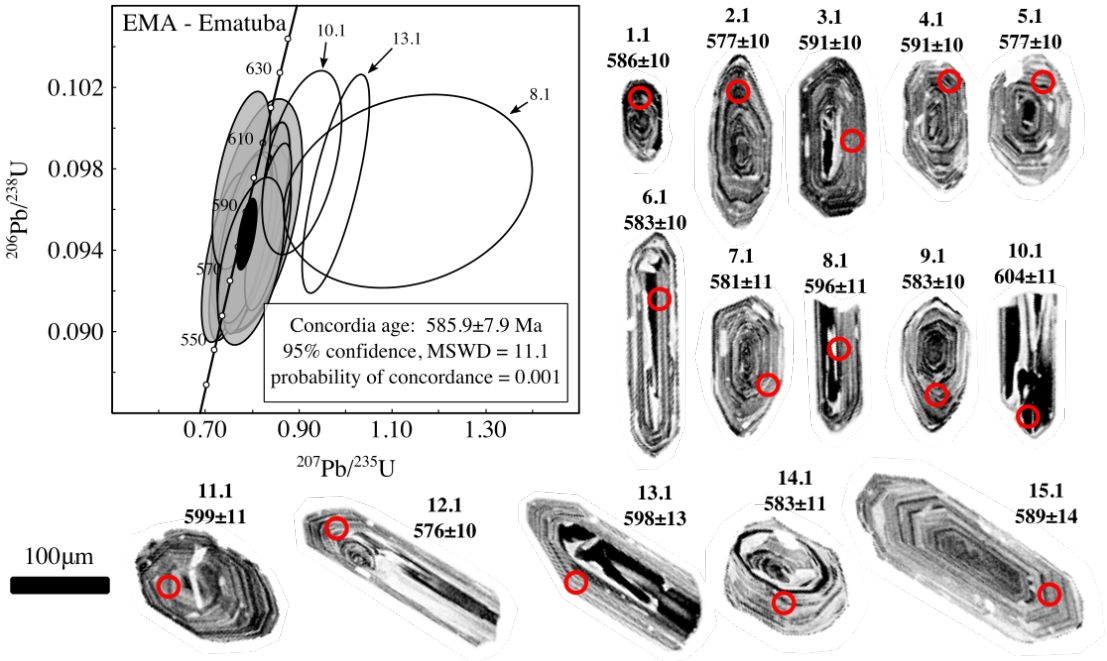

Figura 62 – U-Pb concordia diagram and cathodoluminescence image for Ematuba (EMA sample) zircons. Analysed spots are tagged with $^{206}Pb/^{238}U$ ages at 1σ errors.

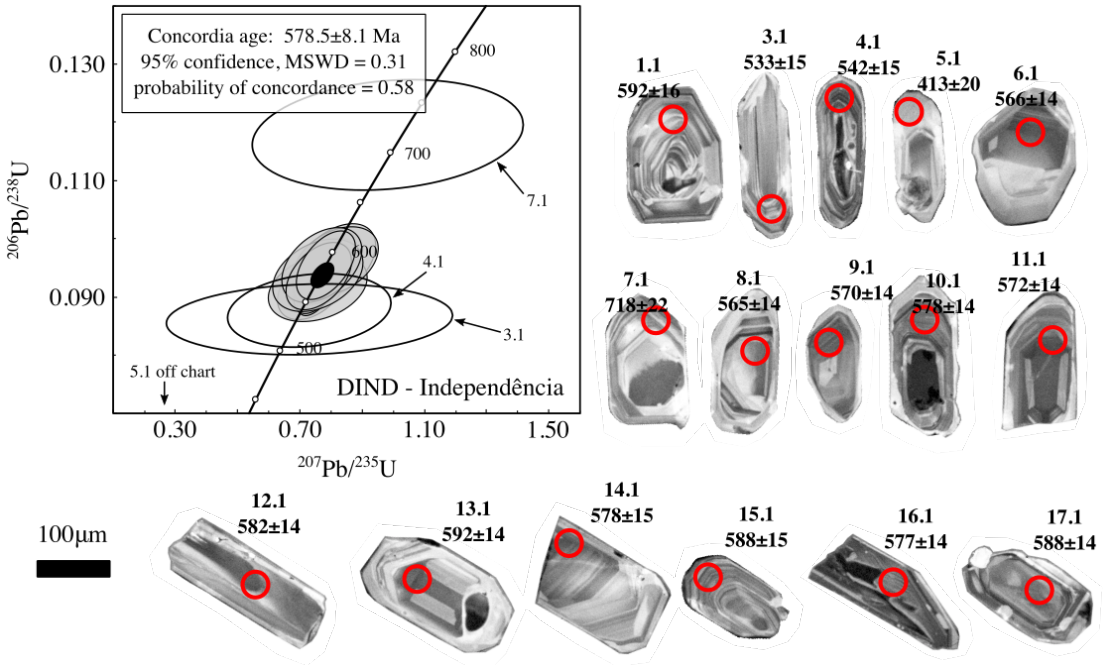

Figura 63 – U-Pb concordia diagram and cathodoluminescence image for Independência (DIND sample) zircons. Analysed spots are tagged with $^{206}Pb/^{238}U$ ages at 1σ errors.

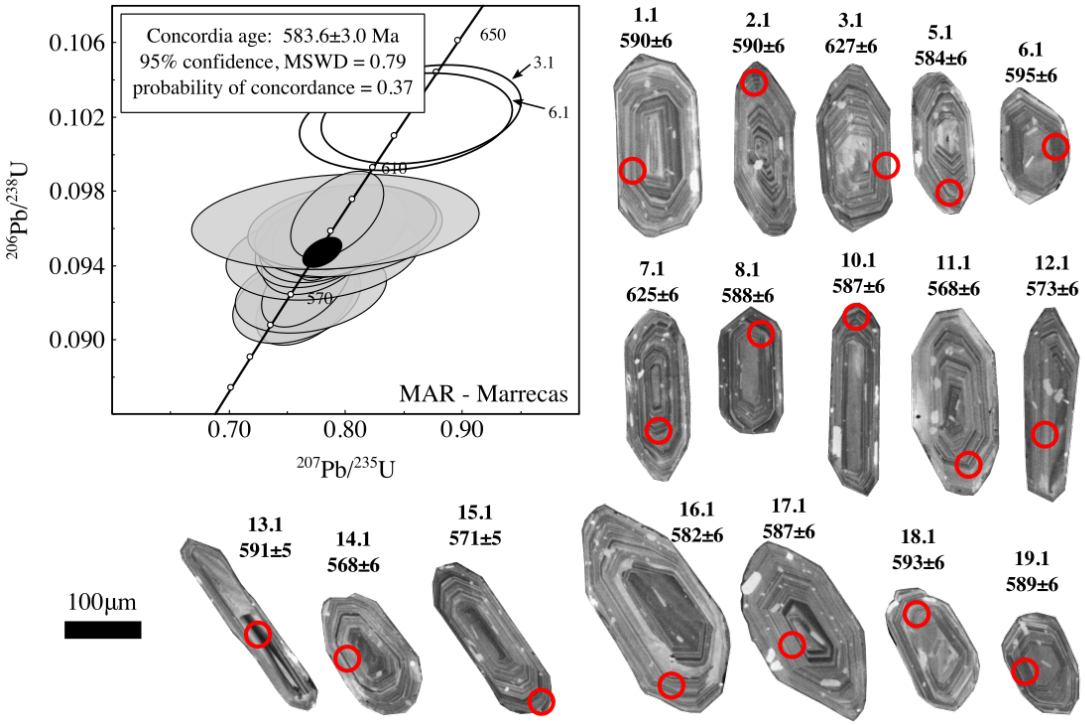

Figura 64 – U-Pb concordia diagram and cathodoluminescence image for Marrecas (MAR sample) zircons. Analysed spots are tagged with $^{206}Pb/^{238}U$ ages at 1σ errors.

APÊNDICE B – Supplementary Material: Shear zone cooling and fabrics of synkinematic plutons evidence timing and rates of orogenic exhumation in the northwest Borborema Province (NE Brazil)

B.1 Rock magnetism and Magnetic Anisotropy data

Magnetic susceptibility and anisotropy measurements for all sites are given in tables 11 for the Lagoa de Pedra stock and 12 for the Várzea do Boi stock, respectively.

Tabela 11 – Magnetic susceptibility and anisotropy measurements for the Lagoa de Pedra stock. N = number of sites, K_M = magnetic susceptibility, P = degree of anisotropy, T = shape paramenter, Dec. = Declination, Inc. = Inclination, αK = maximum angle of 2σ uncertainty ellipse.

	Coordinates						K_{max}			K_{int}			K_{min}		
Site	Lat.	Long.	N	K_M	P	T	Dec.	Inc.	αK_{max}	Dec.	Inc.	αK_{int}	Dec.	Inc.	αK_{min}
78	-5.781691	-40.153442	19	34.100	1.169	0.484	112	17	14	204	9	14	322	71	5
79	-5.782325	-40.146678	11	0.434	1.092	0.466	20	40	11	264	28	9	150	38	7
80	-5.794959	-40.155391	11	0.482	1.027	0.504	77	68	23	221	18	25	315	12	16
81	-5.809958	-40.172940	10	0.410	1.028	0.521	253	15	26	344	2	25	83	75	18
82	-5.823085	-40.155623	12	0.189	1.021	0.288	66	53	14	310	18	14	209	31	11
83	-5.822160	-40.167502	12	0.307	1.054	0.238	78	55	14	334	10	17	237	33	15
84	-5.873064	-40.143155	14	0.776	1.009	0.634	140	7	43	231	5	43	355	82	16
85	-5.867678	-40.139709	10	0.989	1.018	0.643	186	10	27	276	0	27	8	80	7
86	-5.877419	-40.149018	13	0.660	1.058	-0.357	35	0	19	125	69	31	305	21	31
87	-5.802258	-40.115529	13	0.119	1.041	0.872	195	35	47	311	32	47	70	39	16
88	-5.802901	-40.131980	15	0.732	1.024	0.725	159	28	14	69	0	15	338	62	10
89	-5.809615	-40.119221	10	14.500	1.113	0.723	223	36	19	331	23	19	87	45	5
90	-5.806810	-40.137750	11	0.263	1.012	0.379	176	51	50	271	4	51	4	39	44
91	-5.828679	-40.099956	11	0.080	1.011	0.597	70	2	38	335	68	38	161	22	30
92	-5.824945	-40.118627	13	0.026	1.038	0.833	257	26	51	22	50	51	152	28	13
93	-5.827053	-40.123631	11	0.058	1.100	0.453	20	78	17	275	3	14	185	11	17
94	-5.833260	-40.124168	11	0.075	1.031	-0.359	96	60	11	283	30	44	192	3	44
95	-5.858846	-40.133682	11	0.268	1.052	-0.066	53	18	35	316	21	42	180	62	42
96	-5.848467	-40.106535	13	0.282	1.056	0.362	54	51	17	226	39	17	319	4	6
97	-5.847895	-40.114939	14	0.126	1.032	0.483	232	68	14	345	9	17	79	20	14
98	-5.851617	-40.121846	14	0.149	1.017	0.192	38	26	12	136	15	11	253	59	8
99	-5.844682	-40.124530	13	0.849	1.011	0.973	207	8	75	301	28	75	103	61	8
100	-5.811110	-40.129347	16	0.669	1.025	0.566	160	7	35	257	50	35	64	40	25
101	-5.808174	-40.142877	9	0.102	1.017	0.528	360	64	41	109	9	41	203	24	11
102	-5.807440	-40.150510	18	0.121	1.037	0.325	357	17	13	220	67	13	91	15	11
103	-5.817886	-40.128638	15	0.686	1.044	0.617	175	4	18	272	59	20	82	30	12
104	-5.799069	-40.162901	11	1.120	1.023	0.154	167	65	35	317	22	41	51	11	36
105	-5.804356	-40.161510	11	0.669	1.070	0.625	15	63	18	164	24	18	259	13	8
106	-5.790171	-40.139888	9	0.152	1.082	0.461	125	63	11	258	19	13	355	18	8
110	-5.790301	-40.177661	10	0.281	1.035	0.706	45	34	44	146	17	45	258	51	20
111	-5.794787	-40.171127	9	0.632	1.094	0.830	72	59	14	204	22	14	303	20	5
130	-5.787899	-40.162893	11	5.810	1.140	0.453	109	69	14	205	3	17	296	21	13
131	-5.824423	-40.137321	9	0.047	1.024	-0.134	359	44	14	247	21	45	139	39	45
132	-5.853125	-40.130434	9	0.049	1.032	0.557	9	22	24	105	15	24	227	64	11

Tabela 12 – Magnetic susceptibility and anisotropy measurements for the Várzea do Boi stock. N = number of sites, K_M = magnetic susceptibility, P = degree of anisotropy, T = shape parementer, Dec. = Declination, Inc. = Inclination, αK = maximum angle of 2σ uncertainty ellipse.

	Coordinates						K_{max}			K_{int}			K_{min}		
Site	Lat.	Long.	N	K_M	P	T	Dec.	Inc.	αK_{max}	Dec.	Inc.	αK_{int}	Dec.	Inc.	αK_{min}
35	-5.954932	-40.231080	9	5.813	1.104	0.476	65	37	21	171	21	20	285	46	9
36	-5.936287	-40.233145	9	0.962	1.035	0.397	56	70	23	174	10	21	267	17	20
38	-5.882178	-40.195898	15	0.349	1.024	-0.260	13	0	11	104	5	27	280	85	27
39	-5.897267	-40.190535	9	2.850	1.143	0.578	206	13	17	342	73	16	114	12	8
40	-5.842798	-40.228412	18	1.192	1.049	-0.351	125	76	11	263	10	24	355	9	25
43	-5.868402	-40.240085	12	4.853	1.054	-0.324	330	81	21	169	9	49	79	3	49
44	-5.864063	-40.193283	13	6.579	1.176	0.465	134	65	14	325	25	18	233	4	16
45	-5.870538	-40.209185	10	4.961	1.093	-0.505	26	7	8	119	27	8	284	62	8
48	-5.856970	-40.208150	11	0.505	1.016	0.191	243	71	14	140	5	12	49	18	14
49	-5.905662	-40.216262	14	0.498	1.035	0.781	334	67	35	142	22	35	234	4	27
50	-5.896407	-40.235282	11	3.334	1.114	0.111	192	78	10	359	12	8	90	3	8
51	-5.894645	-40.225525	11	0.562	1.007	0.261	99	42	37	360	10	38	259	46	20
52	-5.887935	-40.212492	12	0.554	1.034	0.385	217	13	8	319	39	8	112	48	7
53	-5.918842	-40.197812	8	0.323	1.079	0.546	218	16	20	3	71	21	125	10	11
54	-5.917983	-40.193345	12	0.605	1.042	0.923	41	16	27	159	58	27	302	26	6
55	-5.857315	-40.231273	14	0.505	1.116	0.862	354	5	21	85	12	20	241	77	8
56	-5.845033	-40.231930	14	0.540	1.021	-0.451	76	65	22	208	17	34	303	18	31
57	-5.841390	-40.216475	14	0.640	1.025	0.245	44	0	43	135	82	43	314	8	13
58	-5.868145	-40.225127	9	0.337	1.084	0.734	188	15	15	78	53	12	289	33	10
60	-5.862740	-40.216327	9	0.481	1.071	0.274	142	38	6	9	42	7	254	26	7
61	-5.854993	-40.206783	10	5.385	1.121	0.493	116	74	11	316	15	15	224	5	14
62	-5.955065	-40.214488	8	1.050	1.059	-0.359	73	61	11	312	16	23	215	24	24
63	-5.955295	-40.223563	12	3.886	1.045	0.315	70	35	39	171	15	39	280	51	21
64	-5.934208	-40.240263	12	0.488	1.063	0.417	120	66	17	16	6	21	283	24	14
65	-5.842972	-40.206122	10	9.390	1.190	-0.314	145	61	5	301	27	6	37	10	7
66	-5.906438	-40.203205	11	0.387	1.018	0.235	64	2	20	331	69	20	155	22	16
67	-5.946708	-40.239605	13	0.522	1.037	0.261	155	59	9	21	22	12	283	20	14
68	-5.880360	-40.203025	11	0.474	1.017	-0.205	135	67	23	284	20	43	18	11	42
69	-5.891055	-40.190275	11	0.617	1.040	-0.013	22	37	7	165	47	25	277	19	25
70	-5.921965	-40.219240	9	0.902	1.023	0.184	195	42	14	334	40	20	84	22	22
71	-5.919177	-40.211252	10	0.422	1.024	-0.249	354	67	6	104	9	11	198	21	11
72	-5.906425	-40.211548	10	0.412	1.014	0.501	352	47	11	253	8	12	155	42	9
73	-5.928827	-40.226858	9	0.222	1.016	0.013	224	58	15	355	22	29	95	22	28
74	-5.940983	-40.234760	10	0.549	1.050	0.329	103	51	14	355	15	21	254	36	21
75	-5.862417	-40.213495	10	0.463	1.015	-0.457	171	62	6	19	25	21	284	12	21
76	-5.852757	-40.231235	9	6.022	1.117	0.271	196	38	12	70	37	11	313	31	11
107	-5.947393	-40.207592	9	0.193	1.023	-0.039	40	45	12	259	37	22	152	21	21
108	-5.946925	-40.216506	13	0.489	1.045	-0.533	87	18	10	237	69	29	353	10	29
109	-5.944344	-40.227391	11	1.290	1.076	0.698	130	61	68	10	15	68	274	24	6
116	-5.960936	-40.231099	13	4.500	1.064	0.842	158	18	43	28	63	43	254	20	13
117	-5.959042	-40.236580	9	1.900	1.043	0.971	180	19	82	65	50	82	283	33	11
118	-5.884448	-40.224046	11	1.530	1.037	-0.243	54	13	26	146	7	25	264	75	20
119	-5.847221	-40.222012	10	0.634	1.062	-0.062	96	81	6	306	8	17	215	5	17
120	-5.874414	-40.246577	13	0.669	1.011	-0.681	147	74	39	42	5	73	311	16	73
121	-5.861872	-40.249666	8	0.678	1.034	-0.315	62	73	10	295	11	17	202	13	18
122	-5.859363	-40.238414	8	2.840	1.104	0.288	197	9	8	94	55	8	294	33	5
123	-5.905285	-40.195415	9	0.389	1.024	0.327	215	10	33	9	80	32	124	4	16
124	-5.899325	-40.202369	11	0.770	1.027	0.795	219	5	33	21	84	33	129	2	7
125	-5.877604	-40.234122	13	2.430	1.046	-0.081	246	18	15	338	4	16	81	71	16
126	-5.877675	-40.219129	10	0.669	1.062	0.431	47	15	4	139	5	4	248	75	2
127	-5.923017	-40.202635	8	4.890	1.132	-0.079	243	16	11	15	67	12	149	16	15
128	-5.890269	-40.198433	9	1.280	1.129	0.697	205	12	9	310	49	9	106	39	5
129	-5.899503	-40.210084	11	0.223	1.016	0.659	52	35	49	279	44	49	161	26	16
133	-5.955314	-40.243437	10	5.530	1.085	0.260	185	16	19	64	61	18	282	24	16

B.2 U-Pb isotopic data

U-Pb isotope data from SHRIMP analyses carried out on zircons from the Várzea do Boi (VB1A and CA124), Lagoa de Pedra (LP) and Iapi stocks (IA) are given in Tabela 13. Cathodoluminescence images are given with concordia diagrams in Figures 65, 66, 67 and 68. Error ellipses are labeled to their corresponding spots.

Tabela 13 – U-Pb analysis data. Errors are 1σ. Ages are calculated after correction for common Pb. * Discarded.

												Ages (Ma)			
Spot	$^{206}Pb_c$ (%)	U (ppm)	Th (ppm)	$\frac{Th}{U}$	$\frac{^{206}Pb}{^{238}U}$	1σ (%)	$\frac{^{207}Pb}{^{235}U}$	1σ (%)	ρ^2	$\frac{^{207}Pb}{^{206}Pb}$	1σ (%)	$\frac{^{206}Pb}{^{238}U}$	1σ	$\frac{^{207}Pb}{^{206}Pb}$	1σ
CA124-1.1	0.19	326	242	0.743	0.093	0.84	0.757	1.50	0.56	0.059	1.20	573	5	569	27
CA124-2.1	1.05	199	155	0.776	0.093	0.91	0.772	2.80	0.32	0.060	2.70	576	5	601	58
CA124-3.1	0.37	279	172	0.616	0.093	0.86	0.768	1.80	0.47	0.060	1.60	576	5	591	35
CA124-4.1	0.12	372	221	0.592	0.096	0.85	0.791	1.40	0.60	0.060	1.10	592	5	589	25
CA124-5.1	0.22	128	64	0.498	0.092	0.95	0.749	2.30	0.42	0.059	2.10	567	5	569	45
CA124-6.1	0.79	168	37	0.221	0.093	0.94	0.759	3.20	0.29	0.059	3.10	572	5	579	67
CA124-7.1	0.21	298	310	1.040	0.098	1.13	0.813	2.10	0.54	0.060	1.80	604	7	605	38
CA124-8.1	0.69	181	109	0.601	0.097	0.96	0.816	2.70	0.35	0.061	2.50	599	5	631	55
CA124-10.1	0.11	527	448	0.849	0.097	0.82	0.793	1.30	0.61	0.059	1.10	595	5	584	23
CA124-11.1	0.34	99	34	0.349	0.095	1.63	0.782	3.30	0.49	0.060	2.90	586	9	589	62
CA124-12.1	0.20	310	241	0.776	0.093	0.84	0.755	1.50	0.55	0.059	1.30	572	5	568	28
VB1A-1.1*	0.41	530	253	0.477	0.107	1.00	0.906	2.80	0.30	0.062	2.60	652	6	663	56
VB1A-2.1	0.22	428	451	1.054	0.098	1.30	0.835	1.70	0.70	0.062	1.20	605	7	659	25
VB1A-3.1	0.18	256	186	0.727	0.097	1.00	0.802	1.80	0.60	0.060	1.40	599	6	596	31
VB1A-4.1	0.41	238	210	0.882	0.097	1.00	0.800	2.70	0.40	0.060	2.60	595	6	602	55
VB1A-6.1*	0.28	363	206	0.567	0.107	1.00	0.899	1.90	0.50	0.061	1.60	653	6	646	35
VB1A-10.1	1.55	551	289	0.525	0.099	0.90	0.836	2.60	0.40	0.061	2.40	609	6	644	52
VB1A-11.1	2.39	677	533	0.787	0.099	0.90	0.837	3.20	0.30	0.061	3.10	609	5	647	66
VB1A-13.1	0.36	232	301	1.297	0.096	1.00	0.804	2.00	0.50	0.061	1.70	589	6	638	36
VB1A-14.1	1.81	543	379	0.698	0.099	1.00	0.817	5.00	0.20	0.060	4.90	608	6	601	105
VB1A-15.1*	1.41	729	414	0.568	0.104	1.10	0.869	2.40	0.50	0.061	2.10	637	7	628	45
VB1A-18.1	0.91	237	175	0.738	0.091	1.00	0.748	2.80	0.40	0.059	2.60	564	5	580	56
VB1A-19.1	21.01	274	217	0.792	0.099	1.30	0.850	11.90	0.10	0.062	11.80	607	8	688	252
VB1A-20.1	1.24	1013	432	0.426	0.097	0.90	0.805	1.70	0.50	0.060	1.50	597	5	611	32
VB1A-21.1	1.24	951	328	0.345	0.093	0.90	0.779	3.20	0.30	0.061	3.10	575	5	624	66
VB1A-24.1	0.99	896	417	0.465	0.095	0.90	0.796	2.40	0.40	0.061	2.20	585	5	632	48
VB1A-25.1	3.11	892	551	0.618	0.100	1.10	0.854	11.10	0.10	0.062	11.00	614	7	671	236
VB1A-28.1	5.03	882	315	0.357	0.090	1.00	0.743	5.00	0.20	0.060	4.90	557	5	595	105
VB1A-29.1	6.93	1317	319	0.242	0.093	1.10	0.857	5.90	0.20	0.067	5.80	574	6	829	121
VB1A-30.1	4.82	1007	732	0.727	0.092	0.90	0.757	4.90	0.20	0.060	4.90	564	5	605	105
VB1A-32.1	2.02	756	295	0.390	0.100	2.30	0.836	4.60	0.50	0.060	3.90	616	13	620	85
IA-1.1	1.23	132	108	0.815	0.101	3.80	0.880	6.60	0.58	0.064	5.30	617.1	23	735	113
IA-2.1	0.32	274	349	1.272	0.098	3.80	0.820	4.60	0.82	0.061	2.70	602.8	22	626	58
IA-3.1	0.63	191	202	1.060	0.093	3.80	0.750	5.30	0.71	0.058	3.70	574.2	21	544	82
IA-4.1	0.25	384	456	1.187	0.091	3.80	0.730	4.50	0.84	0.058	2.40	562	20	534	53
IA-5.1	0.73	171	150	0.878	0.098	3.80	0.800	5.60	0.68	0.059	4.10	602.7	22	582	90
IA-6.1	0.54	325	332	1.022	0.098	3.80	0.820	4.60	0.84	0.061	2.40	599.5	22	627	53
IA-7.1	0.80	175	145	0.832	0.095	3.80	0.790	5.60	0.68	0.060	4.10	585.5	21	607	88
IA-8.1	0.47	272	266	0.978	0.098	3.80	0.800	4.60	0.81	0.060	2.70	601.2	22	586	59
IA-9.1	0.51	348	460	1.322	0.094	3.80	0.790	4.50	0.84	0.061	2.50	577.4	21	651	53
IA-10.1	0.68	118	92	0.779	0.099	3.90	0.840	5.20	0.76	0.062	3.40	606.7	23	671	72
IA-11.1	0.85	202	187	0.928	0.089	3.80	0.700	6.40	0.59	0.058	5.10	546.6	20	520	113
IA-12.1	0.47	188	224	1.189	0.097	4.30	0.790	5.50	0.79	0.059	3.40	596	25	561	75
IA-13.1	1.89	78	57	0.735	0.093	3.90	0.820	11.00	0.36	0.064	10.30	572	22	751	218
IA-14.1	0.95	150	138	0.922	0.094	3.80	0.780	6.60	0.58	0.060	5.40	577.9	21	601	117
IA-15.1	0.73	220	259	1.175	0.092	3.90	0.810	6.20	0.63	0.064	4.80	566.5	21	728	103
LP-1.1	0.66	352	255	0.725	0.093	3.50	0.760	6.00	0.59	0.060	4.80	573	20	585	105
LP-2.1	0.77	326	228	0.700	0.093	3.60	0.770	5.80	0.62	0.060	4.60	571	20	605	99
LP-3.1	0.82	425	315	0.741	0.089	3.60	0.710	6.10	0.59	0.058	4.90	550	19	519	108
LP-4.1	0.23	1832	2150	1.174	0.092	3.50	0.760	3.70	0.96	0.060	1.00	569	19	607	23
LP-5.1	0.66	333	228	0.683	0.095	3.90	0.780	7.30	0.54	0.060	6.10	582	22	597	132
LP-6.1	2.18	183	120	0.659	0.091	3.70	0.700	15.50	0.24	0.056	15.00	560	20	443	335
LP-7.1	1.14	236	127	0.536	0.093	3.70	0.810	14.50	0.25	0.063	14.00	574	20	706	298
LP-8.1	0.61	393	226	0.575	0.096	3.50	0.810	5.60	0.63	0.061	4.40	590	20	641	94
LP-9.1	0.88	336	218	0.649	0.097	3.60	0.810	5.90	0.60	0.061	4.70	597	20	626	102
LP-10.1	0.59	477	383	0.804	0.093	3.50	0.760	4.60	0.76	0.059	3.00	573	19	572	65
LP-11.1	0.68	323	175	0.541	0.096	3.60	0.790	5.60	0.63	0.060	4.40	590	20	588	95
LP-12.1	1.11	345	218	0.631	0.088	3.90	0.710	7.10	0.56	0.058	5.90	544	21	540	129
LP-13.1	2.36	156	77	0.496	0.091	3.70	0.750	14.00	0.26	0.060	13.50	561	20	590	294
LP-14.1	0.75	331	208	0.629	0.092	3.50	0.800	5.30	0.67	0.063	3.90	569	19	697	84
LP-15.1	1.31	216	72	0.335	0.099	3.60	0.830	7.60	0.47	0.061	6.70	606	21	652	145

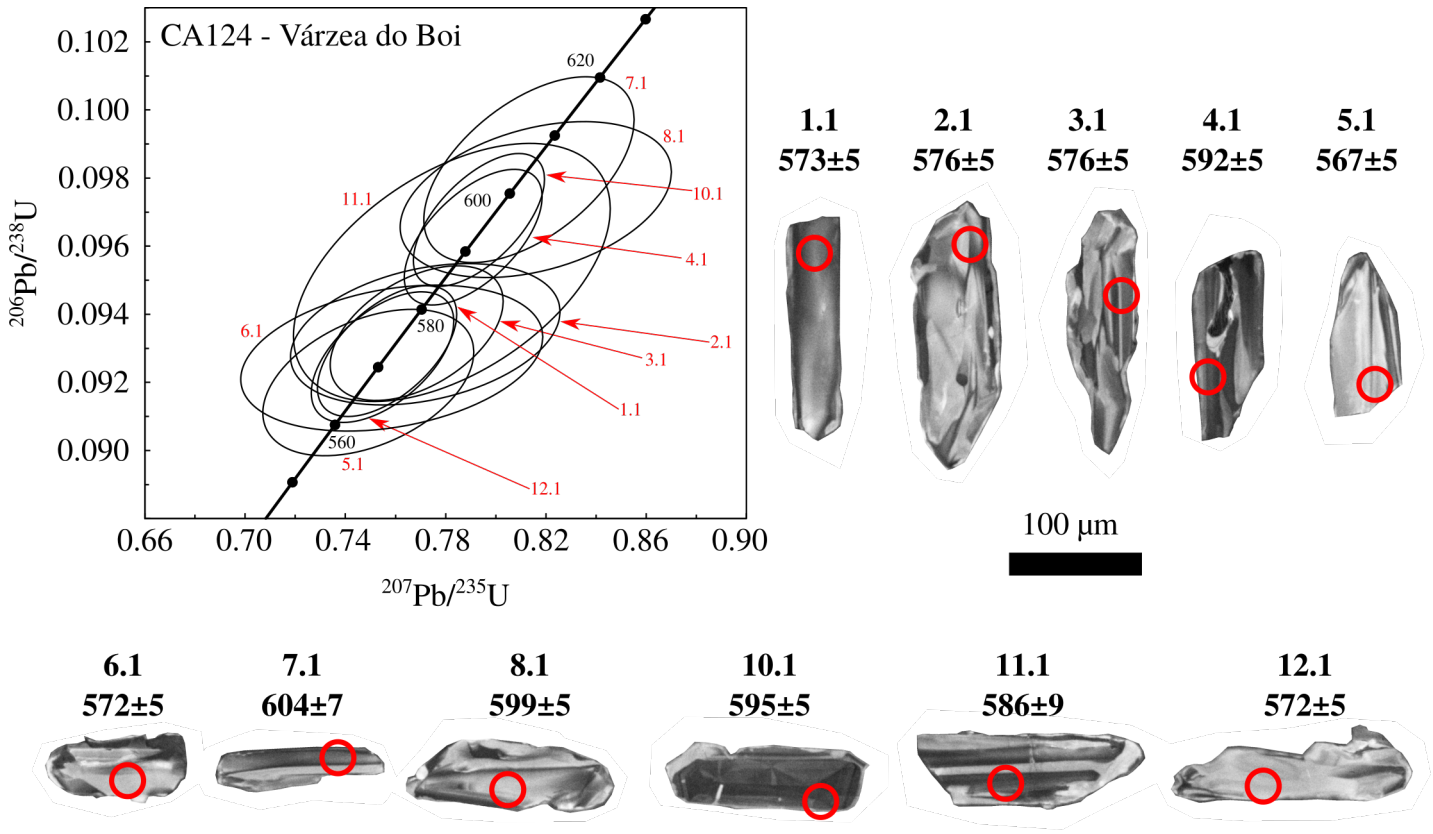

Figura 65 – U-Pb concordia diagram and cathodoluminescence images of zircons from Várzea do Boi stock (CA124). Analysed spots are tagged with $^{206}Pb/^{238}U$ ages at 1σ errors.

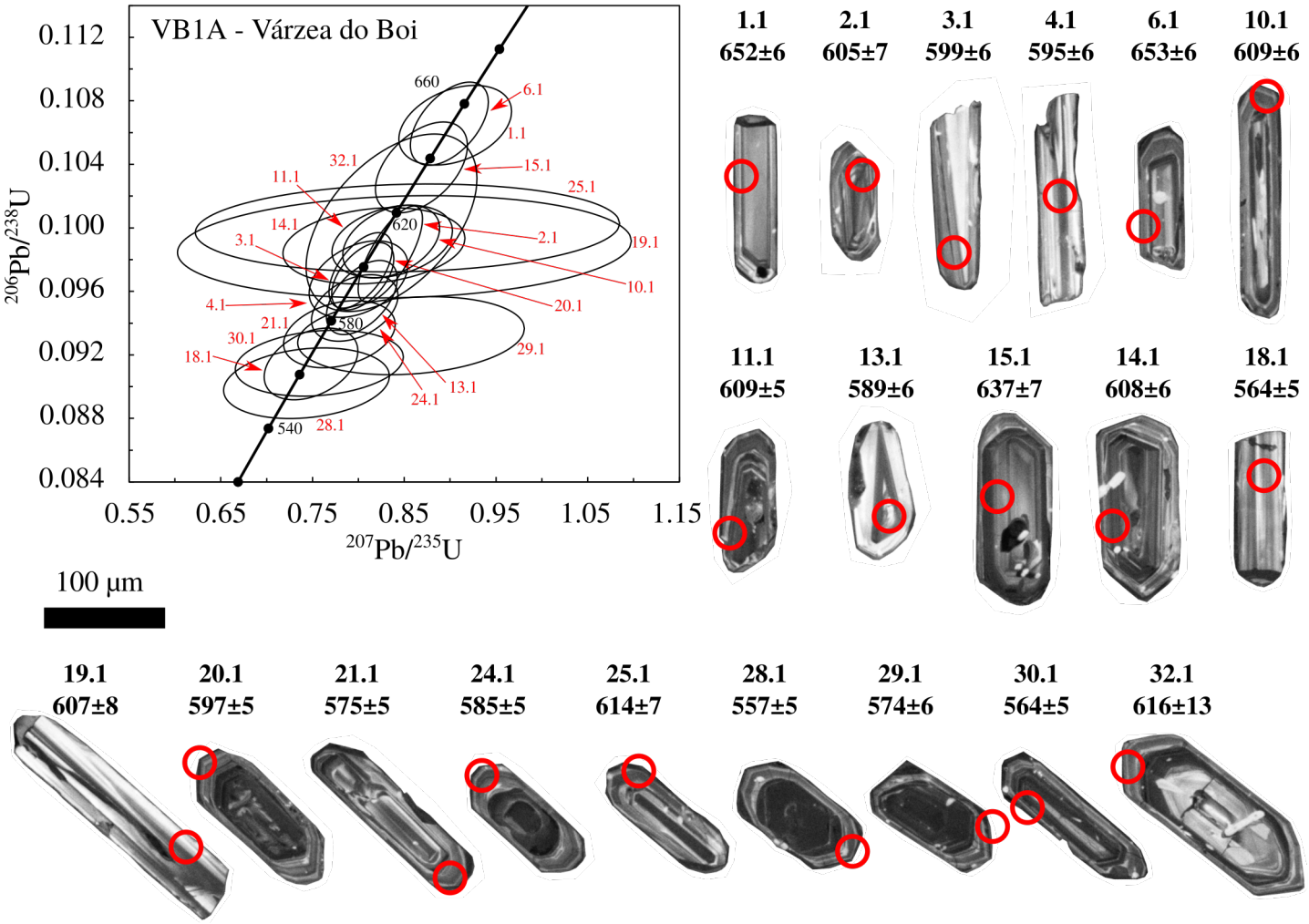

Figura 66 – U-Pb concordia diagram and cathodoluminescence images of zircons from Várzea do Boi stock (VB1A). Analysed spots are tagged with $^{206}Pb/^{238}U$ ages at 1σ errors.

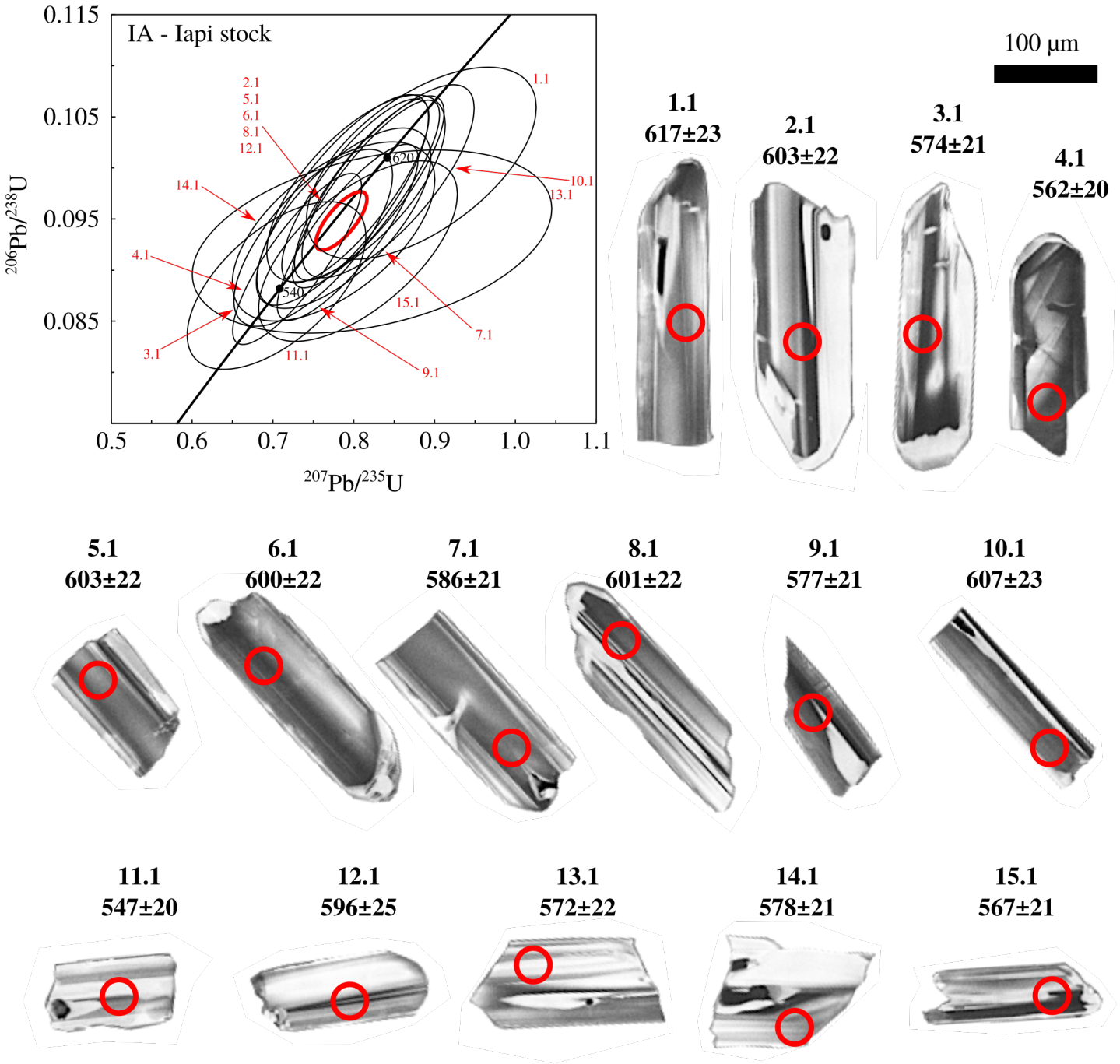

Figura 67 – U-Pb concordia diagram and cathodoluminescence images of zircons from Iapi stock (IA). Analysed spots are tagged with $^{206}Pb/^{238}U$ ages at 1σ errors.

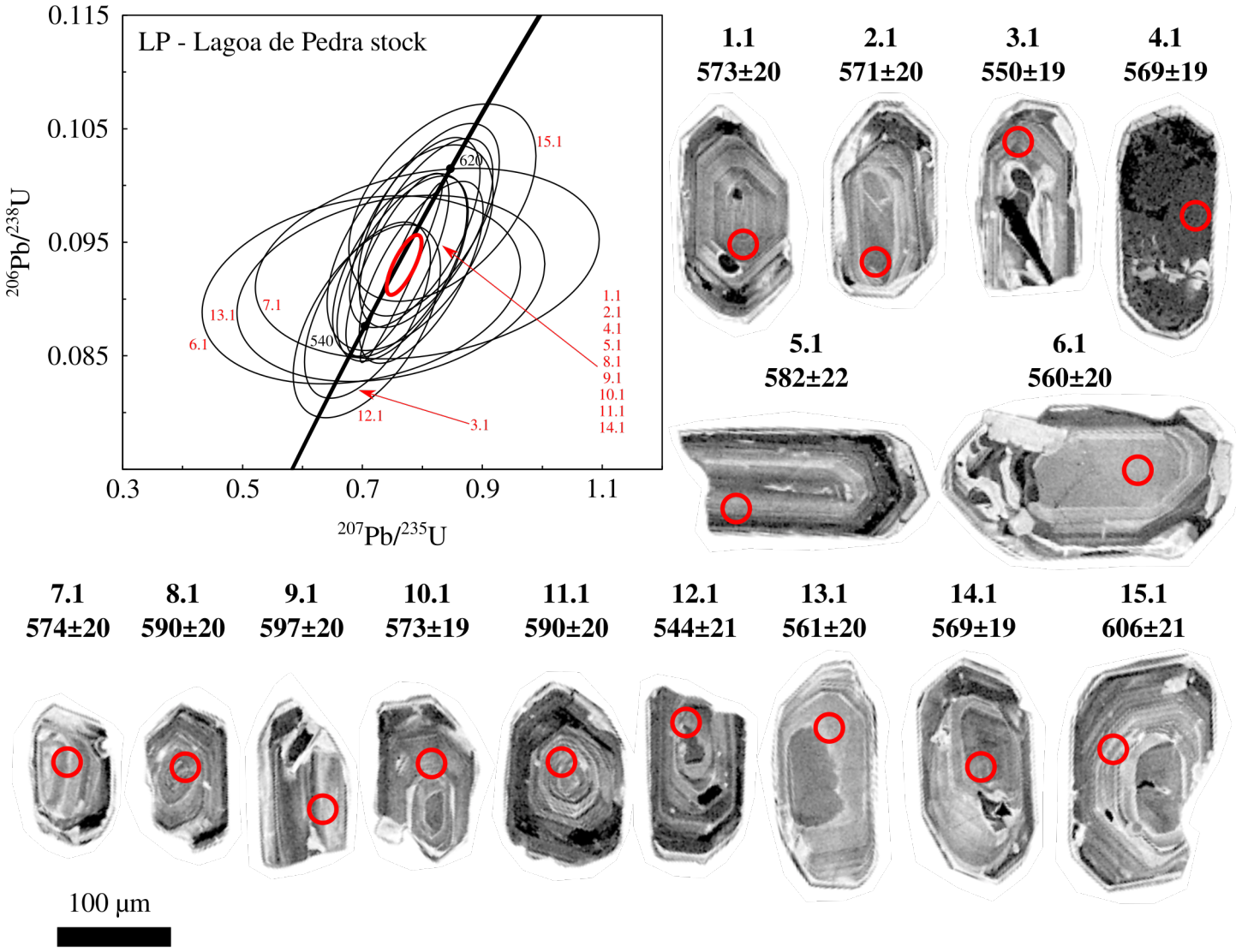

Figura 68 – U-Pb concordia diagram and cathodoluminescence images of zircons from Lagoa de Pedra stock (LP). Analysed spots are tagged with $^{206}Pb/^{238}U$ ages at 1σ errors.

B.3 Ar isotopic data

Tabela 14 – Ar isotope data from step heating analyses. Errors are 2σ.

T	$^{40}Ar/^{39}Ar$	$^{38}Ar/^{39}Ar$	$^{37}Ar/^{39}Ar$	$^{36}Ar/^{39}Ar$	^{39}Ar released (%)	$Ar^{40}*/^{39}Ar$	2σ	Age (Ma)	2σ (Ma)
Ematuba dykes - amphibole							$J = 0.00330800 \pm 0.00000400$		
0.10 W	682.470	0.071	6.024	250.868	610.619	610.619	230.753	1998.607	457.076
0.20 W	150.421	0.068	1.515	3.173	149.753	149.753	18.426	727.634	73.707
0.30 W	119.770	0.029	2.552	40.763	107.996	107.996	13.087	552.369	57.679
0.40 W	119.551	0.013	6.981	4.643	119.296	119.296	2.213	601.499	9.490
0.50 W	113.786	0.008	6.759	2.970	113.969	113.969	1.484	578.505	6.448
0.60 W	112.522	0.029	7.364	0.187	113.630	113.630	3.163	577.035	13.752
0.70 W	107.525	0.019	10.871	9.283	106.417	106.417	7.200	545.398	31.854
0.80 W	105.701	0.337	16.119	18.844	102.508	102.508	34.994	528.020	156.323
0.90 W	113.643	0.054	18.786	55.675	99.813	99.813	26.000	515.941	116.922
1.00 W	131.212	-0.037	17.224	108.399	101.431	101.431	40.825	523.202	182.858
1.20 W	92.740	0.308	14.278	59.289	76.942	76.942	18.818	410.049	89.730
1.40 W	207.122	-0.041	18.914	764.772	-19.929	-19.929	195.530	-123.327	1252.199
Tauá shear zone mylonite - biotite							$J = 0.00328400 \pm 0.00000400$		
0.10 W	111.212	0.012	0.009	0.124	1.102	74.146	6.125	394.078	29.251
0.20 W	110.350	0.006	0.015	0.000	21.506	110.330	0.638	559.118	2.782
0.30 W	110.466	0.013	0.007	-0.002	22.571	111.023	0.554	562.137	2.413
0.40 W	111.293	0.017	0.043	0.000	16.344	111.258	0.804	563.159	3.497
0.50 W	112.392	0.003	0.190	0.000	11.004	112.529	1.909	568.677	8.277
0.60 W	111.349	0.005	0.042	0.017	12.697	106.144	0.504	540.776	2.219
0.70 W	111.712	0.006	0.034	-0.004	12.084	112.764	1.818	569.697	7.881
0.80 W	122.348	-0.020	0.103	-0.024	1.013	129.540	20.739	640.976	86.404
0.90 W	115.208	-0.004	0.348	-0.022	1.203	121.705	10.452	608.035	44.347
1.00 W	142.326	0.034	1.367	-0.064	0.377	161.614	33.619	769.891	130.425
1.20 W	306.661	0.177	-0.317	-0.565	0.044	475.167	537.827	1700.144	1247.391
1.40 W	175.657	0.064	-1.039	-0.584	0.056	349.608	274.409	1382.619	758.607
Iapi stock - amphibole							$J = 0.00330800 \pm 0.00000400$		
0.10 W	334.499	0.186	1.121	0.052	0.171	319.410	210.069	1303.899	611.013
0.20 W	111.980	0.005	0.080	0.015	3.906	107.543	2.423	550.372	10.692
0.30 W	110.729	0.019	2.341	0.003	10.080	110.174	1.127	561.945	4.941
0.40 W	110.702	0.006	3.584	0.001	11.620	111.046	1.069	565.764	4.676
0.50 W	110.671	0.009	4.271	0.003	16.818	110.581	1.191	563.727	5.218
0.60 W	111.379	0.009	4.554	0.003	16.560	111.151	1.108	566.224	4.845
0.70 W	110.742	0.022	4.385	0.002	15.098	110.893	0.878	565.096	3.843
0.80 W	112.823	0.028	4.636	0.003	7.859	112.674	2.097	572.872	9.139
0.90 W	113.880	0.011	4.269	0.006	2.389	112.692	4.401	572.950	19.179
1.00 W	112.422	0.004	5.123	-0.002	7.058	113.716	2.052	577.406	8.920
1.20 W	111.789	0.010	5.167	0.003	7.157	111.816	2.258	569.129	9.861
1.40 W	123.955	0.018	6.646	0.019	1.283	119.287	14.589	601.462	62.575
Iapi stock - biotite							$J = 0.00328400 \pm 0.00000400$		
0.10 W	81.385	-0.002	0.069	0.019	2.215	75.658	3.413	401.288	16.234
0.20 W	106.530	0.013	0.047	0.001	17.603	106.197	0.687	541.009	3.023
0.30 W	110.121	0.010	0.007	0.001	23.727	109.845	0.478	557.002	2.084
0.40 W	110.603	0.012	0.013	0.001	17.844	110.158	0.720	558.366	3.141
0.50 W	111.157	0.018	0.031	-0.001	9.836	111.404	1.070	563.792	4.652
0.60 W	111.967	0.002	0.177	0.001	7.904	111.763	1.152	565.353	5.006
0.70 W	110.344	0.004	0.186	-0.001	11.307	110.635	0.889	560.445	3.870
0.80 W	110.086	0.000	0.196	0.002	5.670	109.663	1.833	556.207	8.005
0.90 W	107.232	0.022	-0.003	0.000	1.049	107.164	8.338	545.263	36.624
1.00 W	103.456	0.003	-0.001	-0.013	0.738	107.353	14.880	546.091	65.330
1.20 W	108.689	0.007	-0.063	-0.010	1.992	111.810	3.555	565.558	15.443
1.40 W	29.307	-0.033	-1.258	-0.010	0.106	32.033	108.963	180.876	585.486
1.60 W	116.087	0.543	0.170	0.307	0.035	24.531	324.696	140.107	1784.457
1.80 W	-72.291	-0.135	3.186	0.247	-0.027	-146.133	395.500	-1182.168	4515.877

Tabela 15 – Ar isotope data from step heating analyses. Errors are 2σ.

T	$^{40}Ar/^{39}Ar$	$^{38}Ar/^{39}Ar$	$^{37}Ar/^{39}Ar$	$^{36}Ar/^{39}Ar$	^{39}Ar released (%)	$Ar^{40}*/^{39}Ar$	2σ	Age (Ma)	2σ (Ma)
Várzea do Boi stock - amphibole								$J = 0.00330800 \pm 0.00000400$	
0.10 W	158.018	0.263	1.899	-0.082	0.081	182.917	142.228	855.658	530.061
0.20 W	93.734	-0.006	0.328	0.041	0.936	81.502	15.215	431.663	71.688
0.30 W	109.350	0.008	3.324	-0.002	7.187	110.337	2.243	562.658	9.831
0.40 W	109.207	0.009	3.239	0.000	10.478	109.801	1.135	560.306	4.981
0.50 W	110.292	0.006	3.092	0.003	12.841	109.883	0.834	560.668	3.657
0.60 W	109.699	0.016	3.743	0.001	17.414	109.839	0.783	560.475	3.437
0.70 W	110.781	0.005	4.005	0.002	10.242	110.754	1.053	564.486	4.610
0.80 W	110.456	0.006	4.212	0.003	14.737	110.328	0.939	562.619	4.113
0.90 W	110.430	0.007	4.045	-0.002	9.128	111.688	1.890	568.568	8.257
1.00 W	109.568	0.007	4.451	0.007	3.446	108.120	5.486	552.918	24.173
1.20 W	108.952	0.005	4.288	0.001	4.735	109.394	3.541	558.521	15.552
1.40 W	110.763	0.010	4.309	0.001	4.476	111.051	2.573	565.784	11.256
1.60 W	108.729	0.012	2.707	-0.009	1.483	111.849	10.055	569.273	43.905
1.80 W	105.900	0.013	2.141	0.015	0.729	101.846	12.281	525.062	54.951
2.00 W	108.191	0.264	3.459	-0.011	0.749	112.088	11.258	570.318	49.127
2.20 W	110.328	0.037	4.233	-0.001	1.338	111.292	8.240	566.840	36.027
Várzea do Boi stock - biotite								$J = 0.00328400 \pm 0.00000400$	
0.10 W	70.406	0.005	0.626	0.008	1.131	68.021	5.943	364.592	28.846
0.20 W	104.817	0.014	0.011	0.000	15.774	104.683	0.841	534.331	3.718
0.30 W	108.967	0.013	0.003	0.001	21.957	108.691	0.412	551.958	1.803
0.40 W	109.386	0.013	0.006	0.000	20.066	109.388	0.493	555.005	2.155
0.50 W	108.923	0.011	0.018	-0.002	13.494	109.521	0.912	555.587	3.983
0.60 W	108.558	0.015	0.016	0.001	8.750	108.298	0.827	550.237	3.622
0.70 W	108.959	0.005	0.026	-0.006	7.163	110.685	1.214	560.663	5.286
0.80 W	109.035	0.005	0.004	-0.004	4.837	110.371	1.138	559.294	4.961
0.90 W	113.718	0.012	0.106	0.005	2.278	112.160	4.459	567.075	19.353
1.00 W	117.908	0.014	0.089	-0.016	0.739	122.681	9.519	612.172	40.293
1.20 W	111.872	0.008	0.043	0.005	3.739	110.471	2.252	559.733	9.815
1.40 W	313.322	0.524	13.381	0.137	0.042	276.078	301.662	1166.984	939.569
1.60 W	297.266	-1.337	-4.214	0.053	0.012	280.190	983.207	1179.743	3040.801
1.80 W	156.786	-1.319	-0.234	-1.116	0.013	489.702	1137.488	1733.545	2589.915
2.00 W	113.190	0.745	11.701	1.431	0.014	-315.581	806.770	0.000	131704.468
2.20 W	-115.611	0.038	-2.884	-0.623	-0.011	69.939	739.672	373.875	3572.111

B.4 Calculation of closure temperatures and cooling rates

An analytical solution for the closure temperature (T_C) of a mineral system with respect to diffusion of argon was derived by Dodson (1973) from the Arrhenius equation $D = D_0 \exp -E/RT$, where D is the diffusion coefficient at temperature T, E is activation energy, R is the gas constant and D_0 is the diffusivity. By assuming a linear cooling path at sufficiently slow rates (dT/dt), T_C is given by

$$E/RT_C = \ln\left(\frac{-ART_C^2 D_0}{a^2 E dT/dt}\right), \tag{B.1}$$

where A is the mineral shape factor (55 for a sphere, 27 for prism and 9 for sheet) and a is the diffusion radius, which can be grain size or the effective diffusion radius if this the former has greater value. Effective diffusion radius is 80μm for amphibole (Harrison, 1982) and 150μm for biotite (Harrison et al., 1985). We have calculated T_C and dT/dt by iterating over dT/dt for every new solution of T_C.

Radiometric dating analyses carried out on mineral concentrates obtained from the same hand sample provided the temperature-time control points to which starting cooling curves were approximated. This was done assuming nominal closure temperatures of 550 °C for amphibole and 300 °C for biotite. Zircon U-Pb ages were also used as control points assuming they record the timing of peak metamorphic temperatures in the shear zones (750 ± 50°C, see main text). Cooling curves were then fit to T-t control points. Linear fits were used in mineral pairs (i.e. amphibole to biotite or zircon to amphibole) and polynomial fits in mineral trios (Dodson, 1973). The polynomial fit will approximate the linear path if cooling rate was constant (a reasonable assumption according to Dunlap, 2000) and there was no argon loss. If argon loss occurred, polynomial fits on mineral trios will prevent the cooling rate through the amphibole closure temperature from being underestimated.

We have used Monte Carlo simulations in the manner conceived by (Scibiorski et al., 2015) to minimise convariances and determine meaningful uncertainties in the calculation of T_C and dT/dt. The probability distributions used for the different parameters input to the closure temperature model of Dodson (1973) are given in Table 16. 20000 trials were performed, of which only the ones yielding positive cooling rates were con-

sidered. Samples with high uncertainties in ages or very steep cooling rates were more susceptible to producing negative cooling rates. The histograms of calculated values of dT/dt are given in Figures 69 and 70, and of calculated values of T_C are given in Figures 71 and 72. Functions developed in Python for the Monte Carlo simulations and iterations of dT/dt and T_C are stable to varying inputs according to our trials so far, and are given in page 199.

Tabela 16 – Probability distributions used for the parameters input to calculations of T_C and dT/dt.

Parameter	Value	Source	Probability distribution
Age [Ma]	$\pm 2\sigma$	see main text	Normal
Peak metamorphic T	750 ± 50	see main text	Triangular
R [J/molK]	8.3145		Constant
		Amphibole	
E [kcal/mol]	64.1 ± 1.7	Harrison (1982)	Triangular
D [cm^{2}s^{-1}]	$0.024^{+0.053}_{-0.011}$	Harrison (1982)	Triangular
a [μm]	80	Harrison (1982)	Constant
A	55	Harrison (1982)	Constant
		Muscovite	
E [kcal/mol]	63.0 ± 7.0	Harrison et al. (2009)	Triangular
D [cm^{2}s^{-1}]	$2.300^{+70.0}_{-2.2}$	Harrison et al. (2009)	Triangular
a [μm]	100	Harrison et al. (2009)	Constant
A	27	Harrison et al. (2009)	Constant
		Biotite	
E [kcal/mol]	47.0 ± 2.0	Harrison et al. (1985)	Triangular
D [cm^{2}s^{-1}]	$0.077^{+0.210}_{-0.060}$	Harrison et al. (1985)	Triangular
a [μm]	150	Harrison et al. (1985)	Constant
A	27	Harrison et al. (1985)	Constant

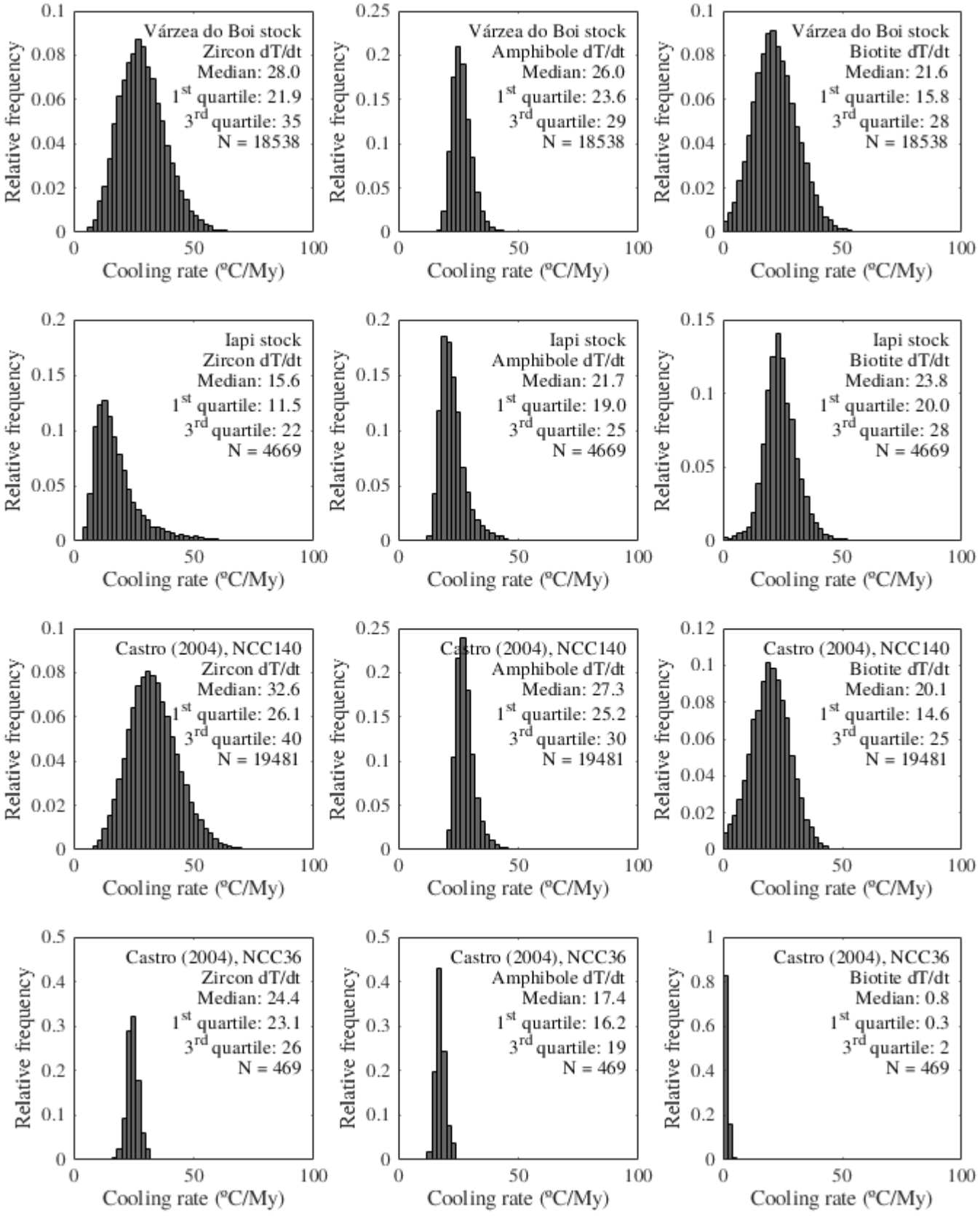

Figura 69 – Histograms of simulated dT/dt.

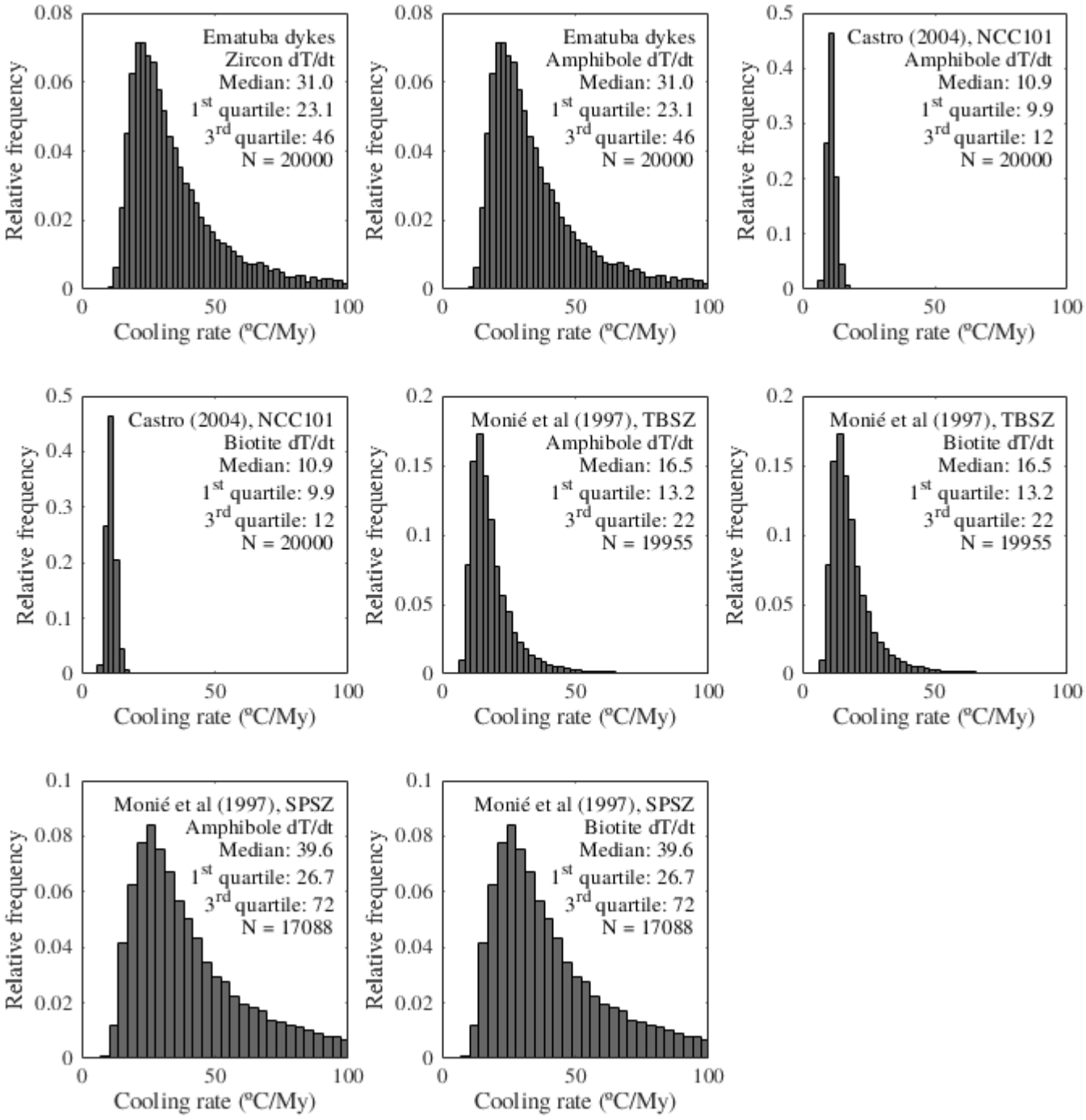

Figura 70 – Histograms of simulated dT/dt.

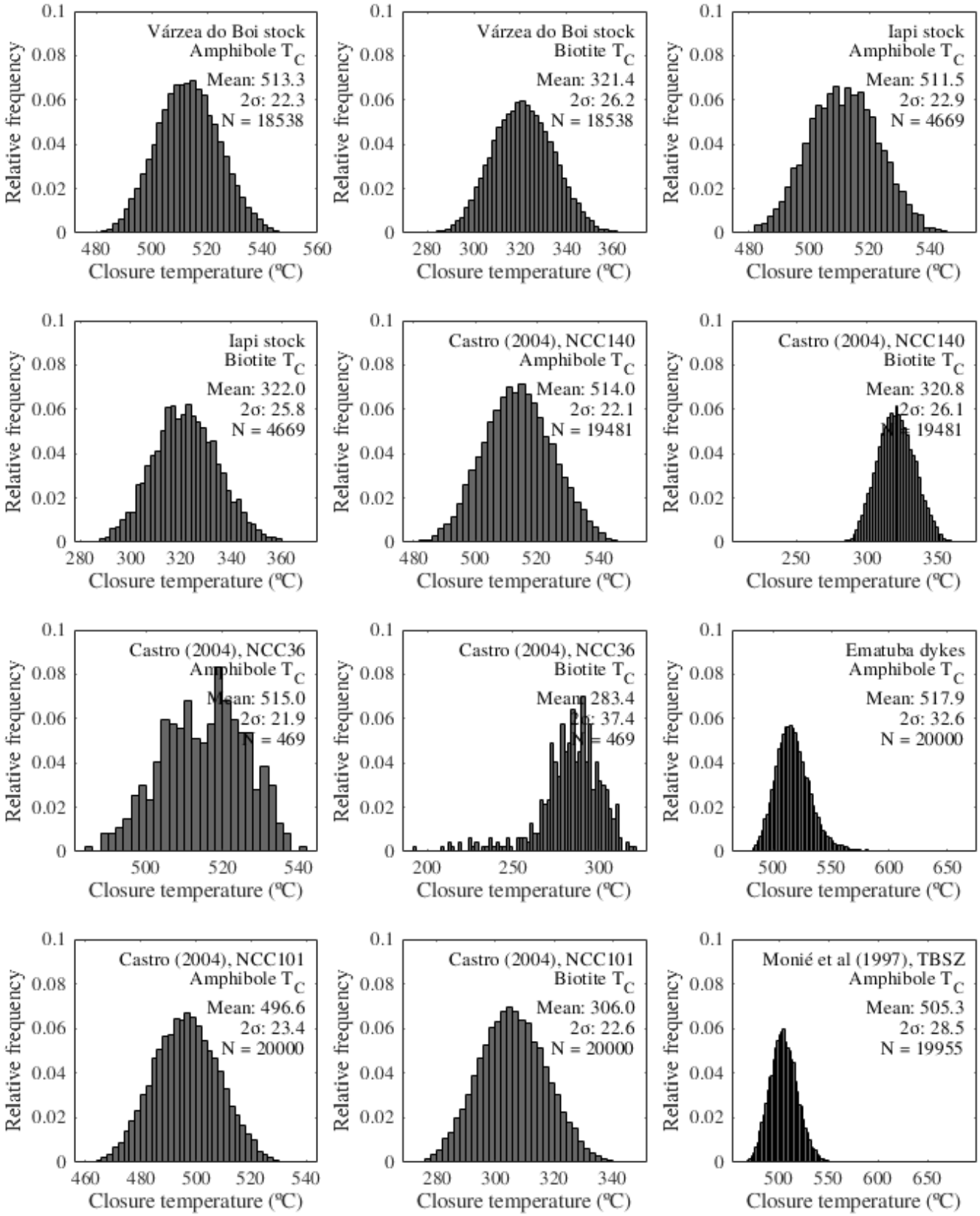

Figura 71 – Histograms of simulated T_C.

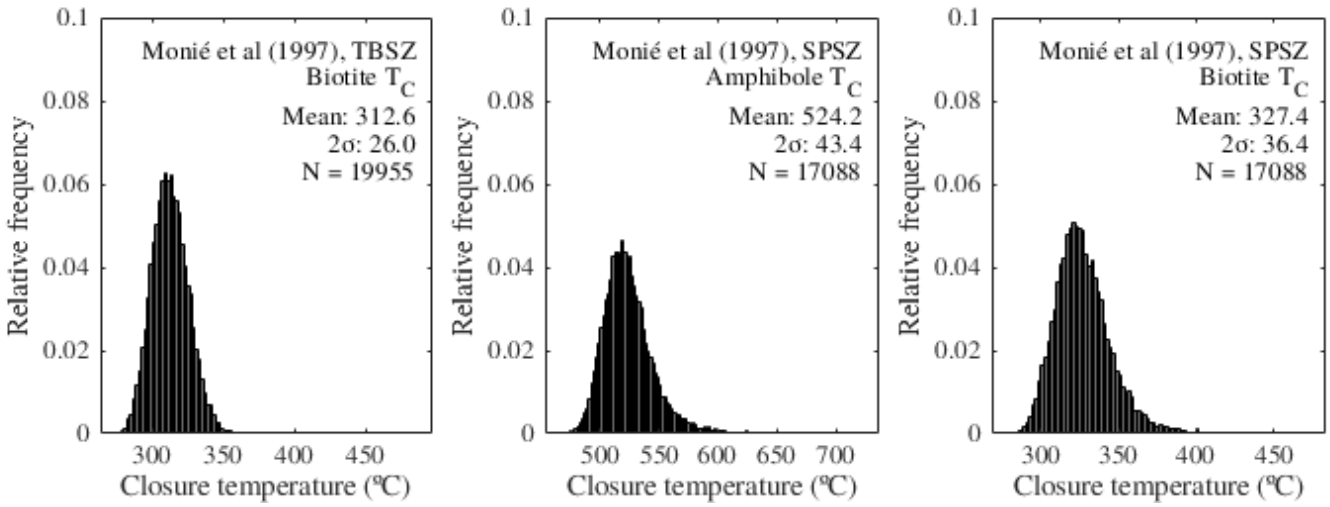

Figura 72 – Histograms of simulated T_C.

B.5 Python sample script

A sample Python script is given below with functions to perform a Monte Carlo simulation of cooling rates and closure temperatures from given thermocrhonometers according to the methods outlined above. Specific instructions are given in the function docstrings.

```
#!/usr/bin/env python3
# -*- coding: utf-8 -*-
"""
Created on Wed Apr 15 09:01:06 2020

@author: carlosavila
"""

def closure_temp(C,error,mineral,a=float('nan'),E=float('nan'),D=
    float('nan')):

    """Newton-Raphson iteration function for Ar closure temperature.
    a, E and D are optional arguments and if not specified the
    standard values of Harrison et al (1985) for biotite, Harrison et
    al (2009) for muscovite and Harrison (1982) for amphibole

    C = [žC/My] = [cooling rate, must be input as negative]
    mineral = [biotite,amphibole] = [mineral of choice]
    error = [01] = [precision required, stoppage criterion]
    a = [ţm] = [effective diffusion radius]
    E = [kcal/mol] = [activation energy]
    D = [cm2/s] = [frequency factor]
    T = [žC] = [starting temperature for iteration]
    A = [nondimensional] = [shape factor]

    Returns (T,i) where T is the iterated closure temperature [K] for
     the given cooling rate and i is the number of iterations
    performed
    """

    import math
    R = 8.3145 # [J/molK] = [gas constant]
```

```
    e = float("inf") # updated error
    i = 0 # iteration number
    T = 273 # [K]
    C = C/3.1536e13 # convert to [K/s]
    if C >= 0:
        print("Error: cooling rate must be negative")
    elif mineral == 'amphibole':
        if math.isnan(a):
            a = 80
        if math.isnan(E):
            E = 64.1 # pm 1.7
        if math.isnan(D):
            D = 0.024 # p 0.053 m 0.011
        a = a*1e-6 # convert to [m]
        E = E*1e3*4.184 # convert to [J/mol]
        D = D*1e-4 # convert to [m2/s]
        A = 55
        while e > error:
            # basic function for closure temperature (render in TeX):
            # f(x) = \ln [(-ART^2D)/(a^2EC)]-(E/(RT))
            # first derivative of basic function of closure
temperature (render in TeX):
            # f'(x) = (E/(RT^2)) + \frac{a^2EC}{ART^2D}\times\frac{2
ARTD}{a^2EC}
            f = math.log((-A*R*T**2*D)/(a**2*E*C))-(E/(R*T)) # basic
function f
            fprime = (E/(R*T**2))+((a**2*E*C)/(A*R*T**2*D))*((2*A*R*T
*D)/(a**2*E*C))
            e = abs((-f/fprime)/T)
            T = T-f/fprime
            i = i+1
    elif mineral == 'muscovite':
        if math.isnan(a):
            a = 100
        if math.isnan(E):
            E = 63 # pm 7
        if math.isnan(D):
            D = 2.3 # +70 -2.2
        a = a*1e-6 # convert to [m]
```

```
62          E = E*1e3*4.184 # convert to [J/mol]
63          D = D*1e-4 # convert to [m2/s]
64          A = 27
65          while e > error:
66              # basic function for closure temperature (render in TeX):
67              # f(x) = \ln [(-ART^2D)/(a^2EC)]-(E/(RT))
68              # first derivative of basic function of closure
    temperature (render in TeX):
69              # f'(x) = (E/(RT^2)) + \frac{a^2EC}{ART^2D}\times\frac{2
    ARTD}{a^2EC}
70              f = math.log((-A*R*T**2*D)/(a**2*E*C))-(E/(R*T)) # basic
    function f
71              fprime = (E/(R*T**2))+((a**2*E*C)/(A*R*T**2*D))*((2*A*R*T
    *D)/(a**2*E*C))
72              e = abs((-f/fprime)/T)
73              T = T-f/fprime
74              i = i+1
75      elif mineral == 'biotite':
76          if math.isnan(a):
77              a = 150
78          if math.isnan(E):
79              E = 47.0 # pm 2
80          if math.isnan(D):
81              D = 0.077 # p 0.21 m 0.06
82          E = E*1e3*4.184 # convert to [J/mol]
83          D = D*1e-4 # convert to [m2/s]
84          a = a*1e-6 # convert to [m]
85          A = 27
86          while e > error:
87              # basic function for closure temperature (render in TeX):
88              # f(x) = \ln [(-ART^2D)/(a^2EC)]-(E/(RT))
89              # first derivative of basic function of closure
    temperature (render in TeX):
90              # f'(x) = (E/(RT^2)) + \frac{a^2EC}{ART^2D}\times\frac{2
    ARTD}{a^2EC}
91              f = math.log((-A*R*T**2*D)/(a**2*E*C))-(E/(R*T)) # basic
    function f
92              fprime = (E/(R*T**2))+((a**2*E*C)/(A*R*T**2*D))*((2*A*R*T
    *D)/(a**2*E*C))
```

```
            e = abs((-f/fprime)/T)
            T = T-f/fprime
            i = i+1
    else:
        print('Invalid mineral')
    return(T,i)

def cooling_poly(mineral,error,age,T,E,D,i=0):

    """
    Brute force recursion of cooling path fit by polynomial

    age = [Ma] = [list of ages of different thermochronometers]
    T = [žC] = [starting temperature of thermochronometers]
    mineral = ['zircon','monazite','amphibole','muscovite','biotite']
     = [list of mineral thermochronometers]
    error = [01] = [precision required, stoppage criterion]
    E = [kcal/mol] = [list of activation energies]
    D = [cm2/s] = [list of frequency factors]

    Returns cooling rates for the different thermochronometers (C, [
    žC/My], returns as negative), their respective closure
    temperatures (T, [žC]) and the number of iterations (i)
    """

    import numpy
    age = numpy.array(age) # convert list of ages to numpy array
    T = numpy.array(T) # convert list of temperatures to numpy array
    p = numpy.polyfit(age,T,len(age)-1) # polynomial fit to n data
    points with n-1 degree
    pprime = [] # creating list for coefficients of first derivative
    for j in range(len(p),1,-1):
        pprime.append((j-1)*p[len(p)-j]) # coefficients of first
    derivative of cooling polynomial
    pprime = numpy.array(pprime)
    C = -numpy.polyval(pprime,age) # cooling rates at the different
    thermochronometers
    if max(C) < 0: # test that all cooling rates are negative
        for j in range(len(mineral)): # iterate closure temperatures
```

```
126             if mineral[j] == 'amphibole':
127                 T_n,k = closure_temp(C[j],error,'amphibole',E=E[j],D=
    D[j])
128                 T[j] = T_n-273
129             elif mineral[j] == 'muscovite':
130                 T_n,k = closure_temp(C[j],error,'muscovite',E=E[j],D=
    D[j])
131                 T[j] = T_n-273
132             elif mineral[j] == 'biotite':
133                 T_n,k = closure_temp(C[j],error,'biotite',E=E[j],D=D[
    j])
134                 T[j] = T_n-273
135         p = numpy.polyfit(age,T,len(age)-1) # polynomial fit to n
    data points with n-1 degree
136         pprime = [] # creating list for first derivative
137         for j in range(len(p),1,-1):
138             pprime.append((j-1)*p[len(p)-j]) # coefficients of first
    derivative of cooling polynomial
139         pprime = numpy.array(pprime)
140         C_n = -numpy.polyval(pprime,age) # cooling rates at the
    different thermochronometers
141         e = max(abs((C-C_n)/C)) # maximum value of error for the
    different cooling rates
142         C = C_n # updated cooling rates
143         i += 1
144         C = list(C)
145         T = list(T)
146         if e > error: # repeat if error is above precision and all
    cooling rates are negative
147             (C,T,i) = cooling_poly(mineral,error,age,T,E,D,i)
148     return(C,T,i)
149
150 def montecarlo_cooling(error,n,mineral,age,age_sigma,temp=float('nan'
    ),temp_sigma=float('nan')):
151
152     """
153     Monte Carlo simulation of cooling rates and closure temperatures.
     Peak temperature (temp) and its uncertainty (temp_sigma) are
    optional arguments to be added if zircon is included as a
```

```
    thermochronometer.
154
155     error = [01] = [precision used in iteration methods]
156     n = [number of trials]
157     mineral = ['zircon','monazite','amphibole','muscovite','biotite']
         = [list of mineral thermochronometers]
158     age = [Ma] = [list of ages]
159     age_sigma = [1, Ma] = [age uncertainties, one standard deviation]
160     temp = [žC] = [list of temperatures]
161     temp_sigma = [žC] = [list of temperature uncertainties]
162
163     Returns a list of cooling rates at the different
    thermochronometers (C_out, [žC/My], returns as negative) and a
    list of their respective closure temperatures (T_out, [žC])
164     """
165
166     import numpy
167     T_out = [] # declaration of output list of temperatures
168     C_out = [] # declaration of output list of cooling rates
169     for i in range(n):
170         age_trial = list(numpy.random.normal(age,age_sigma)) # random
         age
171         T_trial = [] # declare random temperature list
172         E_trial = [] # declare random E list
173         D_trial = [] # declare random D list
174         for j in range(len(mineral)):
175             k = 0
176             if mineral[j] == 'zircon':
177                 T_trial.append(numpy.random.triangular(temp[k]-
    temp_sigma[k],temp[k],temp[k]+temp_sigma[k]))
178                 E_trial.append(float('nan'))
179                 D_trial.append(float('nan'))
180                 k += 1
181             elif mineral[j] == 'monazite':
182                 T_trial.append(numpy.random.triangular(temp[k]-
    temp_sigma[k],temp[k],temp[k]+temp_sigma[k]))
183                 E_trial.append(float('nan'))
184                 D_trial.append(float('nan'))
185                 k += 1
```

```
186             elif mineral[j] == 'amphibole':
187                 T_trial.append(float(550))
188                 E_trial.append(numpy.random.triangular
    (64.1-1.7,64.1,64.1+1.7))
189                 D_trial.append(numpy.random.triangular
    (0.024-0.011,0.024,0.024+0.053))
190             elif mineral[j] == 'muscovite':
191                 T_trial.append(float(425))
192                 E_trial.append(numpy.random.triangular(63-7,63,63+7))
193                 D_trial.append(numpy.random.triangular
    (2.3-2.2,2.3,2.3+70))
194             elif mineral[j] == 'biotite':
195                 T_trial.append(float(300))
196                 E_trial.append(numpy.random.triangular(47-2,47,47+2))
197                 D_trial.append(numpy.random.triangular
    (0.077-0.06,0.077,0.077+0.21))
198
199         (C_res,T_res,i) = cooling_poly(mineral,error,age_trial,
    T_trial,E_trial,D_trial)
200         if max(numpy.array(C_res)) < 0:
201             C_out.append(C_res)
202             T_out.append(T_res)
203     return(C_out,T_out)
```

APÊNDICE C – Supplementary Material: Rheology, shear zone width, microstructural evolution and tectonics of a zippered strike-slip shear zone: the Senador Pompeu shear zone, northern Borborema Province, Brazil

C.1 Mineral chemistry of feldspar and amphibole

Tabela 17 – Mineral chemistry of amphibole.

Wt% and cpfu	Analyses											
SiO_2	47.83	48.66	49.70	50.65	48.36	49.57	47.71	49.78	48.82	48.31	47.98	48.60
Al_2O_3	8.01	7.88	6.05	5.22	7.67	5.74	7.66	6.45	6.81	7.34	7.56	7.29
TiO_2	0.81	1.10	0.88	0.60	0.86	0.84	0.89	0.47	0.61	0.71	1.05	0.86
Cr_2O_3	0.00	0.01	0.00	0.00	0.03	0.01	0.02	0.04	0.04	0.05	0.03	0.05
FeO	17.40	17.69	16.40	16.49	17.69	16.52	17.65	16.32	17.06	16.92	17.60	16.94
MgO	11.21	10.59	12.09	12.64	11.12	12.33	11.33	12.21	11.91	11.57	11.41	11.48
MnO	0.35	0.39	0.42	0.37	0.36	0.38	0.39	0.39	0.36	0.39	0.41	0.36
CaO	11.82	11.51	11.65	11.78	11.68	11.46	11.46	11.75	11.82	11.52	11.44	11.68
Na_2O	0.80	0.92	0.72	0.60	0.85	0.71	0.78	0.69	0.81	0.90	0.97	0.77
K_2O	0.57	0.66	0.39	0.31	0.56	0.42	0.60	0.38	0.40	0.54	0.58	0.50
F	0.02	0.04	0.08	0.07	0.03	0.05	0.03	0.03	0.01	0.11	0.02	0.00
Cl	0.01	0.04	0.00	0.02	0.02	0.02	0.04	0.02	0.01	0.01	0.00	0.02
Total	98.82	99.49	98.39	98.75	99.23	98.08	98.56	98.53	98.64	98.36	99.03	98.54
Si	6.99	7.08	7.25	7.34	7.05	7.25	6.99	7.23	7.12	7.08	7.00	7.10
Al^{IV}	1.01	0.92	0.75	0.66	0.95	0.75	1.01	0.77	0.88	0.92	1.00	0.90
Al^{VI}	0.37	0.43	0.29	0.23	0.36	0.24	0.31	0.34	0.29	0.35	0.30	0.36
Ti^{VI}	0.09	0.12	0.10	0.07	0.09	0.09	0.10	0.05	0.07	0.08	0.11	0.09
Cr	0.00	0.00	0.00	0.00	0.00	0.00	0.00	0.00	0.00	0.01	0.00	0.01
Fe^{3+}	0.29	0.18	0.23	0.26	0.26	0.29	0.38	0.25	0.32	0.28	0.33	0.24
Fe^{2+}	1.84	1.98	1.77	1.74	1.89	1.73	1.78	1.73	1.76	1.79	1.82	1.83
Mg	2.44	2.30	2.63	2.73	2.42	2.69	2.47	2.65	2.59	2.53	2.48	2.50
Mn	0.04	0.05	0.05	0.05	0.04	0.05	0.05	0.05	0.04	0.05	0.05	0.04
$\sum$ Mn	5.07	5.05	5.06	5.07	5.07	5.08	5.09	5.07	5.07	5.08	5.09	5.07
Excess from C	0.07	0.05	0.06	0.07	0.07	0.08	0.09	0.07	0.07	0.08	0.09	0.07
Ca	1.85	1.79	1.82	1.83	1.82	1.80	1.80	1.83	1.85	1.81	1.79	1.83
Na_B	0.08	0.16	0.12	0.10	0.10	0.12	0.11	0.10	0.08	0.11	0.12	0.10
Na_A	0.15	0.10	0.09	0.07	0.14	0.08	0.11	0.10	0.15	0.14	0.16	0.12
K	0.11	0.12	0.07	0.06	0.10	0.08	0.11	0.07	0.07	0.10	0.11	0.09
A	0.25	0.23	0.16	0.13	0.24	0.16	0.23	0.17	0.22	0.24	0.26	0.21
F	0.01	0.02	0.04	0.03	0.01	0.03	0.01	0.02	0.00	0.05	0.01	0.00
Cl	0.00	0.01	0.00	0.01	0.00	0.01	0.01	0.01	0.00	0.00	0.00	0.01
Mg#	0.57	0.54	0.60	0.61	0.56	0.61	0.58	0.60	0.60	0.58	0.58	0.58
$Fe_{tot}/Fe_{tot}+Mg$	0.47	0.48	0.43	0.42	0.47	0.43	0.47	0.43	0.45	0.45	0.46	0.45
P_{HZ}	3.02	2.88	1.31	0.57	2.70	1.05	2.73	1.64	1.97	2.46	2.62	2.39
z_{HZ}	11.18	10.65	4.85	2.09	10.02	3.91	10.11	6.06	7.28	9.10	9.69	8.87
P_{AS}	3.50	3.37	1.90	1.20	3.21	1.66	3.23	2.21	2.51	2.97	3.13	2.92
z_{AS}	12.97	12.48	7.03	4.44	11.88	6.14	11.97	8.17	9.31	11.02	11.57	10.80
P_{AS}	3.26	3.09	1.29	0.43	2.89	0.99	2.92	1.66	2.04	2.61	2.79	2.53
z_{AS}	12.06	11.45	4.76	1.58	10.71	3.67	10.83	6.16	7.56	9.66	10.34	9.39

Tabela 18 – Mineral chemistry of amphibole (continued).

Wt% and cpfu	Analyses										
SiO_2	48.40	48.14	47.74	49.62	47.26	48.01	49.38	48.35	48.50	48.25	47.81
Al_2O_3	7.88	8.02	7.50	6.28	7.73	7.61	6.45	7.57	7.65	7.28	7.64
TiO_2	0.87	0.87	1.35	0.53	1.49	1.21	1.04	1.20	0.97	0.87	1.08
Cr_2O_3	0.05	0.02	0.00	0.04	0.02	0.01	0.02	0.00	0.00	0.00	0.03
FeO	16.18	17.40	17.28	16.27	17.61	17.43	16.93	17.51	17.41	17.33	17.54
MgO	11.90	11.01	10.93	12.17	11.06	11.21	11.81	11.01	11.21	11.32	11.09
MnO	0.37	0.38	0.39	0.39	0.42	0.41	0.40	0.40	0.40	0.39	0.44
CaO	11.74	11.69	11.45	11.81	11.25	11.50	11.56	11.50	11.74	11.64	11.54
Na_2O	0.80	0.85	0.91	0.76	1.05	0.99	0.77	0.94	0.77	0.75	0.97
K_2O	0.53	0.58	0.61	0.38	0.56	0.50	0.46	0.60	0.56	0.58	0.57
F	0.03	0.03	0.08	0.07	0.04	0.05	0.03	0.06	0.05	0.00	0.02
Cl	0.04	0.03	0.02	0.02	0.04	0.02	0.02	0.01	0.02	0.04	0.02
Total	98.80	99.00	98.26	98.34	98.55	98.96	98.87	99.16	99.27	98.44	98.74
Si	7.03	7.03	7.03	7.24	6.94	7.01	7.18	7.05	7.06	7.07	7.01
Al^{IV}	0.97	0.97	0.97	0.76	1.06	0.99	0.82	0.95	0.94	0.93	0.99
Al^{VI}	0.38	0.40	0.33	0.32	0.28	0.32	0.29	0.35	0.37	0.33	0.33
Ti^{VI}	0.10	0.10	0.15	0.06	0.16	0.13	0.11	0.13	0.11	0.10	0.12
Cr	0.01	0.00	0.00	0.00	0.00	0.00	0.00	0.00	0.00	0.00	0.00
Fe^{3+}	0.26	0.24	0.22	0.22	0.31	0.27	0.25	0.23	0.25	0.27	0.27
Fe^{2+}	1.71	1.89	1.91	1.77	1.85	1.86	1.81	1.91	1.87	1.86	1.88
Mg	2.58	2.40	2.40	2.65	2.42	2.44	2.56	2.39	2.43	2.47	2.42
Mn	0.05	0.05	0.05	0.05	0.05	0.05	0.05	0.05	0.05	0.05	0.05
$\sum$ Mn	5.07	5.07	5.06	5.06	5.09	5.08	5.07	5.07	5.07	5.08	5.08
Excess from C	0.07	0.07	0.06	0.06	0.09	0.08	0.07	0.07	0.07	0.08	0.08
Ca	1.83	1.83	1.81	1.85	1.77	1.80	1.80	1.80	1.83	1.83	1.81
Na_B	0.10	0.10	0.13	0.09	0.14	0.12	0.13	0.14	0.10	0.09	0.11
Na_A	0.13	0.14	0.13	0.12	0.16	0.16	0.09	0.13	0.12	0.12	0.16
K	0.10	0.11	0.12	0.07	0.11	0.09	0.09	0.11	0.10	0.11	0.11
A	0.23	0.24	0.24	0.19	0.27	0.25	0.18	0.24	0.22	0.23	0.27
F	0.01	0.01	0.04	0.03	0.02	0.02	0.01	0.03	0.02	0.00	0.01
Cl	0.01	0.01	0.01	0.00	0.01	0.01	0.01	0.00	0.00	0.01	0.00
Mg#	0.60	0.56	0.56	0.60	0.57	0.57	0.59	0.56	0.56	0.57	0.56
$Fe_{tot}/Fe_{tot}+Mg$	0.43	0.47	0.47	0.43	0.47	0.47	0.45	0.47	0.47	0.46	0.47
P_{HZ}	2.87	3.02	2.63	1.51	2.81	2.67	1.64	2.63	2.68	2.41	2.72
z_{HZ}	10.62	11.18	9.74	5.60	10.42	9.88	6.08	9.73	9.91	8.92	10.07
P_{AS}	3.36	3.50	3.14	2.09	3.31	3.17	2.21	3.13	3.18	2.93	3.22
z_{AS}	12.45	12.97	11.62	7.73	12.26	11.76	8.18	11.61	11.78	10.85	11.93
P_{AS}	3.08	3.26	2.81	1.52	3.02	2.85	1.67	2.80	2.86	2.55	2.91
z_{AS}	11.42	12.06	10.40	5.62	11.18	10.56	6.17	10.38	10.60	9.45	10.77

Tabela 19 – Mineral chemistry of amphibole (continued).

Wt% and cpfu	Analyses											
SiO_2	47.58	51.95	47.07	48.77	47.98	47.91	47.93	50.14	47.96	49.29	48.35	49.57
Al_2O_3	7.70	5.20	8.20	6.96	7.71	8.07	7.93	5.73	7.87	6.49	7.60	6.24
TiO_2	1.00	0.12	1.30	0.89	1.08	0.89	0.96	0.78	0.89	1.00	0.86	0.51
Cr_2O_3	0.02	0.00	0.00	0.01	0.04	0.04	0.03	0.03	0.05	0.00	0.02	0.02
FeO	17.62	15.33	17.74	16.97	17.53	17.70	17.46	16.44	17.84	17.05	17.22	16.55
MgO	11.10	12.71	10.65	11.51	11.10	10.92	11.01	12.29	10.99	11.87	11.33	12.17
MnO	0.41	0.33	0.38	0.39	0.38	0.39	0.38	0.42	0.43	0.41	0.38	0.39
CaO	11.32	11.90	11.57	11.64	11.41	11.51	11.60	11.73	11.63	11.49	11.81	11.73
Na_2O	0.92	0.50	0.98	0.70	0.89	0.81	0.84	0.63	0.88	0.82	0.73	0.75
K_2O	0.67	0.21	0.74	0.52	0.62	0.59	0.59	0.41	0.56	0.49	0.55	0.36
F	0.04	0.12	0.06	0.02	0.05	0.07	0.07	0.05	0.01	0.05	0.01	0.02
Cl	0.02	0.01	0.03	0.03	0.00	0.04	0.00	0.02	0.03	0.01	0.02	0.00
Total	98.41	98.36	98.71	98.39	98.78	98.95	98.81	98.66	99.14	98.99	98.86	98.32
Si	6.99	7.51	6.93	7.14	7.02	7.00	7.01	7.29	7.00	7.16	7.05	7.23
Al^{IV}	1.01	0.49	1.07	0.86	0.98	1.00	0.99	0.71	1.00	0.84	0.95	0.77
Al^{VI}	0.33	0.39	0.35	0.34	0.35	0.39	0.38	0.27	0.35	0.28	0.36	0.30
Ti^{VI}	0.11	0.01	0.14	0.10	0.12	0.10	0.11	0.09	0.10	0.11	0.09	0.06
Cr	0.00	0.00	0.00	0.00	0.00	0.00	0.00	0.00	0.01	0.00	0.00	0.00
Fe^{3+}	0.32	0.13	0.23	0.25	0.29	0.29	0.26	0.23	0.29	0.28	0.25	0.26
Fe^{2+}	1.85	1.72	1.95	1.83	1.86	1.87	1.88	1.76	1.89	1.79	1.85	1.76
Mg	2.43	2.74	2.34	2.51	2.42	2.38	2.40	2.66	2.39	2.57	2.46	2.65
Mn	0.05	0.04	0.05	0.05	0.05	0.05	0.05	0.05	0.05	0.05	0.05	0.05
$\sum$ Mn	5.09	5.04	5.07	5.07	5.08	5.08	5.07	5.07	5.08	5.08	5.07	5.07
Excess from C	0.09	0.04	0.07	0.07	0.08	0.08	0.07	0.07	0.08	0.08	0.07	0.07
Ca	1.78	1.84	1.83	1.82	1.79	1.80	1.82	1.83	1.82	1.79	1.85	1.83
Na_B	0.13	0.12	0.11	0.10	0.13	0.11	0.11	0.11	0.10	0.13	0.08	0.09
Na_A	0.14	0.02	0.17	0.09	0.12	0.12	0.13	0.07	0.15	0.10	0.12	0.12
K	0.13	0.04	0.14	0.10	0.12	0.11	0.11	0.08	0.10	0.09	0.10	0.07
A	0.26	0.06	0.31	0.19	0.24	0.23	0.24	0.15	0.25	0.19	0.23	0.19
F	0.02	0.06	0.03	0.01	0.02	0.03	0.03	0.02	0.00	0.02	0.00	0.01
Cl	0.01	0.00	0.01	0.01	0.00	0.01	0.00	0.00	0.01	0.00	0.00	0.00
Mg#	0.57	0.61	0.54	0.58	0.57	0.56	0.56	0.60	0.56	0.59	0.57	0.60
$Fe_{tot}/Fe_{tot}+Mg$	0.47	0.40	0.48	0.45	0.47	0.48	0.47	0.43	0.48	0.45	0.46	0.43
P_{HZ}	2.79	0.54	3.24	2.12	2.77	3.07	2.96	1.02	2.89	1.67	2.65	1.48
z_{HZ}	10.33	1.98	11.99	7.84	10.24	11.38	10.96	3.76	10.71	6.19	9.83	5.46
P_{AS}	3.29	1.17	3.71	2.66	3.26	3.55	3.45	1.62	3.38	2.24	3.16	2.05
z_{AS}	12.18	4.34	13.73	9.84	12.09	13.16	12.76	6.01	12.53	8.29	11.70	7.60
P_{AS}	2.99	0.39	3.51	2.22	2.96	3.32	3.19	0.95	3.11	1.70	2.84	1.48
z_{AS}	11.08	1.45	12.99	8.21	10.97	12.28	11.80	3.50	11.51	6.31	10.50	5.46

Tabela 20 – Mineral chemistry of plagioclase.

							Wt%								
SiO_2	60.91	60.64	57.14	60.47	60.69	59.97	58.73	59.56	61.07	60.71	60.19	60.43	60.22	59.74	58.71
Al_2O_3	25.40	25.46	23.95	25.59	25.29	26.20	26.42	25.93	24.97	25.57	25.53	25.49	25.76	26.01	26.84
Fe_2O_3	0.26	0.16	3.97	0.12	0.32	0.35	0.18	0.11	0.11	0.08	0.03	0.14	0.11	0.07	0.02
MnO	0.00	0.00	0.03	0.01	0.00	0.00	0.02	0.00	0.00	0.00	0.00	0.00	0.00	0.02	0.00
K_2O	0.04	0.04	2.04	0.08	0.09	0.08	0.17	0.16	0.08	0.06	0.07	0.05	0.07	0.10	0.09
CaO	6.05	6.27	4.99	6.32	6.38	6.89	7.28	6.95	5.98	6.42	6.47	6.48	6.56	6.91	7.76
SrO	0.14	0.12	0.14	0.19	0.20	0.18	0.17	0.15	0.14	0.12	0.15	0.21	0.23	0.16	0.20
TiO_2	0.03	0.02	0.24	0.01	0.05	0.01	0.00	0.03	0.02	0.03	0.01	0.06	0.00	0.02	0.00
BaO	0.00	0.03	0.15	0.04	0.04	0.07	0.05	0.00	0.06	0.05	0.01	0.04	0.03	0.00	0.07
Na_2O	8.04	7.99	6.59	7.82	7.82	7.39	7.26	7.41	8.01	7.98	7.73	7.95	7.72	7.53	7.02
MgO	0.00	0.00	1.47	0.00	0.00	0.00	0.00	0.00	0.00	0.00	0.00	0.00	0.00	0.00	0.00
total	100.87	100.74	100.72	100.64	100.88	101.14	100.29	100.29	100.44	101.03	100.18	100.85	100.70	100.56	100.69
							cpfu								
Si	2.68	2.68	2.51	2.67	2.67	2.64	2.61	2.65	2.70	2.67	2.67	2.67	2.66	2.65	2.61
Al	1.32	1.32	1.24	1.33	1.31	1.36	1.39	1.36	1.30	1.33	1.34	1.33	1.34	1.36	1.40
Fe	0.02	0.01	0.29	0.01	0.02	0.03	0.01	0.01	0.01	0.01	0.00	0.01	0.01	0.01	0.00
Mn	0.00	0.00	0.00	0.00	0.00	0.00	0.00	0.00	0.00	0.00	0.00	0.00	0.00	0.00	0.00
K	0.00	0.00	0.11	0.00	0.00	0.00	0.01	0.01	0.00	0.00	0.00	0.00	0.00	0.01	0.00
Ca	0.29	0.30	0.23	0.30	0.30	0.32	0.35	0.33	0.28	0.30	0.31	0.31	0.31	0.33	0.37
Sr	0.00	0.00	0.00	0.00	0.01	0.00	0.00	0.00	0.00	0.00	0.00	0.01	0.01	0.00	0.01
Ti	0.00	0.00	0.01	0.00	0.00	0.00	0.00	0.00	0.00	0.00	0.00	0.00	0.00	0.00	0.00
Ba	0.00	0.00	0.00	0.00	0.00	0.00	0.00	0.00	0.00	0.00	0.00	0.00	0.00	0.00	0.00
Na	0.69	0.68	0.56	0.67	0.67	0.63	0.63	0.64	0.69	0.68	0.67	0.68	0.66	0.65	0.60
Mg	0.00	0.00	0.10	0.00	0.00	0.00	0.00	0.00	0.00	0.00	0.00	0.00	0.00	0.00	0.00
							Feldspar composition								
Ab	0.70	0.70	0.62	0.69	0.69	0.66	0.64	0.65	0.70	0.69	0.68	0.69	0.68	0.66	0.62
Or	0.00	0.00	0.13	0.00	0.00	0.00	0.01	0.01	0.00	0.00	0.00	0.00	0.00	0.01	0.00
An	0.29	0.30	0.26	0.31	0.31	0.34	0.35	0.34	0.29	0.31	0.32	0.31	0.32	0.33	0.38
							Blundy and Holland (1990) themometer								
T_{HB} (°C)	670.74	672.71	692.07	674.42	674.97	681.81	686.75	682.85	670.70	674.03	676.08	674.63	676.84	681.17	691.74

Tabela 21 – Mineral chemistry of plagioclase (continued).

							Wt%								
SiO_2	61.16	60.57	60.52	60.78	58.82	60.32	60.65	59.96	59.94	60.08	57.76	56.88	60.07	60.59	60.29
Al_2O_3	25.14	25.64	25.76	25.62	26.94	25.43	25.07	24.60	25.35	25.67	27.16	28.12	25.48	25.68	25.65
Fe_2O_3	0.09	0.15	0.19	0.20	0.10	0.21	0.19	0.13	0.05	0.25	0.15	0.05	0.16	0.08	0.14
MnO	0.00	0.00	0.00	0.00	0.01	0.00	0.01	0.03	0.00	0.01	0.00	0.01	0.00	0.01	0.00
K_2O	0.09	0.04	0.05	0.05	0.06	0.06	0.04	0.10	0.05	0.06	0.04	0.04	0.09	0.04	0.09
CaO	5.88	6.42	6.40	6.22	7.85	6.27	5.78	5.69	6.19	6.50	8.18	9.14	6.44	6.20	6.44
SrO	0.12	0.14	0.24	0.20	0.18	0.22	0.16	0.22	0.18	0.18	0.16	0.19	0.16	0.21	0.11
TiO_2	0.03	0.00	0.00	0.00	0.00	0.03	0.00	0.00	0.00	0.00	0.03	0.06	0.00	0.03	0.05
BaO	0.09	0.03	0.02	0.02	0.03	0.00	0.08	0.03	0.06	0.01	0.04	0.07	0.10	0.04	0.00
Na_2O	8.25	7.74	7.57	8.13	6.84	7.90	8.23	8.06	7.88	7.83	6.87	6.24	7.93	7.91	7.92
MgO	0.00	0.00	0.00	0.00	0.00	0.00	0.00	0.00	0.00	0.00	0.00	0.00	0.00	0.00	0.00
total	100.86	100.73	100.76	101.23	100.83	100.43	100.21	98.82	99.70	100.59	100.40	100.81	100.44	100.80	100.70
							cpfu								
Si	2.70	2.67	2.67	2.67	2.60	2.67	2.69	2.70	2.67	2.66	2.57	2.53	2.66	2.67	2.66
Al	1.31	1.33	1.34	1.33	1.41	1.33	1.31	1.30	1.33	1.34	1.43	1.48	1.33	1.34	1.34
Fe	0.01	0.01	0.01	0.01	0.01	0.02	0.01	0.01	0.00	0.02	0.01	0.00	0.01	0.01	0.01
Mn	0.00	0.00	0.00	0.00	0.00	0.00	0.00	0.00	0.00	0.00	0.00	0.00	0.00	0.00	0.00
K	0.01	0.00	0.00	0.00	0.00	0.00	0.00	0.01	0.00	0.00	0.00	0.00	0.01	0.00	0.01
Ca	0.28	0.30	0.30	0.29	0.37	0.30	0.27	0.27	0.30	0.31	0.39	0.44	0.31	0.29	0.30
Sr	0.00	0.00	0.01	0.01	0.00	0.01	0.00	0.01	0.00	0.00	0.00	0.00	0.00	0.01	0.00
Ti	0.00	0.00	0.00	0.00	0.00	0.00	0.00	0.00	0.00	0.00	0.00	0.00	0.00	0.00	0.00
Ba	0.00	0.00	0.00	0.00	0.00	0.00	0.00	0.00	0.00	0.00	0.00	0.00	0.00	0.00	0.00
Na	0.71	0.66	0.65	0.69	0.59	0.68	0.71	0.70	0.68	0.67	0.59	0.54	0.68	0.68	0.68
Mg	0.00	0.00	0.00	0.00	0.00	0.00	0.00	0.00	0.00	0.00	0.00	0.00	0.00	0.00	0.00
							Feldspar composition								
Ab	0.71	0.68	0.68	0.70	0.61	0.69	0.72	0.72	0.70	0.68	0.60	0.55	0.69	0.70	0.69
Or	0.01	0.00	0.00	0.00	0.00	0.00	0.00	0.01	0.00	0.00	0.00	0.00	0.01	0.00	0.01
An	0.28	0.31	0.32	0.30	0.39	0.30	0.28	0.28	0.30	0.31	0.40	0.45	0.31	0.30	0.31
							Blundy and Holland (1990) themometer								
T_{HB} (°C)	668.72	675.40	676.47	671.56	693.83	673.40	667.62	668.38	672.84	675.62	696.06	710.69	674.80	672.61	674.88

Tabela 22 – Mineral chemistry of plagioclase (continued).

							Wt%								
SiO_2	57.63	58.92	58.61	60.25	60.65	55.23	55.83	60.40	61.08	56.10	59.92	54.72	60.59	61.80	60.63
Al_2O_3	27.30	25.50	26.92	25.78	25.60	28.78	28.76	25.41	25.31	28.45	25.77	29.51	25.45	24.75	25.50
Fe_2O_3	0.21	1.11	0.25	0.21	0.10	0.04	0.28	0.13	0.27	0.08	0.05	0.08	0.11	0.34	0.16
MnO	0.00	0.01	0.00	0.01	0.00	0.00	0.01	0.00	0.00	0.00	0.01	0.01	0.00	0.00	0.00
K_2O	0.04	0.55	0.04	0.06	0.06	0.02	0.06	0.07	0.06	0.05	0.15	0.03	0.04	0.07	0.04
CaO	8.45	6.56	7.80	6.46	6.22	10.05	9.74	6.36	6.12	9.74	6.71	10.86	6.05	5.41	6.20
SrO	0.18	0.16	0.16	0.18	0.15	0.19	0.16	0.15	0.27	0.14	0.16	0.19	0.18	0.17	0.17
TiO_2	0.06	0.10	0.00	0.03	0.02	0.01	0.17	0.00	0.03	0.00	0.05	0.05	0.00	0.01	0.00
BaO	0.05	0.06	0.03	0.05	0.04	0.03	0.03	0.00	0.00	0.05	0.04	0.00	0.05	0.04	0.04
Na_2O	6.80	7.39	6.97	7.79	8.03	5.65	5.80	8.03	8.09	5.89	7.66	5.30	7.96	8.47	8.05
MgO	0.00	0.35	0.00	0.00	0.00	0.00	0.00	0.00	0.00	0.00	0.00	0.00	0.00	0.00	0.00
total	100.73	100.70	100.76	100.83	100.86	100.00	100.83	100.56	101.23	100.49	100.51	100.74	100.42	101.05	100.78
							cpfu								
Si	2.56	2.60	2.60	2.66	2.67	2.48	2.49	2.67	2.68	2.51	2.66	2.45	2.68	2.71	2.67
Al	1.43	1.33	1.40	1.34	1.33	1.53	1.51	1.33	1.31	1.50	1.35	1.56	1.33	1.28	1.33
Fe	0.02	0.08	0.02	0.02	0.01	0.00	0.02	0.01	0.02	0.01	0.00	0.01	0.01	0.02	0.01
Mn	0.00	0.00	0.00	0.00	0.00	0.00	0.00	0.00	0.00	0.00	0.00	0.00	0.00	0.00	0.00
K	0.00	0.03	0.00	0.00	0.00	0.00	0.00	0.00	0.00	0.00	0.01	0.00	0.00	0.00	0.00
Ca	0.40	0.31	0.37	0.31	0.29	0.48	0.46	0.30	0.29	0.47	0.32	0.52	0.29	0.25	0.29
Sr	0.00	0.00	0.00	0.00	0.00	0.00	0.00	0.00	0.01	0.00	0.00	0.00	0.00	0.00	0.00
Ti	0.00	0.00	0.00	0.00	0.00	0.00	0.01	0.00	0.00	0.00	0.00	0.00	0.00	0.00	0.00
Ba	0.00	0.00	0.00	0.00	0.00	0.00	0.00	0.00	0.00	0.00	0.00	0.00	0.00	0.00	0.00
Na	0.59	0.63	0.60	0.67	0.69	0.49	0.50	0.69	0.69	0.51	0.66	0.46	0.68	0.72	0.69
Mg	0.00	0.02	0.00	0.00	0.00	0.00	0.00	0.00	0.00	0.00	0.00	0.00	0.00	0.00	0.00
							Feldspar composition								
Ab	0.59	0.65	0.62	0.68	0.70	0.50	0.52	0.69	0.70	0.52	0.67	0.47	0.70	0.74	0.70
Or	0.00	0.03	0.00	0.00	0.00	0.00	0.00	0.00	0.00	0.00	0.01	0.00	0.00	0.00	0.00
An	0.41	0.32	0.38	0.31	0.30	0.50	0.48	0.30	0.29	0.48	0.32	0.53	0.30	0.26	0.30
							Blundy and Holland (1990) themometer								
T_{HB} (°C)	698.88	683.61	692.08	675.51	672.23	726.22	721.73	673.36	671.11	720.36	679.13	739.20	671.17	663.97	671.75

Tabela 23 – Mineral chemistry of plagioclase (continued).

							Wt%								
SiO_2	60.69	60.78	56.55	60.21	60.51	60.26	60.63	60.22	60.29	60.16	59.82	60.65	59.72	60.34	60.95
Al_2O_3	25.51	25.61	28.28	25.64	26.10	25.67	25.40	25.37	25.63	25.74	25.69	26.18	25.98	25.42	25.03
Fe_2O_3	0.23	0.28	0.16	0.12	0.15	0.04	0.11	0.22	0.07	0.09	0.08	0.13	0.09	0.25	0.02
MnO	0.00	0.00	0.00	0.00	0.00	0.00	0.00	0.02	0.00	0.01	0.00	0.01	0.00	0.01	0.00
K_2O	0.06	0.06	0.05	0.07	0.03	0.04	0.04	0.07	0.09	0.07	0.06	0.06	0.06	0.06	0.07
CaO	6.21	6.17	9.36	6.43	6.55	6.46	6.32	6.40	6.49	6.44	6.60	6.68	6.77	6.24	5.91
SrO	0.17	0.11	0.18	0.16	0.19	0.22	0.20	0.14	0.17	0.25	0.13	0.18	0.18	0.17	0.19
TiO_2	0.02	0.00	0.00	0.01	0.03	0.02	0.00	0.00	0.00	0.00	0.01	0.08	0.00	0.04	0.05
BaO	0.06	0.08	0.08	0.09	0.06	0.04	0.03	0.03	0.04	0.03	0.07	0.04	0.05	0.01	0.02
Na_2O	7.93	8.14	6.13	7.81	7.56	7.80	8.03	7.80	7.64	7.87	7.67	7.45	7.56	8.03	8.15
MgO	0.00	0.00	0.00	0.00	0.00	0.00	0.00	0.00	0.00	0.00	0.00	0.00	0.00	0.01	0.00
total	100.88	101.23	100.79	100.54	101.18	100.54	100.77	100.28	100.42	100.66	100.13	101.46	100.43	100.59	100.39
							cpfu								
Si	2.67	2.67	2.52	2.67	2.66	2.67	2.68	2.67	2.67	2.66	2.66	2.66	2.65	2.67	2.70
Al	1.32	1.33	1.48	1.34	1.35	1.34	1.32	1.33	1.34	1.34	1.35	1.35	1.36	1.32	1.31
Fe	0.02	0.02	0.01	0.01	0.01	0.00	0.01	0.02	0.01	0.01	0.01	0.01	0.01	0.02	0.00
Mn	0.00	0.00	0.00	0.00	0.00	0.00	0.00	0.00	0.00	0.00	0.00	0.00	0.00	0.00	0.00
K	0.00	0.00	0.00	0.00	0.00	0.00	0.00	0.00	0.00	0.00	0.00	0.00	0.00	0.00	0.00
Ca	0.29	0.29	0.45	0.31	0.31	0.31	0.30	0.30	0.31	0.31	0.31	0.31	0.32	0.30	0.28
Sr	0.00	0.00	0.00	0.00	0.00	0.01	0.01	0.00	0.00	0.01	0.00	0.00	0.00	0.00	0.00
Ti	0.00	0.00	0.00	0.00	0.00	0.00	0.00	0.00	0.00	0.00	0.00	0.00	0.00	0.00	0.00
Ba	0.00	0.00	0.00	0.00	0.00	0.00	0.00	0.00	0.00	0.00	0.00	0.00	0.00	0.00	0.00
Na	0.68	0.69	0.53	0.67	0.64	0.67	0.69	0.67	0.66	0.68	0.66	0.63	0.65	0.69	0.70
Mg	0.00	0.00	0.00	0.00	0.00	0.00	0.00	0.00	0.00	0.00	0.00	0.00	0.00	0.00	0.00
							Feldspar composition								
Ab	0.70	0.70	0.54	0.68	0.68	0.68	0.70	0.69	0.68	0.69	0.68	0.67	0.67	0.70	0.71
Or	0.00	0.00	0.00	0.00	0.00	0.00	0.00	0.00	0.01	0.00	0.00	0.00	0.00	0.00	0.00
An	0.30	0.29	0.46	0.31	0.32	0.31	0.30	0.31	0.32	0.31	0.32	0.33	0.33	0.30	0.28
							Blundy and Holland (1990) themometer								
T_{HB} (°C)	672.77	671.26	713.94	675.26	677.47	675.27	672.84	675.13	676.99	674.97	677.38	679.55	679.44	672.39	669.28

Tabela 24 – Mineral chemistry of plagioclase (continued).

			Wt %		
SiO_2	60.16	60.33	59.86	60.40	55.69
Al_2O_3	25.68	25.38	25.84	25.42	27.86
Fe_2O_3	0.27	0.20	0.30	0.25	0.38
MnO	0.00	0.00	0.02	0.01	0.03
K_2O	0.10	0.04	0.04	0.10	0.06
CaO	6.78	6.29	6.45	6.27	9.29
SrO	0.19	0.20	0.19	0.15	0.19
TiO_2	0.02	0.02	0.02	0.04	0.24
BaO	0.03	0.00	0.08	0.01	0.05
Na_2O	7.53	8.03	7.87	7.85	6.03
MgO	0.00	0.00	0.00	0.00	0.00
total	100.76	100.49	100.66	100.50	99.83
			cpfu		
Si	2.66	2.67	2.65	2.67	2.50
Al	1.34	1.32	1.35	1.32	1.48
Fe	0.02	0.01	0.02	0.02	0.03
Mn	0.00	0.00	0.00	0.00	0.00
K	0.01	0.00	0.00	0.01	0.00
Ca	0.32	0.30	0.31	0.30	0.45
Sr	0.00	0.01	0.00	0.00	0.01
Ti	0.00	0.00	0.00	0.00	0.01
Ba	0.00	0.00	0.00	0.00	0.00
Na	0.64	0.69	0.67	0.67	0.53
Mg	0.00	0.00	0.00	0.00	0.00
			Feldspar composition		
Ab	0.66	0.70	0.69	0.69	0.54
Or	0.01	0.00	0.00	0.01	0.00
An	0.33	0.30	0.31	0.30	0.46
			Blundy and Holland (1990) themometer		
T_{HB} (°C)	680.13	672.63	674.75	674.03	714.75

Referências

Alkmim, F.F., and Marshak, S., 1998, Transamazonian Orogeny in the Southern São Francisco Craton Region, Minas Gerais, Brazil: evidence for Paleoproterozoic collision and collapse in the Quadrilátero Ferrífero: Precambrian Research, v. 90, p. 29–58, doi:10.1016/S0301-9268(98)00032-1.

Allègre, C.J., 2008, Isotope geology: Cambridge, UK; New York, Cambridge University Press, URL https://doi.org/10.1017/CBO9780511809323, oCLC: 615631653.

Almeida, A.R.d., 1987, Petrologia da ProvÍncia subvulcânica de Tauá e Independência - CE [Master's thesis]: Recife, PE, Universidade Federal de Pernambuco.

Almeida, A., 1995, Petrologia e Aspectos Tectônicos do Complexo Granítico QUixadá-Quixeramobim, CE PhD: São Paulo, Universidade de São Paulo.

Almeida, F., Hasui, Y., de Brito Neves, B., and Fuck, R., 1981, Brazilian structural provinces: An introduction: Earth-Science Reviews, v. 17, no. 1-2, p. 1–29, doi:10.1016/0012-8252(81)90003-9, URL https://linkinghub.elsevier.com/retrieve/pii/0012825281900039.

Amaral, W.d.S., Santos, T.J.S.d., Wernick, E., Nogueira Neto, J.d.A., Dantas, E.L., and Matteini, M., 2012, High-pressure granulites from Cariré, Borborema Province, NE Brazil: Tectonic setting, metamorphic conditions and U–Pb, Lu–Hf and Sm–Nd geochronology: Gondwana Research, v. 22, no. 3-4, p. 892–909, doi:10.1016/j.gr.2012.02.011, URL https://linkinghub.elsevier.com/retrieve/pii/S1342937X12000524.

Anderson, J.L., and Smith, D.R., 1995, The effects of temperature and f O_2 on the Al-in-hornblende barometer: American Mineralogist, v. 80, no. 5-6, p. 549–559, doi:10.2138/am-1995-5-614, URL https://pubs.geoscienceworld.org/ammin/article/80/5-6/549-559/43019.

Arbaret, L., Fernandez, A., Jezěk, J., Ildefonse, B., Launeau, P., and Diot, H., 2000, Analogue and numerical modelling of shape fabrics: application to strain and flow determination in magmas: Transactions of the Royal Society of Edinburgh: Earth Sciences, v. 90, p. 97–109, doi:10.1016/0016-7037(82)90301-5, URL https://linkinghub.elsevier.com/retrieve/pii/0016703782903015.

Archanjo, C.J., Hollanda, M.H.B., Rodrigues, S.W., Neves, B.B., and Armstrong, R., 2008, Fabrics of pre- and syntectonic granite plutons and chronology of shear zones in the Eastern Borborema Province, NE Brazil: Journal of Structural Geology, v. 30, no. 3, p. 310–326, doi:10.1016/j.jsg.2007.11.011, URL https://linkinghub.elsevier.com/retrieve/pii/S0191814107002192.

Archanjo, C.J., Launeau, P., Hollanda, M.H.B.M., Macedo, J.W.P., and Liu, D., 2009, Scattering of magnetic fabrics in the Cambrian alkaline granite of Meruoca (Ceará state, northeastern Brazil): International Journal of Earth Sciences, v. 98, no. 8, p. 1793–1807, doi:10.1007/s00531-008-0342-z, URL http://link.springer.com/10.1007/s00531-008-0342-z.

Archanjo, C.J., Trindade, R.I., Bouchez, J.L., and Ernesto, M., 2002, Granite fabrics and regional-scale strain partitioning in the Seridó belt (Borborema Province, NE Brazil): GRANITE FABRICS IN THE SERIDÓ BELT: Tectonics, v. 21, no. 1, p. 3–1–3–14, doi:10.1029/2000TC001269, URL http://doi.wiley.com/10.1029/2000TC001269.

Archanjo, C.J., Viegas, L.G., Hollanda, M.H.B., Souza, L.C., and Liu, D., 2013, Timing of the HT/LP transpression in the Neoproterozoic Seridó Belt (Borborema Province, Brazil): Constraints from UPb (SHRIMP) geochronology and implications for the connections between NE Brazil and West Africa: Gondwana Research, v. 23, no. 2, p. 701–714, doi:10.1016/j.gr.2012.05.005, URL https://linkinghub.elsevier.com/retrieve/pii/S1342937X12001815.

Archanjo, C.J., Hollanda, M.H.B.M.d., and Viegas, L.G.F., 2021, Late Ediacaran lateral-escape tectonics as recorded by the Patos shear zone (Borborema Province, NE Brazil): Brazilian Journal of Geology, v. 51, no. 2, p. e20200,132, doi:10.1590/2317-4889202120200132, URL http://www.scielo.br/scielo.php?script=sci_arttext&pid=S2317-48892021000200309&tlng=en.

Archanjo, C.J., Launeau, P., and Bouchez, J.L., 1995, Magnetic fabric vs. magnetite and biotite shape fabrics of the magnetite-bearing granite pluton of Gameleiras (Northeast Brazil): Physics of the Earth and Planetary Interiors, v. 89, no. 1-2, p. 63–75, doi:10.1016/0031-9201(94)02997-P, URL https://linkinghub.elsevier.com/retrieve/pii/003192019402997P.

Archanjo, C., Bouchez, J.L., Corsini, M., and Vauchez, A., 1994, The Pombal granite pluton: Magnetic fabric, emplacement and relationships with the Brasiliano strike-slip setting of NE Brazil (Paraiba State): Journal of Structural Geology, v. 16, no. 3, p. 323–335, doi:10.1016/0191-8141(94)90038-8, URL https://linkinghub.elsevier.com/retrieve/pii/0191814194900388.

Arthaud, M.H., 2007, Evolução Neoproterozóica do Grupo Ceará (Domínio Ceará Central, NE Brasil): Da Sedimentação à Colisão Continental Brasiliana PhD: Brasília, Universidade de Brasília.

Arthaud, M.H., Caby, R., Fuck, R.A., Dantas, E.L., and Parente, C.V., 2008, Geology of the northern Borborema Province, NE Brazil and its correlation with Nigeria, NW Africa: Geological Society, London, Special Publications, v. 294, no. 1, p. 49–67, doi:10.1144/SP294.4, URL http://sp.lyellcollection.org/lookup/doi/10.1144/SP294.4.

Arthaud, M., Fuck, R., Dantas, E., Santos, T., Caby, R., and Armstrong, R., 2015, The Neoproterozoic Ceará Group, Ceará Central domain, NE Brazil: Depositional age and provenance of detrital material. New insights from U–Pb and Sm–Nd geochronology: Journal of South American Earth Sciences, v. 58, p. 223–237, doi:10.1016/j.jsames.2014.09.007, URL https://linkinghub.elsevier.com/retrieve/pii/S0895981114001187.

Arzi, A.A., 1978, Critical phenomena in the rheology of partially melted rocks: Tectonophysics, v. 44, no. 1-4, p. 173–184, doi:10.1016/0040-1951(78)90069-0, URL https://linkinghub.elsevier.com/retrieve/pii/0040195178900690.

Ávila, C.F., Archanjo, C.J., Fossen, H., and Hollanda, M.H.B.M., 2019, Zippered Shear Zone Model for Interacting Shear Zones in the Borborema Province, Brazil, as

Constrained by U-Pb Dating: Tectonics, doi:10.1029/2019TC005547, URL https://onlinelibrary.wiley.com/doi/abs/10.1029/2019TC005547.

Ávila, C.F., Archanjo, C.J., Hollanda, M.H.B., Macêdo Filho, A.A.d., and Lemos-Santos, D.d.V., 2020, Shear zone cooling and fabrics of synkinematic plutons evidence timing and rates of orogenic exhumation in the northwest Borborema Province (NE Brazil): Precambrian Research, v. 350, p. 105,940, doi:10.1016/j.precamres.2020.105940, URL https://linkinghub.elsevier.com/retrieve/pii/S0301926820305295.

Axen, G., Selverstone, J., Byrne, T., and Fletcher, J., 1998, If the strong crust leads will the weak crust follow: GSA Today, v. 8, no. 12.

Baëta, R.D., and Ashbee, K.H.G., 1969, Slip systems in quartz: I. Experiments: American Mineralogist, v. 54, no. 11-12, p. 1551–1573.

Barbosa, P., 2009, Caracterização Microestrutural e Textural de Agregados de Magnetita do Quadrilátero Ferrífero [Master's thesis]: Ouro Preto, Universidade Federal de Ouro Preto.

Barnicoat, A.C., Rex, D.C., Guise, P.G., and Cliff, R.A., 1995, The timing of and nature of greenschist facies deformation and metamorphism in the upper Pennine Alps: Tectonics, v. 14, no. 2, p. 279–293, doi:10.1029/94TC02017, URL http://doi.wiley.com/10.1029/94TC02017.

Bateman, R., 1995, The interplay between crystallization, replenishment and hybridization in large felsic magma chambers: Earth-Science Reviews, v. 39, no. 1-2, p. 91–106, doi:10.1016/0012-8252(95)00003-S, URL https://linkinghub.elsevier.com/retrieve/pii/001282529500003S.

Batt, G.E., Braun, J., Kohn, B.P., and McDougall, I., 2000, Thermochronological analysis of the dynamics of the Southern Alps, New Zealand: Geological Society of America Bulletin, v. 112, no. 2, p. 250–266, doi:10.1130/0016-7606(2000)112<250:TAOTDO>2.0.CO;2, URL https://pubs.geoscienceworld.org/gsabulletin/article/112/2/250-266/183602.

Beaumont, C., Jamieson, R.A., Nguyen, M.H., and Lee, B., 2001, Himalayan tectonics explained by extrusion of a low-viscosity crustal channel coupled to focused surface denudation: Nature, v. 414, no. 6865, p. 738–742, doi:10.1038/414738a, URL http://www.nature.com/articles/414738a.

Beaumont, C., Nguyen, M.H., Jamieson, R.A., and Ellis, S., 2006, Crustal flow modes in large hot orogens: Geological Society, London, Special Publications, v. 268, no. 1, p. 91–145, doi:10.1144/GSL.SP.2006.268.01.05, URL http://sp.lyellcollection.org/lookup/doi/10.1144/GSL.SP.2006.268.01.05.

Behr, W.M., and Platt, J.P., 2011, A naturally constrained stress profile through the middle crust in an extensional terrane: Earth and Planetary Science Letters, v. 303, no. 3-4, p. 181–192, doi:10.1016/j.epsl.2010.11.044, URL https://linkinghub.elsevier.com/retrieve/pii/S0012821X1000751X.

Benisek, A., Dachs, E., and Kroll, H., 2010, A ternary feldspar-mixing model based on calorimetric data: development and application: Contributions to Mineralogy and Petrology, v. 160, no. 3, p. 327–337, doi:10.1007/s00410-009-0480-8, URL http://link.springer.com/10.1007/s00410-009-0480-8.

Biedermann, A.R., 2017, Towards a holistic understanding of complex magnetic fabrics: The IRM Quarterly, v. 26, no. 4, p. 6.

Black, L.P., Kamo, S.L., Allen, C.M., Davis, D.W., Aleinikoff, J.N., Valley, J.W., Mundil, R., Campbell, I.H., Korsch, R.J., Williams, I.S., and Foudoulis, C., 2004, Improved 206Pb/238U microprobe geochronology by the monitoring of a trace-element-related matrix effect; SHRIMP, ID–TIMS, ELA–ICP–MS and oxygen isotope documentation for a series of zircon standards: Chemical Geology, v. 205, no. 1-2, p. 115–140, doi:10.1016/j.chemgeo.2004.01.003, URL https://linkinghub.elsevier.com/retrieve/pii/S0009254104000361.

Blenkinsop, T.G., 2005, Deformation microstructures and mechanisms in minerals and rocks: New York, Kluwer Academic Publishers, URL http://accesbib.uqam.ca/cgi-bin/bduqam/transit.pl?&noMan=25127234, oCLC: 757106978.

Blumenfeld, P., Mainprice, D., and Bouchez, J., 1986, C-slip in quartz from subsolidus deformed granite: Tectonophysics, v. 127, no. 1-2, p. 97–115, doi:10.1016/0040-1951(86)90081-8, URL https://linkinghub.elsevier.com/retrieve/pii/0040195186900818.

Blundy, J.D., and Holland, T.J.B., 1990, Calcic amphibole equilibria and a new amphibole-plagioclase geothermometer: Contributions to Mineralogy and Petrology, v. 104, no. 2, p. 208–224, doi:10.1007/BF00306444, URL http://link.springer.com/10.1007/BF00306444.

Borradaile, G., and Henry, B., 1997, Tectonic applications of magnetic susceptibility and its anisotropy: Earth-Science Reviews, v. 42, no. 1-2, p. 49–93, doi:10.1016/S0012-8252(96)00044-X, URL https://linkinghub.elsevier.com/retrieve/pii/S001282529600044X.

Borradaile, G.J., and Jackson, M., 2010, Structural geology, petrofabrics and magnetic fabrics (AMS, AARM, AIRM): Journal of Structural Geology, v. 32, no. 10, p. 1519–1551, doi:10.1016/j.jsg.2009.09.006, URL https://linkinghub.elsevier.com/retrieve/pii/S0191814109002041.

Bouchez, J.L., 1997, Bouchez - 1997 - Granite is never isotropic An introduction to AMS studies of granitic rocks.pdf, *in* Granite: From Segregation of Melt to Emplacement Fabrics, Petrology and Structural Geology, v. 8: 1st edn., Netherlands, Springer.

Bouchez, J.L., Delas, C., Gleizes, G., Nédélec, A., and Cuney, M., 1992, Submagmatic microfractures in granites: Geology, v. 20, no. 1, p. 35, doi:10.1130/0091-7613(1992)020<0035:SMIG>2.3.CO;2, URL https://pubs.geoscienceworld.org/geology/article/20/1/35-38/189255.

Bouchez, J.L., and Pecher, A., 1981, The Himalayan Main Central Thrust pile and its quartz-rich tectonites in central Nepal: Tectonophysics, v. 78, no. 1-4, p. 23–50, doi:10.1016/0040-1951(81)90004-4, URL https://linkinghub.elsevier.com/retrieve/pii/0040195181900044.

Brito Neves, B.B., 1975, Regionalização Geotectônica do Precambriano Nordestino PhD: São Paulo, Universidade de São Paulo.

Brown, M., and Solar, G.S., 1998, Granite ascent and emplacement during contractional deformation in convergent orogens: Journal of Structural Geology, v. 20, no. 9-10, p. 1365–1393, doi:10.1016/S0191-8141(98)00074-1, URL https://linkinghub.elsevier.com/retrieve/pii/S0191814198000741.

Brun, J., and Pons, J., 1981, Strain patterns of pluton emplacement in a crust undergoing non-coaxial deformation, Sierra Morena, Southern Spain: Journal of Structural Geology, v. 3, no. 3, p. 219–229, doi:10.1016/0191-8141(81)90018-3, URL https://linkinghub.elsevier.com/retrieve/pii/0191814181900183.

Bürgmann, R., and Dresen, G., 2008, Rheology of the Lower Crust and Upper Mantle: Evidence from Rock Mechanics, Geodesy, and Field Observations: Annual Review of Earth and Planetary Sciences, v. 36, no. 1, p. 531–567, doi:10.1146/annurev.earth.36.031207.124326, URL http://www.annualreviews.org/doi/10.1146/annurev.earth.36.031207.124326.

Burov, E., and Watts, A., 2006, The long-term strength of continental lithosphere: "jelly sandwich" or "crème brûlée"?: GSA Today, v. 16, no. 1, p. 4, doi:10.1130/1052-5173(2006)016<4:TLTSOC>2.0.CO;2, URL http://www.geosociety.org/gsatoday/archive/16/1/pdf/i1052-5173-16-1-4.pdf.

Butler, R.F., 1992, Paleomagnetism: magnetic domains to geologic terranes: Boston, Blackwell Scientific Publications.

Butler, R.F., Gehrels, G.E., McClelland, W.C., May, S.R., and Klepacki, D., 1989, Discordant paleomagnetic poles from the Canadian Coast Plutonic Complex: Regional tilt rather than large-scale displacement?: Geology, v. 17, p. 691–694.

Byerlee, J., Mjachkin, V., Summers, R., and Voevoda, O., 1978, Structures developed in fault gouge during stable sliding and stick-slip: Tectonophysics, v. 44, no. 1-4, p. 161–171, doi:10.1016/0040-1951(78)90068-9, URL https://linkinghub.elsevier.com/retrieve/pii/0040195178900689.

Caby, R., and Arthaud, M., 1986, Major Precambrian nappes of the Brazilian belt, Ceara, northeast Brazil: Geology, v. 14, no. 10, p. 871, doi:10.1130/0091-7613(1986)14<871:MPNOTB>2.0.CO;2, URL https://pubs.geoscienceworld.org/geology/article/14/10/871-874/203908.

Caby, R., and Boessé, J., 2001, Pan-African nappe system in southwest Nigeria: the Ife-Ilesha schist belt: Journal of African Earth Sciences, v. 33, no. 2, p. 211–225, doi:10.1016/S0899-5362(01)80060-9, URL https://linkinghub.elsevier.com/retrieve/pii/S0899536201800609.

Caby, R., 1989, Precambrian terranes of Benin-Nigeria and northeast Brazil and the Late Proterozoic south Atlantic fit, *in* Geological Society of America Special Papers, v. 230: Geological Society of America, p. 145–158, doi:10.1130/SPE230-p145, URL https://pubs.geoscienceworld.org/books/book/365/chapter/3796834/.

Carosi, R., Petroccia, A., Iaccarino, S., Simonetti, M., Langone, A., and Montomoli, C., 2020, Kinematics and Timing Constraints in a Transpressive Tectonic Regime: The Example of the Posada-Asinara Shear Zone (NE Sardinia, Italy): Geosciences, v. 10, no. 8, p. 288, doi:10.3390/geosciences10080288, URL https://www.mdpi.com/2076-3263/10/8/288.

Castro, N.A., 2004, Evolução Geológica Proterozóica da Região entre Madalena e Taperuaba, Domínio Tectônico Ceará Central (Província Borborema) PhD: São Paulo, Universidade de São Paulo.

Cavalcante, A.S.Á., 2006, Evolução termocronológica do sistema de falhas Senador Pompeu - CE [Master's thesis]: Natal, Universidade Federal do Rio Grande do Norte.

Cavalcante, C., Lagoeiro, L., Fossen, H., Egydio-Silva, M., Morales, L.F., Ferreira, F., and Conte, T., 2018, Temperature constraints on microfabric patterns in quartzofeldsphatic mylonites, Ribeira belt (SE Brazil): Journal of Structural Geology, v. 115, p. 243–262, doi:10.1016/j.jsg.2018.07.013, URL https://linkinghub.elsevier.com/retrieve/pii/S0191814118301263.

Cavalcante, G.C.G., Viegas, G., Archanjo, C.J., and da Silva, M.E., 2016, The influence of partial melting and melt migration on the rheology of the continental crust: Journal of Geodynamics, v. 101, p. 186–199, doi:10.1016/j.jog.2016.06.002, URL https://linkinghub.elsevier.com/retrieve/pii/S0264370716301119.

Cavalcante, J.C., 2003, Mapa Geológico do Estado do Ceará: .

Cavalcanti, J.A.D., Gomes, I.P., Calado, B.d.O., and Rodrigues, J.B., 2012, GEOLOGIA E RECURSOS MINERAIS DA FOLHA VÁRZEA DO BOI - SB.24-V-D-IV ESTADO DO CEARÁ, ESCALA 1:100.000, , CPRM - Serviço Geológico do Brasil, Fortaleza.

Cherniak, D., Watson, E., Grove, M., and Harrison, T., 2004, Pb diffusion in monazite: a combined RBS/SIMS study: Geochimica et Cosmochimica Acta, v. 68, no. 4, p. 829–840, doi:10.1016/j.gca.2003.07.012, URL https://linkinghub.elsevier.com/retrieve/pii/S0016703703005593.

Coleman, D.S., Gray, W., and Glazner, A.F., 2004, Rethinking the emplacement and evolution of zoned plutons: Geochronologic evidence for incremental assembly of the Tuolumne Intrusive Suite, California: Geology, v. 32, no. 5, p. 433, doi:10.1130/G20220.1, URL https://pubs.geoscienceworld.org/geology/article/32/5/433-436/29474.

Cook, R.D., and Crawford, M.L., 1994, Exhumation and tilting of the western metamorphic belt of the Coast orogen in southern southeastern Alaska: Tectonics, v. 13, no. 3, p. 528–537, doi:10.1029/93TC03152, URL http://doi.wiley.com/10.1029/93TC03152.

Cooper, F.J., Platt, J.P., and Behr, W.M., 2017, Rheological transitions in the middle crust: insights from Cordilleran metamorphic core complexes: Solid Earth, v. 8, no. 1, p. 199–215, doi:10.5194/se-8-199-2017, URL https://www.solid-earth.net/8/199/2017/.

Corfu, F., 2003, Atlas of Zircon Textures: Reviews in Mineralogy and Geochemistry, v. 53, no. 1, p. 469–500, doi:10.2113/0530469, URL https://pubs.geoscienceworld.org/rimg/article/53/1/469-500/87484.

Corsini, M., de Figueiredo, L.L., Caby, R., Féraud, G., Ruffet, G., and Vauchez, A., 1998, Thermal history of the Pan-African/Brasiliano Borborema Province of northeast Brazil deduced from 40Ar/39Ar analysis: Tectonophysics, v. 285, no. 1-2, p. 103–117, doi:10.1016/S0040-1951(97)00192-3, URL https://linkinghub.elsevier.com/retrieve/pii/S0040195197001923.

Costa, A.P.d., Nascimento, M.A.L.d., Galindo, A.C., and Dantas, A.R., 2015a, Geology, petrology and U-Pb geochronology of Serra da Rajada Granitic Pluton: implications about ediacaran magmatic evolution in NE portion of the Rio Piranhas-Seridó Domain (NE of Borborema Province): Geologia USP. Série Científica, v. 15, no. 3-4, p. 83, doi:10.11606/issn.2316-9095.v15i3-4p83-105, URL http://www.revistas.usp.br/guspsc/article/view/110250.

Costa, F.G., Klein, E.L., Lafon, J.M., Milhomem Neto, J.M., Galarza, M.A., Rodrigues, J.B., Naleto, J.L., and Corrêa Lima, R.G., 2018, Geochemistry and U–Pb–Hf zircon data for plutonic rocks of the Troia Massif, Borborema Province, NE Brazil: Evidence for reworking of Archean and juvenile Paleoproterozoic crust during Rhyacian accretionary and collisional tectonics: Precambrian Research, v. 311, p. 167–194, doi:10.1016/j.precamres.2018.04.008, URL https://linkinghub.elsevier.com/retrieve/pii/S0301926817303480.

Costa, F.G.D., J.B. Rodrigues, J.A.D. Cavalcanti, E.S.M. Palheta, and A.M. Vasconcelos, 2014, U-Pb LA-ICPMS AGES OF DETRITAL ZIRCONS FROM THE PALEOPROTEROZOIC ALGODÕES AND SERRA DAS PIPOCAS GREENSTONE-LIKE SEQUENCES, CEARÁ CENTRAL DOMAIN: Unpublished, doi:10.13140/2.1.4352.5440, URL http://rgdoi.net/10.13140/2.1.4352.5440.

Costa, F.G.d., Palheta, E.S.d.M., Rodrigues, J.B., Gomes, I.P., and Vasconcelos, A.M., 2015b, Geochemistry and U–Pb zircon ages of plutonic rocks from the Algodões granite-greenstone terrane, Troia Massif, northern Borborema Province, Brazil: Implications for Paleoproterozoic subduction-accretion processes: Journal of South American Earth Sciences, v. 59, p. 45–68, doi:10.1016/j.jsames.2015.01.007, URL https://linkinghub.elsevier.com/retrieve/pii/S0895981115000152.

Costa, F.G.d., Palheta, E.S.d.M., Rodrigues, J.B., Gomes, I.P., and Vasconcelos, A.M., 2015c, Geochemistry and U–Pb zircon ages of plutonic rocks from the Algodões granite-greenstone terrane, Troia Massif, northern Borborema Province, Brazil: Implications for Paleoproterozoic subduction-accretion processes: Journal of South American Earth Sciences, v. 59, p. 45–68, doi:

10.1016/j.jsames.2015.01.007, URL https://linkinghub.elsevier.com/retrieve/pii/S0895981115000152.

Cox, A., and Hart, R.B., 2009, Plate Tectonics: How It Works.: Chichester, John Wiley & Sons, URL http://www.123library.org/book_details/?id=14131, oCLC: 609843835.

Cross, A.J., Prior, D.J., Stipp, M., and Kidder, S., 2017, The recrystallized grain size piezometer for quartz: An EBSD-based calibration: EBSD-Based Quartz Grain Size Piezometer: Geophysical Research Letters, v. 44, no. 13, p. 6667–6674, doi:10.1002/2017GL073836, URL http://doi.wiley.com/10.1002/2017GL073836.

Cross, A.J., Kidder, S., and Prior, D.J., 2015, Using microstructures and TitaniQ thermobarometry of quartz sheared around garnet porphyroclasts to evaluate microstructural evolution and constrain an Alpine Fault Zone geotherm: Journal of Structural Geology, v. 75, p. 17–31, doi:10.1016/j.jsg.2015.02.012, URL https://linkinghub.elsevier.com/retrieve/pii/S0191814115000553.

Cruden, A.R., Tobisch, O.T., and Launeau, P., 1999, Magnetic fabric evidence for conduit-fed emplacement of a tabular intrusion: Dinkey Creek Pluton, central Sierra Nevada batholith, California: Journal of Geophysical Research: Solid Earth, v. 104, no. B5, p. 10,511–10,530, doi:10.1029/1998JB900093, URL http://doi.wiley.com/10.1029/1998JB900093.

Daly, M.C., Andrade, V., Barousse, C.A., Costa, R., McDowell, K., Piggott, N., and Poole, A.J., 2014, Brasiliano crustal structure and the tectonic setting of the Parnaíba basin of NE Brazil: Results of a deep seismic reflection profile: Crustal structure of the Parnaíba basin: Tectonics, v. 33, no. 11, p. 2102–2120, doi:10.1002/2014TC003632, URL http://doi.wiley.com/10.1002/2014TC003632.

Daout, S., Doin, M.P., Peltzer, G., Lasserre, C., Socquet, A., Volat, M., and Sudhaus, H., 2018, Strain Partitioning and Present-Day Fault Kinematics in NW Tibet From Envisat SAR Interferometry: Journal of Geophysical Research: Solid Earth, v. 123, no. 3, p. 2462–2483, doi:10.1002/2017JB015020, URL http://doi.wiley.com/10.1002/2017JB015020.

Davidson, J., Morgan, D., Charlier, B., Harlou, R., and Hora, J., 2007, Microsampling and Isotopic Analysis of Igneous Rocks: Implications for the Study of Magmatic Systems: Annual Review of Earth and Planetary Sciences, v. 35, no. 1, p. 273–311, doi:10.1146/annurev.earth.35.031306.140211, URL http://www.annualreviews.org/doi/10.1146/annurev.earth.35.031306.140211.

De Bresser, J., Ter Heege, J., and Spiers, C., 2001, Grain size reduction by dynamic recrystallization: can it result in major rheological weakening?: International Journal of Earth Sciences, v. 90, no. 1, p. 28–45, doi:10.1007/s005310000149, URL http://link.springer.com/10.1007/s005310000149.

de Saint Blanquat, M., Horsman, E., Habert, G., Morgan, S., Vanderhaeghe, O., Law, R., and Tikoff, B., 2011, Multiscale magmatic cyclicity, duration of pluton construction, and the paradoxical relationship between tectonism and plutonism in continental arcs: Tectonophysics, v. 500, no. 1-4, p. 20–33, doi:10.1016/j.tecto.2009.12.009, URL https://linkinghub.elsevier.com/retrieve/pii/S0040195109006970.

de Wit, M.J., Stankiewicz, J., and Reeves, C., 2008, Restoring Pan-African-Brasiliano connections: more Gondwana control, less Trans-Atlantic corruption: Geological Society, London, Special Publications, v. 294, no. 1, p. 399–412, doi:10.1144/SP294.20, URL http://sp.lyellcollection.org/lookup/doi/10.1144/SP294.20.

Derby, B., 1991, The dependence of grain size on stress during dynamic recrystallisation: Acta Metallurgica et Materialia, v. 39, no. 5, p. 955–962, doi:10.1016/0956-7151(91)90295-C, URL https://linkinghub.elsevier.com/retrieve/pii/095671519190295C.

Dewey, J.F., 1988, Extensional collapse of orogens: Tectonics, v. 7, no. 6, p. 1123–1139, doi:10.1029/TC007i006p01123, URL http://doi.wiley.com/10.1029/TC007i006p01123.

Dickin, A.P., 2018, Radiogenic Isotope Geology:: 3rd edn., Cambridge University Press, doi:10.1017/9781316163009, URL https://www.cambridge.org/core/product/identifier/9781316163009/type/book.

D'Lemos, R.S., Brown, M., and Strachan, R.A., 1992, Granite magma generation, ascent and emplacement within a transpressional orogen: Journal of the Geological Society, v. 149, no. 4, p. 487–490, doi:10.1144/gsjgs.149.4.0487, URL http://jgs.lyellcollection.org/lookup/doi/10.1144/gsjgs.149.4.0487.

Dodson, M.H., 1973, Closure temperature in cooling geochronological and petrological systems: Contributions to Mineralogy and Petrology, v. 40, no. 3, p. 259–274, doi:10.1007/BF00373790, URL http://link.springer.com/10.1007/BF00373790.

Doherty, R.D., Hughes, D.A., Humphreys, F.J., Jonas, J.J., Jensen, D.J., Kassner, M.E., King, W.E., McNelley, T.R., McQueen, H.J., and Rollett, A.D., 1997, Current issues in recrystallization: a review: Materials Science and Engineering A, p. 56.

Dunlap, W.J., 2000, Nature's diffusion experiment: The cooling-rate cooling-age correlation: Geology, v. 28, no. 2, p. 139, doi:10.1130/0091-7613(2000)28<139:NDETCC>2.0.CO;2, URL https://pubs.geoscienceworld.org/geology/article/28/2/139-142/207206.

Dunlop, D.J., and Özdemir, Ö., 1997, Rock Magnetism: Fundamentals and Frontiers: 1st edn., Cambridge University Press, doi:10.1017/CBO9780511612794, URL https://www.cambridge.org/core/product/identifier/9780511612794/type/book.

Dutta, D., and Mukherjee, S., 2019, Opposite shear senses: Geneses, global occurrences, numerical simulations and a case study from the Indian western Himalaya: Journal of Structural Geology, v. 126, p. 357–392, doi:10.1016/j.jsg.2019.05.008, URL https://linkinghub.elsevier.com/retrieve/pii/S0191814119301749.

Egydio-Silva, M., and Mainprice, D., 1999, Determination of stress directions from plagioclase fabrics in high grade deformed rocks (AleÂ m ParaõÂ ba shear zone, Ribeira fold belt, southeastern Brazil): Journal of Structural Geology, p. 21.

El-Hadj Tidjani, M., Affaton, P., Louis, P., Lesquer, A., Socohou, A., and Caby, R., 1993, Gravity characteristics of the northern part of the Dahomeyides: continental aggregation-collision orogen and gravity smoothing in the Pan-African (600 ± 100 Ma): Journal of African Earth Sciences (and the Middle East), v. 17, no. 2, p. 203–211, doi:10.1016/0899-5362(93)90036-P, URL https://linkinghub.elsevier.com/retrieve/pii/089953629390036P.

England, P., 1997, Active Deformation of Asia: From Kinematics to Dynamics: Science, v. 278, no. 5338, p. 647–650, doi:10.1126/science.278.5338.647, URL http://www.sciencemag.org/cgi/doi/10.1126/science.278.5338.647.

England, P., and Molnar, P., 1990, Surface uplift, uplift of rocks, and exhumation of rocks: Geology, v. 18, no. 12, p. 1173, doi:10.1130/0091-7613(1990)018<1173:SUUORA>2.3.CO;2, URL https://pubs.geoscienceworld.org/geology/article/18/12/1173-1177/198513.

Faleiros, F., Moraes, R., Pavan, M., and Campanha, G., 2016, A new empirical calibration of the quartz c-axis fabric opening-angle deformation thermometer: Tectonophysics, v. 671, p. 173–182, doi:10.1016/j.tecto.2016.01.014, URL https://linkinghub.elsevier.com/retrieve/pii/S0040195116000512.

Festa, V., 2014, The amount of pure shear and thinning in the Hercynian continental lower crust exposed in the Serre Massif (Calabria, southern Italy): an application of the vorticity analysis to quartz c-axis fabrics: Italian Journal of Geosciences, v. 133, no. 2, p. 214–222, doi:10.3301/IJG.2014.03, URL http://journal.socgeol.it/244/fulltext.html?ida=215.

Fetter, A.H., 1999, U-Pb and Sm-Nd geochronological constraints on the crustal framework and geologic history of Ceara State, NW Borborema Province, NE Brazil: Implications for the assembly of Gondwana PhD: Kansas, University of Kansas.

Fetter, A.H., Hackspacherl, P.C., Neto, N., and Wernickl, E., 2003, Evidence for Neoproterozoic Continental Arc Magmatism in the Santa Quitéria Batholith of Ceará State, NW Borborerma Province, NE Brazil: Implications for the Assembly of West Gondwana: Gondwana Research, v. 6, no. 2, p. 265–273.

Field, D.P., 1997, Recent advances in the application of orientation imaging: Ultramicroscopy, v. 67, no. 1-4, p. 1–9, doi:10.1016/S0304-3991(96)00104-0, URL https://linkinghub.elsevier.com/retrieve/pii/S0304399196001040.

Filho, F.F.B.d.S., Magini, C., Chiozza, S.G., and Castelo Branco, R.M.G., 2021, The architecture of the Eopaleozoic Cococi Basin, northeastern Brazil: 2D geological modelling from magnetic and gravimetric data: Journal of South American Earth Sciences, v. 106, p. 102,903, doi:10.1016/j.jsames.2020.102903, URL https://linkinghub.elsevier.com/retrieve/pii/S0895981120304466.

Flowers, R.M., Mahan, K.H., Bowring, S.A., Williams, M.L., Pringle, M.S., and Hodges, K.V., 2006, Multistage exhumation and juxtaposition of lower continental crust in the western Canadian Shield: Linking high-resolution U-Pb and ^{40}Ar/^{39}Ar thermochronometry with pressure-temperature-deformation paths: MULTISTAGE EXHUMATION OF LOWER CRUST: Tectonics, v. 25, no. 4, p. n/a–n/a, doi:10.1029/2005TC001912, URL http://doi.wiley.com/10.1029/2005TC001912.

Fossen, H., and Cavalcante, G.C.G., 2017, Shear zones – A review: Earth-Science Reviews, v. 171, p. 434–455, doi:10.1016/j.earscirev.2017.05.002, URL https://linkinghub.elsevier.com/retrieve/pii/S0012825217300272.

Fossen, H., Gabrielsen, R.H., Faleide, J.I., and Hurich, C.A., 2014, Crustal stretching in the Scandinavian Caledonides as revealed by deep seismic data: Geology, v. 42, no. 9, p. 791–794, doi:10.1130/G35842.1, URL http://pubs.geoscienceworld.org/geology/article/42/9/791/131653/Crustal-stretching-in-the-Scandinavian-Caledonides.

Fowler, T.K., and Paterson, S.R., 1997, Timing and nature of magmatic fabrics from structural relations around stoped blocks: Journal of Structural Geology, v. 19, no. 2, p. 209–224, doi:10.1016/S0191-8141(96)00058-2, URL https://linkinghub.elsevier.com/retrieve/pii/S0191814196000582.

Freed, A.M., Hirth, G., and Behn, M.D., 2012, Using short-term postseismic displacements to infer the ambient deformation conditions of the upper mantle: POSTSEISMIC INFERRED MANTLE CONDITIONS: Journal of Geophysical Research:

Solid Earth, v. 117, no. B1, p. n/a–n/a, doi:10.1029/2011JB008562, URL https://onlinelibrary.wiley.com/doi/10.1029/2011JB008562.

Froitzheim, N., Pleuger, J., and Nagel, T.J., 2006, Extraction faults: Journal of Structural Geology, v. 28, no. 8, p. 1388–1395, doi:10.1016/j.jsg.2006.05.002, URL https://linkinghub.elsevier.com/retrieve/pii/S0191814106001283.

Fry, N., 1979, Random point distributions and strain measurement in rocks: Tectonophysics, v. 60, no. 1-2, p. 89–105, doi:10.1016/0040-1951(79)90135-5, URL https://linkinghub.elsevier.com/retrieve/pii/0040195179901355.

Gallagher, K., Hawkesworth, C.J., and Mantovani, M.S.M., 1994, The denudation history of the onshore continental margin of SE Brazil inferred from apatite fission track data: Journal of Geophysical Research: Solid Earth, v. 99, no. B9, p. 18,117–18,145, doi:10.1029/94JB00661, URL http://doi.wiley.com/10.1029/94JB00661.

Ganade, C.E., Basei, M.A., Grandjean, F.C., Armstrong, R., and Brito, R.S., 2017, Contrasting Archaean (2.85–2.68 Ga) TTGs from the Tróia Massif (NE-Brazil) and their geodynamic implications for flat to steep subduction transition: Precambrian Research, v. 297, p. 1–18, doi:10.1016/j.precamres.2017.05.007, URL https://linkinghub.elsevier.com/retrieve/pii/S0301926816304764.

Ganade, C.E., Lanari, P., Rubatto, D., Hermann, J., Weinberg, R.F., Basei, M.A.S., Tesser, L.R., Caby, R., Agbossoumondé, Y., and Ribeiro, C.M., 2021a, Magmatic flare-up causes crustal thickening at the transition from subduction to continental collision: Communications Earth & Environment, v. 2, no. 1, p. 41, doi:10.1038/s43247-021-00103-z, URL http://www.nature.com/articles/s43247-021-00103-z.

Ganade, C.E., Weinberg, R.F., Caxito, F.A., Lopes, L.B.L., Tesser, L.R., and Costa, I.S., 2021b, Decratonization by rifting enables orogenic reworking and transcurrent dispersal of old terranes in NE Brazil: Scientific Reports, v. 11, no. 1, p. 5719, doi:10.1038/s41598-021-84703-x, URL http://www.nature.com/articles/s41598-021-84703-x.

Ganade de Araujo, C.E., 2014, Evolução tectônica da margem ativa Neoproterozóica do Orógeno Gondwana Oeste na Província Borborema (NE-Brasil) Doutorado em Geotectônica: São Paulo, Universidade de São Paulo, doi:10.11606/T.44.2014.tde-25092014-144415, URL http://www.teses.usp.br/teses/disponiveis/44/44141/tde-25092014-144415/.

Ganade de Araujo, C.E., Cordani, U.G., Basei, M.A., Castro, N.A., Sato, K., and Sproesser, W.M., 2012, U–Pb detrital zircon provenance of metasedimentary rocks from the Ceará Central and Médio Coreaú Domains, Borborema Province, NE-Brazil: Tectonic implications for a long-lived Neoproterozoic active continental margin: Precambrian Research, v. 206-207, p. 36–51, doi:10.1016/j.precamres.2012.02.021, URL https://linkinghub.elsevier.com/retrieve/pii/S0301926812000745.

Ganade de Araujo, C.E., Cordani, U.G., Weinberg, R.F., Basei, M.A., Armstrong, R., and Sato, K., 2014a, Tracing Neoproterozoic subduction in the Borborema Province (NE-Brazil): Clues from U-Pb geochronology and Sr-Nd-Hf-O isotopes on granitoids and migmatites: Lithos, v. 202-203, p. 167–189, doi:10.1016/j.lithos.2014.05.015, URL https://linkinghub.elsevier.com/retrieve/pii/S0024493714001790.

Ganade de Araujo, C.E., Rubatto, D., Hermann, J., Cordani, U.G., Caby, R., and Basei, M.A.S., 2014b, Ediacaran 2,500-km-long synchronous deep continental subduction in the West Gondwana Orogen: Nature Communications, v. 5, no. 1, doi:10.1038/ncomms6198, URL http://www.nature.com/articles/ncomms6198.

Ganade de Araujo, C.E., Weinberg, R.F., and Cordani, U.G., 2014c, Extruding the Borborema Province (NE-Brazil): a two-stage Neoproterozoic collision process: Terra Nova, v. 26, no. 2, p. 157–168, doi:10.1111/ter.12084, URL http://doi.wiley.com/10.1111/ter.12084.

Garcia, M.d.G.M., Parente, C.V., Silva Filho, W.F.d., and Almeida, A.R.d., 2018, Age of magmatic events in the Eopaleozoic Jaibaras Basin, NE Brazil: Constraints from U-Pb zircon geochronology: Journal of South American Earth Sciences, v. 84, p. 113–126, doi:10.1016/j.jsames.2018.03.009, URL https://linkinghub.elsevier.com/retrieve/pii/S0895981117301293.

Garcia, M.d.G.M., Saraiva dos Santos, T.J., and da Silva Amaral, W., 2014, Provenance and tectonic setting of neoproterozoic supracrustal rocks from the Ceará Central Domain, Borborema Province (NE Brazil): constraints from geochemistry and detrital zircon ages: International Geology Review, v. 56, no. 4, p. 481–500, doi:10.1080/00206814.2013.875489, URL https://www.tandfonline.com/doi/full/10.1080/00206814.2013.875489.

Gilchrist, A.R., and Summerfield, M.A., 1990, Differential denudation and flexural isostasy in formation of rifted-margin upwarps: Nature, v. 346, no. 6286, p. 739–742, doi:10.1038/346739a0, URL http://www.nature.com/articles/346739a0.

Glazner, A.F., Bartley, J.M., Coleman, D.S., Gray, W., and Taylor, R.Z., 2004, Are plutons assembled over millions of years by amalgamation from small magma chambers?: GSA Today, v. 14, no. 4, p. 4, doi:10.1130/1052-5173(2004)014<0004:APAOMO>2.0.CO;2, URL http://www.geosociety.org/gsatoday/archive/14/4/pdf/i1052-5173-14-4-4.pdf.

Godoy, D.F., 2010, Evolução termocronológica por traços de fissão em apatita e zircão das bacias da transição Proterozóico-Fanerozóico de Camaquã (RS), Castro (PR), Eleutério (SP/MG), Jaibaras e Cococi (CE) PhD: Rio Claro, Brazil, Universidade Estadual Paulista.

Goscombe, B.D., and Passchier, C.W., 2003, Asymmetric boudins as shear sense indicatorsÐan assessment from ®eld data: Journal of Structural Geology, p. 15.

Gualda, G.A., and Vlach, S.R., 2007, The Serra da Graciosa A-type Granites and Syenites, southern Brazil: Lithos, v. 93, no. 3-4, p. 310–327, doi:10.1016/j.lithos.2006.06.002, URL https://linkinghub.elsevier.com/retrieve/pii/S002449370600171X.

Guineberteau, B., Bouchez, J.L., and Vigneresse, J.L., 1987, The Mortagne granite pluton (France) emplaced by pull-apart along a shear zone: Structural and gravimetric arguments and regional implication: Geological Society of America Bulletin, v. 99, no. 6, p. 763, doi:10.1130/0016-7606(1987)99<763:TMGPFE>2.0.CO;2, URL https://pubs.geoscienceworld.org/gsabulletin/article/99/6/763-770/203280.

Hammarstrom, J.M., and Zen, E.a., 1986, Aluminum in hornblende: An empirical igneous geobarometer: American Mineralogist, v. 71, p. 1297–1313.

Hanson, G., and Gast, P., 1967, Kinetic studies in contact metamorphic zones: Geochimica et Cosmochimica Acta, v. 31, no. 7, p. 1119–1153, doi:10.1016/S0016-7037(67)80053-X, URL https://linkinghub.elsevier.com/retrieve/pii/S001670376780053X.

Harrison, T.M., 1982, Diffusion of 40Ar in hornblende: Contributions to Mineralogy and Petrology, v. 78, no. 3, p. 324–331, doi:10.1007/BF00398927, URL http://link.springer.com/10.1007/BF00398927.

Harrison, T.M., Célérier, J., Aikman, A.B., Hermann, J., and Heizler, M.T., 2009, Diffusion of 40Ar in muscovite: Geochimica et Cosmochimica Acta, v. 73, no. 4, p. 1039–1051, doi:10.1016/j.gca.2008.09.038, URL https://linkinghub.elsevier.com/retrieve/pii/S0016703708006819.

Harrison, T., Duncan, I., and McDougall, I., 1985, Diffusion of 40Ar in biotite: Temperature, pressure and compositional effects: Geochimica et Cosmochimica Acta, v. 49, no. 11, p. 2461–2468, doi:10.1016/0016-7037(85)90246-7, URL https://linkinghub.elsevier.com/retrieve/pii/0016703785902467.

Heilbronner, R., and Kilian, R., 2017, The grain size(s) of Black Hills Quartzite deformed in the dislocation creep regime: Solid Earth, v. 8, no. 5, p. 1071–1093, doi:10.5194/se-8-1071-2017, URL https://se.copernicus.org/articles/8/1071/2017/.

Heilbronner, R., and Tullis, J., 2006, Evolution of c axis pole figures and grain size during dynamic recrystallization: Results from experimentally sheared quartzite: Journal of Geophysical Research, v. 111, no. B10, p. B10,202, doi:10.1029/2005JB004194, URL http://doi.wiley.com/10.1029/2005JB004194.

Hielscher, R., Silbermann, C.B., Schmidl, E., and Ihlemann, J., 2019, Denoising of crystal orientation maps: Journal of Applied Crystallography, v. 52, no. 5, p. 984–996, doi:10.1107/S1600576719009075, URL http://scripts.iucr.org/cgi-bin/paper?S1600576719009075.

Hippertt, J., and Tohver, E., 1999, On the development of zones of reverse shearing in mylonitic rocks: Journal of Structural Geology, v. 21, no. 11, p. 1603–1614, doi: 10.1016/S0191-8141(99)00107-8, URL https://linkinghub.elsevier.com/retrieve/pii/S0191814199001078.

Hippertt, J., 1998, Breakdown of feldspar, volume gain and lateral mass transfer during mylonitization of granitoid in a low metamorphic grade shear zone: Journal of Structural Geology, v. 20, no. 2-3, p. 175–193, doi:10.1016/S0191-8141(97)00083-7, URL https://linkinghub.elsevier.com/retrieve/pii/S0191814197000837.

Hirth, G., Teyssier, C., and Dunlap, J.W., 2001, An evaluation of quartzite flow laws based on comparisons between experimentally and naturally deformed rocks: International Journal of Earth Sciences, v. 90, no. 1, p. 77–87, doi:10.1007/s005310000152, URL http://link.springer.com/10.1007/s005310000152.

Hirth, G., and Tullis, J., 1992, Dislocation creep regimes in quartz aggregates: Journal of Structural Geology, v. 14, no. 2, p. 145–159, doi:10.1016/0191-8141(92)90053-Y, URL https://linkinghub.elsevier.com/retrieve/pii/019181419290053Y.

Hobbs, B., 1968, Recrystallization of single crystals of quartz: Tectonophysics, v. 6, no. 5, p. 353–401, doi:10.1016/0040-1951(68)90056-5, URL https://linkinghub.elsevier.com/retrieve/pii/0040195168900565.

Hoffman, P.F., 1987, Continental transform tectonics: Great Slave Lake shear zone (ca. 1.9 Ga), northwest Canada: Geology, v. 15, no. 9, p. 785, doi:10.1130/0091-7613(1987)15<785:CTTGSL>2.0.CO;2, URL https://pubs.geoscienceworld.org/geology/article/15/9/785-788/204508.

Hofmann, M., Linnemann, U., Gerdes, A., Ullrich, B., and Schauer, M., 2009, Timing of dextral strike-slip processes and basement exhumation in the Elbe Zone (Saxo-Thuringian Zone): the final pulse of the Variscan Orogeny in the Bohemian Massif constrained by LA-SF-ICP-MS U-Pb zircon data: Geological Society, London, Special Publications, v. 327, no. 1, p. 197–214, doi:10.1144/SP327.10, URL http://sp.lyellcollection.org/lookup/doi/10.1144/SP327.10.

Holdsworth, R.E., 2004, PLANETARY SCIENCE: Enhanced: Weak Faults–Rotten Cores: Science, v. 303, no. 5655, p. 181–182, doi:10.1126/science.1092491, URL http://www.sciencemag.org/cgi/doi/10.1126/science.1092491.

Hollanda, M.H.B.M., Pimentel, M.M., and Jardim de Sá, E.F., 2003, Paleoproterozoic subduction-related metasomatic signatures in the lithospheric mantle beneath NE Brazil: inferences from trace element and Sr–Nd–Pb isotopic compositions of Neoproterozoic high-K igneous rocks: Journal of South American Earth Sciences, v. 15, no. 8, p. 885–900, doi:10.1016/S0895-9811(03)00014-2, URL https://linkinghub.elsevier.com/retrieve/pii/S0895981103000142.

Hollanda, M., Archanjo, C., Bautista, J., and Souza, L., 2015, Detrital zircon ages and Nd isotope compositions of the Seridó and Lavras da Mangabeira basins (Borborema Province, NE Brazil): Evidence for exhumation and recycling associated with a major shift in sedimentary provenance: Precambrian Research, v. 258, p. 186–207, doi:10.1016/j.precamres.2014.12.009, URL https://linkinghub.elsevier.com/retrieve/pii/S0301926814004628.

Hollister, L.S., Grissom, G., Peters, E., Stowell, H., and Sisson, V., 1987, Confirmation of the empirical correlation of Al in hornblende with pressure of solidification of calc-alkaline plutons: American Mineralogist, v. 72, p. 231–239.

Hollister, L.S., 1993, The role of melt in the uplift and exhumation of orogenic belts: Chemical Geology, v. 108, no. 1-4, p. 31–48, doi:10.1016/0009-2541(93)90316-B, URL https://linkinghub.elsevier.com/retrieve/pii/000925419390316B.

Hollister, L.S., and Crawford, M.L., 1986, Melt-enhanced deformation: A major tectonic process: Geology, v. 14, no. 7, p. 558, doi:10.1130/0091-7613(1986)14<558:MDAMTP>2.0.CO;2, URL https://pubs.geoscienceworld.org/geology/article/14/7/558-561/204076.

Hoover, S.R., Cashman, K.V., and Manga, M., 2001, The yield strength of subliquidus basalts Ð experimental results: Journal of Volcanology and Geothermal Research, p. 18.

Houseman, G.A., McKenzie, D.P., and Molnar, P., 1981, Convective instability of a thickened boundary layer and its relevance for the thermal evolution of continental convergent belts: Journal of Geophysical Research: Solid Earth, v. 86, no. B7, p. 6115–6132, doi:10.1029/JB086iB07p06115, URL http://doi.wiley.com/10.1029/JB086iB07p06115.

Hutton, D.H.W., and Reavy, R.J., 1992, Strike-slip tectonics and granite petrogenesis: Tectonics, v. 11, no. 5, p. 960–967, doi:10.1029/92TC00336, URL http://doi.wiley.com/10.1029/92TC00336.

Hutton, D.H.W., 1988a, Granite emplacement mechanisms and tectonic controls: inferences from deformation studies: Earth and Environmental Science Transactions of the Royal Society of Edinburgh, v. 79, no. 2-3, p. 245–255, doi:10.1017/S0263593300014255, URL https://www.cambridge.org/core/product/identifier/S0263593300014255/type/journal_article.

Hutton, D.H.W., 1988b, Igneous emplacement in a shear-zone termination: The biotite granite at Strontian, Scotland: Geological Society of America Bulletin, v. 100, p. 1392–1399.

Imber, J., Holdsworth, R.E., Butler, C.A., and Strachan, R.A., 2001, A reappraisal of the Sibson-Scholz fault zone model: The nature of the frictional to viscous ("brittle-ductile") transition along a long-lived, crustal-scale fault, Outer Hebrides, Scotland: Tectonics, v. 20, no. 5, p. 601–624, doi:10.1029/2000TC001250, URL http://doi.wiley.com/10.1029/2000TC001250.

Ingram, G.M., and Hutton, D.H., 1994, The Great Tonalite Sill: Emplacement into a contractional shear zone and implications for Late Cretaceous to early Eocene tectonics in southeastern Alaska and British Columbia: Geological Society of America Bulletin, v. 106, no. 5, p. 715, doi:10.1130/0016-7606(1994)106<0715:TGTSEI>2.3.CO;2, URL https://pubs.geoscienceworld.org/gsabulletin/article/106/5/715-728/182969.

Irvine, T.N., and Baragar, W.R.A., 1971, A Guide to the Chemical Classification of the Common Volcanic Rocks: Canadian Journal of Earth Sciences, v. 8, no. 5,

p. 523–548, doi:10.1139/e71-055, URL http://www.nrcresearchpress.com/doi/10.1139/e71-055.

Ishii, K., Kanagawa, K., Shigematsu, N., and Okudaira, T., 2007, High ductility of K-feldspar and development of granitic banded ultramylonite in the Ryoke metamorphic belt, SW Japan: Journal of Structural Geology, v. 29, no. 6, p. 1083–1098, doi:10.1016/j.jsg.2007.02.008, URL https://linkinghub.elsevier.com/retrieve/pii/S0191814107000211.

Jackson, J., 2002, Strength of the continental lithosphere: Time to abandon the jelly sandwich?: GSA Today, v. 12, no. 9, p. 4, doi:10.1130/1052-5173(2002)012<0004:SOTCLT>2.0.CO;2, URL http://www.geosociety.org/gsatoday/archive/12/9/pdf/i1052-5173-12-9-4.pdf.

Jackson, M., 1991, Anisotropy of magnetic remanence: A brief review of mineralogical sources, physical origins, and geological applications, and comparison with susceptibility anisotropy: Pure and Applied Geophysics PAGEOPH, v. 136, no. 1, p. 1–28, doi:10.1007/BF00878885, URL http://link.springer.com/10.1007/BF00878885.

Jackson, M., Gruber, W., Marvin, J., and Banerjee, S.K., 1988, Partial anhysteretic remanence and its anisotropy: Applications and grainsize-dependence: Geophysical Research Letters, v. 15, no. 5, p. 440–443, doi:10.1029/GL015i005p00440, URL http://doi.wiley.com/10.1029/GL015i005p00440.

Janecke, S.U., and Evans, J.P., 1988, Feldspar-influenced rock rheologies: Geology, v. 16, p. 1064–1067.

Jelínek, V., 1978, Statistical processing of anisotropy of magnetic susceptibility measured on groups of specimens: Studia Geophysica et Geodaetica, v. 22, no. 1, p. 50–62, doi:10.1007/BF01613632, URL http://link.springer.com/10.1007/BF01613632.

Jelinek, V., 1981, Characterization of the magnetic fabric of rocks: Tectonophysics, v. 79, no. 3-4, p. T63–T67, doi:10.1016/0040-1951(81)90110-4, URL https://linkinghub.elsevier.com/retrieve/pii/0040195181901104.

Johnson, M.C., and Rutherford, M.J., 1989, Experimentally Determined Conditions in the Fish Canyon Tuff, Colorado, Magma Chamber: Journal of Petrology, v. 30, no. 3, p. 711–737, doi:10.1093/petrology/30.3.711, URL https://academic.oup.com/petrology/article-lookup/doi/10.1093/petrology/30.3.711.

Jordan, T., and Watts, A., 2005, Gravity anomalies, flexure and the elastic thickness structure of the India–Eurasia collisional system: Earth and Planetary Science Letters, v. 236, no. 3-4, p. 732–750, doi:10.1016/j.epsl.2005.05.036, URL https://linkinghub.elsevier.com/retrieve/pii/S0012821X05003390.

Karlstrom, K.E., and Williams, M.L., 1998, Heterogeneity of the middle crust: Implications for strength of continental lithosphere: Geology, v. 26, no. 9, p. 815, doi:10.1130/0091-7613(1998)026<0815:HOTMCI>2.3.CO;2, URL https://pubs.geoscienceworld.org/geology/article/26/9/815-818/206976.

Karlstrom, K.E., and Williams, M.L., 2008, Nature and evolution of the middle crust: heterogeneity of structure and process due to pluton-enhanced tectonism, *in* Brown, M., and Rushmer, T., eds., Evolution and Differentiation of the Continental Crust: Cambridge, Cambridge University Press, p. 553.

Kerr, R.C., and Lister, J.R., 1991, The Effects of Shape on Crystal Settling and on the Rheology of Magmas: The Journal of Geology, v. 99, no. 3, p. 457–467, URL http://www.jstor.org/stable/30062628.

Kirschner, D., and Teyssier, C., 1991, Quartz c-axis fabric differences between porphyroclasts and recrystallized grains: Journal of Structural Geology, v. 13, no. 1, p. 105–109, doi:10.1016/0191-8141(91)90106-S, URL https://linkinghub.elsevier.com/retrieve/pii/019181419190106S.

Klaper, E.M., 1988, Quartz c-axis fabric development and large-scale post-nappe folding (Wandfluhhorn Fold, Penninic nappes): Journal of Structural Geology, v. 10, no. 8, p. 795–802, doi:10.1016/0191-8141(88)90095-8, URL https://linkinghub.elsevier.com/retrieve/pii/0191814188900958.

Klemperer, S.L., Kennedy, B.M., Sastry, S.R., Makovsky, Y., Harinarayana, T., and Leech, M.L., 2013, Mantle fluids in the Karakoram fault: Helium isotope evidence: Earth and Planetary Science Letters, v. 366, p. 59–70, doi: 10.1016/j.epsl.2013.01.013, URL https://linkinghub.elsevier.com/retrieve/pii/S0012821X13000216.

Knesel, K.M., Souza, Z.S., Vasconcelos, P.M., Cohen, B.E., and Silveira, F.V., 2011, Young volcanism in the Borborema Province, NE Brazil, shows no evidence for a trace of the Fernando de Noronha plume on the continent: Earth and Planetary Science Letters, v. 302, no. 1-2, p. 38–50, doi: 10.1016/j.epsl.2010.11.036, URL https://linkinghub.elsevier.com/retrieve/pii/S0012821X10007430.

Koppers, A.A., 2002, ArArCALC—software for 40Ar/39Ar age calculations: Computers & Geosciences, v. 28, no. 5, p. 605–619, doi:10.1016/S0098-3004(01)00095-4, URL https://linkinghub.elsevier.com/retrieve/pii/S0098300401000954.

Krol, M.A., Zeitler, P.K., Poupeau, G., and Pecher, A., 1996, Temporal variations in the cooling and denudation history of the Hunza plutonic complex, Karakoram Batholith, revealed by ^{40} Ar/ ^{39} Ar thermochronology: Tectonics, v. 15, no. 2, p. 403–415, doi:10.1029/95TC02424, URL http://doi.wiley.com/10.1029/95TC02424.

Kruhl, J.H., 2003, Prism- and basal-plane parallel subgrain boundaries in quartz: a microstructural geothermobarometer: Journal of Metamorphic Geology, v. 14, no. 5, p. 581–589, doi:10.1046/j.1525-1314.1996.00413.x, URL http://doi.wiley.com/10.1046/j.1525-1314.1996.00413.x.

Kruse, R., Stünitz, H., and Kunze, K., 2001, Dynamic recrystallization processes in plagioclase porphyroclasts: Journal of Structural Geology, v. 23, no. 11, p. 1781–1802, doi:10.1016/S0191-8141(01)00030-X, URL https://linkinghub.elsevier.com/retrieve/pii/S019181410100030X.

Kuiper, Y.D., 2002, The interpretation of inverse isochron diagrams in 40 Ar/ 39 Ar geochronology: Earth and Planetary Science Letters, v. 203, no. 1, p. 499–506, doi:

10.1016/S0012-821X(02)00833-6, URL https://linkinghub.elsevier.com/retrieve/pii/S0012821X02008336.

Kylander-Clark, A.R., Hacker, B.R., and Mattinson, C.G., 2012, Size and exhumation rate of ultrahigh-pressure terranes linked to orogenic stage: Earth and Planetary Science Letters, v. 321-322, p. 115–120, doi:10.1016/j.epsl.2011.12.036, URL https://linkinghub.elsevier.com/retrieve/pii/S0012821X11007564.

Lagroix, F., and Borradaile, G.J., 2000, Magnetic fabric interpretation complicated by inclusions in mafic silicates: Tectonophysics, v. 325, no. 3-4, p. 207–225, doi:10.1016/S0040-1951(00)00125-6, URL https://linkinghub.elsevier.com/retrieve/pii/S0040195100001256.

Law, R., Searle, M., and Simpson, R., 2004, Strain, deformation temperatures and vorticity of flow at the top of the Greater Himalayan Slab, Everest Massif, Tibet: Journal of the Geological Society, v. 161, no. 2, p. 305–320, doi:10.1144/0016-764903-047, URL http://jgs.lyellcollection.org/lookup/doi/10.1144/0016-764903-047.

Law, R.D., 2014, Deformation thermometry based on quartz c-axis fabrics and recrystallization microstructures: A review: Journal of Structural Geology, v. 66, p. 129–161, doi:10.1016/j.jsg.2014.05.023, URL https://linkinghub.elsevier.com/retrieve/pii/S019181411400128X.

Le Maitre, R.W., 2002, Igneous rocks: a classification and glossary of terms ; recommendations of the International Union of Geological Sciences, Subcommission on the Systematics of Igneous Rocks: Cambridge, Cambridge University Press, URL http://site.ebrary.com/lib/academiccompletetitles/home.action, oCLC: 837865586.

Leake, B.E., Woolley, A.R., Arps, C.E.S., Birch, W.D., Gilbert, M.C., Grice, J.D., Hawthorne, F.C., Kato, A., Kisch, H.J., Krivovichev, V.G., Linthout, K., Laird, J., Mandarino, J., Maresch, W.V., Nickel, E.H., Rock, N.M.S., Schumacher, J.C., Smith, D.C., Stephenson, N.C.N., Ungaretti, L., Whittaker, E.J.W., and Youzhi, G., 1997, Nomenclature of Amphiboles; Report of the Subcommittee on Amphiboles of the International Mineralogical Association Commission on New Minerals and Mineral

Names: Mineralogical Magazine, v. 61, no. 405, p. 295–310, doi:10.1180/minmag.1997.061.405.13, URL https://www.cambridge.org/core/product/identifier/S0026461X00011373/type/journal_article.

Leech, M., 2008, Does the Karakoram fault interrupt mid-crustal channel flow in the western Himalaya?: Earth and Planetary Science Letters, v. 276, no. 3-4, p. 314–322, doi:10.1016/j.epsl.2008.10.006, URL https://linkinghub.elsevier.com/retrieve/pii/S0012821X08006651.

Leloup, P.H., Ricard, Y., Battaglia, J., and Lacassin, R., 1999, Shear heating in continental strike-slip shear zones:model and field examples: Geophysical Journal International, v. 136, no. 1, p. 19–40, doi:10.1046/j.1365-246X.1999.00683.x, URL https://academic.oup.com/gji/article-lookup/doi/10.1046/j.1365-246X.1999.00683.x.

Leloup, P.H., Lacassin, R., Tapponnier, P., Schärer, U., Zhong, D., Liu, X., Zhang, L., Ji, S., and Trinh, P.T., 1995, The Ailao Shan-Red River shear zone (Yunnan, China), Tertiary transform boundary of Indochina: Tectonophysics, v. 251, no. 1-4, p. 3–84, doi:10.1016/0040-1951(95)00070-4, URL https://linkinghub.elsevier.com/retrieve/pii/0040195195000704.

Leuthold, J., Müntener, O., Baumgartner, L.P., Putlitz, B., Ovtcharova, M., and Schaltegger, U., 2012, Time resolved construction of a bimodal laccolith (Torres del Paine, Patagonia): Earth and Planetary Science Letters, v. 325-326, p. 85–92, doi:10.1016/j.epsl.2012.01.032, URL https://linkinghub.elsevier.com/retrieve/pii/S0012821X12000593.

Lexa, O., 2003, Numerical approaches in structural and microstructural analyses PhD: Prague, Charles University.

Lister, G., and Dornsiepen, U., 1982, Fabric transitions in the Saxony granulite terrain: Journal of Structural Geology, v. 4, no. 1, p. 81–92, doi:10.1016/0191-8141(82)90009-8, URL https://linkinghub.elsevier.com/retrieve/pii/0191814182900098.

Lloyd, G.E., Butler, R.W., Casey, M., and Mainprice, D., 2009, Mica, deformation fabrics and the seismic properties of the continental crust: Earth and Planetary Science

Letters, v. 288, no. 1-2, p. 320–328, doi:10.1016/j.epsl.2009.09.035, URL https://linkinghub.elsevier.com/retrieve/pii/S0012821X0900569X.

Lopes de Castro, D., Mariano Gomes Castelo Branco, R., Martins, G., and Araújo de Castro, N., 2002, Radiometric, magnetic, and gravity study of the Quixadá batholith, central Ceará domain (NE Brazil): evidence for Pan-African/Brasiliano extension-controlled emplacement: Journal of South American Earth Sciences, v. 15, no. 5, p. 543–551, doi:10.1016/S0895-9811(02)00082-2, URL https://linkinghub.elsevier.com/retrieve/pii/S0895981102000822.

Lowrie, W., 2007, Fundamentals of geophysics: 2nd edn., Cambridge ; New York, Cambridge University Press, oCLC: ocn124025605.

Ludwig, K.R., 2009, SQUID 2: .

Lusk, A.D.J., and Platt, J.P., 2020, The Deep Structure and Rheology of a Plate Boundary-Scale Shear Zone: Constraints from an Exhumed Caledonian Shear Zone, NW Scotland: Lithosphere, v. 2020, p. 33.

Mahan, K.H., Williams, M.L., and Baldwin, J.A., 2003, Contractional uplift of deep crustal rocks along the Legs Lake shear zone, western Churchill Province, Canadian Shield: Canadian Journal of Earth Sciences, v. 40, no. 8, p. 1085–1110, doi:10.1139/e03-039, URL http://www.nrcresearchpress.com/doi/10.1139/e03-039.

Mainprice, D., Bachmann, F., Hielscher, R., Schaeben, H., and Lloyd, G.E., 2015, Calculating anisotropic piezoelectric properties from texture data using the MTEX open source package: Geological Society, London, Special Publications, v. 409, no. 1, p. 223–249, doi:10.1144/SP409.2, URL http://sp.lyellcollection.org/lookup/doi/10.1144/SP409.2.

Mainprice, D., Bouchez, J.L., Blumenfeld, P., and Tubià, J.M., 1986, Dominant c slip in naturally deformed quartz: Implications for dramatic plastic softening at high temperature: Geology, v. 14, no. 10, p. 819, doi:10.1130/0091-7613(1986)14<819:DCSIND>2.0.CO;2, URL https://pubs.geoscienceworld.org/geology/article/14/10/819-822/203864.

Mancktelow, N.S., 1987, Atypical textures in quartz veins from the Simplon Fault Zone: Journal of Structural Geology, v. 9, no. 8, p. 995–1005, doi:10.1016/0191-8141(87)90007-1, URL https://linkinghub.elsevier.com/retrieve/pii/0191814187900071.

Martelat, J.E., Schulmann, K., Lardeaux, J.M., Nicollet, C., and Cardon, H., 1999, Granulite microfabrics and deformation mechanisms in southern Madagascar: Journal of Structural Geology, v. 21, no. 6, p. 671–687, doi:10.1016/S0191-8141(99)00052-8, URL https://linkinghub.elsevier.com/retrieve/pii/S0191814199000528.

Martins, G., 2000, Litogeoquímica e Controles Geocronológicos da Suíte Metamórfica Algodões-Choró PhD: Campinas, Universidade de Campinas.

Martins, G., Oliveira, E.P., and Lafon, J.M., 2009, The Algodões amphibolite–tonalite gneiss sequence, Borborema Province, NE Brazil: Geochemical and geochronological evidence for Palaeoproterozoic accretion of oceanic plateau/back-arc basalts and adakitic plutons: Gondwana Research, v. 15, no. 1, p. 71–85, doi:10.1016/j.gr.2008.06.002, URL https://linkinghub.elsevier.com/retrieve/pii/S1342937X08001032.

McCaffrey, K.J.W., and Petford, N., 1997, Are granitic intrusions scale invariant?: Journal of the Geological Society, v. 154, no. 1, p. 1–4, doi:10.1144/gsjgs.154.1.0001, URL http://jgs.lyellcollection.org/lookup/doi/10.1144/gsjgs.154.1.0001.

Mendes, L.d.C., Santos, T.J.S.d., and Gomes, N.B., 2021, Geochemistry and provenance of the metasedimentary rocks surrounding the Santa Quitéria magmatic arc, NE Brazil: Tectonic and paleogeographic implications for the assembly of West Gondwana: Precambrian Research, v. 356, p. 106,063, doi:10.1016/j.precamres.2020.106063, URL https://linkinghub.elsevier.com/retrieve/pii/S0301926820306525.

Mendes, M., and Lagoeiro, L., 2012, Microstructures, crystallographic fabric development and deformation mechanisms in natural hematite aggregates deformed under varied metamorphic conditions: Journal of Structural Geology, v. 40, p. 29–43,

doi:10.1016/j.jsg.2012.04.005, URL https://linkinghub.elsevier.com/retrieve/pii/S0191814112001034.

Mercier, J.C.C., Anderson, D.A., and Carter, N.L., 1977, Stress in the Lithosphere: Inferences from Steady State Flow of Rocks, *in* Wyss, M., ed., Stress in the Earth: Basel, Birkhäuser Basel, p. 199–226, doi:10.1007/978-3-0348-5745-1_12, URL http://link.springer.com/10.1007/978-3-0348-5745-1_12.

Miles, A., and Woodcock, N., 2018, A combined geochronological approach to investigating long lived granite magmatism, the Shap granite, UK: Lithos, v. 304-307, p. 245–257, doi:10.1016/j.lithos.2018.02.012, URL https://linkinghub.elsevier.com/retrieve/pii/S0024493718300549.

Miller, R.B., and Paterson, S.R., 1994, The transition from magmatic to high-temperature solid-state deformation: implications from the Mount Stuart batholith, Washington: Journal of Structural Geology, v. 16, no. 6, p. 853–865, doi:10.1016/0191-8141(94)90150-3, URL https://linkinghub.elsevier.com/retrieve/pii/0191814194901503.

Miller, R.B., and Paterson, S.R., 1999, In defense of magmatic diapirs: Journal of Structural Geology, v. 21, no. 8-9, p. 1161–1173, doi:10.1016/S0191-8141(99)00033-4, URL https://linkinghub.elsevier.com/retrieve/pii/S0191814199000334.

Miranda, T.S., Neves, S.P., Celestino, M.A.L., and Roberts, N.M., 2020, Structural evolution of the Cruzeiro do Nordeste shear zone (NE Brazil): Brasiliano-Pan-African-ductile-to-brittle transition and Cretaceous brittle reactivation: Journal of Structural Geology, v. 141, p. 104,203, doi:10.1016/j.jsg.2020.104203, URL https://linkinghub.elsevier.com/retrieve/pii/S0191814120304235.

Mizusaki, A., Thomaz-Filho, A., Milani, E., and de Césero, P., 2002, Mesozoic and Cenozoic igneous activity and its tectonic control in northeastern Brazil: Journal of South American Earth Sciences, v. 15, no. 2, p. 183–198, doi:10.1016/S0895-9811(02)00014-7, URL https://linkinghub.elsevier.com/retrieve/pii/S0895981102000147.

Molnar, P., and Dayem, K.E., 2010, Major intracontinental strike-slip faults and contrasts in lithospheric strength: Geosphere, v. 6, no. 4, p. 444–467, doi:10.1130/GES00519.1, URL https://pubs.geoscienceworld.org/geosphere/article/6/4/444-467/132380.

Monié, P., Caby, R., and Arthaud, M.H., 1997, The Neoproterozoic Brasiliano orogeny in northeast Brazil: 40Ar/39Ar and petrostructural data from Ceará: Precambrian Research, v. 81, p. 241–264.

Morales, L.F., Lloyd, G.E., and Mainprice, D., 2014, Fabric transitions in quartz via viscoplastic self-consistent modeling part I: Axial compression and simple shear under constant strain: Tectonophysics, v. 636, p. 52–69, doi:10.1016/j.tecto.2014.08.011, URL https://linkinghub.elsevier.com/retrieve/pii/S0040195114004697.

Moskowitz, B.M., Jackson, M., and Kissel, C., 1998, Low-temperature magnetic behavior of titanomagnetites: Earth and Planetary Science Letters, v. 157, no. 3-4, p. 141–149, doi:10.1016/S0012-821X(98)00033-8, URL https://linkinghub.elsevier.com/retrieve/pii/S0012821X98000338.

Mulchrone, K.F., 2003, Application of Delaunay triangulation to the nearest neighbour method of strain analysis: Journal of Structural Geology, v. 25, no. 5, p. 689–702, doi:10.1016/S0191-8141(02)00067-6, URL https://linkinghub.elsevier.com/retrieve/pii/S0191814102000676.

Muto, J., Hirth, G., Heilbronner, R., and Tullis, J., 2011, Plastic anisotropy and fabric evolution in sheared and recrystallized quartz single crystals: Journal of Geophysical Research, v. 116, no. B2, p. B02,206, doi:10.1029/2010JB007891, URL http://doi.wiley.com/10.1029/2010JB007891.

Neves, S.P., 1991, A ZONA DE CISALHAMENTO TAUÁ, CEARÁ: SENTIDO E ESTIMATIVA DO DESLOCAMENTO, EVOLUÇÃO ESTRUTURAL E GRANITOGÊNESE ASSOCIADA: Revista Brasileira de Geociências, v. 21, no. 2, p. 161–173, doi:10.25249/0375-7536.1991161173, URL http://bjg.siteoficial.ws/1991/n.2/7.pdf.

Neves, S.P., Mariano, G., and Guimarães, I.P., 2000a, Intralithospheric differentiation and crustal growth: Evidence from the Borborema province, northeastern Brazil: , p. 4.

Neves, S., and Vauchez, A., 1995, Magma emplacement and shear zone nucleation and development in northeast Brazil (Fazenda Nova and Pernambuco shear zones; State of Pernambuco): Journal of South American Earth Sciences, v. 8, no. 3-4, p. 289–298, doi:10.1016/0895-9811(95)00014-7, URL https://linkinghub.elsevier.com/retrieve/pii/0895981195000147.

Neves, S., Vauchez, A., and Archanjo, C., 1996, Shear zone-controlled magma emplacement or magma-assisted nucleation of shear zones? Insights from northeast Brazil: Tectonophysics, v. 262, no. 1-4, p. 349–364, doi:10.1016/0040-1951(96)00007-8, URL https://linkinghub.elsevier.com/retrieve/pii/0040195196000078.

Neves, S., Vauchez, A., and Feraud, G., 2000b, Tectono-thermal evolution, magma emplacement, and shear zone development in the Caruaru area (Borborema Province, NE Brazil): Precambrian Research, v. 99, no. 1-2, p. 1–32, doi:10.1016/S0301-9268(99)00026-1, URL https://linkinghub.elsevier.com/retrieve/pii/S0301926899000261.

Nogueira, J.F., 2004, ESTRUTURA, GEOCRONOLOGIA E ALOJAMENTO DOS BATÓLITOS DE QUIXADÁ, QUIXERAMOBIM E SENADOR POMPEU – CEARÁ CENTRAL PhD: São Paulo, Universidade de São Paulo.

Norris, R.J., and Cooper, A.F., 2003, Very high strains recorded in mylonites along the Alpine Fault, New Zealand: implications for the deep structure of plate boundary faults: Journal of Structural Geology, v. 25, no. 12, p. 2141–2157, doi:10.1016/S0191-8141(03)00045-2, URL https://linkinghub.elsevier.com/retrieve/pii/S0191814103000452.

Nye, J.F., 1984, Physical properties of crystals: their representation by tensors and matrices: 1st edn., Oxford [Oxfordshire] : New York, Clarendon Press ; Oxford University Press.

O'Handley, R.C., 2000, Modern magnetic materials: principles and applications: New York, Wiley.

Oliveira, R.G., and Medeiros, W.E., 2018, Deep crustal framework of the Borborema Province, NE Brazil, derived from gravity and magnetic data: Precambrian Research, v. 315, p. 45–65, doi:10.1016/j.precamres.2018.07.004, URL https://linkinghub.elsevier.com/retrieve/pii/S0301926818302110.

Oriolo, S., Oyhantçabal, P., Heidelbach, F., Wemmer, K., and Siegesmund, S., 2015, Structural evolution of the Sarandí del Yí Shear Zone, Uruguay: kinematics, deformation conditions and tectonic significance: International Journal of Earth Sciences, v. 104, no. 7, p. 1759–1777, doi:10.1007/s00531-015-1166-2, URL http://link.springer.com/10.1007/s00531-015-1166-2.

Oriolo, S., Wemmer, K., Oyhantçabal, P., Fossen, H., Schulz, B., and Siegesmund, S., 2018, Geochronology of shear zones – A review: Earth-Science Reviews, v. 185, p. 665–683, doi:10.1016/j.earscirev.2018.07.007, URL https://linkinghub.elsevier.com/retrieve/pii/S0012825218301132.

Özdemir, Ö., Dunlop, D.J., and Moskowitz, B.M., 1993, The effect of oxidation on the Verwey transition in magnetite: Geophysical Research Letters, v. 20, no. 16, p. 1671–1674, doi:10.1029/93GL01483, URL http://doi.wiley.com/10.1029/93GL01483.

Padilha, A.L., Vitorello, I., Pádua, M.B., and Fuck, R.A., 2017, Cryptic signatures of Neoproterozoic accretionary events in northeast Brazil imaged by magnetotellurics: Implications for the assembly of West Gondwana: Tectonophysics, v. 699, p. 164–177, doi:10.1016/j.tecto.2017.01.022, URL https://linkinghub.elsevier.com/retrieve/pii/S0040195117300318.

Palin, R., Searle, M., St-Onge, M., Waters, D., Roberts, N., Horstwood, M., Parrish, R., and Weller, O., 2015, Two-stage cooling history of pelitic and semi-pelitic mylonite (sensu lato) from the Dongjiu–Milin shear zone, northwest flank of the eastern Himalayan syntaxis: Gondwana Research, v. 28, no. 2, p. 509–530, doi:10.1016/j.gr.2014.07.009, URL https://linkinghub.elsevier.com/retrieve/pii/S1342937X14002378.

Parente, C.V., and Arthaud, M.H., 1995, O Sistema Orós-Jaguaribe no Ceará, NE do Brasil: Revista Brasileira de Geociências, v. 25, no. 4, p. 297–306.

Parsons, A.J., Law, R.D., Lloyd, G.E., Phillips, R.J., and Searle, M.P., 2016, Thermo-kinematic evolution of the Annapurna-Dhaulagiri Himalaya, central Nepal: The Composite Orogenic System: KINEMATIC EVOLUTION OF ANNAPURNA HIMAL: Geochemistry, Geophysics, Geosystems, v. 17, no. 4, p. 1511–1539, doi:10.1002/2015GC006184, URL http://doi.wiley.com/10.1002/2015GC006184.

Passchier, C.W., and Trouw, R.A.J., 2005, Microtectonics: Berlin; New York, Springer, URL https://link.springer.com, oCLC: 1131976086.

Passchier, C.W., 1987, Stable positions of rigid objects in non-coaxial flowma study in vorticity analysis: Journal of Structural Geology, v. 9, no. 5/6, p. 679–690.

Passchier, C.W., and Platt, J.P., 2017, Shear zone junctions: Of zippers and freeways: Journal of Structural Geology, v. 95, p. 188–202, doi:10.1016/j.jsg.2016.10.010, URL https://linkinghub.elsevier.com/retrieve/pii/S0191814116301791.

Paterson, M.S., and Luan, F.C., 1990, Quartzite rheology under geological conditions: Geological Society, London, Special Publications, v. 54, no. 1, p. 299–307, doi:10.1144/GSL.SP.1990.054.01.26, URL http://sp.lyellcollection.org/lookup/doi/10.1144/GSL.SP.1990.054.01.26.

Paterson, S.R., Fowler, T., Schmidt, K.L., Yoshinobu, A.S., Yuan, E., and Miller, R.B., 1998, Interpreting magmatic fabric patterns in plutons: Lithos, v. 44, no. 1-2, p. 53–82, doi:10.1016/S0024-4937(98)00022-X, URL https://linkinghub.elsevier.com/retrieve/pii/S002449379800022X.

Paterson, S.R., Vernon, R.H., and Tobisch, O.T., 1989, A review of criteria for the identification of magmatic and tectonic foliations in granitoids: Journal of Structural Geology, v. 11, no. 3, p. 349–363, doi:10.1016/0191-8141(89)90074-6, URL https://linkinghub.elsevier.com/retrieve/pii/0191814189900746.

Paterson, S., and Schmidt, K., 1999, Is there a close spatial relationship between faults and plutons?: Journal of Structural Geology, v. 21, no. 8-9, p. 1131–1142, doi: 10.1016/S0191-8141(99)00024-3, URL https://linkinghub.elsevier.com/retrieve/pii/S0191814199000243.

Peccerillo, A., and Taylor, S.R., 1976, Geochemistry of eocene calc-alkaline volcanic rocks from the Kastamonu area, Northern Turkey: Contributions to Mineralogy and Petrology, v. 58, no. 1, p. 63–81, doi:10.1007/BF00384745, URL http://link.springer.com/10.1007/BF00384745.

Pessoa, R., and Archanjo, C., 1984, Tectônica de empurrão na região de Tróia - CE, *in* Anais, v. 4: Rio de Janeiro, Brazil, Sociedade Brasileira de Geologia, p. 1721–1728.

Petford, N., 2009, Which effective viscosity?: Mineralogical Magazine, v. 73, no. 2, p. 167–191, doi:10.1180/minmag.2009.073.2.167, URL https://www.cambridge.org/core/product/identifier/S0026461X00007799/type/journal_article.

Petford, N., Cruden, A.R., McCaffrey, K.J.W., and Vigneresse, J.L., 2000, Granite magma formation, transport and emplacement in the Earth's crust: Nature, v. 408, no. 6813, p. 669–673, doi:10.1038/35047000, URL http://www.nature.com/articles/35047000.

Peulvast, J.P., Claudino Sales, V., Bétard, F., and Gunnell, Y., 2008, Low post-Cenomanian denudation depths across the Brazilian Northeast: Implications for long-term landscape evolution at a transform continental margin: Global and Planetary Change, v. 62, no. 1-2, p. 39–60, doi:10.1016/j.gloplacha.2007.11.005, URL https://linkinghub.elsevier.com/retrieve/pii/S0921818107001944.

Phillips, D., and Matchan, E., 2013, Ultra-high precision 40Ar/39Ar ages for Fish Canyon Tuff and Alder Creek Rhyolite sanidine: New dating standards required?: Geochimica et Cosmochimica Acta, v. 121, p. 229–239, doi: 10.1016/j.gca.2013.07.003, URL https://linkinghub.elsevier.com/retrieve/pii/S0016703713003827.

Phillips, R.J., Parrish, R.R., and Searle, M.P., 2004, Age constraints on ductile deformation and long-term slip rates along the Karakoram fault zone, Ladakh: Earth and Planetary Science Letters, v. 226, no. 3-4, p. 305–319, doi:10.1016/j.epsl.2004.07.037, URL https://linkinghub.elsevier.com/retrieve/pii/S0012821X0400473X.

Philpotts, A.R., Shi, J., and Brustman, C., 1998, Role of plagioclase crystal chains in the differentiation of partly crystallized basaltic magma: Nature, v. 395, no. 6700, p. 343–346, doi:10.1038/26404, URL http://www.nature.com/articles/26404.

Pitombeira, J.P.A., Amaral, W.d.S., Santos, T.J.d., Dantas, E.L., and Fuck, R.A., 2021, A new record of continental arc magmatism in the Ceará Central Domain, Borborema Province (NE Brazil): evidence from the Pacatuba-Maranguape Complex: Precambrian Research, v. 359, p. 106,192, doi:10.1016/j.precamres.2021.106192, URL https://linkinghub.elsevier.com/retrieve/pii/S0301926821001200.

Pitzer, K.S., and Sterner, S.M., 1995, Equations of state valid continuously from zero to extreme pressures with H2O and CO2 as examples: International Journal of Thermophysics, v. 16, no. 2, p. 511–518, doi:10.1007/BF01441917, URL http://link.springer.com/10.1007/BF01441917.

Platt, J.P., and Behr, W.M., 2011a, Deep structure of lithospheric fault zones: Geophysical Research Letters, v. 38, no. 24, p. n/a–n/a, doi:10.1029/2011GL049719, URL http://doi.wiley.com/10.1029/2011GL049719.

Platt, J.P., 2015a, Influence of shear heating on microstructurally defined plate boundary shear zones: Journal of Structural Geology, v. 79, p. 80–89, doi:10.1016/j.jsg.2015.07.009, URL https://linkinghub.elsevier.com/retrieve/pii/S0191814115300183.

Platt, J.P., 2015b, Rheology of two-phase systems: A microphysical and observational approach: Journal of Structural Geology, v. 77, p. 213–227, doi:10.1016/j.jsg.2015.05.003, URL https://linkinghub.elsevier.com/retrieve/pii/S0191814115001029.

Platt, J.P., and Passchier, C.W., 2016, Zipper junctions: A new approach to the intersections of conjugate strike-slip faults: Geology, v. 44, no. 10, p. 795–798, doi:10.1130/G38058.1, URL https://pubs.geoscienceworld.org/geology/article/44/10/795-798/195017.

Platt, J., 1993, Exhumation of high-pressure rocks: a review of concepts and processes: Terra Nova, v. 5, no. 2, p. 119–133, doi:10.1111/j.1365-3121.1993.tb00237.x, URL http://doi.wiley.com/10.1111/j.1365-3121.1993.tb00237.x.

Platt, J., and Behr, W., 2011b, Grainsize evolution in ductile shear zones: Implications for strain localization and the strength of the lithosphere: Journal of Structural Geology, v. 33, no. 4, p. 537–550, doi:10.1016/j.jsg.2011.01.018, URL https://linkinghub.elsevier.com/retrieve/pii/S0191814111000265.

Platt, J., and Behr, W., 2011c, Lithospheric shear zones as constant stress experiments: Geology, v. 39, no. 2, p. 127–130, doi:10.1130/G31561.1, URL http://pubs.geoscienceworld.org/geology/article/39/2/127/130486/Lithospheric-shear-zones-as-constant-stress.

Pons, J., Oudin, C., and Valero, J., 1992, Kinematics of large syn-orogenic intrusions: example of the Lower Proterozoic Saraya batholith (Eastern Senegal): Geologische Rundschau, v. 81, no. 2, p. 473–486, doi:10.1007/BF01828610, URL http://link.springer.com/10.1007/BF01828610.

Potter, D.K., and Stephenson, A., 1988, Single-domain particles in rocks and magnetic fabric analysis: Geophysical Research Letters, v. 15, no. 10, p. 1097–1100, doi:10.1029/GL015i010p01097, URL http://doi.wiley.com/10.1029/GL015i010p01097.

Prior, D.J., Mariani, E., and Wheeler, J., 2009, EBSD in the Earth Sciences: Applications, Common Practice, and Challenges, *in* Schwartz, A.J., Kumar, M., Adams, B.L., and Field, D.P., eds., Electron Backscatter Diffraction in Materials Science: Boston, MA, Springer US, p. 345–360, doi:10.1007/978-0-387-88136-2_26, URL http://link.springer.com/10.1007/978-0-387-88136-2_26.

Pryer, L., and Robin, P.Y., 1996, Differential stress control on the growth and orientation of flame perthite: A palaeostress-direction indicator: Journal of Structural Geology,

v. 18, no. 9, p. 1151–1166, doi:10.1016/0191-8141(96)00037-5, URL https://linkinghub.elsevier.com/retrieve/pii/0191814196000375.

Pryer, L.L., 1993, Microstructures in feldspars from a major crustal thrust zone: The Grenville Front, Ontario, Canada: Journal of Structural Geology, v. 15, no. 1, p. 21–36, doi:10.1016/0191-8141(93)90076-M, URL https://linkinghub.elsevier.com/retrieve/pii/019181419390076M.

Ramsay, J.G., and Graham, R.H., 1970, Strain variation in shear belts: Canadian Journal of Earth Sciences, v. 7, no. 3, p. 786–813, doi:10.1139/e70-078, URL http://www.nrcresearchpress.com/doi/10.1139/e70-078.

Ramsay, J.G., 1989, Emplacement kinematics of a granite diapir: the Chindamora batholith, Zimbabwe: Journal of Structural Geology, v. 11, no. 1-2, p. 191–209, doi:10.1016/0191-8141(89)90043-6, URL https://linkinghub.elsevier.com/retrieve/pii/0191814189900436.

Ramsay, J.G., and Huber, M.I., 1983, The techniques of modern structural geology: London ; New York, Academic Press.

Reed, S.J.B., 2006, Electron Microprobe Analysis and Scanning Electron Microscopy in Geology: Cambridge, Cambridge University Press, oCLC: 938940441.

Rochette, P., Aubourg, C., and Perrin, M., 1999, Is this magnetic fabric normal? A review and case studies in volcanic formations: Tectonophysics, v. 307, no. 1-2, p. 219–234, doi:10.1016/S0040-1951(99)00127-4, URL https://linkinghub.elsevier.com/retrieve/pii/S0040195199001274.

Roman Berdiel, T., Gapais, D., and Brun, J.P., 1997, Granite intrusion along strike-slip zones in experiment and nature: American Journal of Science, v. 297, no. 6, p. 651–678, doi:10.2475/ajs.297.6.651, URL http://www.ajsonline.org/cgi/doi/10.2475/ajs.297.6.651.

Rosenberg, C.L., 2004, Shear zones and magma ascent: A model based on a review of the Tertiary magmatism in the Alps: SHEAR ZONES AND MAGMA ASCENT: Tectonics, v. 23, no. 3, p. n/a–n/a, doi:10.1029/2003TC001526, URL http://doi.wiley.com/10.1029/2003TC001526.

Rosenberg, C.L., and Handy, M.R., 2005, Experimental deformation of partially melted granite revisited: implications for the continental crust: Journal of Metamorphic Geology, v. 23, no. 1, p. 19–28, doi:10.1111/j.1525-1314.2005.00555.x, URL http://doi.wiley.com/10.1111/j.1525-1314.2005.00555.x.

Royden, L.H., Burchfiel, B.C., and van der Hilst, R.D., 2008, The Geological Evolution of the Tibetan Plateau: Science, v. 321, no. 5892, p. 1054–1058, doi:10.1126/science.1155371, URL http://www.sciencemag.org/cgi/doi/10.1126/science.1155371.

Rubatto, D., 2017, Zircon: The Metamorphic Mineral: Reviews in Mineralogy and Geochemistry, v. 83, no. 1, p. 261–295, doi:10.2138/rmg.2017.83.9, URL https://pubs.geoscienceworld.org/msa/rimg/article/83/1/261/520746/Zircon-The-Metamorphic-Mineral.

Rutter, E., and Brodie, K., 2004, Experimental grain size-sensitive flow of hot-pressed Brazilian quartz aggregates: Journal of Structural Geology, v. 26, no. 11, p. 2011–2023, doi:10.1016/j.jsg.2004.04.006, URL https://linkinghub.elsevier.com/retrieve/pii/S0191814104000793.

Rybacki, E., and Dresen, G., 2000, Dislocation and diffusion creep of synthetic anorthite aggregates: Journal of Geophysical Research: Solid Earth, v. 105, no. B11, p. 26,017–26,036, doi:10.1029/2000JB900223, URL http://doi.wiley.com/10.1029/2000JB900223.

Sacek, V., Morais Neto, J.M., Vasconcelos, P.M., and Oliveira Carmo, I., 2019, Numerical Modeling of Weathering, Erosion, Sedimentation, and Uplift in a Triple Junction Divergent Margin: Geochemistry, Geophysics, Geosystems, doi:10.1029/2018GC008124, URL https://onlinelibrary.wiley.com/doi/abs/10.1029/2018GC008124.

Samperton, K.M., Schoene, B., Cottle, J.M., Brenhin Keller, C., Crowley, J.L., and Schmitz, M.D., 2015, Magma emplacement, differentiation and cooling in the middle crust: Integrated zircon geochronological–geochemical constraints from the Bergell Intrusion, Central Alps: Chemical Geology, v. 417, p. 322–340, doi:10.

1016/j.chemgeo.2015.10.024, URL https://linkinghub.elsevier.com/retrieve/pii/S0009254115300711.

Santos, T.J.S.d., Fetter, A.H., Hackspacher, P., Van Schmus, W., and Nogueira Neto, J., 2008, Neoproterozoic tectonic and magmatic episodes in the NW sector of Borborema Province, NE Brazil, during assembly of Western Gondwana: Journal of South American Earth Sciences, v. 25, no. 3, p. 271–284, doi: 10.1016/j.jsames.2007.05.006, URL https://linkinghub.elsevier.com/retrieve/pii/S089598110700065X.

Santos, T.J.S.d., Garcia, M.d.G.M., Amaral, W.S., Caby, R., Wernick, E., Arthaud, M.H., Dantas, E.L., and Santosh, M., 2009, Relics of eclogite facies assemblages in the Ceará Central Domain, NW Borborema Province, NE Brazil: Implications for the assembly of West Gondwana: Gondwana Research, v. 15, no. 3-4, p. 454–470, doi:10.1016/j.gr.2009.01.003, URL https://linkinghub.elsevier.com/retrieve/pii/S1342937X09000045.

Sassier, C., Leloup, P.H., Rubatto, D., Galland, O., Yue, Y., and Lin, D., 2009, Direct measurement of strain rates in ductile shear zones: A new method based on syntectonic dikes: DIRECT MEASUREMENT OF STRAIN RATES: Journal of Geophysical Research: Solid Earth, v. 114, no. B1, doi:10.1029/2008JB005597, URL http://doi.wiley.com/10.1029/2008JB005597.

Sato, K., Tassinari, C.C.G., Basei, M.A.S., Siga Júnior, O., Onoe, A.T., and Souza, M.D.d., 2014, Sensitive High Resolution Ion Microprobe (SHRIMP IIe/MC) of the Institute of Geosciences of the University of São Paulo, Brazil: analytical method and first results: Geologia USP. Série Científica, v. 14, no. 3, p. 3–18, doi: 10.5327/Z1519-874X201400030001, URL http://www.revistas.usp.br/guspsc/article/view/85372.

Schmid, S.M., and Casey, M., 1986, Complete fabric analysis of some commonly observed quartz C-axis patterns, *in* Hobbs, B.E., and Heard, H.C., eds., Geophysical Monograph Series, v. 36: Washington, D. C., American Geophysical Union, p. 263–286, doi:10.1029/GM036p0263, URL http://www.agu.org/books/gm/v036/GM036p0263/GM036p0263.shtml.

Schmidt, K.L., and Paterson, S.R., 2000, Analyses fail to find coupling between deformation and magmatism: Eos, Transactions American Geophysical Union, v. 81, no. 18, p. 197, doi:10.1029/00EO00133, URL http://doi.wiley.com/10.1029/00EO00133.

Schmidt, M.W., 1992, Amphibole composition in tonalite as a function of pressure: an experimental calibration of the Al-in-hornblende barometer: Contributions to Mineralogy and Petrology, v. 110, no. 2-3, p. 304–310, doi:10.1007/BF00310745, URL http://link.springer.com/10.1007/BF00310745.

Schoene, B., 2014, U–Th–Pb Geochronology, *in* Treatise on Geochemistry: Elsevier, p. 341–378, doi:10.1016/B978-0-08-095975-7.00310-7, URL https://linkinghub.elsevier.com/retrieve/pii/B9780080959757003107.

Schoene, B., Schaltegger, U., Brack, P., Latkoczy, C., Stracke, A., and Günther, D., 2012, Rates of magma differentiation and emplacement in a ballooning pluton recorded by U–Pb TIMS-TEA, Adamello batholith, Italy: Earth and Planetary Science Letters, v. 355-356, p. 162–173, doi:10.1016/j.epsl.2012.08.019, URL https://linkinghub.elsevier.com/retrieve/pii/S0012821X12004475.

Scholz, C.H., 1988, The brittle-plastic transition and the depth of seismic faulting: Geologische Rundschau, v. 77, no. 1, p. 319–328, doi:10.1007/BF01848693, URL http://link.springer.com/10.1007/BF01848693.

Scibiorski, E., Tohver, E., and Jourdan, F., 2015, Rapid cooling and exhumation in the western part of the Mesoproterozoic Albany-Fraser Orogen, Western Australia: Precambrian Research, v. 265, p. 232–248, doi:10.1016/j.precamres.2015.02.005, URL https://linkinghub.elsevier.com/retrieve/pii/S0301926815000467.

Scibiorski, E., Tohver, E., Jourdan, F., Kirkland, C.L., and Spaggiari, C., 2016, Cooling and exhumation along the curved Albany-Fraser orogen, Western Australia: Lithosphere, v. 8, no. 5, p. 551–563, doi:10.1130/L561.1, URL https://pubs.geoscienceworld.org/lithosphere/article/8/5/551-563/196598.

Searle, M., Elliott, J., Phillips, R., and Chung, S.L., 2011, Crustal–lithospheric structure and continental extrusion of Tibet: Journal of the Geological Society, v. 168, no. 3, p. 633–672, doi:10.1144/0016-76492010-139, URL http://jgs.lyellcollection.org/lookup/doi/10.1144/0016-76492010-139.

Şengör, A.C., Zabcı, C., and Natal'in, B.A., 2019, Continental Transform Faults: Congruence and Incongruence With Normal Plate Kinematics, *in* Transform Plate Boundaries and Fracture Zones: Elsevier, p. 169–247, doi:10.1016/B978-0-12-812064-4.00009-8, URL https://linkinghub.elsevier.com/retrieve/pii/B9780128120644000098.

Shigematsu, N., Prior, D.J., and Wheeler, J., 2006, First combined electron backscatter diffraction and transmission electron microscopy study of grain boundary structure of deformed quartzite: Journal of Microscopy, v. 224, no. 3, p. 306–321, doi:10.1111/j.1365-2818.2006.01697.x, URL http://doi.wiley.com/10.1111/j.1365-2818.2006.01697.x.

Shinevar, W.J., Behn, M.D., and Hirth, G., 2015, Compositional dependence of lower crustal viscosity: COMPOSITIONAL DEPENDENCE OF L.C. VISCOSITY: Geophysical Research Letters, v. 42, no. 20, p. 8333–8340, doi:10.1002/2015GL065459, URL http://doi.wiley.com/10.1002/2015GL065459.

Sial, A.N., 1986, Granite types of northeast Brazil: Current knowledge: Revista Brasileira de Geociências, v. 16, no. 1, p. 54–72.

Sibson, R.H., 1974, Frictional constraints on thrust, wrench and normal faults: Nature, v. 249, p. 524–544.

Sibson, R.H., 1977, Fault rocks and fault mechanisms: Journal of the Geological Society, v. 133, no. 3, p. 191–213, doi:10.1144/gsjgs.133.3.0191, URL http://jgs.lyellcollection.org/lookup/doi/10.1144/gsjgs.133.3.0191.

Sibson, R.H., 1986, Earthquakes and Rock Deformation in Crustal Fault Zones: Annual Review of Earth and Planetary Sciences, v. 14, p. 149–175, doi:10.1146/annurev.ea.14.050186.001053.

Silva, A.J.F.d., 2017, Processos de migmatização no Complexo Granulítico de Granja (Domínio Médio Coreaú, Ceará, Brasil) PhD: Aveiro, Portugal, Universidade de Aveiro.

Silva, H.F., 1989, Alguns aspectos petrográficos e geoquímicos do batólito de Quixadá: Revista Brasileira de Geociências, v. 19, no. 1, p. 101–107.

Silva, L.C., Armstrong, R., Pimentel, M.M., Scandolara, J., Ramgrab, G., Wildner, W., Angelim, L.A.d.A., Vasconcelos, A.M., Rizzoto, G., Quadros, M.L.d.E.S., Sander, A., and Rosa, A.L.Z.d., 2002, Reavaliação da Evolução Geológica em Terrenos Pré-Cambrianos Brasileiros com Base em Novos Dados U-Pb SHRIMP, Parte III: Províncias Borborema, Mantiqueira Meridional e Rio Negro-Juruena: Revista Brasileira de Geociências, v. 32, no. 4, p. 529–544.

Simpson, C., and Wintsch, R.P., 1989, Evidence for deformation-induced K-feldspar replacement by myrmekite: Journal of Metamorphic Geology, v. 7, no. 2, p. 261–275, doi:10.1111/j.1525-1314.1989.tb00588.x, URL http://doi.wiley.com/10.1111/j.1525-1314.1989.tb00588.x.

Snyder, D., and Tait, S., 1995, Replenishment of magma chambers: comparison of fluid-mechanic experiments with field relations: Contributions to Mineralogy and Petrology, v. 122, no. 3, p. 230–240, doi:10.1007/s004100050123, URL http://link.springer.com/10.1007/s004100050123.

Sousa, H.P.d., 2016, Caracterização das unidades máficas-ultramáficas e potencial metalogenético da sequência metavulcanossedimentar Serra das Pipocas (Ceará): Um provável greenstone belt [Master's thesis]: Fortaleza, Universidade Federal do Ceará.

Stein, S., and Sella, G.F., 2013, Plate Boundary Zones: Concepts and Approaches, *in* Stein, S., and Freymueller, J.T., eds., Geodynamics Series: Washington, D. C., American Geophysical Union, p. 1–26, doi:10.1029/GD030p0001, URL http://doi.wiley.com/10.1029/GD030p0001.

Stephenson, A., 1994, Distribution anisotropy: two simple models for magnetic lineation and foliation: Physics of the Earth and Planetary Interiors, v. 82, no. 1, p. 49–53, doi:10.1016/0031-9201(94)90101-5, URL https://linkinghub.elsevier.com/retrieve/pii/0031920194901015.

Stevenson, C., 2009, The relationship between forceful and passive emplacement: The interplay between tectonic strain and magma supply in the Rosses Granitic Complex, NW Ireland: Journal of Structural Geology, v. 31, no. 3, p. 270–287, doi:10.1016/j.jsg.2008.11.009, URL https://linkinghub.elsevier.com/retrieve/pii/S0191814108002010.

Stipp, M., Fügenschuh, B., Gromet, L.P., Stünitz, H., and Schmid, S.M., 2004, Contemporaneous plutonism and strike-slip faulting: A case study from the Tonale fault zone north of the Adamello pluton (Italian Alps): CONTEMPORANEOUS PLUTONISM AND FAULTING: Tectonics, v. 23, no. 3, p. n/a–n/a, doi:10.1029/2003TC001515, URL http://doi.wiley.com/10.1029/2003TC001515.

Stipp, M., and Kunze, K., 2008, Dynamic recrystallization near the brittle-plastic transition in naturally and experimentally deformed quartz aggregates: Tectonophysics, v. 448, no. 1-4, p. 77–97, doi:10.1016/j.tecto.2007.11.041, URL https://linkinghub.elsevier.com/retrieve/pii/S0040195107003915.

Stipp, M., Stünitz, H., Heilbronner, R., and Schmid, S.M., 2002a, Dynamic recrystallization of quartz: correlation between natural and experimental conditions: Geological Society, London, Special Publications, v. 200, no. 1, p. 171–190, doi:10.1144/GSL.SP.2001.200.01.11, URL http://sp.lyellcollection.org/lookup/doi/10.1144/GSL.SP.2001.200.01.11.

Stipp, M., Stünitz, H., Heilbronner, R., and Schmid, S.M., 2002b, The eastern Tonale fault zone: a 'natural laboratory' for crystal plastic deformation of quartz over a temperature range from 250 to 700°C: Journal of Structural Geology, v. 24, no. 12, p. 1861–1884, doi:10.1016/S0191-8141(02)00035-4, URL https://linkinghub.elsevier.com/retrieve/pii/S0191814102000354.

Stipp, M., and Tullis, J., 2003, The recrystallized grain size piezometer for quartz: Geophysical Research Letters, v. 30, no. 21, doi:10.1029/2003GL018444, URL http://doi.wiley.com/10.1029/2003GL018444.

Stipp, M., Tullis, J., and Behrens, H., 2006, Effect of water on the dislocation creep microstructure and flow stress of quartz and implications for the recrystallized grain

size piezometer: Journal of Geophysical Research, v. 111, no. B4, doi:10.1029/2005JB003852, URL http://doi.wiley.com/10.1029/2005JB003852.

Stipp, M., Tullis, J., Scherwath, M., and Behrmann, J.H., 2010, A new perspective on paleopiezometry: Dynamically recrystallized grain size distributions indicate mechanism changes: Geology, v. 38, no. 8, p. 759–762, doi:10.1130/G31162.1, URL http://pubs.geoscienceworld.org/geology/article/38/8/759/130364/A-new-perspective-on-paleopiezometry-Dynamically.

Storti, F., Holdsworth, R.E., and Salvini, F., 2003, Intraplate strike-slip deformation belts: Geological Society, London, Special Publications, v. 210, no. 1, p. 1–14, doi:10.1144/GSL.SP.2003.210.01.01, URL http://sp.lyellcollection.org/lookup/doi/10.1144/GSL.SP.2003.210.01.01.

Stünitz, H., 1998, Syndeformational recrystallization - dynamic or compositionally induced?: Contributions to Mineralogy and Petrology, v. 131, no. 2-3, p. 219–236, doi:10.1007/s004100050390, URL http://link.springer.com/10.1007/s004100050390.

Stüwe, K., 2007, Geodynamics of the Lithosphere An Introduction: Berlin; Heidelberg, Springer, oCLC: 781029854.

Sutherland, R., 1994, Displacement since the Pliocene along the southern section of the Alpine fault, New Zealand: Geology, v. 22, no. 4, p. 327–330, doi:10.1130/0091-7613(1994)022<0327:DSTPAT>2.3.CO;2.

Swanson, M.T., 1989, Sidewall ripouts in strike-slip faults: Journal of Structural Geology, v. 11, no. 8, p. 933–948, doi:10.1016/0191-8141(89)90045-X, URL https://linkinghub.elsevier.com/retrieve/pii/019181418990045X.

Tapponnier, P., Peltzer, G., Le Dain, A.Y., Armijo, R., and Cobbold, P., 1982, Propagating extrusion tectonics in Asia: New insights from simple experiments with plasticine: Geology, v. 10, no. 12, p. 611, doi:10.1130/0091-7613(1982)10<611:PETIAN>2.0.CO;2, URL https://pubs.geoscienceworld.org/geology/article/10/12/611-616/203380.

Tapponnier, P., Zhiqin, X., Roger, F., Meyer, B., Arnaud, N., Wittlinger, G., and Jingsui, Y., 2001, Oblique Stepwise Rise and Growth of the Tibet Plateau: Science, v. 294, no. 5547, p. 1671–1677, doi:10.1126/science.105978, URL https://www.sciencemag.org/lookup/doi/10.1126/science.105978.

Tauxe, L., 2005, Lectures in Paleomagnetism: URL http://earthref.org/MAGIC/books/Tauxe/2005/.

Taylor, M., and Peltzer, G., 2006, Current slip rates on conjugate strike-slip faults in central Tibet using synthetic aperture radar interferometry: STRIKE-SLIP SAR RATES, CENTRAL TIBET: Journal of Geophysical Research: Solid Earth, v. 111, no. B12, p. n/a–n/a, doi:10.1029/2005JB004014, URL http://doi.wiley.com/10.1029/2005JB004014.

Thatcher, W., 2007, Microplate model for the present-day deformation of Tibet: Journal of Geophysical Research, v. 112, no. B1, p. B01,401, doi:10.1029/2005JB004244, URL http://doi.wiley.com/10.1029/2005JB004244.

Thiede, R.C., Bookhagen, B., Arrowsmith, J., Sobel, E.R., and Strecker, M.R., 2004, Climatic control on rapid exhumation along the Southern Himalayan Front: Earth and Planetary Science Letters, v. 222, no. 3-4, p. 791–806, doi:10.1016/j.epsl.2004.03.015, URL https://linkinghub.elsevier.com/retrieve/pii/S0012821X04001980.

Tokle, L., Hirth, G., and Behr, W., 2019, Flow laws and fabric transitions in wet quartzite: Earth and Planetary Science Letters, v. 505, p. 152–161, doi:10.1016/j.epsl.2018.10.017, URL https://linkinghub.elsevier.com/retrieve/pii/S0012821X18306137.

Tommasi, A., Vauchez, A., Femandes, L.A.D., and Porcher, C.C., 1994, Magma-assisted strain localization in an orogen-parallel transcurrent shear zone of southern Brazil: Tectonics, v. 13, no. 2, p. 421–437, doi:10.1029/93TC03319, URL http://doi.wiley.com/10.1029/93TC03319.

Townend, J., and Zoback, M.D., 2000, How faulting keeps the crust strong: , p. 4.

Toy, V.G., Prior, D.J., and Norris, R.J., 2008, Quartz fabrics in the Alpine Fault mylonites: Influence of pre-existing preferred orientations on fabric development during progressive uplift: Journal of Structural Geology, v. 30, no. 5, p. 602–621, doi:10.1016/j.jsg.2008.01.001, URL https://linkinghub.elsevier.com/retrieve/pii/S0191814108000035.

Trindade, R.I., Raposo, M.B., Ernesto, M., and Siqueira, R., 1999, Magnetic susceptibility and partial anhysteretic remanence anisotropies in the magnetite-bearing granite pluton of Tourão, NE Brazil: Tectonophysics, v. 314, no. 4, p. 443–468, doi:10.1016/S0040-1951(99)00220-6, URL https://linkinghub.elsevier.com/retrieve/pii/S0040195199002206.

Tullis, J., 1983, Deformation of feldspars, *in* Feldspar Mineralogy: 2nd edn., no. 2 in Reviews in mineralogy, Washington, DC, Mineralogical Soc. of America, p. 297–324.

Tullis, J., and Yund, R.A., 1985, Dynamic recrystallization of feldspar: A mechanism for ductile shear zone formation: Geology, v. 13, no. 4, p. 238, doi:10.1130/0091-7613(1985)13<238:DROFAM>2.0.CO;2, URL https://pubs.geoscienceworld.org/geology/article/13/4/238-241/185761.

Twiss, R.J., 1977, Theory and applicability of a recrystallized grain size paleopiezometer: v. 115, p. 18.

van der Woerd, J., Klinger, Y., Sieh, K., Tapponnier, P., Ryerson, F.J., and Mériaux, A.S., 2006, Long-term slip rate of the southern San Andreas Fault from 10Be-26Al surface exposure dating of an offset alluvial fan: Journal of Geophysical Research, v. 11, p. 1–17, doi:10.1029/2004JB003559.

van Schmus, W.R., Oliveira, E.P., da Silva Filho, A.F., Toteu, S.F., Penaye, J., and Guimarães, I.P., 2008, Proterozoic links between the Borborema Province, NE Brazil, and the Central African Fold Belt: Geological Society, London, Special Publications, v. 294, no. 1, p. 69–99, doi:10.1144/SP294.5, URL http://sp.lyellcollection.org/lookup/doi/10.1144/SP294.5.

Vance, J.A., 1969, On synneusis: Contributions to Mineralogy and Petrology, v. 24, no. 1, p. 7–29, doi:10.1007/BF00398750, URL http://link.springer.com/10.1007/BF00398750.

Vanderhaeghe, O., 2012, The thermal–mechanical evolution of crustal orogenic belts at convergent plate boundaries: A reappraisal of the orogenic cycle: Journal of Geodynamics, v. 56-57, p. 124–145, doi:10.1016/j.jog.2011.10.004, URL https://linkinghub.elsevier.com/retrieve/pii/S0264370711001165.

Vauchez, A., Neves, S., Caby, R., Corsini, M., Egydio-Silva, M., Arthaud, M., and Amaro, V., 1995, The Borborema shear zone system, NE Brazil: Journal of South American Earth Sciences, v. 8, no. 3-4, p. 247–266, doi:10.1016/0895-9811(95)00012-5, URL https://linkinghub.elsevier.com/retrieve/pii/0895981195000125.

Vauchez, A., and Tommasi, A., 2003, Wrench faults down to the asthenosphere: geological and geophysical evidence and thermomechanical effects: Geological Society, London, Special Publications, v. 210, no. 1, p. 15–34, doi:10.1144/GSL.SP.2003.210.01.02, URL http://sp.lyellcollection.org/lookup/doi/10.1144/GSL.SP.2003.210.01.02.

Vaughan, A.P.M., and Scarrow, J.H., 2003, K-rich mantle metasomatism control of localization and initiation of lithospheric strike-slip faulting: Terra Nova, v. 15, no. 3, p. 163–169, doi:10.1046/j.1365-3121.2003.00485.x, URL http://doi.wiley.com/10.1046/j.1365-3121.2003.00485.x.

Viegas, G., Menegon, L., and Archanjo, C., 2016, Brittle grain-size reduction of feldspar, phase mixing and strain localization in granitoids at mid-crustal conditions (Pernambuco shear zone, NE Brazil): Solid Earth, v. 7, no. 2, p. 375–396, doi:10.5194/se-7-375-2016, URL https://www.solid-earth.net/7/375/2016/.

Viegas, L.G.F., Archanjo, C.J., Hollanda, M.H.B., and Vauchez, A., 2014, Microfabrics and zircon U–Pb (SHRIMP) chronology of mylonites from the Patos shear zone (Borborema Province, NE Brazil): Precambrian Research, v. 243, p. 1–17, doi:10.1016/j.precamres.2013.12.020, URL https://linkinghub.elsevier.com/retrieve/pii/S0301926814000023.

Viegas, L.G.F., Archanjo, C.J., and Vauchez, A., 2013, Fabrics of migmatites and the relationships between partial melting and deformation in high-grade transpressional shear zones: The Espinho Branco anatexite (Borborema Province, NE Brazil): Journal of Structural Geology, v. 48, p. 45–56, doi:10.1016/j.jsg.2012.12.008, URL https://linkinghub.elsevier.com/retrieve/pii/S0191814112002799.

Vigneresse, J.L., 1995, Control of granite emplacement by regional deformation: Tectonophysics, v. 249, no. 3-4, p. 173–186, doi:10.1016/0040-1951(95)00004-7, URL https://linkinghub.elsevier.com/retrieve/pii/0040195195000047.

von Blanckenburg, F., and Davies, J.H., 1995, Slab breakoff: A model for syncollisional magmatism and tectonics in the Alps: Tectonics, v. 14, no. 1, p. 120–131, doi:10.1029/94TC02051, URL http://doi.wiley.com/10.1029/94TC02051.

von Blanckenburg, F., Villa, I.M., Baur, H., Morteani, G., and Steiger, R.H., 1989, Time calibration of a PT-path from the Western Tauern Window, Eastern Alps: the problem of closure temperatures: Contributions to Mineralogy and Petrology, v. 101, no. 1, p. 1–11, doi:10.1007/BF00387196, URL http://link.springer.com/10.1007/BF00387196.

Wadge, G., and Cross, A., 1988, Quantitative methods for detecting aligned points: An application to the volcanic vents of the Michoacan-Guanajuato volcanic field, Mexico: Geology, v. 16, p. 815–818.

Wallis, D., Phillips, R.J., and Lloyd, G.E., 2013, Fault weakening across the frictional-viscous transition zone, Karakoram Fault Zone, NW Himalaya: FAULT WEAKENING, KARAKORAM FAULT ZONE: Tectonics, v. 32, no. 5, p. 1227–1246, doi:10.1002/tect.20076, URL http://doi.wiley.com/10.1002/tect.20076.

Wallis, S.R., Platt, J.P., and Knott, S.D., 1993, Recognition of syn-convergence extension in accretionary wedges with examples from the Calabrian Arc and the Eastern Alps: American Journal of Science, v. 293, no. 5, p. 463–494, doi:10.2475/ajs.293.5.463, URL http://www.ajsonline.org/cgi/doi/10.2475/ajs.293.5.463.

Weinberg, R., Sial, A., and Mariano, G., 2004, Close spatial relationship between plutons and shear zones: Geology, v. 32, no. 5, p. 377, doi:10.1130/G20290.1, URL https://pubs.geoscienceworld.org/geology/article/32/5/377-380/29425.

Weinberg, R.F., Mark, G., and Reichardt, H., 2006, Magma ponding in the Karakoram shear zone, Ladakh, NW India: Geological Society of America Bulletin, v. preprint, no. 2008, p. 1, doi:10.1130/B26358.1, URL https://pubs.geoscienceworld.org/gsabulletin/article/121/1-2/278-285/2336.

Weinberg, R.F., and Podladchikov, Y., 1994, Diapiric ascent of magmas through power law crust and mantle: Journal of Geophysical Research: Solid Earth, v. 99, no. B5, p. 9543–9559, doi:10.1029/93JB03461, URL http://doi.wiley.com/10.1029/93JB03461.

Wenk, H.R., Yu, R., Vogel, S., and Vasin, R., 2019, Preferred Orientation of Quartz in Metamorphic Rocks from the Bergell Alps: Minerals, v. 9, no. 5, p. 277, doi:10.3390/min9050277, URL https://www.mdpi.com/2075-163X/9/5/277.

West, D.P., and Hubbard, M.S., 1997, Progressive localization of deformation during exhumation of a major strike-slip shear zone: Norumbega fault zone, south-central Maine, USA: Tectonophysics, v. 273, no. 3-4, p. 185–201, doi:10.1016/S0040-1951(96)00306-X, URL https://linkinghub.elsevier.com/retrieve/pii/S004019519600306X.

Wetherill, G.W., 1956, Discordant uranium-lead ages, I: Transactions, American Geophysical Union, v. 37, no. 3, p. 320, doi:10.1029/TR037i003p00320, URL http://doi.wiley.com/10.1029/TR037i003p00320.

White, S., Burrows, S., Carreras, J., Shaw, N., and Humphreys, F., 1980, On mylonites in ductile shear zones: Journal of Structural Geology, v. 2, no. 1-2, p. 175–187, doi:10.1016/0191-8141(80)90048-6, URL https://linkinghub.elsevier.com/retrieve/pii/0191814180900486.

Wiebe, R.A., 2016, Mafic replenishments into floored silicic magma chambers: American Mineralogist, v. 101, no. 2, p. 297–310, doi:10.2138/am-2016-5429,

URL https://pubs.geoscienceworld.org/ammin/article/101/2/297-310/104943.

Wilson, C.J.L., 1975, Preferred Orientation in Quartz Ribbon Mylonites: Geological Society of America Bulletin, v. 86, p. 968–974.

Wright, T.J., Elliott, J.R., Wang, H., and Ryder, I., 2013, Earthquake cycle deformation and the Moho: Implications for the rheology of continental lithosphere: Tectonophysics, v. 609, p. 504–523, doi:10.1016/j.tecto.2013.07.029, URL https://linkinghub.elsevier.com/retrieve/pii/S0040195113004708.

Xia, H., and Platt, J.P., 2018, Quartz grainsize evolution during dynamic recrystallization across a natural shear zone boundary: Journal of Structural Geology, v. 109, p. 120–126, doi:10.1016/j.jsg.2018.01.007, URL https://linkinghub.elsevier.com/retrieve/pii/S0191814118300415.

Yakovlev, P.V., and Clark, M.K., 2014, Conservation and redistribution of crust during the Indo-Asian collision: Mass balance of the Indo-Asian orogen: Tectonics, v. 33, no. 6, p. 1016–1027, doi:10.1002/2013TC003469, URL http://doi.wiley.com/10.1002/2013TC003469.

Zen, E.a., and Hammarstrom, J.M., 1984, Magmatic epidote and its petrologic significance: Geology, v. 12, no. 9, p. 515, doi:10.1130/0091-7613(1984)12<515:MEAIPS>2.0.CO;2, URL https://pubs.geoscienceworld.org/geology/article/12/9/515-518/186205.

Zhang, P.Z., Shen, Z., Wang, M., Gan, W., Bürgmann, R., Molnar, P., Wang, Q., Niu, Z., Sun, J., Wu, J., Hanrong, S., and Xinzhao, Y., 2004, Continuous deformation of the Tibetan Plateau from global positioning system data: Geology, v. 32, no. 9, p. 809, doi:10.1130/G20554.1, URL https://pubs.geoscienceworld.org/geology/article/32/9/809-812/103748.

Zoback, M.D., Zoback, M.L., Mount, V.S., Suppe, J., Eaton, J.P., Healy, J.H., Oppenheimer, D., Reasenberg, P., Jones, L., Raleigh, C.B., Wong, I.G., Scotti, O., and Wentworth, C., 1987, New Evidence on the State of Stress of the San Andreas Fault System: Science, v. 238, no. 4830, p. 1105–1111, doi:10.1126/science.

238.4830.1105, URL http://www.sciencemag.org/cgi/doi/10.1126/science.238.4830.1105.

Zulauf, G., 2001, Structural style, deformation mechanisms and paleodifferential stress along an exposed crustal section: constraints on the rheology of quartzofeldspathic rocks at supra- and infrastructural levels (Bohemian Massif): Tectonophysics, v. 332, no. 1-2, p. 211–237, doi:10.1016/S0040-1951(00)00258-4, URL https://linkinghub.elsevier.com/retrieve/pii/S0040195100002584.